TECHNISCHE UNIVERSITÄT MÜNCHEN
Lehrstuhl für Technische Elektrochemie

The Influence of Irreversible Electrochemical Reactions on the Fundamental Mechanisms Governing Capacity and Cycle Life of Li-O_2 Batteries

Stefano Meini

Vollständiger Abdruck der von der Fakultät für Chemie der Technischen Universität München zur Erlangung des akademischen Grades eines

Doktors der Naturwissenschaften

genehmigten Dissertation.

Vorsitzender:	Univ.-Prof. Dr. S. Günther
Prüfer der Dissertation:	
	1. Univ.-Prof. H. Gasteiger, Ph.D.
	2. Univ.-Prof. Dr. T. Nilges
	3. Univ.-Prof. Dr. K.-O. Hinrichsen

Die Dissertation wurde am 20.06.2013 bei der Technischen Universität München eingereicht und durch die Fakultät für Chemie am 19.07.2013 angenommen.

Maiori Forsan cum Timore Sententiam in Me Fertis Quam Ego Accipiam

Giordano Bruno (1600)

Contents

List of Acronyms **7**
Abstract **9**

Chapter 1 .... **11**
  Introduction **11**

Chapter 2 .... **19**
  Experimental Backgrounds and Methods **19**
    2.1 General Background on Battery Electrochemistry **19**
      2.1.1 Electrochemical Reactions 19
      2.1.2 Battery Thermodynamics 19
      2.1.3 Voltage Losses 21
      2.1.4 Cell Setup and Potential Scale 21
    2.2 Electrode Preparation **23**
      2.2.1 Different Requirements of Li-air Compared to Li-ion Electrodes 23
      2.2.2 Background on Battery Electrode Preparation 24
      2.2.3 Preparation of Air Electrodes 25
      2.2.4 Preparation of Pre-Filled Electrodes 25
    2.3 Electrolyte Solutions **27**
      2.3.1 General Handling Procedures 27
      2.3.2 Investigation on Reactivity of Electrolyte Solvents with Superoxide 27
      2.3.3 Long Term Stability of Electrolyte Solvents with Superoxide 29
    2.4 Battery Test Cell Design and Assembly **29**
      2.4.1 Cell Design 29
      2.4.2 Cell Assembly 30
    2.5 Electrochemical Methods **32**
      2.5.1 Battery Cycling 32
      2.5.2 State of Charge (SOC) 32
      2.5.3 Determination of Background Currents in Li-O_2 Cells 33
      2.5.4 Electrochemical Impedance Spectroscopy (EIS) 34
    2.6 Product Selectivity of Li-O_2 Cells Via O_2 Consumption **35**
      2.6.1 Principles of Product Selectivity Measurements in Li-Air Batteries 35
      2.6.2 Oxygen Consumption Experimental Setup 37
    2.7 On-Line Electrochemical Mass Spectrometry (OEMS) **38**
      2.7.1 Background on Electrochemical Mass Spectrometry 38
      2.7.2 Online Electrochemical Mass Spectrometry Experimental Setup 39
      2.7.3 OEMS Data Acquisition and Data Treatment 40
    2.8 Electrode Characterization **42**
      2.8.1 Carbon Loading of Air Electrodes 42
      2.8.2 Surface Analysis of Air Electrodes: BET Method 42
      2.8.3 Characterization of Pre-Filled Electrodes by X-Ray Diffraction (XRD) 43

2.8.4 Characterization of Pre-Filled Electrodes by IR-ATR Spectroscopy 44
2.8.5 Thermogravimetric Analysis - Mass Spectrometry (TGA-MS) 45

Chapter 3 49

Investigations on Li-air Battery Discharge Limitations and Effect of Contaminants on Capacity and Cycling Performace 49

3.1 The Effect of Water on the Discharge Capacity of a Non-Catalyzed Carbon Cathode for Li-O_2 Batteries 50
3.2 Effect of Carbon Surface Area on First Discharge Capacity of Li-O_2 Cathodes and Cycle-Life Behavior in Ether-Based Electrolytes 55
3.3 Stability of Superoxide Radicals in Glyme Solvents for Non-Aqueous Li-O_2 Battery Electrolytes 59
3.4 Conclusions 63

Chapter 4 65

Understanding the Charge Process of Li-Air Batteries: Role of Electrolyte Solution and Electrode Material on Reversibility and Cycle Life 65

4.1 A Novel On-Line Mass Spectrometer Design for the Study of Multiple Charging Cycles of a Li-O_2 Battery 66
4.2 Rechargeability of Li-Air Cathodes Pre-Filled with Discharge Products Using an Ether Based Electrolyte Solution 71
4.3 Thermal and Electrochemical Decomposition of Lithium Peroxide in Non-Catalyzed Carbon Cathodes for Li-Air Batteries 75
4.4 Conclusions 79

Chapter 5 81

Conclusions 81

References 85
List of Figures 89
List of Tables 91
Acknowledgements 93
Curriculum Vitae 95
List of Publications 97
Patents 97

List of Acronyms

EV	Electric Vehicle
FC	Fuel Cell
PEMFC	Polymer Electrolyte Membrane Fuel Cell
LIB	Li-ion Batteries
Ni-MH	Ni-Metal Hydride
AM	Active Material
ORR	Oxygen Reduction Reaction
OER	Oxygen Evolution Reaction
PC	Propylene Carbonate
LiTFSI	Li bis(TriFluoromethyl-Sulfonyl)Imide
DMSO	Di-Methyl Sulfoxide
OCV	Open Circuit Voltage
WE	Working Electrode
CE	Counter Electrode
RE	Reference Electrode
SOC	State of Charge
CB	Carbon Black
GDL	Gas Diffusion Layer
IPA	Iso-Propyl Alcohol
NMP	N-Methyl Pyrrolydone
PEO	Poly Ethylene Oxide
PTFE	Poly(TetraFluoro-Ethylene)
PCTFE	Poly(ChloroTrifluoro-Ethylene)
PVdF	Poly(Vinilidene-di-Fluoride)
BET	Brunauer Emmet Teller
XRD	X-Ray Diffraction
IR-ATR	Infra Red - Attenuated Total Reflectance
TGA-MS	Thermo Gravimetric Analysis - Mass Spectrometry
OEMS	On-line Electrochemical Mass Spectrometry
GC-MS	Gas Chromatography - Mass Spectrometry
DEMS	Differential Electrochemical Mass Spectrometry

Abstract

Die 3-fach höhere spezifische Energie von nicht-wässrigen Lithium-Luft Batterien im Vergleich zu herkömmlichen Li-Ionen Batterien könnte ein bedeutender Schritt in Richtung Elektromobilität sein. Diese Batterieform ist jedoch noch durch geringe Wiederaufladbarkeit und Kapazität limitiert. In dieser Arbeit wurden die Mechanismen, welche Kapazität und Entladungsrate limitieren, vor allem die Bildung von einer passivierenden Produktschicht auf der positiven Elektrodenoberfläche, untersucht. Die Ladung von Modellelektroden, die mit möglichen Entladungsprodukten gefüllt sind, zeigte, dass Li_2O_2 als einziges Reaktionsprodukt zur gewünschten Reversibilität des Systems führt. Eine weitere Herausforderung ist die bisher unzureichende Stabilität des Elektrodenmaterials für die positive Elektrode, wodurch sich die Lebensdauer der Batterie reduziert.

The 3-fold higher specific energy of non-aqueous Li-air batteries compared to state-of-the-art Li-Ion batteries could represent a fundamental step for electrical storage technology for automotive applications. Unfortunately, that promising technology is still affected by low rate capability and rechargeability. In this work, the mechanisms that limit capacity and rate capability were investigated, with particular focus on the formation of a discharge product passivation layer on the positive electrode surface. Charge experiments of model electrodes pre-filled with possible discharge products showed that only Li_2O_2 can ensure the desired reversibility of the system, and other discharge products must be avoided. The fundamental reactions that limit the stability of positive electrode materials based on carbon during the charge process were also chemically and electrochemically investigated.

This doctoral thesis is the cumulative integration of the scientific papers resulting from my work as a doctoral candidate at the Chair of Technical Electrochemistry (TEC). After an introduction about the topic of Li-air batteries, the main experimental methods employed are described. Subsequently, my three scientific publications are presented together with three other relevant publications in which my contribution was crucial. The results are presented in two main topics (chapters), i.e. "Investigations on Li-air battery discharge" and "Understanding the charge process of Li-air batteries". The thesis is closed with an overall conclusion section regarding my whole work at TEC.

Chapter 1

Introduction

The automobile is undoubtedly one of the devices that deeply changed mankind's life. Since the early twentieth century, automobiles changed their shapes, and many improvements were achieved in terms of stability, power, safety and efficiency. However, since the introduction of internal combustion engines, petroleum derivatives have been the main power sources for automotive applications. Due to the environmental concerns related to their use as energy source within dense urban agglomerates, and due to expected shortages in the medium future [1], the electrification of the vehicular fleet is a possible solution to mitigate environmental threats and dependence on fossil fuels.

Electric motors of modern electric vehicles (EVs) can be powered by either fuel cells (FCs) or batteries. There is a main difference between those devices that one has to take into account when designing an electric car; modern EV fuel cells systems (PEMFC) rely on a fuel *tank* for providing the needed energy, therefore the electrodes are only *chemical-to-electrical-energy converters*. On the other hand, a *battery* works both as *energy converter* and *energy storage* device; the electrical energy that can be stored in a battery is therefore directly proportional to the electrode weight/extension, for given electrode materials. Similarly to internal combustion engine systems, the required electrical energy (kWh) provided by a Fuel Cell system can be increased by increasing its specific energy (Wh/Kg), i.e. by increasing the dimensions of the fuel tank. On the other hand, the required electrical energy provided by a battery can be increased only by increasing the size (and weight) of the *whole system*, since its specific energy is fixed [2].

Rechargeable batteries have several advantages over fuel cells. First, battery electrochemistry does not in principle rely on noble metals (Pt); second, batteries generally have much higher energy efficiency (up to 95 %, to be compared to 50-60 % tank-to-wheel for FC systems [3]); third, batteries do not need in principle a deep redesign of the electrical grid infrastructure (widespread use of H_2 fuel cells implies the development of a H_2 supply infrastructure *ex novo*).

Li-ion is at present the most advanced rechargeable battery technology commercially available. Due to their outstanding energy density (650 Wh/L), higher specific energy (210 Wh/Kg) [4], long cycle life and lack of memory effect in comparison with other rechargeable battery chemistries (e.g. nickel-metal hydride, Ni-MH), Li-ion batteries (LIBs) are extensively used for powering personal electronic devices. However, the application of Li-ion technology for automotive purposes is facing major challenges.

The state of the art specific energy of 100-200 Wh_{net}/Kg_{pack} obtainable for an EV battery system [2] puts severe constrains to the development of battery powered full electric vehicles. For example, the battery pack used by the commercial EV Tesla Roadster provides weighs 450 kg and provides 53 kWh, corresponding to up to 350 km of range. The integration of such heavy (and expensive) storage system is clearly not an easy task for smaller and inexpensive models. For that reason, reduction of battery weight and cost is mandatory for allowing LIB powered EVs to become a widespread commercial reality.

The weight of Li-ion battery packs for automotive applications consists of 4 main contributions [2]:

- The pack components and electronics. ≈ 50% of the total weight.
- The positive electrode material. ≈ 25% of the total weight.
- The negative electrode material. ≈ 15% of the total weight.
- The electrolyte solution. ≈ 10% of the total weight.

As a reduction of mass of the pack components (the most important contribution to weight) would necessary result in a reduced safety in case of accident, that direction seems precluded unless much lighter materials are developed with the same mechanical properties. The second major contribution to weight is the positive electrode material; the working principle of all modern Li-ion battery materials is the *intercalation* of Li ions within the inter-planar space of layered structures such as graphite (negative electrode) or layered metal oxides ($LiCoO_2$, positive electrode). Commercial positive electrode materials have practical capacities commonly smaller than 200 mAh/g (e.g. 140 mAh/g for $LiCoO_2$) and working potentials ranging between 3.5-4.0 V vs. the Li^+/Li standard reduction potential [5]. Since the positive electrode is the heaviest in a commercial Li-ion battery, a substantial increase of its specific energy (in other words a substantial reduction in weight) would result in a substantial improvement of the overall battery pack energy density.

The specific energy of any battery can be described as follows, and it is reported as [J/g] or more commonly as [Wh/kg]:

$$Specific\ energy = Q \cdot U \qquad \text{(Eq. 1.1)}$$

Q is the cell's specific capacity in [C/g] and U the cell's voltage in [V]. Increasing either cell voltage or specific capacity results in an improved specific energy. At the present time, both paths are submitted to extensive research and development. For example, high voltage layered materials such as Li phosphoolivines ($LiCoPO_4$) working in the potential range 4.5-5.2 V_{Li} can provide an enhancement in specific energy of ≈20 % compared to the state-of-the-art Li-ion technology [4-6]. High capacity materials based on metals more abundant than Co [7], like Mn spinel, are also interesting.

In order to overcome the intrinsic limitations of intercalation materials and obtain more remarkable improvements, completely innovative chemistries (commonly referred to as *post Li-ion*) must be pursued. Rechargeable non-aqueous Li-air batteries have the highest projected specific energy among *post Li-ion* technologies under investigation (e.g. Li-Sulfur), and they are therefore the most interesting for automotive applications. Non-aqueous Li-air batteries were introduced in 1996 by K.M. Abraham and coworkers [8], and they are based on the reversible electrochemical reduction of O_2 at a high surface positive electrode (the *air electrode*) [9] with Li^0. The air electrode is the key aspect of this technology and the source of its high projected specific energy [10]. A suitable material for the air electrode should fulfill the following requirements; low cost, low density, high electrical conductivity, mesoporous structure (to allow fast O_2 diffusion and to store the discharge products) and preferably high surface areas (faster oxygen reduction reaction and evolution kinetics). As the air electrode does not in principle participate in the electrochemical reaction, the choice of the air electrode material was made regardless of its chemical nature for more than one decade; both porous metals (e.g., Ni foam) and high structured carbon materials were employed. Carbon-based materials were however preferred, because of their structural variety and relatively low cost. Typically, positive electrodes are based on high surface carbon blacks [11], but more advanced materials such as carbon nanotubes [12,13] or graphene sheets [14-16] have been also used.

Most of the reports in the literature make use of pure O_2 instead of atmospheric air for testing Li-air cells, therefore the nomenclature *Li-O_2 batteries* is preferred when discussing about the pertaining results. *Li-air batteries*, however, a widely used nomenclature when referring to the general *concept* and *technology*.

The highly exergonic reaction of O_2 with Li metal provides energy to Li-air batteries. During battery *discharge*, O_2 is reduced electrochemically at the air electrode surface, and Li is oxidized at the Li metal/electrolyte solution interface. Thermodynamically, the expected reaction product of Li-air batteries is Li_2O_2 (R. 1.1). Li_2O is also a possible discharge product (R. 1.2), and due to the similar thermodynamic potential to that of Li_2O_2 ($E_{rev} \approx 2.9\ V_{Li}$), its partial formation in Li-air cells was previously proposed [17].

$$2Li^+ + 2e^- + O_{2(g)} \rightleftarrows Li_2O_{2(s)} \quad \Delta G^0 = -570.2\ \text{kJ/mol} / E_{rev} = 2.96\ V_{Li} \qquad \text{(R. 1.1)}$$

$$4Li^+ + 4e^- + O_{2(g)} \rightleftarrows 2Li_2O_{(s)} \quad \Delta G^0 = -561.2\ \text{kJ/mol} / E_{rev} = 2.91\ V_{Li} \qquad \text{(R. 1.2)}$$

During *charge*, the process is inverted. Ideally, Li_2O_x particles produced during discharge are oxidized and O_2 is evolved (Figure 1.1).

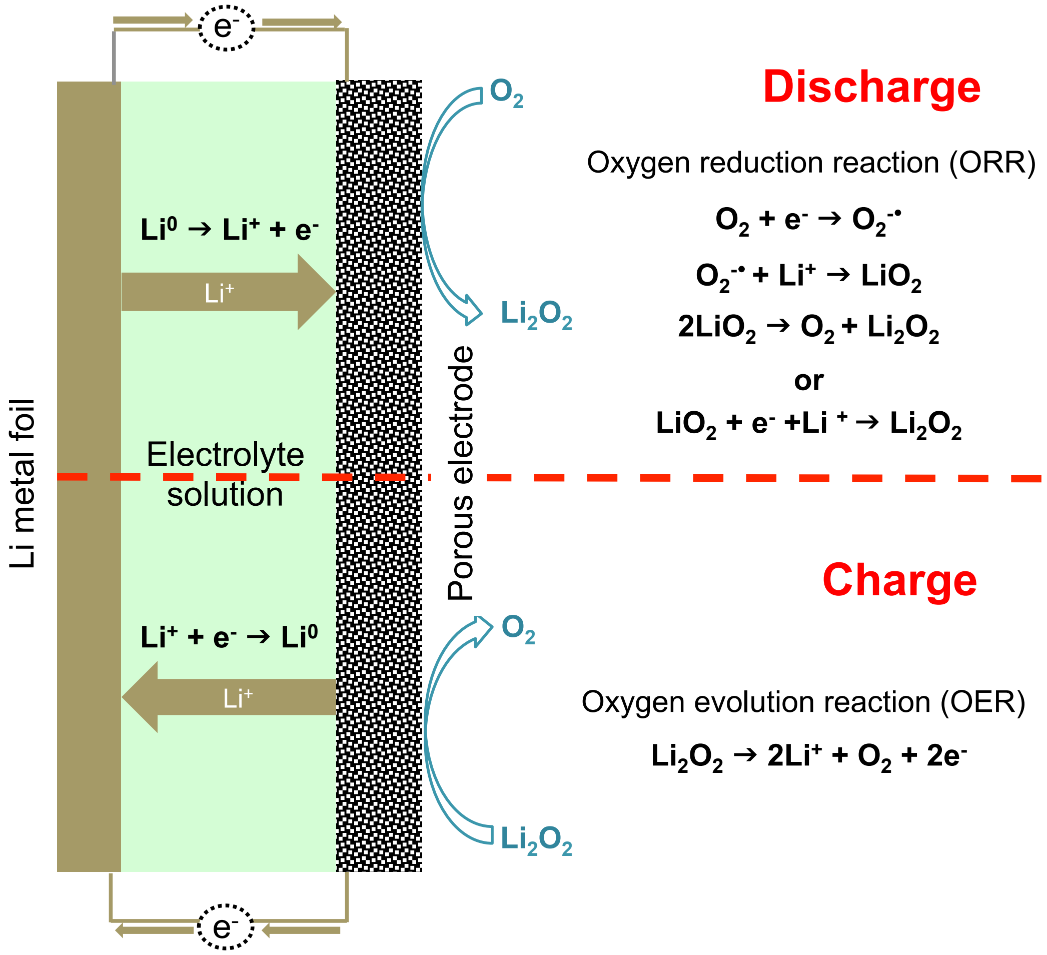
e-
Li metal foil
$Li^0 \rightarrow Li^+ + e^-$
Li^+
Electrolyte solution
$Li^+ + e^- \rightarrow Li^0$
Li^+
Porous electrode
O_2
Li_2O_2
Discharge
Oxygen reduction reaction (ORR)
$O_2 + e^- \rightarrow O_2^{-\bullet}$
$O_2^{-\bullet} + Li^+ \rightarrow LiO_2$
$2LiO_2 \rightarrow O_2 + Li_2O_2$
or
$LiO_2 + e^- + Li^+ \rightarrow Li_2O_2$
Charge
O_2
Li_2O_2
Oxygen evolution reaction (OER)
$Li_2O_2 \rightarrow 2Li^+ + O_2 + 2e^-$
e-

Figure 1.1. Schematic working principle of a Li-air battery during discharge (Li^0 is oxidized electrochemically by O_2) and charge (Li_2O_2 is electrooxidized to Li^0 and O_2).

Despite the lower nominal voltage of Li-air batteries compared to LIBs based on $LiMO_2$ type intercalation materials (2.9 V_{Li} vs. 3.7 V_{Li} respectively), the substantially higher specific capacity of the products (1168 mAh/g_{Li2O2}, to be compared to a maximum of 200 $mAh/g_{intercal.}$) concurs to the higher specific energy. For example, the specific energy of Li_2O_2 (i.e., the specific energy of an electrochemical system in which O_2 is reduced by Li^0 to Li_2O_2) is 3460 Wh/Kg_{Li2O2}, to be compared to 1030 Wh/Kg_{LiMO2} for $LiMO_2$ type battery materials [9]. Now, assuming the same specific energy loss observed for LIBs passing from the active material level to the commercial battery pack (1030 Wh/Kg_{LiMO2} typically translate into 100-200 Wh/Kg_{pack} i.e. at least a factor of 5), a fully packed Li-air battery would provide a maximum of ≈700 Wh/Kg_{pack}, corresponding to a substantial ≈3-fold improvement [9]. In addition, to that, O_2 is abundant and readily available from the ambient atmosphere.

The several theoretical advantages of Li-air batteries are unfortunately accompanied by low rate capability (the ability to be discharged at high current, i.e. high powers) [18-22] and very high overpotential for the oxygen evolution reaction (OER) upon charge (Figure 1.2), resulting in a much lower round-trip efficiency in comparison with commercial rechargeable batteries [23,24].

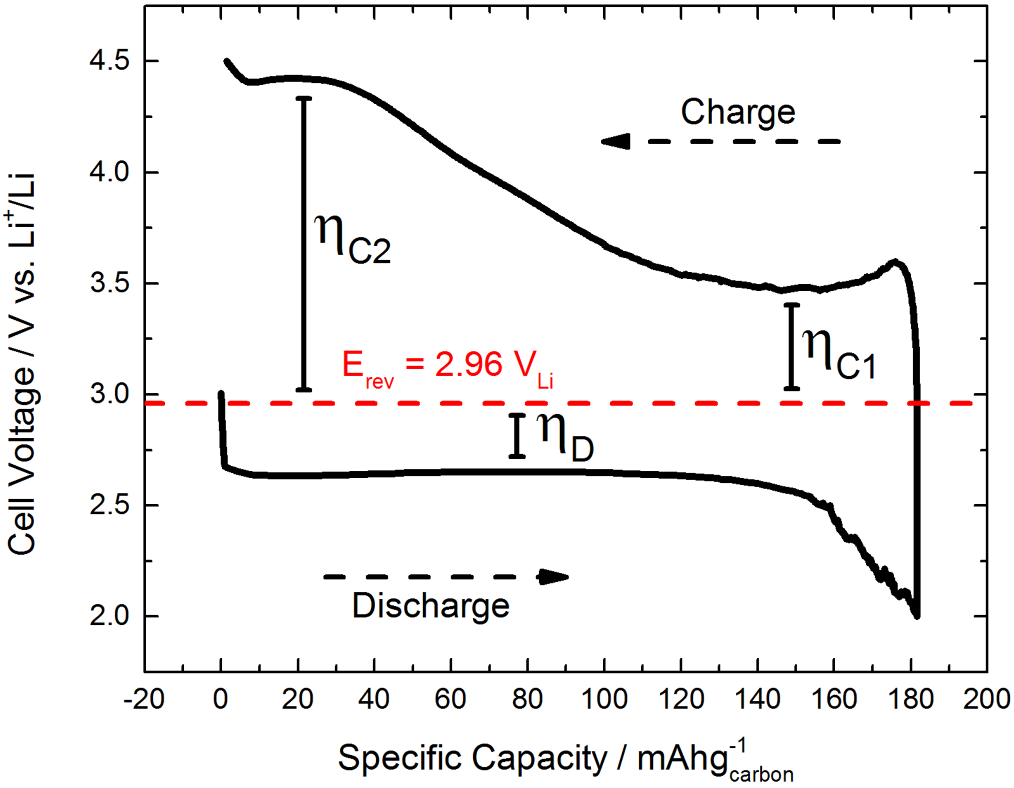

Figure 1.2. Typical voltage profile of a Li-air cell comprising a Li metal negative electrode, a carbon black based positive electrode and an ether-based electrolyte solution. The discharge proceeds as a single, flat voltage plateau corresponding to ORR, whereas the charge (OER) is a more complex process characterized by much higher overpotentials.

Typical currents for Li-air prototypes are on the order of 0.1 $mA/cm^2_{electrode}$, several orders of magnitude lower than Li-ion batteries (1-10 $mA/cm^2_{electrode}$). That issue was in the first place ascribed to the slow O_2 diffusion through the non-aqueous electrolyte solutions and to the sluggish oxygen reduction reaction (ORR) kinetics, resulting in high overpotentials and low rate capability. For that reason, engineering of the air electrode and optimization of the electrolyte solutions for enhanced O_2 mass transport to the electroactive surfaces was performed [21,25]. Furthermore, several researchers focused on ORR kinetics and on the use of catalysts [26-29] for reducing overpotential at the air electrode. Several inspiring works were published on noble metal electrocatalysis in non-aqueous Li^+ containing electrolytes, where bifunctional Pt-Au catalysts showed their activity for both ORR (Pt) and OER (Au) [22,23,26].

Non-noble metal oxides such as α-MnO_2 nanowires were employed as electrocatalyst in full Li-air cells for enhancing the kinetics of Li_2O_2 electrooxidation (OER), showing interesting catalytic activity and round trip efficiencies as high as 70% [24,30,31]. Nowadays, the influence of catalysts on Li_2O_2 electrooxidation is a controversial topic, wherein different groups working on catalysis obtain conflicting results. More precisely, McCloskey et al. have reported that no catalytic effect can be observed by charging previously discharged catalyzed electrodes [32]; on the other hand, Harding et al. demonstrated a strong catalytic effect when charging model electrodes *pre-filled* with chemically produced Li_2O_2 (commercially available), whereby Pt and Ru nanoparticles enhance electrooxidation currents by at least two orders of magnitude compared to non-catalyzed carbon at 4.0 V_{Li} [33]. These results are in agreement with those obtained in our laboratory, however it is yet unclear whether the morphology of Li_2O_2 particles (several monolayers of Li_2O_2 in McCloskey's work, ≈1 µm particles in Harding's work) could play a major role in determining the reduction on overpotential for OER. The influence of the product's morphology on the catalytic activity upon charge of Li-air cathodes is currently under investigation at TUM.

Similarly to Li-ion batteries, the performance and cycle life of non-aqueous Li-air batteries are strongly influenced by the nature of the electrolyte solution. Basic requirements of a Li-air battery electrolyte solution are:

- Ability to stabilize the negative electrode surface (Li metal) by forming a Li^+ conductive passivation layer (Solid Electrolyte Interface, SEI) [34]
- High O_2 solubility and diffusivity
- Low vapor pressure
- Stability at high potentials
- Chemical stability towards dissolved O_2
- Chemical stability towards Li_2O_2
- Chemical stability towards oxygen reduction reaction intermediates ($O_2^{-\bullet}$)

The well-characterized Li-ion battery electrolyte solutions based on alkyl carbonate solvents (e.g. Propylene Carbonate, PC) and $LiPF_6$ were extensively employed also in Li-air research from the early stages of the Li-air research up to 2011. In fact, alkyl carbonate electrolyte solutions are known to efficiently stabilize the negative electrolyte surface, furthermore O_2 solubility and diffusivity are sufficient for Li-air applications [25]. Unfortunately, thorough characterization of the electrodes after discharge using alkyl carbonate based electrolyte solution revealed that Li(alkyl)carbonates and Li_2CO_3 were produced as main discharge products instead of Li_2O_2 and Li_2O expected from the reaction of Li with O_2 [35-37].

Fundamental electrochemical studies on ORR in Li^+ containing non-aqueous electrolyte solutions carried out using a three electrode cell setup revealed that the reduction of O_2 does not proceed as a direct two-electrons process to Li_2O_2, but rather as a one-electron process to solvated $O_2^{-\bullet}$ or LiO_2 (superoxide ion radical or Li superoxide, from now on referred to as *ORR intermediates*), that can be either further reduced or disproportionate and precipitate as Li_2O_2 [38,39]. Unfortunately, alkyl-carbonate solvents readily react with those ORR intermediates, leading to Li(alkyl)carbonates and Li_2CO_3 [40-42] (Figure 1.3). For that reason, most of the data available on the topic from that time period must be critically evaluated.

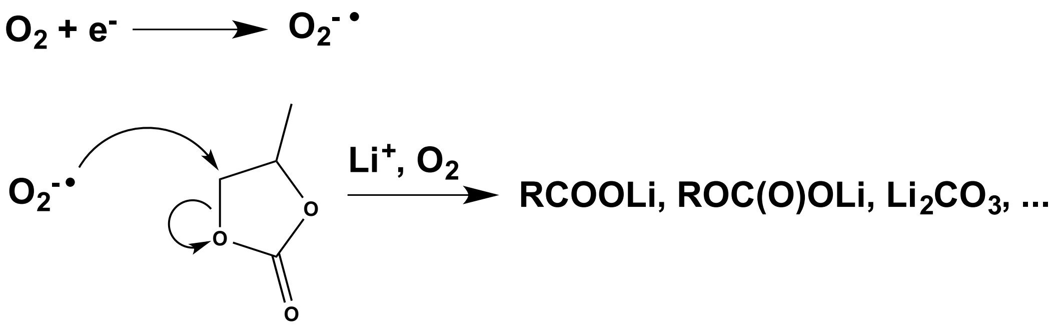
$O_2 + e^- \rightarrow O_2^{-\bullet}$
$O_2^{-\bullet}$
O
O
O
Li^+, O_2
RCOOLi, ROC(O)OLi, Li_2CO_3, ...

Figure 1.3. Proposed mechanism for the degradation of alkyl-carbonate based electrolyte solutions by nucleophile attack of superoxide to a typical solvent molecule (Propylene Carbonate, PC), leading to ring opening and several degradation products [34].

The search for solvents that are stable towards ORR intermediates identified ethers, several amides, dimethyl sulfoxide (DMSO) and some ionic liquids as promising candidates [42-45]. Using these solvents and more stable electrolytes (e.g. bis-trifluoromethylsulfonyl imide Li salt, LiTFSI) fairly reversible O_2/Li_2O_2 electrochemistry was obtained, and Li_2O_2 was demonstrated to be the only discharge product [9]; Li_2O, proposed as possible product, was never observed in discharged air electrodes.

Li-air battery discharge using stable non-aqueous electrolyte solutions is a complex process involving intermediates ($O_2^{-\bullet}$ or LiO_2) that have a finite solubility. The morphology of Li_2O_2 particles from the disproportionation of those intermediates is strongly dependent on the discharge rate [46]. More precisely, using high discharge rates (i.e. high currents) Li_2O_2 tends to precipitate as a *film* on the electrode surface [47-50], which is passivated after a critical thickness is reached (nm range) [13,49,50]; on the other hand, lower rates promote the crystallization of bigger particles (µm range) from the solution [12,13,29,51,52]. Because of the variety of electrode materials and electrolyte solutions used in the field (e.g. carbon blacks vs. carbon nanotubes; glymes vs. DMSO), it is yet difficult to define a normalized discharge rate value that establishes a *threshold* between the two limit cases. Anyways, since Li_2O_2 is an insulating material [49], its morphology and electrooxidation kinetics upon charge are strongly related [46,51].

In this work, we directed our attention on the fundamental mechanisms governing Li-O_2 cell discharge in terms of the nature and morphology of the discharge products. First, we developed custom-made cell hardware with improved sealing that allowed the reduction of contaminant permeation from the ambient air (Section 3.1). In fact, contaminants like CO_2 and H_2O were demonstrated to strongly increase the discharge capacity of Li-air cells by reacting with the ORR intermediates and leading to more soluble/mobile species and thus to different product morphologies [53-55]. Second, we investigated the capacity limitations of Li-air cells at a relatively fast discharge rate (120 mA/g_{carbon}), wherein discharge products tend to precipitate as a film on the electrode surface. By thoroughly analyzing the surface properties of several carbon blacks electrode materials and the corresponding discharge capacity, we demonstrated that 1-2 monolayers of Li_2O_2 ($\approx$0.5 nm) are sufficient to electrically insulate the electroactive surface and stop the ORR. This corresponds to an average of ≈500 µC/cm$^2_{real}$ for all carbons surfaces [50] (Section 3.2).

Although stable electrolyte solutions towards ORR intermediates attack were developed, the reversibility during charge and cycle life of Li-air batteries is yet suffering severe limitations. Little mechanistic understanding is available on the electrooxidation of insulating Li-air discharge products particles on carbon surfaces. For that reason, we investigated the charge process of model electrodes *pre-filled* with possible products of the reaction of Li with O_2, namely Li_2O_2 and Li_2O, and of alternative discharge products possibly arising by contamination of the cell with CO_2 and H_2O, namely Li_2CO_3 and LiOH (Section 4.2). Analysis of the evolved gases by mass spectrometry revealed that the only truly rechargeable product is Li_2O_2, whereby O_2 was the main gas evolved; however, several parasitic reactions consume O_2 right upon charge and limit the O_2 recovery efficiency to <80 % [56]. One of our recent reports [57] (Section 4.3), in accord with other relevant publications in the field [58-60], revealed that the severe carbon corrosion by Li_2O_2 and reactive oxygen species ("nascent oxygen") evolved upon charge leads to O_2 loss and Li_2CO_3 formation. The natural implications of that for a cycling cell are the accumulation of Li_2CO_3 in the electrode matrix, increased charge overpotentials, incomplete recharge and thus poor cycle life. In fact, the only example of a Li-air battery with a cycle life > 100 cycles was reported by Peter G. Bruce and coworkers, whereby carbon black is replaced by a nano-porous Au in the air electrode composition [59]; although not a practical solution for commercial applications, those findings represented a basic conceptual breakthrough for Li-air technology, and suggest replacement of carbon with alternative O_2 and Li_2O_2 resistant, electrically conductive, mesoporous materials.

Chapter 2

Experimental Backgrounds and Methods

2.1 General Background on Battery Electrochemistry

2.1.1 Electrochemical Reactions

An electrochemical reaction consists of the electron transfer from/to an electrochemically active species to/from an *electrode* surface, leading to an oxidation or reduction of the active species:

$$Ox + ne^- \rightleftarrows Red \qquad \text{(Eq. 2.1)}$$

The main driving force of an electrochemical reaction is the electrode potential, in addition to pressure and temperature, driving forces for all chemical reactions. For an electrochemical reaction, the equilibrium potential E_{rev} [V] is given by the Nernst equation

$$E_{rev} = E^0 + \frac{RT}{nF} ln \frac{C_{Ox}}{C_{Red}} \qquad \text{(Eq. 2.2)}$$

which describes E_{rev} as a function of the actual concentrations C_{Ox} and C_{Red} of the involved redox species [61]. E^0 is the redox potential in [V] in standard conditions, R is the gas constant in [J/K•mol], F the Faraday constant in [C/mol], T is the temperature in [K], and n the number of transferred electrons (Eq. 2.1). The equilibrium potential E_{rev} is often referred to as *reversible* potential.

2.1.2 Battery Thermodynamics

By definition, a battery is a device consisting of one or more electrochemical cells that convert stored chemical energy into electrical energy. In a battery cell, a spontaneous electrochemical reaction (e.g. $2Li + O_2 \rightarrow Li_2O_2$) is split in two half-reactions ($Li \rightarrow Li^+ + e^-$ and $O_2 + e^- \rightarrow O_2^{-\bullet}$), carried out at two electrodes (negative and positive); electrodes are separated by a porous electrically insulating membrane soaked with electrolyte solution, called *separator*.

The *negative* electrode is the one at which the reaction characterized by the lower standard electrode potential (E_N) takes place, or, in other words, the electrode that comprises the most electropositive metal or substance (e.g. Li^0). On the other hand, the *positive* electrode is the one at which the reaction (e.g. O_2 reduction) characterized by the higher standard electrode potential (E_P) is carried out. The nomenclature "positive" and "negative" electrode is absolute, and does not depend on whether the battery is being charged or discharged (Figure 2.1) [62].

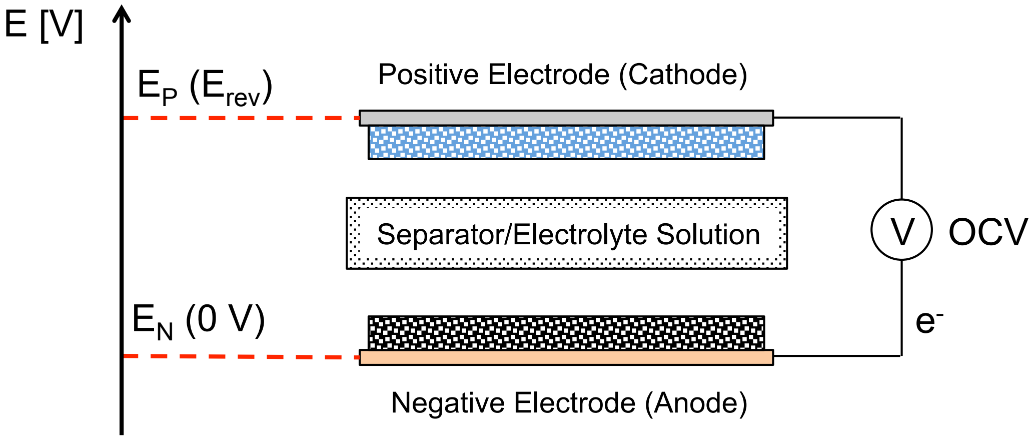
E [V]
E_P (E_{rev})
Positive Electrode (Cathode)
Separator/Electrolyte Solution
V
OCV
E_N (0 V)
e⁻
Negative Electrode (Anode)

Figure 2.1. Scheme of a typical battery cell configuration. The vertical axis on the left shows the potential difference between negative (E_N) and positive (E_P) electrode, and the potential scale relative to the negative electrode (E_N arbitrarily considered "0 V").

The electrical potential measured between the two terminals of the battery (open circuit voltage, OCV [V]) in standard conditions should be identical to the thermodynamic potential E_{rev} of the spontaneous electrochemical reaction typical for that battery chemistry, calculated from the Gibbs free energy ($\Delta G_{reaction}$, [J/mol]) using the following equation [63].

$$E_{rev} = -\frac{\Delta G_{reaction}}{nF} \approx OCV \qquad \text{(Eq. 2.3)}$$

In practice, the OCV of the battery is influenced by many parasitic processes (e.g. electrolyte solution corrosion) parallel to the desired battery reaction, and rarely matches exactly the potential E_{rev} estimated by thermodynamics.

Basically two kinds of batteries can be built: *primary* batteries are designed to be discharged once and be disposed after use. *Secondary* batteries are designed to be *recharged* and used multiple times [62].

Discharging a battery consists of closing the electrical circuit of which the device is the power source, and let the spontaneous electrochemical reactions proceed as determined by thermodynamics. During discharge, an *oxidation* reaction (e.g., $Li^0 \rightarrow Li^+ + e^-$) occurs at the negative electrode; therefore the electrode behaves as *anode*. On the other hand, at the positive electrode a *reduction* reaction (e.g., $O_2 + e^- \rightarrow O_2^{-\bullet}$) is spontaneous; therefore the electrode behaves as *cathode* [N5]. The resulting voltage E_{cell} ([V]) is the driving force that generates a faradaic current i ([A]) through an external circuit, which results in usable electrical power P ([W]).

$$P = i \times E_{cell} \qquad \text{(Eq. 2.4)}$$

When a battery is being *charged*, i.e. when the current flow is reversed by applying an external voltage, the electrochemical reactions are inverted accordingly (in the previous example, $Li^+ + e^- \rightarrow Li^0$, and $O_2^{-\bullet} \rightarrow O_2 + e^-$); therefore, the negative electrode behaves now as *cathode* and the positive electrode as an *anode*. By convention, battery electrodes are often referred to as *anode* and *cathode* on the basis of the reactions carried out upon discharge, i.e. the negative electrode is often referred to as "the anode" of the battery, and the positive electrode as "the cathode" of the battery. Accordingly, electrode materials are often called "anode material" and "cathode material" respectively [62].

2.1.3 Voltage Losses

Several voltage losses make the measured cell potential E_{cell} deviate from the thermodynamic potential E_{rev} when a current i is flowing during cell discharge and charge (polarization). The difference between those two values is defined as *overpotential* or *overvoltage* η [63].

$$\eta = E_{cell} - E_{rev} \qquad \text{(Eq. 2.5)}$$

Cell overpotential for electrochemical devices like fuel cells and batteries can be split into three main contributions:

$$\eta = \eta_{ohm} + \eta_{kin} + \eta_{tr} \qquad \text{(Eq. 2.6)}$$

η_{ohm} is the ohmic drop related to the cell's internal resistance R_{int} by the equation:

$$\eta_{ohmic} = iR_{int} \qquad \text{(Eq. 2.7)}$$

η_{kin} is the overpotential related to the charge-transfer reaction kinetics, and can be obtained from the Butler-Volmer equation [63]:

$$i = i_{0(T,C_O,C_R)} \cdot rf \cdot \left(e^{\frac{\alpha_a \cdot F}{R \cdot T}\eta_{kin}} - e^{\frac{-\alpha_C \cdot F}{R \cdot T}\eta_{kin}} \right) \qquad \text{(Eq. 2.8)}$$

η_{tr} is the overpotential generated by the resistance to mass transport of the reactants to the electroactive surface (e.g. O_2 diffusion through the electrolyte solution, Li^+ diffusion/migration). In Li-air batteries, η_{ohm} and η_{tr} can be often neglected due to the very low currents applied, and η_{kin} is the only relevant term; the latter can be ascribed to the sluggish O_2 reduction reaction kinetics at the positive electrode surface, and it can contribute to lower the discharge - increase the charge voltage by several hundreds of millivolts, depending on the cycling rate.

2.1.4 Cell Setup and Potential Scale

Electrochemical reactions are commonly studied using volt-amperometric techniques such as cyclic voltammetry. Typically, the potential E(t) of an interesting electrode surface (working electrode, WE) is scanned or varied, and the current i(E) related to electrochemical reactions is recorded as a function of potential. In this work, the following convention for the sign of the current is used: at the WE, a *negative* current corresponds to a *cathodic* process (electroactive species in solution are *reduced*), a *positive* current to an *anodic* process (electroactive species in solution are *oxidized*). As absolute electrode potentials cannot be measured directly, the potential E(t) of WE must be measured relative to a reference electrode (RE), whose potential is known and stable throughout the whole experiment. For the electroneutrality principle, in a two-electrode cell setup a current with opposite sign flowing through the RE has to counterbalance the charge involved in the reaction at the WE. In such configuration the RE potential deviates from its equilibrium value by an overpotential η, which can be described as presented in Section 2.1.3; at current values wherein η can be neglected or estimated, the reference electrode is called *pseudo-reference* electrode (Figure 2.2 a)). On the other hand, in order to guarantee accurate control of the WE potential, current flowing through the RE must be avoided; for that reason, in a three-electrode setup, the current drawn at the WE is counterbalanced by third auxiliary electrode, commonly called counter electrode (CE), where the opposite electrochemical reaction carried out at the WE takes place (i.e., if a *reduction* is performed at the WE, an *oxidation* takes place at the CE). The CE potential is not controlled (Figure 2.2 b)) [63,64].

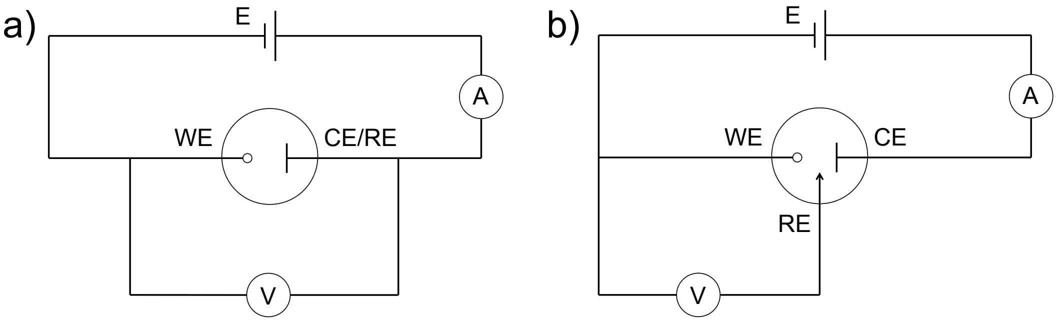

Figure 2.2. Comparison between, a) two-electrode cell setup with pseudo-reference electrode, and b) a three-electrode cell setup. WE is the working electrode, CE is the counter electrode, and RE is the reference electrode. A and V are an ammeter and a voltmeter respectively. E is the applied potential.

In the field of Li batteries potentials are commonly reported as a relative value relative to the Li^+/Li^0 RE potential ($E^0 = -3.05\ V_{SHE}$) in [V vs. Li^+/Li^0] or [V_{Li}]. A Li metal RE can be used in a three-electrode setup, however more commonly it serves as both RE and CE (pseudo-reference) in a two-electrode setup (Figure 2.2 a)).

2.2 Electrode Preparation

2.2.1 Different Requirements of Li-air Compared to Li-ion Electrodes

Li-ion battery electrodes consist of an active material powder (AM), an electrically conductive material like carbon black (CB), and a polymeric binder.

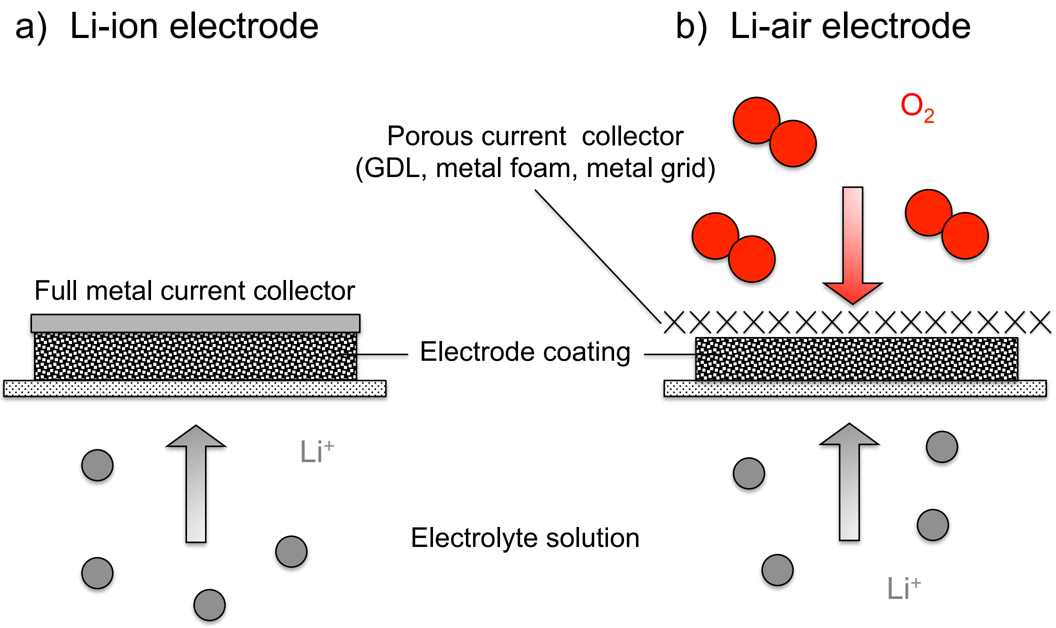

Figure 2.3. Design differences between Li-ion and Li-air positive electrodes: a) Li-ion positive electrodes supported on a full metal current collector (commonly Al), and b) air electrode coating supported on a porous membrane separator. The air electrode's current collector must be permeable to gases.

In Li-ion batteries, the key aspects that make an electrode a good electrode are: first, high AM/binder and AM/CB mass ratios. Second, high electrical conductivity. Third, high packing of the electrode coating, to enhance mass transport of Li^+ ions to the active material. The latter requirement can be practically met by compressing electrodes before use [65]. Low surface area (i.e. specific surface of the active material and carbon black expressed as m^2/g) is also desired. Because degradation processes of the electrolyte solution occur on the surface, high surface area carbon blacks or high amounts of CB in the electrode composition are detrimental to battery efficiency and cycle-life [65].

On the other hand, Li-O_2 battery positive electrodes have quite different requirements, indeed more similar to those of Fuel Cells: first, high porosity, to allow fast O_2 diffusion to the active sites where ORR occurs. Second, high surface area, to enhance ORR kinetics. Third, porous or permeable current collector, to allow O_2 diffusion from the ambient to the electroactive surface (Figure 2.3). Typical current collectors are Gas Diffusion Layer (GDL), porous metal foams or metal grids.

2.2.2 Background on Battery Electrode Preparation

Battery electrode preparation consists in coating on a solid support a slurry (or "ink") comprising active material, carbon black, binder and a solvent. The slurry is prepared by dispersing powders of AM and CB in a convenient solvent/binder solution by either ultrasonication, stirring or milling. Solvents are chosen for their ability to disperse the electrode material and to dissolve the binder. Common solvents are N-methyl pyrrolydone (NMP) or iso-propyl alcohol (IPA) (Figure 2.4).

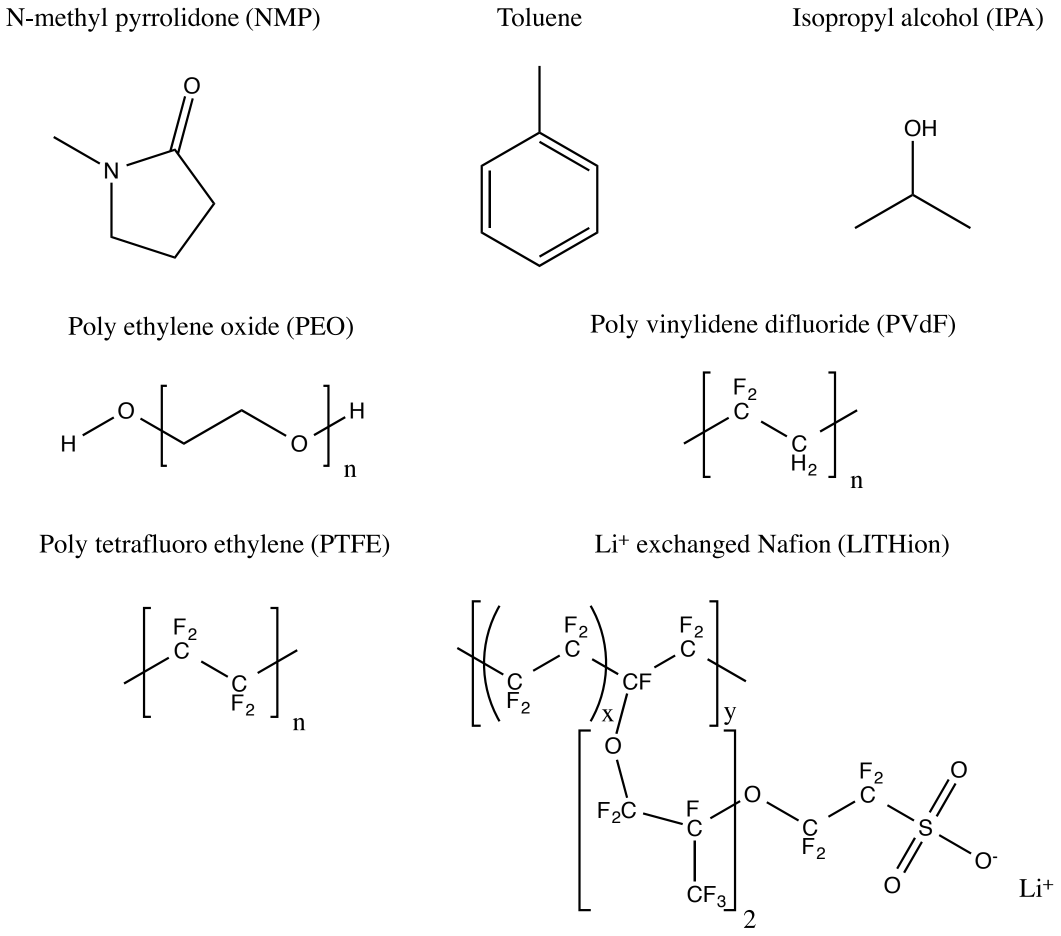
N-methyl pyrrolidone (NMP)

Toluene

Isopropyl alcohol (IPA)

Poly ethylene oxide (PEO)

Poly vinylidene difluoride (PVdF)

Poly tetrafluoro ethylene (PTFE)

Li$^+$ exchanged Nafion (LITHion)

Figure 2.4. Chemical structures of commonly used solvents and binders used for Li-ion and Li-air battery electrode preparation.

The role of a binder is to confer adhesion to the current collector/support and enduring mechanical stability to the coating in the operating conditions of the battery. Common binders are poly(vinylidene-di-fluoride) (PVdF) and poly(tetrafluoro-ethylene) (Teflon PTFE) (Figure 2.4). The obtained slurry can be coated using several techniques:

- *Spray coating*: spray coating leads to highly porous electrodes, and it is particularly suitable for fuel cells and Li-O_2 batteries, whereby porosity and mass transport are of primary importance. In general, it requires low viscosity slurries.

- *Doctor-Blade*: this technique consists in spreading viscous slurry on a perfectly flat support using a blade or rod. The gap between the support and the blade/rod determines the loading ($mg_{AM}/cm^2_{electrode}$). By far the most used coating technique in the Li-ion battery field, it is particularly suitable in the range 100-500 µm "wet film" thicknesses.
- *Mayer-Rod technique*: this coating technique makes use of a "wounded" rod (Figure 2.5 a)), whereby the thickness of the groves determines the loading. An important difference with Doctor-Blade is that Mayer-Rods are in contact with the support; therefore they flatten it as they coat. Using the Mayer-Rod technique, very thin wet films (even below 10 µm) can be achieved.

2.2.3 Preparation of Air Electrodes

In this work, Li^+ exchanged Nafion (Figure 2.4) bonded air electrodes supported on a commercial porous polymer membrane battery separator (Celgard®, 25 µm thick, 50% porosity) were prepared. Following the procedure presented by Yang Shao-Horn and coworkers [17,22], carbon black materials were dispersed in organic solvents such as NMP and IPA by high-power ultrasonication with a Branson® sonicating horn (10 min, Figure 2.5 c)). Because the binder (Li^+ exchanged Nafion, commercially available as LITHion, Ion Power, USA) tends to agglomerate during sonication, it was added afterward as 10.6% alcoholic solution and mixed by hand with a spatula for 30 seconds.

The obtained inks ($\approx 30\ mg_{carbon}/ml_{ink}$) were coated on Celgard® separator using a 100 µm wet film Mayer Rod (Figure 2.5 d)). This approach allows the preparation of uniform and very thin (10-15 µm, typical loadings 0.3-0.5 $mg_{carbon}/cm^2_{electrode}$) electrode coatings, suitable for studies on oxygen reduction/evolution kinetics.

Coatings were preliminarily dried on air, cut in 15 mm ⃠ discs (Figure 2.5 f) and g)), vacuum dried below the Celgard® and binder melting points, and finally transferred in an Ar-filled glovebox where cell are assembled. Further experimental details on air electrode preparation can be found in Sections 3.1 and 3.2.

2.2.4 Preparation of Pre-Filled Electrodes

In order to study the charge of single and defined discharge products (e.g. Li_2O), as well as the catalytic activity of catalysts towards Li_2O_2 electrooxidation, it is convenient to assemble air electrodes in the *discharged state*, in other words *pre-filled* with a discharge product of interest. Before mixing it with carbon black, the particle size of a discharge product must be reduced by ball milling in Ar atmosphere (Section 4.2), using an airtight jar filled in an Ar-filled glovebox (Figure 2.6 a)). The active material can be subsequently mixed with carbon black either by hand in a mortar or by ball milling. In this work, commercially available Li_2O_2, Li_2O, LiOH and Li_2CO_3 powders were only mixed by hand with carbon black. In fact, dry milling those compounds together with carbon leads to thermal decomposition reactions as the temperature in the jar increases (Section 2.8.5).

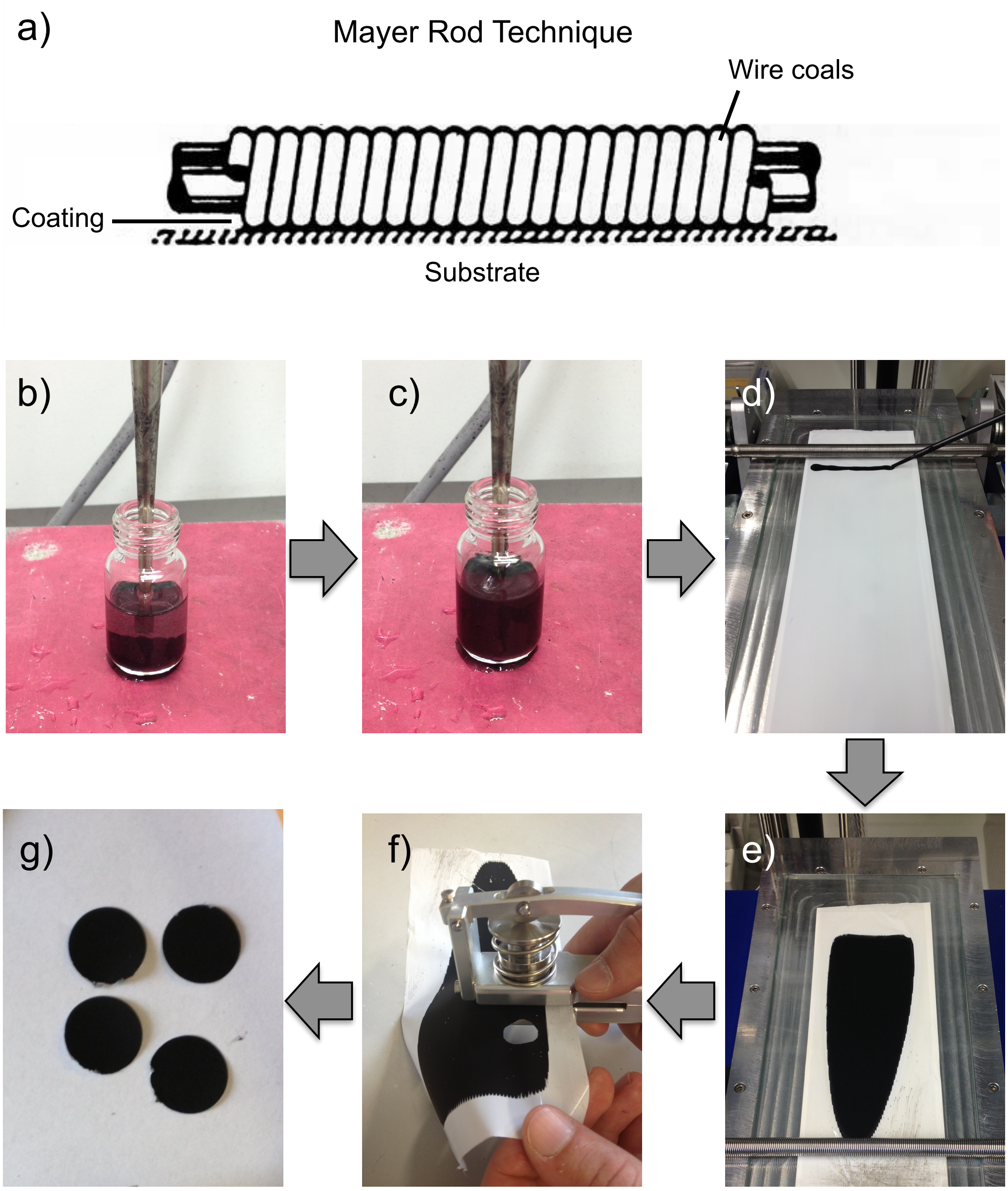

Figure 2.5. Electrode preparation using the Mayer Rod technique. a) Working principle of a wounded rod. b) Mix carbon black, active material, a convenient solvent and binder. c) Prepare the slurry by ultrasonication. d) Pour the slurry on a porous membrane support. e) Coat the slurry by pulling forward the wounded rod. f) Cut electrodes of the desired shape and size. g) Final electrodes.

The reactivity of Li_2O powder with nearly any common binder and solvent (for example, colorless PVdF/NMP solutions become a black viscous fluid after addition of Li_2O) incited us to develop an electrode preparation procedure alternative to the one presented in Section 2.2.3. All pre-filled electrodes slurries were prepared by ultrasonication of a 1/1 mixture of one discharge product with carbon black in a 0.66 % poly(ethyleneoxide) (PEO) solution in toluene. Both the binder PEO and toluene do not react with Li_2O. The suspension was prepared inside an Ar-filled glovebox and poured into an airtight vessel for ultrasonication outside the glovebox in Ar atmosphere (Figure 2.6 b)). The obtained slurries (≈30 mg_{carbon}/ml_{ink}) were coated on Celgard® separator using a 100 µm wet film Mayer Rod in the glovebox (Section 4.2).

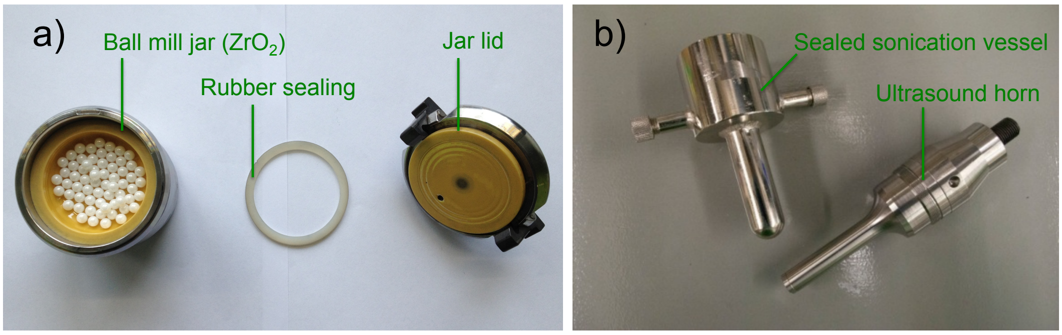

Figure 2.6. a) Airtight ZrO_2 ball mill jar and balls for milling in Ar atmosphere. The sealing can sustain up to 10 bar inner pressure before leaking. b) Airtight sonication vessel and horn for ink preparation in Ar atmosphere.

2.3 Electrolyte Solutions

2.3.1 General Handling Procedures

In this work, glymes were extensively employed as electrolyte solvents for Li-air batteries, due to their good stability towards ORR intermediates and at the strongly reducing Li metal surface.

Electrolyte solvents were stored in an Ar-filled glovebox over molecular sieves (Sylobead MS 564C zeolytes, 3 Å, Grace Division) to reduce their water content typically below 10 ppm. Water content and purity of electrolyte solvents was regularly controlled by Karl Fischer titration, IR-ATR (Spectrum Two, Perkin Elmer, USA, placed in an Ar-filled glovebox) and NMR spectroscopy (Advance I, Bruker Instruments, Germany) respectively. Li^+ salts are commonly dried overnight in vacuum at 150 °C before use [66].

2.3.2 Investigation on the Reactivity of Electrolyte Solvents with Superoxide

The reactivity of electrolyte solvents was investigated qualitatively by exposing them to chemically generated $O_2^{-\bullet}$ provided as KO_2, commercially available (96.5 %, Alfa Aesar) (Section 3.3). Suspensions of 0.45 g of KO_2 and 5 g of the solvent under investigation were prepared in an Ar-filled glovebox. Due to the very low solubility of KO_2 in some of the solvent tested (e.g. glymes), the suspensions were stirred for 8 days to ensure sufficient reaction time. Unfortunately, the use of crown ethers, known to enhance the solubility of K^+ salts in organic solvents, was not an option due to the high amounts of reactive impurities contained in those compounds, which introduced artifacts in the characterization procedure. Subsequently, the liquid phase was separated from the solid residue by centrifugation, and submitted to ^{1}H-NMR (DMSO-d6, 128 scans,) and IR-ATR analysis (diamond-ATR). Residual solvent was removed from the solid residues by vacuum drying at temperatures between 50-80 °C, depending on the solvent's vapor pressure. Solid residues were characterized by IR-ATR spectroscopy (as-is) and ^{1}H-NMR (dissolved in D_2O). The characterization procedure is schematically summarized in Figure 2.8.

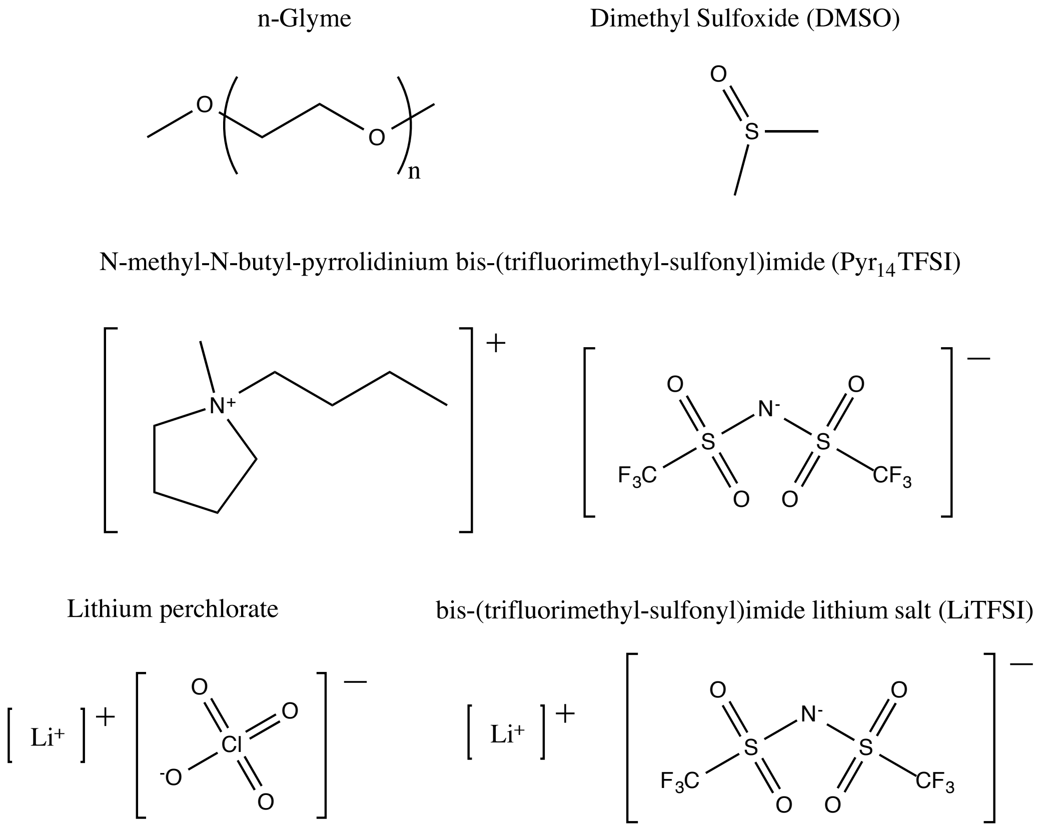
n-Glyme

Dimethyl Sulfoxide (DMSO)

N-methyl-N-butyl-pyrrolidinium bis-(trifluorimethyl-sulfonyl)imide ($Pyr_{14}TFSI$)

Lithium perchlorate

bis-(trifluorimethyl-sulfonyl)imide lithium salt (LiTFSI)

Figure 2.7. Chemical structures of typical solvents and salts used to prepare electrolyte solutions for Li-air batteries.

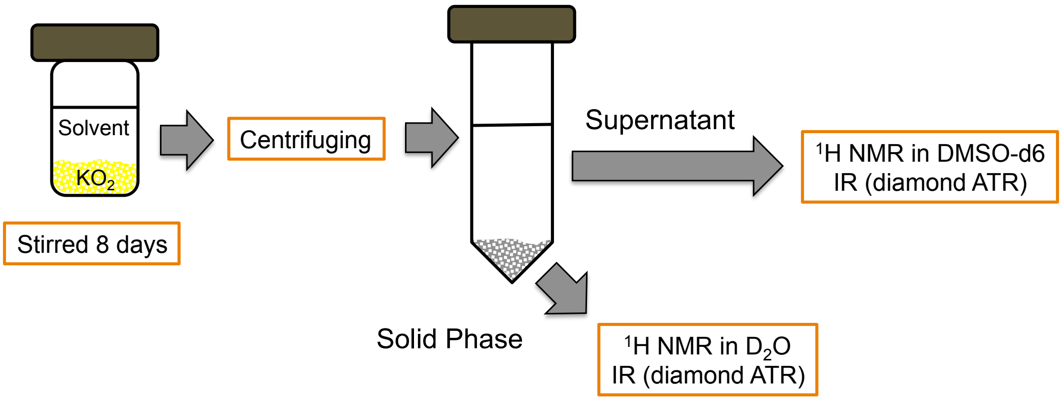
Solvent
KO2
Stirred 8 days
Centrifuging
Supernatant
1H NMR in DMSO-d6
IR (diamond ATR)
Solid Phase
1H NMR in D2O
IR (diamond ATR)

Figure 2.8: Schematic illustration of the standard procedure for qualitative determination of electrolyte solvents stability towards superoxide.

2.3.3 Long Term Stability of Electrolyte Solvents with Superoxide

The long term stability of organic electrolyte solvents towards the intermediate superoxide ion radical ($O_2^{-\bullet}$) was quantitatively determined by exposing them to chemically produced superoxide (KO_2) and measuring UV-vis absorption of the latter in the range 250-270 nm as a function of time (Section 3.3). Although they are doubts about the role of the alkali metal ion on the degradation reactions triggered by $O_2^{-\bullet}$, this method serves as a convenient screening before more complicated electrochemical investigations in presence of Li^+ ion are performed (LiO_2 is unstable and not commercially available).

A 3 mM KO_2 solution in DMSO was prepared in an Ar-filled glovebox by stirring commercially available KO_2 powder for 90 min. During this time water traces are removed by reaction with free superoxide anions; considering the maximum water content of ≈5 ppm, it is possible that superoxide concentration could have been reduced by ≈20 %, corresponding to the stoichiometry of 2 superoxide ions per water molecule [67,68]. The obtained KO_2 solution (0.7 ml) was transferred into a quartz cuvette with a sealed screw cap (1/ST/C/Q/2 mm, Starna, USA) and a UV-Vis spectrum was recorded (Lambda35, Perkin Elmer, USA) to determine the initial absorbance, correlated with the $O_2^{-\bullet}$ concentration at time zero. Subsequently, a 50-fold molar excess of the solvent under investigation ($n(\text{solvent})/n(KO_2) = 50$, 8-23 µl depending on the solvent) was added to the solution in the glove box. The solvent degradation rate is expected to be pseudo first order with respect to $O_2^{-\bullet}$ due to the large molar excess of solvent. UV-vis spectra were collected at constant temperature (25 °C) and corrected with a baseline of the corresponding mixture of DMSO and the solvent. To visualize the decay of the superoxide radical concentration, related to the reactivity with solvent molecules, the absorbance at 270 nm was plotted as a function of time. The dilution of the KO_2 solution due to addition of different volumes of the examined solvents was arithmetically corrected.

2.4 Battery Test Cell Design and Assembly

2.4.1 Cell Design

Li-air batteries are definitely more complex systems than Li-on batteries, from an engineering point of view. The need to provide fresh air (or pure O_2) to the cathode defines several constrains regarding cell design than for other battery chemistries. However, almost all cell designs previously used for Li-ion battery research (e.g. Swagelok T-cells, Coin cells or pouch cells) were successfully adapted by several research groups for being used as Li-air cells, whereby O_2 supply was provided either by exposing them to an O_2 atmosphere (e.g. inside sealed boxes), or by directly connecting them to a dynamic O_2 supply. Several examples of custom cell designs can be also found in the literature, whereby the effort of re-designing completely new cell hardware is justified by the need of providing a convenient connection to advanced in-situ characterization techniques.

As we planned to make extensive use of in-situ Mass Spectrometry and infra-red spectroscopy, we decided to design a sealed cell hardware that allowed to accommodate electrodes of variable sizes (up to 20 mm diameter) and to contain sufficient O_2 for sustaining high capacity cell discharge in a relatively compact shape. Starting from the previous experience of Prof. Hubert A. Gasteiger at the Massachusetts Institute of Technology (MIT), we slightly modified the electrochemical cell reported in one of his papers published with prof. Yang Shao-Horn [17] to enhance sealing and increase internal volume. The current custom electrochemical cell used at TUM comprises two stainless steel plates separated by a 28 mm diameter Kel-F (poly(chlorotrifluoro-ethyene)) spacer, defining an internal volume of $\approx$10 cm^3. Two Teflon O-rings placed into two groves of the metallic parts provide sealing to the cell. Electrical contact between the positive electrode current collector (1 mm mesh stainless steel grid) and the upper metal plate is given by a stainless steel compression spring (Figure 2.9 a)).

The novel cell hardware developed in our group has several advantages: first, very good sealing and low gas permeation rates ($\approx$100-fold lower than for PTFE, s. Section 3.1). Second, the inner volume of the cell ensures a sufficient amount of O_2 stored, therefore no dynamic O_2 supply is needed (10 cm^3_{STP} of O_2 correspond to $\approx 4.09 \cdot 10^{-4}$ mol_{O2}, that would provide 78.9 C for the 2 e^- reduction of O_2 to Li_2O_2. Our carbon electrodes have a loading $\approx$1 mg_{carbon}, and provide specific discharge capacities between 100-2000 mAh/g_{carbon}, corresponding to 0.36-7.2 C. Therefore, effect of the pressure change arising from the consumption of maximum 10 % of the O_2 contained in the electrochemical cell is negligible). Third, cell assembly is very simple and reproducible.

2.4.2 Cell Assembly

Cell assembly was performed with the procedure shown in Figure 2.9 c) in an Ar-filled glovebox:

1. The negative electrode (Li^0 foil) is placed on the bottom current collector
2. 40 µl of electrolyte solutions are added in the center of the electrode
3. Two Celgard® separators are placed on the negative electrode
4. 40 µl of electrolyte solutions are added in the center of the separators
5. The positive electrode is placed on the separators with the coating facing up
6. 40 µl of electrolyte solutions are added in the center of the electrode
7. The stainless steel grid is placed on the positive electrode
8. Cell is sealed by at 6 Nm torque on all 4 screws.

The sealed cell is brought outside the glovebox, connected to the oxygen supply line (Figure 2.9 d)) and filled with pure O_2 using the following procedure:

1. Purge the oxygen supply line (valves 1-2 open, 3-4 closed, 15 min)
2. Purge the cell with O_2 at 80 sccm (valves 1-2 open, 3-4 closed, 0.5 min)
3. Close valves 3-4 and disconnect the cell from the supply line

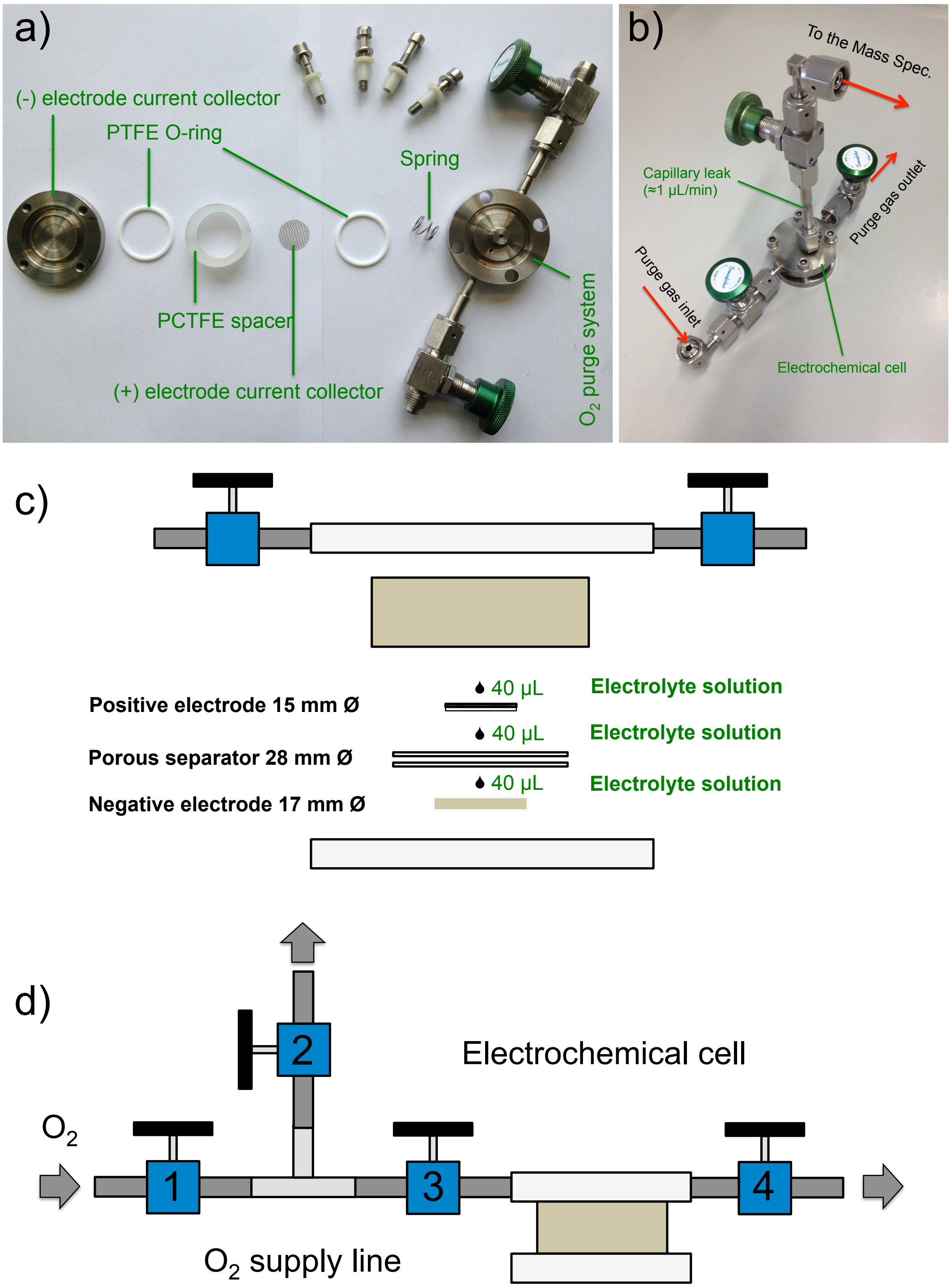
a)
(-) electrode current collector
PTFE O-ring
Spring
PCTFE spacer
(+) electrode current collector
O_2 purge system
b)
To the Mass Spec.
Capillary leak
(≈1 µL/min)
Purge gas outlet
Purge gas inlet
Electrochemical cell
c)
40 µL
Electrolyte solution
Positive electrode 15 mm Ø
40 µL
Electrolyte solution
Porous separator 28 mm Ø
40 µL
Electrolyte solution
Negative electrode 17 mm Ø
d)
2
Electrochemical cell
O_2
1
3
4
O_2 supply line

Figure 2.9. a) Exploded view of the Li-air cell developed at TUM in Prof. Gasteiger's group. b) Modified electrochemical cell for Mass Spectrometry studies; the tube protruding from the upper part contains a capillary leak for sampling gases from the cell headspace. c) Schematic illustration of the cell assembly procedure. d) Experimental procedure for filling the battery cell with pure O_2.

2.5 Electrochemical Methods

2.5.1 Battery Cycling

Rechargeable or secondary batteries should be able to be discharged and charged multiple times, in other words they should have the ability to *cycle*. Cycle life is defined as the number of complete discharge-charge cycles that the battery cell can perform before its nominal capacity falls below an defined value (typically 80 % of the original nominal capacity). Battery cells can be discharged and charged either by galvanostatic (constant current) or potentiostatic (constant potential) procedures, galvanostatic cycling is generally preferred. Commonly used galvanostatic cycling procedures consist in applying a constant current to the battery cell, until its potential or capacity reach a limit value. When the pre-defined limit is reached, the sign of the current is inverted (Figure 2.10). Capacity in [mAh] can be calculated simply by multiplying the discharge or charge duration in [h] by the current in [mA] applied. The voltage response of the cell provides information on the electrochemical reactions taking place; for instance, defined potential plateaus can be ascribed to a particular reaction (e.g. O_2 reduction during discharge in our Li-O_2 systems provides a flat potential plateau at ≈2.65 V_{Li}). For some applications, combined potentiostatic-galvanostatic techniques can be used.

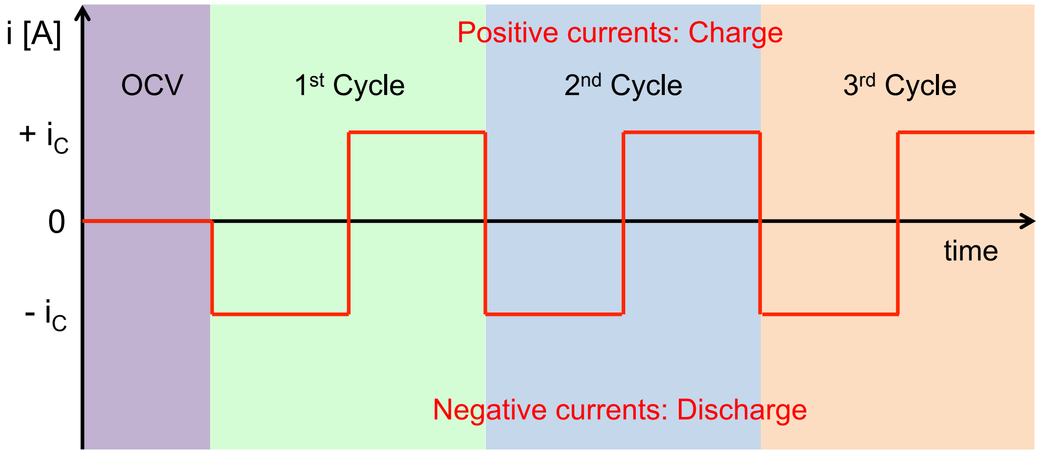

Figure 2.10. Current profile of a rechargeable battery cell during galvanostatic cycling. A constant current ±i_c is applied until a certain voltage or capacity limit is reached, at which the sign of the current is inverted.

In this work, mostly galvanostatic charge and cycling procedures were employed. As Li-O_2 cells are built in the charged state, all cycling procedures started with a discharge. Before cycling started, a rest period at OCV was set (commonly 0.5 h) to allow the electrolyte solution to be absorbed in the electrode porosity.

2.5.2 State of Charge (SOC)

The State of charge (SOC) in [%] of a battery electrode is defined by the following equation:

$$SOC = \frac{Q_{actual}}{Q_{total}} \times 100 \qquad \text{(Eq. 2.9)}$$

Q_{actual} is the charge in [C] or [mAh] actually extracted/injected from/into the electrode and Q_{total} is the total amount of [C] or [mAh] involved for a complete charge/discharge of that particular electrode. In this work, we assumed that Q_{total} = $Q_{theoretical}$, whereby $Q_{theoretical}$ is defined as:

$$Q_{theoretical} = \frac{nF}{M_{AM}} m_{AM} \qquad \text{(Eq. 2.10)}$$

Where n is the moles of electrons involved in the reaction, F is the Faraday constant in [C/mol], M_{AM} is the formula weight of the active material in [g/mol] and m_{AM} is the weight of the active material actually stored in the electrode in [g].

2.5.3 Determination of Background Currents in Fully Assembled Li-O_2 Cells

The polarization of battery electrodes at high potentials (typically >4 V_{Li}) upon charge leads to the electrochemical decomposition of the electrolyte solution and eventually to the corrosion of metallic current collectors. Those processes originate background currents superimposed to the studied electrochemical reactions (e.g. Li_2O_2 electrooxidation). It is crucial to determine background currents in order to correct measured current values and mitigate interpretation artifacts.

Background currents can be determined by chronoamperometry, i.e. by measuring the faradaic current originated in fully assembled battery cells by increasing the positive electrode potential to values higher than the OCV (≈3.2 V_{Li} for our batteries), without any prior discharge. Experimentally this is done by increasing cell potential by 0.15 V every hour and measuring the resulting current (Figure 2.11 a)). Typically, the current increases abruptly every time that the voltage is varied, and slowly decays to a constant value at the end of the step. This behavior is related to the capacitive currents arising from the accumulation of charge (e.g. e^-, Li^+) at the electrode surface, often referred to as *double layer capacity*.

$$i_{cap} = \frac{dQ}{dt} = C\frac{dV}{dt} \qquad \text{(Eq. 2.11)}$$

i_{cap} is the capacitive current in [A], Q is the charge in [C] involved in the process, C is the capacitance of the electrode surface in [F] and V is the voltage in [V]. As cell voltage is kept constant after the step, the capacitive current exponentially decay to zero. For that reason, a good approximation of the faradaic current $i_{far}(E)$ related to electrooxidation reactions of the cell components is the value at the end of the potential step. Those current values are commonly plotted as $\log(i_{far}(E))$ as a function of potential.

A different approach is to estimate the cell components' stability by determining the corrosion potential E_a at the charge rate used in the cycling experiments by chronopotentiometry. This method consists in applying a constant positive current i_a at the positive electrode (WE), and measure cell voltage as a function of time without prior discharge (Figure 2.11 b)). Ideally, the background current measured in chronoamperometry at the cell voltage determined by chronopotentiometry $i_{far}(E_a)$, should match with the current i_a set by the user in the chronopotentiometry experiment.

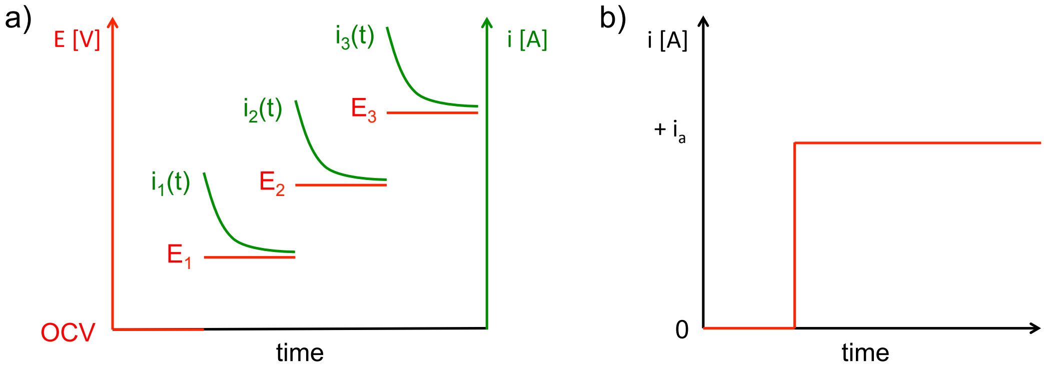

Figure 2.11. a) Procedure for the determination of background currents in fully assembled Li-O_2 cells by chronoamperometry without any prior discharge. b) Current profile for the determination of the anodic corrosion potential by chronopotentiometry.

2.5.4 Electrochemical Impedance Spectroscopy (EIS)

Impedance is defined as frequency (ω) dependent resistance of electrical or electrochemical circuits to a voltage or current perturbation. Impedance is an extension of the Ohm's law for direct current (DC) circuits, and describes other impeding mechanisms like inductance and capacitance occurring in alternate current (AC) circuits [69,70]. In quantitative terms, it is the complex ratio of the voltage to the current in an (AC) circuit.

$$Z_{(\omega)} = \frac{\hat{E}_{AC(\omega)}}{\hat{\imath}_{AC(\omega)}} \cdot e^{-j\cdot\theta} \qquad \text{(Eq. 2.12)}$$

$E_{AC(\omega)}$ is the voltage in [V], $i_{AC(\omega)}$ is the current in [A], ω is the frequency in [Hz] and j corresponds to $\sqrt{-1}$. Using Euler's formula, real and imaginary part of complex impedance can be separated.

$$Z_{(\omega)} = \frac{\hat{E}_{AC(\omega)}}{\hat{\imath}_{AC(\omega)}} \cdot (\cos(\theta) - j\sin(\theta)) = \underbrace{\frac{\hat{E}_{AC(\omega)}}{\hat{\imath}_{AC(\omega)}} \cdot \cos(\theta)}_{\mathrm{Re}_{(Z)}} + j\underbrace{\left(-\frac{\hat{E}_{AC(\omega)}}{\hat{\imath}_{AC(\omega)}} \cdot \sin(\theta)\right)}_{\mathrm{Im}_{(Z)}}$$

Electrochemical impedance spectroscopy (EIS) consists in measuring the impedance response of an electrochemical system to a small AC voltage perturbation (≈10 mV) as a function of frequency [69,70].

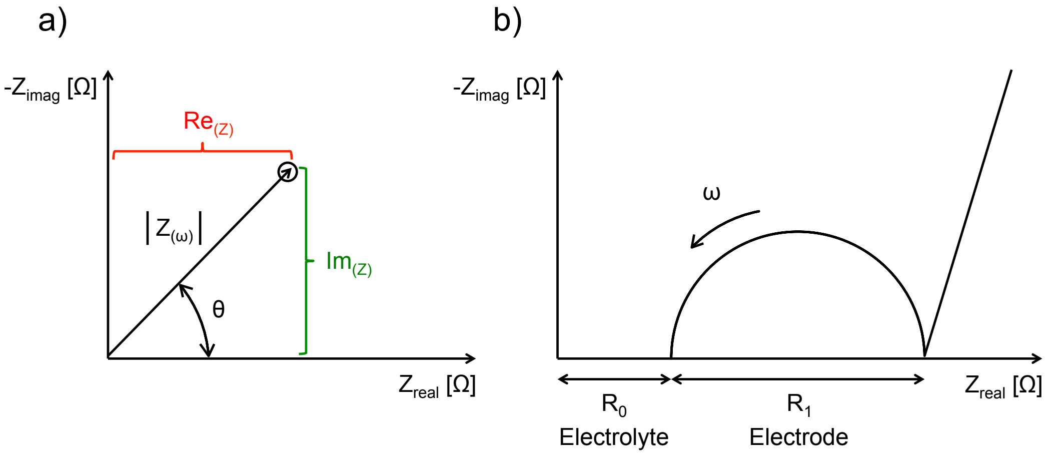

Figure 2.12. a) Nyquist plot for presenting electrochemical impedance spectroscopy (EIS) data. The plot consists of a complex plane with the ordinate values mirrored about the abscissa. b) Typical EIS response of a non-aqueous Li-O_2 battery cell.

Real and Imaginary part of complex impedance as a function of frequency (ω) are plotted on a Nyquist plot (Figure 2.12 a)). It is customary to plot impedance as $-Z_{imag}$ vs. Z_{real} (with the ordinate values mirrored about the abscissa) because EIS rarely involves inductance ($Z_{imag} > 0$) and usually involves capacitance ($Z_{imag} < 0$).

The behavior of an electrochemical system can be modeled using ideal circuit elements such as resistors (R), inductors (L) and capacitors (C). For example, a simple model circuit for an electroactive surface is a capacitor and a resistor in parallel, that results in a semicircle as the one comprising typical EIS response of a Li-O_2 battery (Figure 2.12 b). The interception of the semicircle at high frequency (left) defines a real resistance R_0 related to the electrolyte solution ionic conduction, whereas the interception of the semicircle at low frequency (right) defines a second real resistance R_1 related to the charge transfer across the electrode surface corresponding to an electrochemical reaction (e.g. Li^+/Li) [69,70].

In this work, EIS technique was used for fast qualitative characterization of Li-O_2 cells. By confronting the high frequency and low frequency resistances with the average values previously obtained for the same kind of battery cells, it was possible to identify eventual mistakes during cell assembly, or the variation of electrochemical behavior of an electrode surface when impurities or additives were added to the electrolyte solution.

2.6 Product Selectivity of Li-O_2 Cells Via O_2 Consumption

2.6.1 Principles of Product Selectivity Measurements in Li-Air Batteries

Product selectivity has been a fundamental subject in Li-air research. Thermodynamically, two reduction products of O_2 with Li^0 are possible when discharging a Li-O_2 cell, that is lithium *peroxide* Li_2O_2 and lithium *oxide* Li_2O (Re. 1.1 and 1.2). Despite the discharge of Li-O_2 cells leads mostly to Li_2O_2, there was until nowadays a strong interest to maximize the yield of the most reduced oxide Li_2O because of its much higher specific capacity (1794 mAh/g_{Li2O} vs.

1168 mAh/g_{Li2O2}). For that reason, it is necessary to get more mechanistic insights on the parameters that influence oxygen reduction reaction's product selectivity.

A simple method to determine the product selectivity of a Li-O_2 battery is to measure the pressure drop inside a sealed cell using a manometer or pressure transducer during the discharge process at constant temperature. A typical pressure profile during the first cycle (discharge-charge) of a sealed Li-O_2 cell thermostated at 25 °C is shown in Figure 2.13. In the assumption that O_2 behaves as an ideal gas in the conditions of the experiment (101.3 kPa_{abs}, 25 °C), the moles of O_2 consumed (Δn) can be obtained using the recorded pressure drop (ΔP between the base pressure at OCV and at the end of discharge) and the ideal gas law.

$$(\Delta P)V = (\Delta n)RT \qquad \text{(Eq. 2.13)}$$

R is the ideal gas constant in [J/K•mol], T is kept constant at 298 K and V is the internal volume in [m^3]. From the comparison between the capacity in [C] involved in the discharge and the moles of O_2 consumed it is possible to obtain the e^-/O_2 ratio and determine the product selectivity ($e^-/O_2 = 2$, pure Li_2O_2; $e^-/O_2 = 4$, pure Li_2O; $2 < e^-/O_2 < 4$, mixtures of Li_2O_2 and Li_2O).

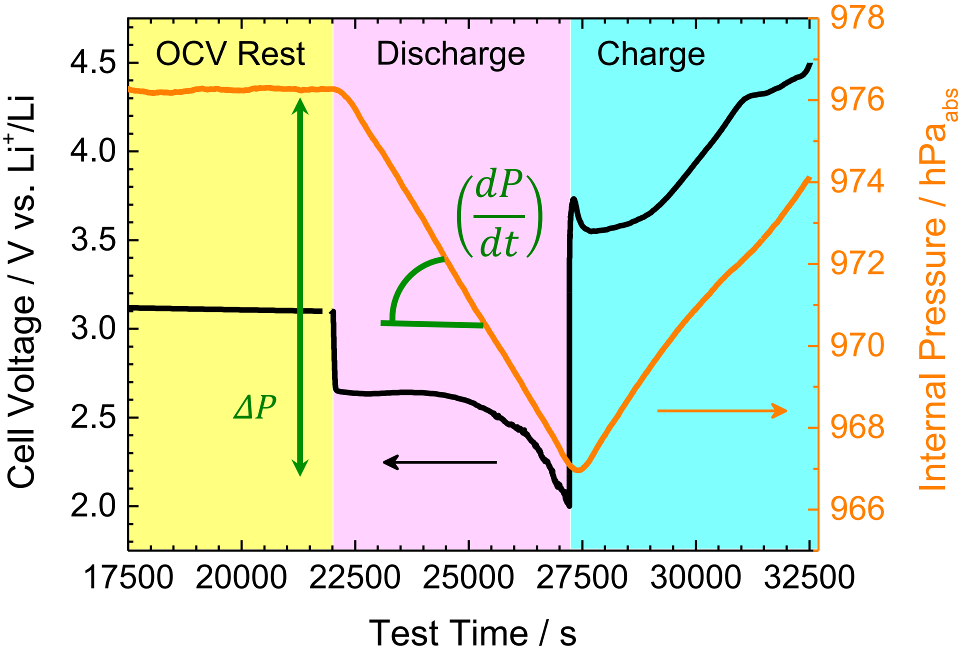

Figure 2.13. Voltage (black line) and inner pressure profile (orange line) on the first cycle of a sealed Li-O_2 cell - Baratron system for product selectivity studies performed at 25°C. The slope of the discharge curve corresponds to the pressure variation as a function of time used to calculate the fraction of Li_2O_2/Li_2O produced upon discharge.

A more accurate way to calculate the e^-/O_2 ratio is by determining the O_2 consumption rate in [mol/s] from the pressure variation corresponding to the slope of the pressure profile measured, using the following equation.

$$\dot{n} = \left(\frac{dn}{dt}\right)_T = \frac{V}{RT}\left(\frac{dP}{dt}\right)_T \quad \text{(Eq. 2.14)}$$

For a given discharge current i, the e^-/O_2 ratio can be determined as follows.

$$e^-/O_2 = \frac{i}{\dot{n}F} \quad \text{(Eq. 2.15)}$$

Finally the fraction of Li_2O_2 and Li_2O [$\%_{mol}$] can be calculated using the following equations.

$$f_{Li_2O_2} = \left(2 - \frac{e^-/O_2}{2}\right) \times 100 \quad \text{(Eq. 2.16)}$$

$$f_{Li_2O} = \left(\frac{e^-/O_2}{2} - 1\right) \times 100 \quad \text{(Eq. 2.17)}$$

This method is unfortunately not reliable for the charge of Li-O_2 cells, as several gases beyond O_2 are commonly evolved at potentials >4 V_{Li} (CO_2, electrolyte solvent fragments). It is however possible to carry out the same kind of calculations to obtain the e^-/gas evolution ratio; data treatment is complicated by the non-linearity of the pressure profile (Figure 2.13), and a more accurate differentiation procedure must be employed. O_2 consumption measurements can be very useful to integrate and corroborate data obtained via mass spectrometry (Section 2.7).

2.6.2 Oxygen Consumption Experimental Setup

In this work, oxygen consumption measurements were performed using an MKS 627D Baratron absolute capacitance analog manometer connected to a sealed battery cell. Pressure data (in [torr]) were collected (1 pressure point every 10 s) by a National Instruments data acquisition card interfaced to a personal computer via a Labview program developed in our laboratory. The uncertainty of the pressure measurement is 0.7 hPa, much less than the signals detected, typically 10-90 hPa.

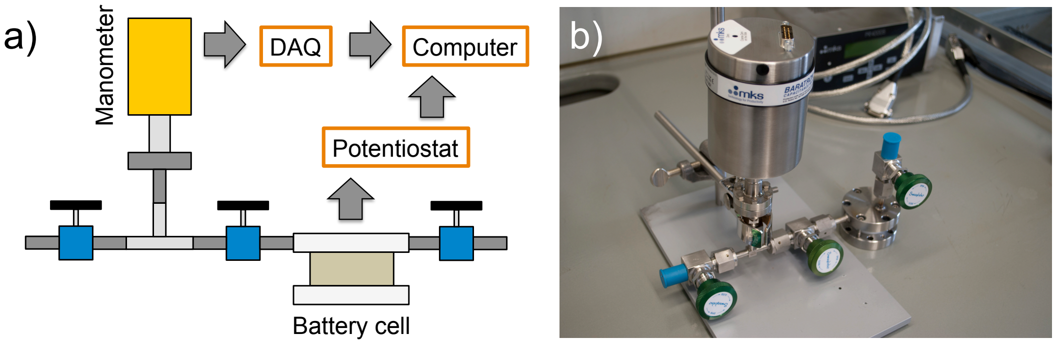

Figure 2.14. a) Scheme of the system used for O_2 consumption measurements, comprising a battery cell hardware identical to the one presented in Figure 2.9 and an absolute capacitance analog manometer. b) Photo of the O_2 consumption system.

The internal volume V of the system (cell + manometer) was determined by geometry, and it was 20.2 ml; the electrochemical cell comprises ≈10 ml, the manometer ≈7 ml (provided by the constructor) and the connections ≈3 ml.

Setting up an O_2 consumption measurement with our system consists of the following steps:

1. Evacuate the manometer using a rotary vane pump (1 h)
2. Connect the manometer to the O_2 supply line
3. Purge the manometer with pure O_2 (5 min)
4. Connect the electrochemical cell to the manometer
5. Purge the system (manometer + electrochemical cell) with O_2 (5 min)
6. Close inlet and outlet valves
7. Insert the system in a climatic chamber at 25 °C
8. Connect manometer to data acquisition card and cell to potentiostat

Cells are kept at OCV for 6 h before starting the cycling procedure in order to stabilize the temperature and the inner pressure of the system.

2.7 On-Line Electrochemical Mass Spectrometry (OEMS)

2.7.1 Background on Electrochemical Mass Spectrometry

Mass Spectrometry (MS) is a powerful method to analyze complex electrochemical systems such as Fuel Cells and batteries *in-operando*. Albeit MS applications for battery operation diagnostics is relatively recent, Differential Electrochemical Mass Spectrometry (DEMS) setups were extensively used for obtaining the composition of the exhaust gas of Fuel Cells, and it allowed researchers to get information on the instability of Fuel Cell components (e.g. depolymerization of ionomer membranes in Polymer Electrolyte Membrane Fuel Cells (PEMFCs)) by analyzing the corresponding volatile fragments. DEMS consists of a two stage pressure reduction from ambient pressure (the system to be studied) to the high vacuum needed for the mass spectrometer to operate. That is obtained by differential pumping, i.e. part of the inlet gas is pumped out of the system before reaching the MS inlet on a first stage, and the residual pressure is further lowered to high vacuum within the MS. This approach requires relatively high flows of gas (on the order of ml/min). Although this is possible for Fuel Cells, DEMS is not suitable "as-is" for battery applications due to the limited volume of gas available in electrochemical cells.

Researchers at IBM have adapted a DEMS system wherein, in order to avoid evacuation, the cell headspace is sampled in intervals of 15 min integration time [37]. Another approach was developed by W. Xu and coworkers at the Pacific Northwest National Laboratory in Richland, WA (USA), whereby a Gas Chromatography-Mass Spectrometry system (GC-MS) is connected to the cell headspace constantly purged with helium gas [71].

2.7.2 Online Electrochemical Mass Spectrometry Experimental Setup

We decided to pursue an even different approach, by designing a Mass Spectrometry system with a single stage pressure reduction from ambient pressure (the Li-O_2 cell) to the high vacuum of the MS (Pfeiffer Vacuum QMA 410). That goal can be achieved by sampling the cell's headspace at a flow rate of ≈1 μl/min through a calibrated crimped-capillary (Ar leak rate of 1.8 10^{-8} mbar·ml/s at 24ºC).

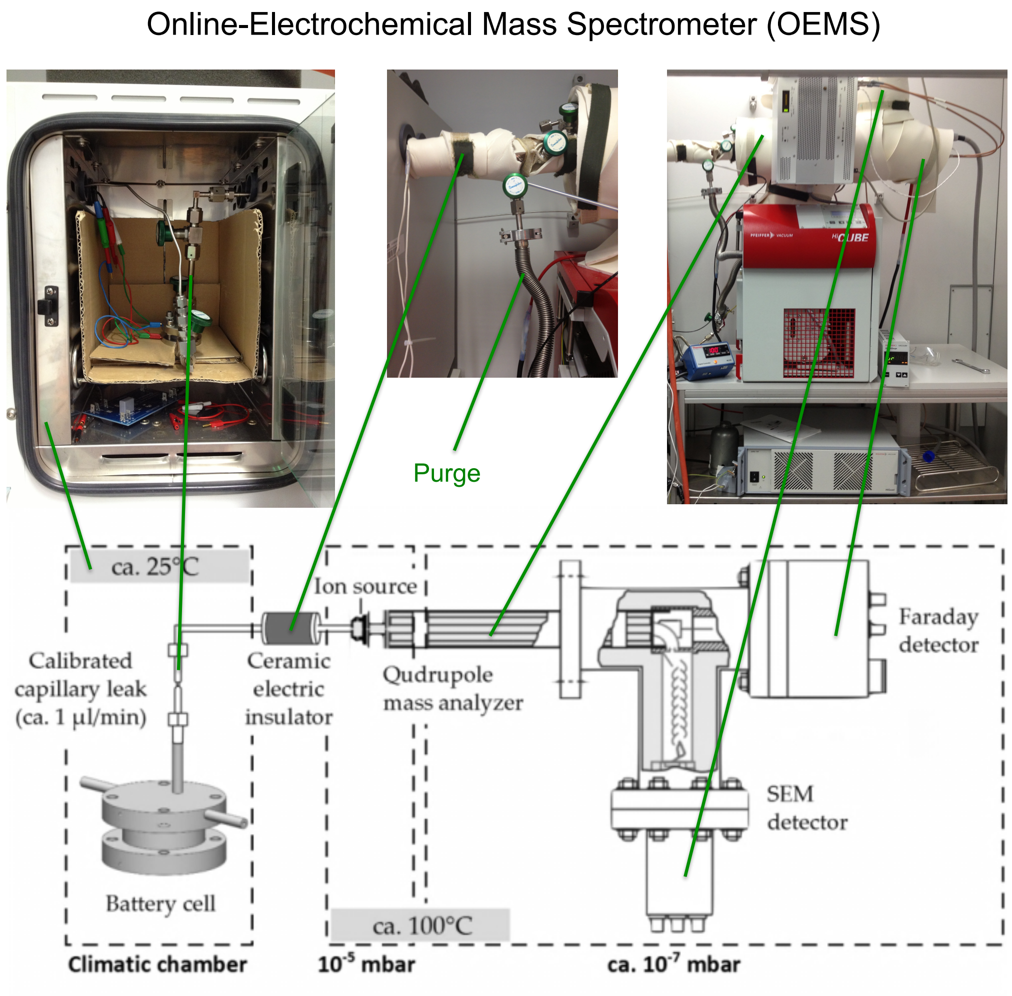
Online-Electrochemical Mass Spectrometer (OEMS)

Purge
ca. 25°C
Ion source
Calibrated capillary leak (ca. 1 μl/min)
Ceramic electric insulator
Qudrupole mass analyzer
Faraday detector
SEM detector
Battery cell
ca. 100°C
Climatic chamber
10⁻⁵ mbar
ca. 10⁻⁷ mbar

Figure 2.15. Technical scheme and real pictures of the On-line Electrochemical Mass Spectrometer (OEMS). The white band in which the system is wrapped up is used to maintain it at a temperature of 100 °C, in order to avoid the adsorption of H_2O and other contaminants on the internal metal surface of the instrument.

The main advantage of using a crimped-capillary over differential pumping is its very low leak rate combined with a fast response time (on the order of 1 second). The inlet is guided through a tube directly into a differentially pumped cross-beam ionization chamber. The resulting pressure in the ionization chamber is ≈$1\cdot10^{-6}$ mbar and ≈$1\cdot10^{-7}$ mbar at the off-axis Secondary Electron Multiplier (SEM) of the MS, allowing for quantification of ppm-level gas constituents (detection limit of ≈10^{-14} mbar).

Our custom cell hardware introduced in Section 2.4, with an inner volume of ≈10 ml of gas, allows us to perform MS experiments up to 30 hours long in a sealed system and without significantly affecting cell's base pressure (it should be noted that Li-air battery performance are fairly influenced by O_2 partial pressure [25,72]). Figure 2.15 shows a schematic view of the system developed by Dr. Nikolaos Tsiouvaras in our group, called On-line Electrochemical Mass Spectrometer or OEMS.

The main disadvantage of a single stage pressure reduction inlet, however, is the mass fractionation of the sampled gas [36]; therefore, in order to perform quantitative study of the gases evolved during operation, the signals of the components of interest must be calibrated using calibration gas mixtures with the same background matrix (Ar).

2.7.3 OEMS Data Acquisition and Data Treatment

In contrast to differentially pumped systems, gas evolution during OEMS operation results in a continuous accumulation of substances (e.g. O_2 evolution upon Li_2O_2 electrooxidation) in the headspace of the battery. In order to obtain the *gas evolution rates* (highly interesting because they allow to discern between different charge/discharge mechanisms/products) from the *integral* signals provided by OEMS (i.e. ion currents [A], corresponding to *concentrations*, Figure 2.16 b)), the following data processing must be carried out. First, the interesting *integral* signals (say, O_2) must be normalized by the mass trace of an inert compound for compensating the pressure reduction due to the OEMS sampling. ^{36}Ar is a convenient isotope due to its chemical inertia (its partial pressure depends only on temperature, kept constant, and sampling time) and its relatively high concentration (0.336 %). Normalized signals (Figure 2.16 c), dimensionless) are subsequently calibrated, smoothed and differentiated to gas evolution rates in [mol/s] (Figure 2.16 d)). However, it is more convenient to report gas evolution rates in terms of current-normalized molar flow rates in [μmol/(As)] (Figure 2.16 e)), since a 2-electron oxidation process of Li_2O_2 would correspond to a rate of 5.18 $\mu mol_{O2}/(As)$, independent of the applied current (this value is obtained from $(2 \cdot F)^{-1}$, where F is the Faraday constant (96485 As/mol)) so that experiments conducted at different absolute currents can be compared easily (e.g., electrodes with different carbon loadings charged at equal carbon mass-normalized currents).

Although in some cases (like the one shown in Figure 2.16 c)) O_2 evolution rates are constant throughout the whole charge process, leading to linear increase of O_2 concentration and thus to expected constant O_2 evolution rate [mol/s], the differentiation of such noisy signals can result in rather wavy evolution rates (Figure 2.16 d)). Smoothing the integral signal does mitigate this effect, however in some cases a linear fit of the normalized signal to calculate the evolution rate [mol/s] from the obtained slope can be more convenient.

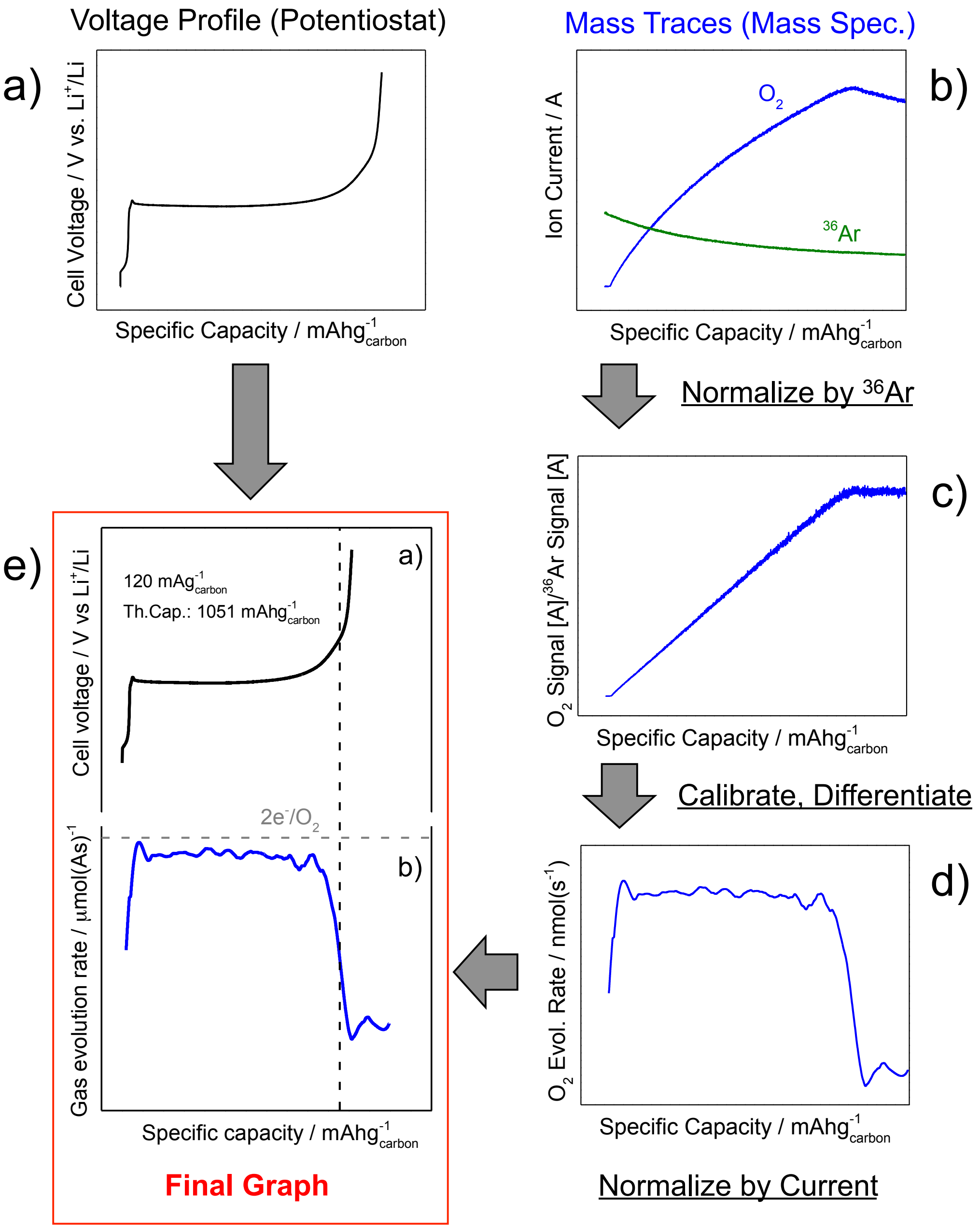

Figure 2.16. Schematic illustration of the data processing needed for interpreting OEMS data. a) Voltage profile of the electrochemical cell, b) raw ion-current signals [A] detected by the Mass Spec., c) O_2 signal normalized by ^{36}Ar signal [A/A], d) differentiated and calibrated O_2 signal, that is O_2 evolution rate [nmol/s], e) superimposed voltage profile to current-normalized O_2 evolution rate; the vertical dotted line indicates the theoretical specific capacity of the electrode, whereas the orizontal dotted line indicates the current normalized O_2 evolution rate corresponding to a $2e^-/O_2$ evolved process. The x-axis is a time axis expressed in terms of specific capacity, whereby 1h corresponds to 120 $mAhg^{-1}{}_{carbon}$.

2.8 Electrode Characterization

2.8.1 Carbon Loading of Air Electrodes

Carbon loading of air electrodes is a fundamental parameter to calculate the discharge rate in [A/g_{carbon}] and the specific capacity in [mAh/g_{carbon}]. All air electrodes discussed in this study are made of non-catalyzed carbon black and a binder. It is trivial task to calculate the carbon loading in [$mg_{carbon}/cm^2_{electrode}$] by just weighing the final electrodes and assuming that the binder/carbon/catalyst ratio set at the beginning of the electrode preparation are still valid for the final electrode.

$$L_{AM} = \left(m_{electrode} - m_{support}\right) \times \frac{f_{AM}}{A} \qquad \text{(Eq. 2.18)}$$

Where L_{AM} is the loading of the active material in [mg/cm^2], $m_{electrode}$ and $m_{support}$ is the total mass of electrode and support respectively in [mg], f_{AM} is the fraction of coating mass comprising the active material, and A is the electrode area in [cm^2]. This approach has shown good results for most experiments performed in this work, whereby deviations on the order of 10% for the capacity of repeated cycling experiments are considered acceptable.

2.8.2 Surface Analysis of Air Electrodes: BET Method

Surface analysis provides precise specific surface area evaluation of materials by N_2 multilayer adsorption measured as a function of relative pressure using fully automated analyzers. The technique encompasses external area and pore area evaluations to determine the total specific surface area in m^2/g. Data are treated by the instrument according to the Brunauer Emmett and Teller (BET) adsorption isotherm:

$$\frac{1}{\left[V_a\left(\frac{P_0}{P}-1\right)\right]} = \frac{C-1}{V_m C} \times \frac{P}{P_0} + \frac{1}{V_m C} \qquad \text{(Eq. 2.19)}$$

In this work, surface analysis by BET method was used for obtaining useful data about the pore size distribution of seven different carbon blacks employed for air electrode preparation (Section 3.2).

Surface and porosity analyses were conducted on both the raw electrode materials (CB powder) and on the final electrode, for further investigating the influence of the binder (namely Li^+ exchanged Nafion) on the surface properties (and thus on its electrochemical performance). As a relevant pore size distribution analysis requires a minimum of ≈20 m^2 total absolute surface to be introduced in the instrument, the latter task could not be carried out on Celgard® supported air electrodes (L_{carbon} = 0.3-0.5 $mg_{carbon}/cm^2_{electrode}$) for basically two reasons: first, the low carbon loading, desired for faster O_2 mass transport, would have required the introduction of large electrode pieces inside the BET instrument, mechanically not feasible, and second due to high mass fraction of Celgard® support (≈60 % of the electrode mass) and its high porosity (50 % of its volume), the accuracy of the measurement was heavily affected.

For example, the surface analysis of the lowest surface material, characterized by ≈70 m^2/g, required ≈450 mg of coating, corresponding to ≈300 mg of CB. Because our CB slurries are optimized for ≈180 mg of CB per ink, those requirements incited us to "scale-up" inks up to double the quantities (i.e. ≈360 mg CB). 3-fold thicker electrode coatings were spread on Al-foil and vacuum dried overnight at 95 °C; subsequently, the coatings were scraped off the support, grinded and submitted to surface analysis. Experimental details are reported in Section 3.2.

2.8.3 Characterization of Pre-Filled Electrodes by X-Ray Diffraction (XRD)

X-Ray powder Diffraction (XRD) was regularly employed for preliminary qualitative characterization of as-prepared pre-filled electrodes. The different crystal structures of Li_2O_2, LiOH, Li_2CO_3 and Li_2O determine characteristic X-ray diffraction patterns. X-ray powder diffraction data were collected using a Stadi MP diffractometer (STOE, Germany) equipped with a one dimensional silicon strip detector Mythen 1K (Dectris, Switzerland) and monochromatized Mo(Kα_1) radiation ($\lambda = 0.7093$ Å, 50 kV, 40 mA) in Debye-Scherrer or transmission geometry.

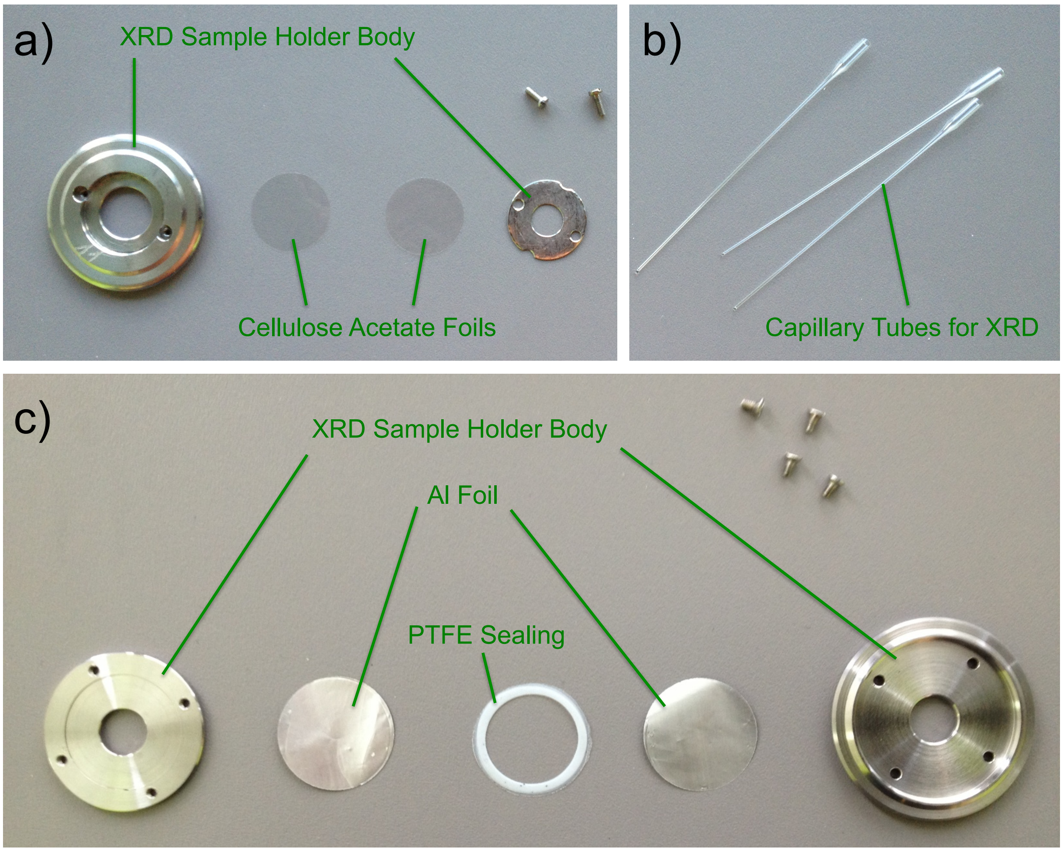

Figure 2.17. a) Regular sample holder for flat samples for measurements in Debye-Scherer geometry. b) Capillary tubes for XRD measurements of powder with the same geometry. c) Exploded view of the airtight sample holder for XRD analysis of flat samples in Debye-Scherer geometry developed at TUM.

At first, the standard sample holder for measurements in Debye-Scherrer geometry was used for X-ray diffraction experiments on a single electrode. The original sample holder from the manufacturer consisted of a pierced metal disk and two polymer foils (in our case, 10 µm thick cellulose acetate) to hold a flat sample (Figure 2.17 a)). Because of the high permeability of H_2O vapor through the cellulose acetate foils, leading to quantitative conversion of Li_2O into $LiOH•H_2O$ in less than 15 minutes of exposure to ambient air, capillary glass sample holders were preferred. By introducing the material of 4-5 electrodes (scraped off the Celgard® support) into 0.7 mm ⃠ capillaries (Figure 2.17 b)), we were able to drastically increase the signal to noise ratio of the measurements and to avoid H_2O permeation, making feasible data acquisition over long periods of time even for Li_2O electrodes. The capillaries were filled and sealed insidean Ar-filled glovebox.

XRD characterization of Li_2O electrodes charged at different state of charge (SOC) could not be performed using a capillary sample holder, since the amount of material of a single electrode is not sufficient. For that purpose, a novel airtight sample holder for XRD analysis of flat samples was developed. That sample holder, shown in Figure 2.17 c), consists of a stainless steel body, two Al foils (Al and Li_2O reflections do not superimpose) and a PTFE sealing. Because axial permeation of H_2O vapor through the Al foils does not occur, exposition to ambient air for more than 10 h does not lead to conversion of Li_2O into LiOH and $LiOH•H_2O$, as with the previous setup.

Charged electrodes were extracted from electrochemical cells in an Ar-filled glovebox, cut into four pieces and stacked in in the sample holder for improved signal/noise ratio.

2.8.4 Characterization of Pre-Filled Electrodes by IR-ATR Spectroscopy

IR-ATR analysis at different SOC was preferred to XRD for LiOH and Li_2CO_3 pre-filled electrodes due to its simplicity. LiOH and Li_2CO_3 have strong IR absorption bands in (O-H stretching ≈3700 cm^{-1} (LiOH) – CO_3^{2-} asymmetric stretching ≈1450 cm^{-1} and out-of-plane bending ≈850 cm^{-1} (Li_2CO_3)). The measurement consists in compressing the electrode's coating against a Ge crystal placed on the IR-ATR instrument, and to record the attenuation of the IR beam, totally reflected through the crystal, resulting by the exposure to an absorbing sample. In order to obtain reproducible and significant results with solid samples, it is important to ensure a good contact on the whole crystal surface (several mm^2). In our case, this practically translates in making sure that the region of the coating investigated is uniform, with no protruding particles and no evident cracks. Despite the relatively strong absorption of carbon throughout the range explored (4000-600 cm^{-1}) and the corresponding reduction of the signal/noise ratio passing from the pure compounds to the final electrode, absorbance peaks for both compounds are decisively distinguishable from the background, allowing their semi-quantitative determination. The electrolyte solvent (diglyme, main absorptions between 3000-2800 cm^{-1} (C-H stretching) and 1200-1000 cm^{-1} (C-O stretching))) was removed by vacuum drying overnight at 50°C, with no further treatment. The residual

LiTFSI electrolyte is characterized by well-defined strong absorptions between 1250-950 cm^{-1}, that allows the normalization of the spectra by the strongest TFSI$^-$ band at 1200 cm^{-1} for better comparison. For the same reason, pristine electrodes (i.e. 0 % charged) were characterized after exposition to battery conditions by assembling them in full battery cells for 2 h (typical rest period at OCV before the cells are charged). Experimental details are reported in Section 4.2.

2.8.5 Thermogravimetric Analysis - Mass Spectrometry (TGA-MS) Characterization of Pre-Filled Electrodes

In this work, thermo gravimetric analysis coupled to mass spectrometry (TGA-MS) was used for determining the composition of pre-filled electrodes. TGA continuously measures the weight of a sample as a function of temperature and time. Thermally activated events are recorded, and expressed as weight loss or weight change for a given time or temperature.

TGA is in principle a suitable technique for the characterization of Li_2O_2, Li_2CO_3, LiOH and L_2O *pre-filled* electrodes. Pure Li_2O_2, Li_2CO_3 and LiOH decompose into Li_2O by releasing O_2, CO_2 and H_2O respectively when heated in inert atmosphere (Ar) in the temperature range 25-1250 °C. Those thermal events take place in defined and typical temperature regions. On the other hand, Li_2O is stable throughout the whole temperature range (Table 2.1). Mass Spectrometer coupled to the TGA system through quartz capillary can easily detect the evolved gases.

The preliminary thermal analyses of the pure lithium compounds were performed in the temperature range 25-1250 °C, whereby the maximum temperature achievable with our TGA furnace is 1600 °C. However, as the capillary that connects the TGA furnace to the MS tend to melt or deform at temperatures >1000 °C (after several experiments the capillary was clogged), we decided to set the maximum for further experiments to 925 °C. Already at this temperature, all lithium compounds used (from now on referred to as Active Material or AM) are quantitatively decomposed to Li_2O.

Table 2.1. Thermal decomposition of inorganic lithium compounds used for preparing *pre-filled* electrodes. The decomposition temperature ranges are experimentally determined with our TGA-MS system (scan rate 20 K/min), whereas all other values are tabulated.

N°	T range [°C]	Reaction	Δm [% of LiX]	Evolved Gases	m.p. [°C]
(1)	25–1250	Li_2O does not react	–	–	1570
(2)	280–400	$Li_2O_2 \rightarrow Li_2O + ½ O_2$	-34.9	$O_2\uparrow$	~340
(3)	400–600	$2 LiOH \rightarrow Li_2O + H_2O$	-37.6	$H_2O\uparrow$	471
(4)	700–1100	$Li_2CO_3 \rightarrow Li_2O + CO_2$	-59.6	$CO_2\uparrow$	723

The following heating program was used for routine *pre-filled* electrodes characterization. First, the sample is heated from room temperature to 925 °C at a scan rate of 10 K/min in inert atmosphere (Ar) to decompose the AM, as in the pure case (s. Table 2.1). Second, the final temperature is held 30 minutes after the atmosphere is switched to 67% O_2 in Ar, in order to combust the organic compounds and leave Li_2O as only residue. In contrast with the pure AM case, thermal analysis of final carbon electrodes is much more complex, as the presence of carbon black and binder opens a whole plethora of chemical reactions. As a rule, Li_2O_2, LiOH and Li_2O tend to react at different temperatures with binder and carbon black (Vulcan XC72), leading to Li_2CO_3, finally decomposed into Li_2O, CO and CO_2 at temperatures >700 °C. Due to that complex reaction path, a qualitative determination of the active material is not feasible. For that reason, a complementary XRD characterization was necessary (Section 2.8.3).

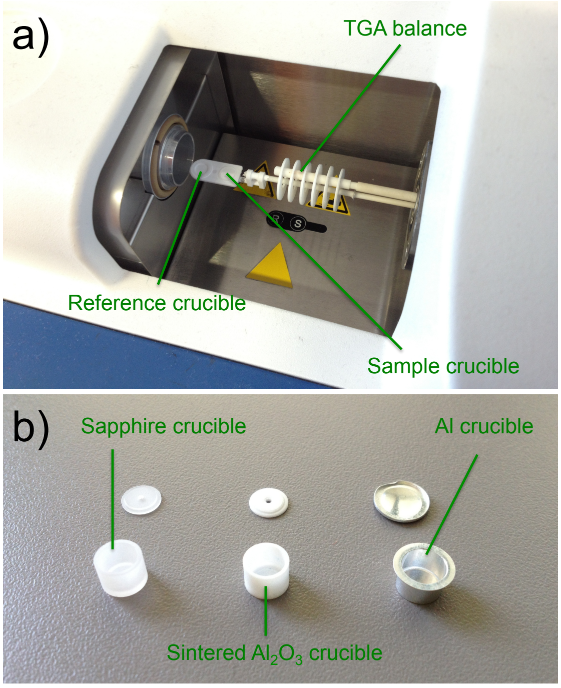

Figure 2.18. a) Inner view of the TGA furnace, and b) crucibles made of different materials; sapphire (supported Temp. 25-1600 °C), sintered Al_2O_3 (Supported Temp. 25-1600 °C), and sealable Al (supported Temp. 25-600 °C).

In case of Li_2O_2 electrodes, the reaction with carbon becomes violent at scan rates ≥20 K/min (Li_2O_2 is a source of oxygen, carbon is combustible), and the gases released (mostly CO) can spread powders and ashes in the TGA furnace. That is the reason for setting the scan rate to 10 K/min, at which no violent reaction is observed.

Another concern regarding the accuracy of the TGA measurements is the reactivity of some active materials (LiOH and Li_2O) with moisture and CO_2, as well as the tendency of carbon black to absorb humidity. Even if the sample is prepared inside an Ar-filled glovebox, weighing it outside next to the TGA instrument requires at least 1 min during which it is being exposed to ambient air. A possible way to prevent artifacts is to prepare a sample in an Al crucible sealed in an Ar-filled glovebox, and to pierce it after weighing it, just before introducing it in the TGA furnace. However, that approach cannot be used when temperatures >600 °C are investigated. For that reason, we decided to just weigh the sample directly inside the glovebox, although using a much less accurate scale (0.1 mg vs. 0.001 mg).

Electrode coatings as scraped off their support are flake-shaped black particles, very light and easily carried in a gas stream. In order to obtain accurate results, mass loss due to stripping of solids by expanding gases generated from the sample must be prevented. That goal was achieved by using 150 µl sapphire crucibles capped with a perforated sapphire lid that allows the release of gases without letting out bigger coating particles, mitigating like this major undesired mass losses. As the material of the crucible is concerned, the use of single crystal sapphire (Al_2O_3) crucibles was mandatory because more inexpensive materials such as sintered alumina (also Al_2O_3) let molten salts (mainly LiOH) through their porosity, thereby several crucibles were literally "welded" on the TGA scale after cooling down back at room temperature. Al_2O_3 and sapphire crucibles can be cleaned by washing with aqua regia, and subsequently annealing them in air at 1100 °C.

Despite all that was discussed above, quantitative information can still be obtained using the final Li_2O residue value. The final electrode composition, expressed as AM/carbon ratio, can be obtained using Eq. 2.20:

$$R_{AM} = \frac{\left[(r-f_{cat})\frac{M_x}{M_{Li_2O}}\right]}{\left\{\left[100-(r-f_{cat})\frac{M_x}{M_{Li_2O}}-cat\right]/(1+f_B)\right\}} \qquad \text{(Eq. 2.20)}$$

Where R_{AM} is the final AM/carbon ratio, r is the final Li_2O residue in [%] as obtained from Thermal Analysis, f_{cat} is the theoretical catalyst mass fraction in [%], M_x is the formula weight of the AM considered in [g/mol], M_{Li2O} is the formula weight of Li_2O in [g/mol], and f_B is the theoretical binder/carbon ratio in [g/g]. In our case, the desired value for R_{AM} is always 1.0 (1/1 AM/carbon, as expected by ink recipe). Any strong deviation from that value suggests exposure to moisture and/or contamination of the sample. Results and experimental details of TGA-MS analyses are reported in Sections 4.2 and 4.3.

Chapter 3

Investigations on Li-air Battery Discharge Limitations and Effect of Contaminants on Capacity and Cycling Performance

The outstanding projected specific energy of Li-air batteries rely on the very high theoretical specific capacity of Li_2O_x in comparison to the active materials used in Li-ion battery positive electrodes (>1000 mAh/g_{Li2Ox} vs. <200 mAh/$g_{interc.}$). As discussed in Section 2.2, battery electrodes are composed of a conductive carbon black, a binder and the active material. In Li-ion technology, practical positive electrodes comprise ≈95 % of active material [65] (say, $LiCoO_2$), therefore the specific capacity of the AM almost equals the specific capacity of the electrode coating (140 mAh/g_{LiCoO2} translate into 133 mAh/$g_{coating}$). On the other hand, Li-air positive electrodes are commonly made of a carbon material (say, Vulcan XC72 carbon black) used as electroactive surface for the oxygen reduction reaction, but ideally not participating in the discharge/charge reactions. Capacities of Li-air batteries are commonly reported as [mAh/g_{carbon}]; capacity expressed as [mAh/$g_{electrode}$] is however a more reliable descriptor for practical applications. Assuming Li_2O_2 is the only product, a specific capacity of 1168 mAh/g_{carbon} (corresponding to 1 g_{Li2O2}) for an electrode comprising 1 g_{carbon}, would translate in maximum 584 mAh/$g_{electrode}$, considering that a discharged electrode comprised at least the carbon support and Li_2O_2:

$$C_{electrode} = \frac{(1168\, mAh/g_{carbon} \times 1 g_{carbon})}{1 g_{Li2O2} + 1 g_{carbon}} = 584\, mAh/g_{electrode} \qquad \text{(Eq. 3.1)}$$

For that reason, in order to take full advantage of the superior specific capacity of Li-air discharge products, capacities in the order of ≈10000 mAh/g_{carbon} are highly desired. For example, a specific capacity of 11680 mAh/g_{carbon} provided by the same electrode would translate into 1062 mAh/$g_{electrode}$, largely outperforming a typical Li-ion positive electrode.

$$C_{electrode} = \frac{(11680\, mAh/g_{carbon} \times 1 g_{carbon})}{10 g_{Li2O2} + 1 g_{carbon}} = 1062\, mAh/g_{electrode} \qquad \text{(Eq. 3.2)}$$

Unfortunately, such high specific capacities are rather exceptional when practical electrode materials (e.g. non-catalyzed Vulcan XC72) are employed, being generally below 1000 mAh/g_{carbon} [36,50,73]. The reason for that is the formation of an insulating layer of discharge products (namely, Li_2O_2) on the electrode surface at relatively high discharge currents, which limits the discharge to much lower capacity values than would be expected if the whole electrode porosity was filled with products [47,49,50].

Several reports investigated the growth of the passivation layer on a flat glassy carbon electrode surface in three electrode cells that mimic Li-O_2 batteries, using both alkyl carbonates and ethers as electrolyte solvents. The increasing electronic resistance across the product layer, from the electrode to the O_2 molecules, was identified as the main factor limiting oxygen reduction reaction [48]. The critical thickness value at which the electrode surface is passivated and oxygen reduction reaction is stopped was measured to be 50-70 nm [47] and 5-8 nm [49] respectively, using comparable discharge currents. The apparent discrepancy between those two systems lies in the reactivity of alkyl carbonate electrolyte solvents with oxygen reduction reaction intermediates, and the subsequent formation of more soluble species that can cover longer distances before precipitating as Li(alkyl)carbonates. In this chapter, we extended those studies to real Li-O_2 cells comprising a mesoporous carbon black cathode and a Li foil anode. Understanding the fundamental electrochemistry of Li-air battery discharge is essential to design strategies for overcoming the discussed limitations and exploit the full potential of the technology.

3.1 The Effect of Water on the Discharge Capacity of a Non-Catalyzed Carbon Cathode for Li-O_2 Batteries

The paper entitled "The effect of water on the discharge capacity of a non-catalyzed carbon cathodes for Li-O_2 batteries" is presented in this section. That work was the first published by our group in the field of Li-air batteries, and reports on the first experimental results regarding the discharge of Li-O_2 cells.

As previous reports pointed out, the discharge capacity of Li-air batteries is very much influenced by the presence of some contaminants, which can be present as impurity in the O_2 feed (say, CO_2) or dissolved in the electrolyte solution. More precisely, Takechi et al. have shown that CO_2, deliberately added to the O_2 feed at concentrations between 10-80 %, is able to multiply the discharge capacity by a factor of 2-3 [54]. That result warned the scientific community that Li-air cell testing in a carefully controlled environment is essential for obtaining reproducible results and mitigating artifacts. For that reasons, it was essential to improve the sealing of our cell hardware.

In this section, a detailed description of a novel cell hardware design for LiO_2 battery testing is shown. That new cell allowed us to drastically reduce permeation of gases (mostly interesting were H_2O and CO_2, as N_2 was believed to be relatively inert on the cathode side) from ambient atmosphere, ensuring a controlled environment for long-term experiments (several days).

The use of that cell design resulted in a much lower discharge capacity of the carbon cathodes tested, which could not be explained only by the reduced permeation of CO_2 in the system, as its effect on capacity starts to be substantial at concentration in the order of percent, whereby atmospheric concentration of CO_2 is ≈400 ppm. However, by accidentally using leaking cell hardware the discharge capacity of our *Li-air* cells based on a superoxide-stable electrolyte solution could be increased by one order or magnitude, reaching again the values obtained with cell hardware previously used. As the CO_2 concentration in atmospheric air could not explain that improvement, a more abundant "contaminant", that is H_2O, was taken into consideration (H_2O concentration ≈1.5 % in air at 25 °C and 50% relative humidity). By intentionally providing H_2O saturated O_2 feed, the discharge capacity of *sealed* Li-O_2 cells could be increased by a factor of 14.

The discharge capacity of Li-O_2 cells is increased also when electrolyte solutions known to be reacting with ORR intermediates are used; more precisely a ≈2.5-fold improvement is obtained using 2/1 vol/vol propylene carbonate/dimethoxyethane blend as electrolyte solvent.

Based on those evidences, we developed a discharge mechanism for non-catalyzed carbon electrodes, whereby the precipitation of the discharge products on the electrode surface limits O_2 reduction by limited electron conduction (i.e. electrode passivation). In this hypothesis, discharge capacity is limited by the electrode surface area. On the other hand, when ORR intermediates react with either the electrolyte solvent or H_2O forming more soluble species, electrode passivation is strongly delayed, therefore the discharge capacity is limited by the ability of the electrode to "store" discharge products, thus by its porosity. Despite the fact that higher discharge voltage (≈50 mV) is observed using H_2O contaminated O_2, suggesting the formation of LiOH instead of Li_2O_2, recent results obtained in our laboratory seem to invalidate that hypothesis. Further studies are currently being carried out in order to address that point.

The Effect of Water on the Discharge Capacity of a Non-Catalyzed Carbon Cathode for Li-O_2 Batteries

S. Meini, M. Piana, N. Tsiouvaras, A. Garsuch and H.A. Gasteiger

Electrochemical & Solid-Stale Letters, 2012, Volume 15, Issue 4, Pages A45-A48

Permanent weblink:

http://dx.doi.org/10.1149/2.005204esl

Reproduced by permission of The Electrochemical Society

Electrochemical and Solid-State Letters, **15** (4) A45-A48 (2012)
1099-0062/2012/15(4)/A45/4/$28.00 © The Electrochemical Society

The Effect of Water on the Discharge Capacity of a Non-Catalyzed Carbon Cathode for Li-O_2 Batteries

Stefano Meini,[a,z] Michele Piana,[a,*] Nikolaos Tsiouvaras,[a,*]
Arnd Garsuch,[b] and Hubert A. Gasteiger[a,*]

[a] *Institute of Technical Electrochemistry, Technische Universität München, D-85748 Garching, Germany*
[b] *BASF SE, GC, Ludwigshafen am Rhein 67056, Germany*

In this study we report the strong effect of water or organic carbonates on the specific capacity during the first discharge of the cathode of a Li-O_2 cell, using Vulcan-based positive electrodes. An improved cell design allowed us to avoid contaminations from atmospheric air and to compare the discharge in water-free electrolyte with that of water contaminated cells, getting an increased specific capacity up to one order of magnitude. Understanding the mechanism that limits or enhances the specific capacity of the positive electrode is very important in order to improve performance and durability of Li-O_2 cells.

© 2012 The Electrochemical Society. [DOI: 10.1149/2.005204esl] All rights reserved.

Manuscript submitted September 26, 2011; revised manuscript received December 15, 2011. Published January 23, 2012.

Since the specific energy of state-of-the-art lithium ion batteries (LiBs) is mostly limited by the positive electrode (cathode), novel cathode concepts are required to substantially increase battery specific energy and thus battery electric vehicle (BEV) range.[1] The theoretically highest specific energy is promised by Li-air batteries[2,3] due to the 4 to 6 times higher specific energy of the Oxygen Reduction Reaction (ORR) cathode in aprotic organic electrolytes,[4] which could lead to a 3– to 4–fold increase in specific energy for fully packaged Li-air batteries compared to state-of-the-art LiBs.[4,5]

However, lithium-air battery cathode rate capability is very low and capacity decreases as the current density is increased from typically 0.04–0.10 mA/cm^2 up to 1.0 mA/cm^2.[6–11] To account for the widely varying carbon loadings of ≈0.4[10] to ≈25 mg$_{carbon}$/cm^2,[6] current densities are often referenced to the weight of carbon (mA/g$_{carbon}$), whereby most experiments are conducted at ≈70–100 mA/g$_{carbon}$.[4,12–14] Cathode specific capacities at low current densities, which are conventionally normalized to the weight of carbon, range from ≈500 to ≈3000 mAh/g$_{carbon}$,[6,9–11,13] corresponding to very low C-rates of 1/10 h^{-1} or less. For cathodes using non-catalyzed carbons, the specific capacity depends on the type of carbon[6,11] as well as on the oxygen solubility of the aprotic organic electrolyte.[9,15] Thus, specific capacities from different studies can only be compared at different discharge rates and if the same carbons and electrolytes are used. However, recent findings showed that lithium-air cathode discharge in alkyl carbonate electrolytes produces lithium (alkyl) carbonates rather than the desired lithium peroxide, due to the reaction of superoxide radicals with alkyl carbonates like propylene carbonate (PC).[16–19] Conversely, lithium peroxide (Li_2O_2) is predominantly formed during the first discharge in ether-based electrolytes like dimethoxy ethane (DME)[17] although not exclusively in subsequent cycles.[19]

In addition to developing more stable electrolytes as well as cathode designs which enable high capacity at C-rates of ≈1 h^{-1} (i.e., at thousands mA/g$_{carbon}$) and utilize catalysts to increase round-trip voltage efficiencies (≈70% for MnO_2[13] and ≈75% for PtAu[14]), the sensitivity of the lithium-air battery to contaminants in atmospheric air[20] (CO_2, H_2O) and/or produced upon cycling (CO_2, Li-alkyl-carbonates[21]) has to be considered.

In the present work, we introduce a Li-O_2 test cell design with improved sealing and reduced permeation of CO_2 and H_2O from the ambient. With this cell, we compare specific capacities in the first discharge in aprotic solvents which lead to lithium (alkyl) carbonate discharge products (i.e., PC:DME mixtures) with those which lead to lithium peroxide (i.e., DME). Furthermore, we explore the effect of water contamination in pure DME, illustrating that it significantly enhances specific capacity in the first discharge, so that widely varying capacities are obtained if water contamination is not carefully controlled.

Experimental

Electrode design and testing.—The positive electrodes with a binder/carbon ratio of 0.5/1 g/g were prepared by Mayer-rod coating of an ink composed of carbon, isopropanol, and a lithium-ion exchanged Nafion solution (LITHion, Ion Power, USA) onto a Celgard C480 separator. The ink was prepared adding Vulcan XC72 carbon to isopropanol (Sigma-Aldrich, 99.9%), and the mixture was sonicated for 20 minutes (Branson 250 probe-sonifier). Afterwards, LITHion solution (10.6%wt. in isopropanol) was added, and the ink was mixed with a spatula for half a minute. After solvent evaporation at room temperature, 15 mm diameter cathode electrodes were punched out, dried under dynamic vacuum at 95°C for 6 hours in a glass oven (Büchi, Switzerland), and transferred for cell assembly into an argon-filled glove box ($O_2 < 1$ ppm, $H_2O < 0.5$ ppm; Jacomex, France) avoiding exposure to ambient air. The carbon loading of the cathodes of 0.41 mg$_{carbon}$/cm$^2_{electrode}$ (13 µm thickness) was obtained by weighing. Electrolytes were prepared with battery grade $LiClO_4$ (Sigma-Aldrich, 99.99% trace metal basis) vacuum dried at 150°C for 24 hours before use. Anhydrous DME (Aldrich, 99.5%), PC (Aldrich, 99.7%), and PC:DME blends (2:1 and 4:1 v:v) were dried for 24 hours over Sylobead MS 564C zeolites (3 Å, Grace Division). The water content of the 0.1 M $LiClO_4$ electrolytes, unless reported otherwise, was ≤4 ppm (Karl Fischer titration).

Cell assembly.—A 17 mm ø lithium disk (0.45 µm thick, 99.9%; Chemetall, Germany) is placed onto the anode current collector, wetted with 40 µl of electrolyte, and covered with two Celgard C480 separators. The cathode is placed onto the separators before and after dropping 40 µl of electrolyte and then covered with a 21 mm ø stainless steel (316SS) mesh (0.22 mm ø wire, 1.0 mm openings, Spörl KG, Germany) cathode current collector. The cell is sealed with four screws at a torque of 6 Nm, then connected to an oxygen line (all 316SS tubing to avoid moisture intrusion) and purged with O_2 (80 sccm for 0.5 minutes). After a 30 minute rest at open circuit voltage (OCV), cells were discharged at 0.05 mA/cm$^2_{electrode}$ (≡ 120mA/g$_{carbon}$) at room temperature to a lower limit of 2.0 V (VMP3, Bio-Logic, France).

Cell design.—The cell design is shown in Figure 1a, with several modifications to the design used by Lu et al.:[4] i) a double step in the anode plate ① to align the Li foil and to contain the electrolyte; ii) a poly(chlorotrifluoroethylene) (PCTFE, Kel-F) spacer ② instead of virgin poly(tetrafluoroethylene) (PTFE), due to its much lower gas permeability and higher hardness;[22] iii) single-use PTFE O-rings ③ to ensure gastight sealing (2.6 mm cross-section and 30 mm ID, Angst Pfister AG, Switzerland). The cell inner volume is ≈10 mL. Electrical

---

[*] Electrochemical Society Active Member.
[z] E-mail: stefanomeini@tum.de

Downloaded 01 Feb 2012 to 138.246.2.183. Redistribution subject to ECS license or copyright; see http://www.ecsdl.org/terms_use.jsp

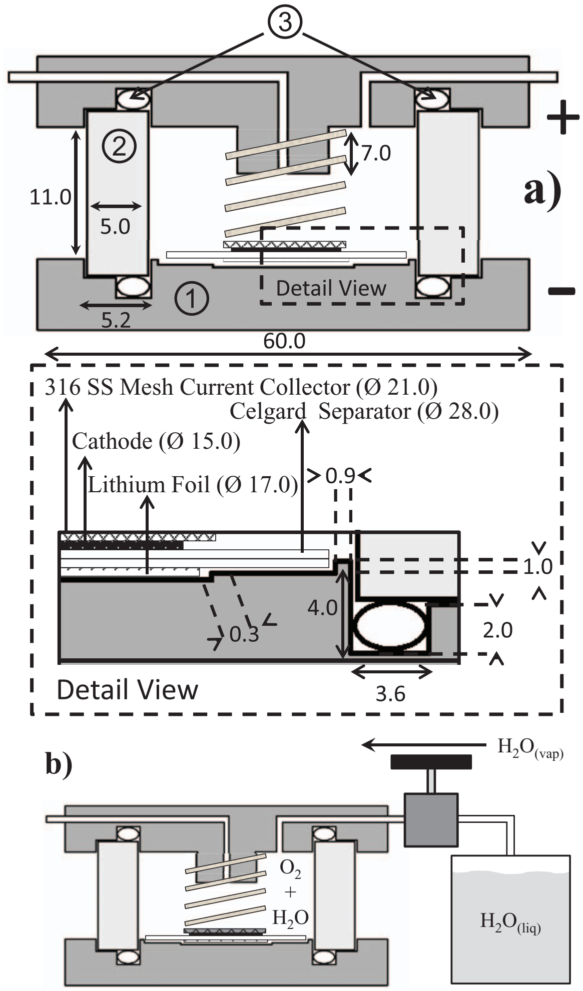

Figure 1. a) Cross-section of the Li-air cell design used for the tests with all dimensions given in units of mm: ① cell body made of 316SS-Ti; ② Kel-F annulus; ③ virgin-PTFE O-ring seal; b) "Water Vapor" cell design: water (∼2 mL) is placed in a small vessel and the vapor phase connected to the electrochemical cell.

contact between the cathode plate and the cathode is made by a spring (316SS, 2.3 N/mm, 0.5 inch ø and length, Lee Springs, UK).

The effect of the lower permeability of Kel-F vs. PTFE for the spacer is illustrated in the following: 1000 mAh/g_{carbon} average specific discharge capacity, when forming Li_2O_2, would yield an oxygen consumption rate of ≈45 × 10^{-11} mol/s (based on 0.41 mg_{carbon}/cm^2, 1.77 cm^2 electrodes, and a discharge rate of 120 mA/g_{carbon}). Using the PTFE permeability data for CO_2 and H_2O (0.7 × 10^{-12} and 2.5 × 10^{-12} $cm^2/s/Pa$[22]) and their partial pressure in ambient air (≈40 Pa for CO_2 and ≈1500 Pa for H_2O at 25°C and 50% relative humidity), the permeation rate of CO_2 and H_2O are ≈0.003 × 10^{-11} and ≈1 × 10^{-11} mol/s (wall thickness of 5 mm, external area 20 cm^2). While the projected CO_2 permeation rate is 10^4-fold lower than the oxygen consumption rate and thus cannot affect the discharge chemistry, H_2O permeation would lead to significant contamination during extended cycling. Since the gas permeabilities of Kel-F are ≈100–fold lower than that of PTFE,[22] its use ensures an uncontaminated system.

Some cells were deliberately exposed to water vapor by connecting them to an external water-filled vessel ("Water Vapor Cell," Figure 1b). The valve connecting the cell and the water-filled vessel was opened after careful O_2 purging of the cell. Alternatively, the effect of contamination from the ambient was studied in a so-called "Leaker Cell," which had a small leak at a welding connection had (when evacuated, the cell pressure increased by ≈25 Torr/s).

Results and Discussion

Figure 2 compares the discharge specific capacities (mAh/g_{carbon}) of Vulcan cathodes using different solvents with 0.1 M $LiClO_4$ at 0.05 $mA/cm^2_{electrode}$ (120 mA/g_{carbon}). The discharge voltage profile in DME electrolyte shows a flat plateau at ≈2.66 V, whereas two plateaus are visible in PC/DME electrolytes (≈2.6 V and ≈2.3 V). The same was observed by McCloskey et al.,[17] whereby the discharge products were found to be mostly lithium (alkyl) carbonates in PC/DME and mostly Li_2O_2 in DME. The specific capacities for pure DME are ≈2.5-fold lower than for PC:DME 2:1 and 4:1 electrolytes. Surprisingly, one would expect the opposite behavior due to the ≈2-fold higher oxygen solubility in DME vs. PC:DME (1:2 v:v) and the observation that the discharge capacity increases with oxygen solubility.[15] This correlation is also supported by the observed ≈3-fold higher discharge capacity of ≈1000 mAh/g_{carbon} in PC:DME (1:2 v:v) at 100 mA/g_{carbon}[14] vs. ≈3000 mAh/g_{carbon} in pure DME[10] using similarly prepared electrodes and the same electrolyte. In contrast, we observed ≈15-fold lower discharge capacities in pure DME at ≈200 mAh/g_{carbon} (see Fig. 2).

During repeat experiments, large specific capacities were occasionally observed for one set of cell hardware. Upon closer examination, we discovered a small hole in the welding that allowed atmospheric air to enter into the cell. Subsequent, experiments with this so-called "Leaker Cell" yielded reproducibly high capacities of ≈2200 mAh/g_{carbon} in pure DME (see Fig. 3a). As reported by Takechi et al.,[23] adding 10 vol% CO_2 to pure O_2 leads to a ≈2-fold specific capacity gain in EC:DEC (3:7 v:v), but the CO_2 level in air of ≈0.04 vol% is too low to produce the observed ≈10-fold capacity gain between a sealed cell and the "Leaker Cell." The only other candidate to affect the specific capacity is water vapor, the concentration of which is ≈1.6 vol% in ambient air (assuming 25°C and 50% relative humidity).

Conversely, the specific capacity in pure DME using the "Water Vapor Cell" reaches up to 2800 mAh/g_{carbon}, about 14-fold higher values than in the Sealed Cell design (see Fig. 3a). Surprisingly, this specific capacity value is now comparable to the above discussed value of ≈3000 mAh/g_{carbon}.[10] As evident from Fig. 3a, the discharge voltage plateau in the water vapor cell is ≈50 mV higher than for a sealed cell (≈2.71 V versus ≈2.66 V). This effect can be related to the reversible potential for LiOH formation compared to Li_2O_2:[4,24]

$$4\,Li + 2\,H_2O + O_2 \rightarrow 4\,LiOH \quad E^\circ = 3.35\,V \qquad [1]$$

$$2\,Li + O_2 \rightarrow Li_2O_2 \quad E^\circ = 2.96\,V \qquad [2]$$

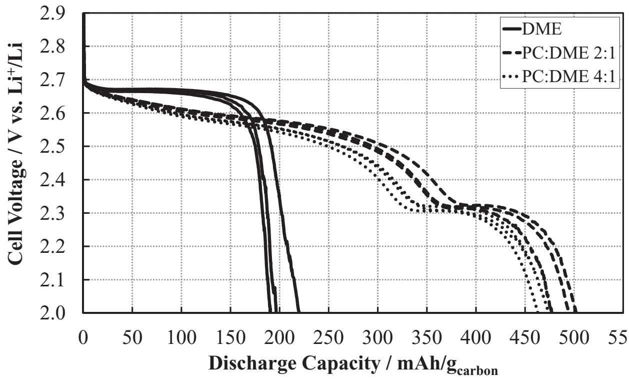

Figure 2. Comparison between the discharge capacity (1st cycle) of sealed $Li\text{-}O_2$ cells using different water-free (<4 ppm water) non-aqueous electrolytes: 0.1 M $LiClO_4$ in DME (—), PC:DME (2:1 v:v) (---), and PC:DME (4:1 v:v) (···). The cells were galvanostatically discharged at 120 mA/g_{carbon} (0.05 $mA/cm^2_{electrode}$) after a 30 minute rest period at OCV in pure 100 kPa_{abs} O_2. The reproducibility of the results is shown in three similar discharge profiles obtained from three repeated experiments.

Downloaded 01 Feb 2012 to 138.246.2.183. Redistribution subject to ECS license or copyright; see http://www.ecsdl.org/terms_use.jsp

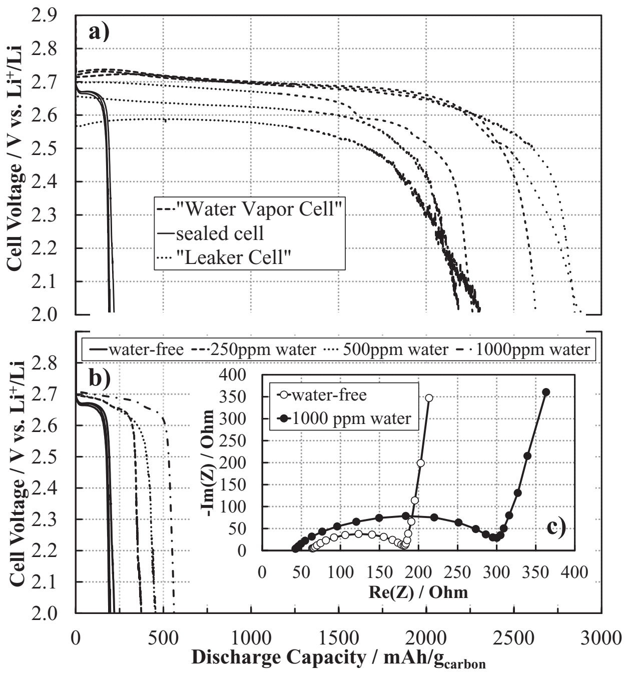

Figure 3. a) Comparison between discharge capacity (1st cycle) of Li-O_2 cells with 0.1 M $LiClO_4$ in DME using H_2O-free (—) or H_2O contaminated oxygen (100 kPa_{abs}), whereby water was introduced by means of a small leak between the cell and ambient air (---) in the "Leaker Cell" or by connecting a water reservoir to produce H_2O–saturated O_2 inside the cell (···) in the "Water Vapor Cell" (see Fig. 1b). b) Comparison between the discharge capacity (1st cycle) of sealed Li-O_2 cells using water-free (—) or deliberately water contaminated electrolyte (0.1 M $LiClO_4$ in DME) with 250 (---), 500 (···) and 1000 (-·-) ppm of water. The cells are galvanostatically discharged at 120 mA/g_{carbon} (0.05 $mA/cm^2{}_{electrode}$) after a 30 minute rest period at OCV in pure 100 kPa_{abs} O_2. c) Nyquist impedance plots of Li-O_2 cells using water-free (○) and water contaminated (1000 ppm) (●) electrolytes registered after the 30 min OCV rest period (100 kHz to 0.1 Hz at an AC perturbation of 5.0 mV).

For further insight, experiments were conducted with water-contaminated DME electrolyte. Increasing the water content to 1000 ppm, the discharge capacity increases from ≈200 mAh/g_{carbon} without water addition to ≈560 mAh/g_{carbon} in the presence of 1000 ppm (Fig. 3b), with discharge potentials approaching those observed in the "Water Vapor Cell." While these capacities are much smaller than the ≈2200 and ≈2800 mAh/g_{carbon} obtained for the "Leaker Cell" and the "Water Vapor Cell," this can be explained by the limited amount of water available for Reaction 1 in the water-contaminated electrolytes vs. the unlimited supply in the "Water Vapor Cell": 1000 ppm of water in the 120 µl electrolyte amount to $\approx 0.7 \cdot 10^{-5}$ mol_{H_2O} which via Reaction 1 could produce a charge of ≈1.35 As equating to ≈520 mAh/g_{carbon}, not too different from the observed 560 mAh/g_{carbon}. Closer inspection of the discharge potentials in Fig. 3b suggests the presence of two discharge plateaus for water-contaminated electrolytes, one plateau near 2.70 V and a subsequent lower plateau near 2.66 V, characteristic of water-free DME. The above calculation is only a rough estimate, since some of the water will be consumed through reaction with the metallic lithium anode. Nevertheless, based on the results in Fig. 3, it is reasonable that the overall discharge process in the presence of water traces is actually a superimposition of Reactions 1 and 2, effecting an increase in discharge capacity. An analogous, but much smaller increase in discharge capacity caused by water contamination was reported for a similar system, a Si-O_2 battery.[25]

Nyquist plots of Li-O_2 cells built using water-free and water-contaminated (1000 ppm) 0.1 M $LiClO_4$ in DME electrolyte are shown in Figure 3c. Similar curves are observed, except that the intercept with the real axis at low frequencies increases from ≈180 Ω in water-free electrolyte to ≈300 Ω in water-contaminated electrolyte (1000 ppm water). The same phenomenon was observed in the Si-O_2 battery system,[25] explained by the authors with the formation of a thick layer of Si oxides. In analogy, the impedance data in Fig. 3c may indicate the formation of a layer of lithium hydroxides on the lithium anode in water-contaminated electrolyte, leading to an increased low-frequency impedance.

In trying to understand the observed strong enhancement of water (vapor) on the discharge capacity of lithium-oxygen cells, one may speculate on the possible rate limiting steps during the growth of discharge deposits on the carbon (or catalyst) surface when water-free DME electrolyte is used: i) an electron-transport-limited reaction of Li^+ and O_2 at the film/solution interface (see Fig. 4a) proposed in a study on a flat glassy carbon electrode by Albertus et al.[26] and examined in a theoretical study by Hummelshøj et al.[27] ii) slow diffusion of Li^+ and/or O_2 through the deposit, hindering the reaction at the carbon/film interface (see Fig. 4b). The ultimate deposit layer thickness on Vulcan electrodes can be estimated from the external surface area of Vulcan of ≈100 m^2/g_{carbon} (assuming spherical carbon particles of 30 nm diameter with a density of ≈2 g/cm^3 [28]) and the charge for a monolayer of LiO_2 or Li_2O_2 deposit. The former was estimated to be ≈200 $\mu C/cm^2$ [29] and the latter can be estimated to be ≈260 $\mu C/cm^2$ based on its crystal structure.[30] If referenced to the effective carbon surface area, these values equate to ≈50 mAh/g_{carbon} and ≈70 mAh/g_{carbon} for one monolayer of LiO_2 and Li_2O_2, re-

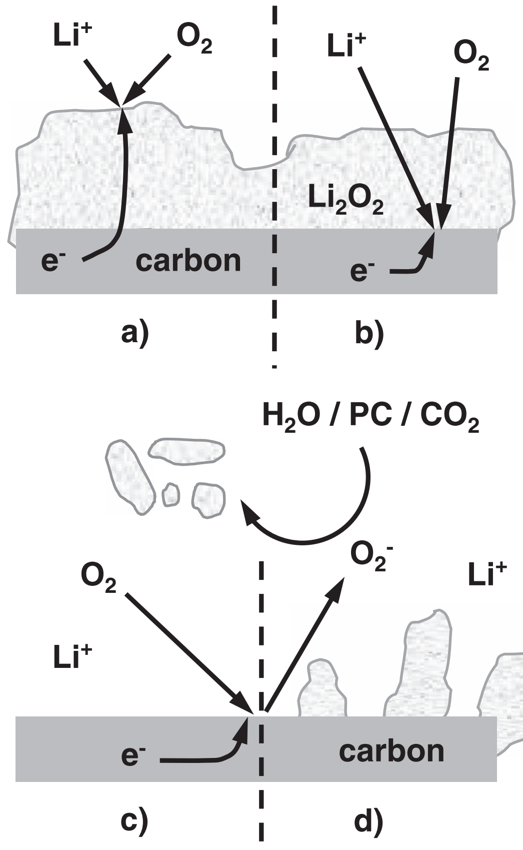

Figure 4. Possible reaction mechanisms of the discharge reaction at the cathode of a Li-O_2 cell in aprotic organic electrolytes: a) ORR at the interface between deposited Li_2O_2 and the solvent, limited by electron conduction through the Li_2O_2 deposit; b) ORR at the interface between deposited Li_2O_2 and the carbon surface, limited by the diffusion of lithium ions and molecular oxygen through Li_2O_2; reaction of superoxide ion radical with contaminants (H_2O/PC/CO_2) and formation of c) soluble reaction products or d) formation of a non-homogeneous solid layer on the carbon surface.

Downloaded 01 Feb 2012 to 138.246.2.183. Redistribution subject to ECS license or copyright; see http://www.ecsdl.org/terms_use.jsp

spectively. Based on the discharge capacity in water-free DME ($\approx$200 mAh/g_{carbon}), this would suggest that only 3 to 4 monolayers of Li_xO_2 deposit might stop the discharge reaction at the rate of 120 mA/g_{carbon}.

In the presence of a reactive electrolyte (e.g., PC) or other contaminants like water, one might hypothesize that $O_2^{\bullet-}$ reacts preferentially with them rather than forming LiO_2 followed by disproportionation to Li_2O_2,[31,32] leading to two possible scenarios: i) the reaction products could be slightly soluble in the electrolyte and diffuse into the bulk of the solution, preventing the formation of a passivating film (Fig. 4c), as is suggested by recent data,[33] where the formation of Li_2O_2 particles disconnected from the carbon-substrate of the electrode was observed; ii) when the solid product on the electrode were to grow in form of a cracked layer (Fig. 4d) that partially exposes the underlying substrate to the electrolyte. The latter is similar to the case of the oxygen reduction reaction (ORR) in proton exchange membrane fuel cells at –20°C, where the ORR kinetics of platinum are observed throughout the discharge, despite the formation of thick water-ice layers on the platinum/carbon surface.[34] Since solid-state diffusion of O_2 through water-ice or through a Li_2O_2 deposit would be expected to be slow at room temperature, a buildup of more than three monolayers would only be possible if the formed deposit would be substantially "cracked" rather than forming a smooth film (Fig. 4d). Both scenarios could explain the capacity-enhancing effect in PC/DME (Fig. 2) and in the presence of water (Fig. 3). We plan to report in future work experimental evidences for admittedly speculative mechanisms discussed here.

Conclusions

We showed an improved design of a Li-O_2 test cell, developed in order to avoid any contamination from atmospheric air. We used this to study the discharge capacity in absence of water (vapor) contamination and compared this to data obtained with cells to which water or water vapor was added deliberately. The data demonstrate a very strong capacity enhancing effect of water at relatively low concentrations. This can lead to possible misinterpretations on the discharge capacity of non-aqueous Li-O_2 cells. A similar effect, but to a lesser extent, is observed in presence of alkyl carbonate electrolytes. Several possible discharge capacity limiting reaction mechanisms were hypothesized to rationalize the observed capacity gains.

Acknowledgments

Financial support of this research by BASF SE through the framework of its Scientific Network on Electrochemistry and Batteries is gratefully acknowledged by TUM. The TUM Graduate School (TUM-GS) is gratefully acknowledged by Stefano Meini for scholarly and financial support.

References

1. F. T. Wagner, B. Lakshmanan, and M. F. Mathias, *J. Phys. Chem. Lett.*, **1**, 2204 (2010).
2. K. M. Abraham and Z. Jiang, *J. Electrochem. Soc.*, **143**, 1 (1996).
3. G. Girishkumar, B. McCloskey, A. C. Lunz, S. Swanson, and W. Wilcke, *J. Phys. Chem. Lett.*, **1**, 2193 (2010).
4. Y.-C. Lu, H. A. Gasteiger, M. C. Parent, V. Chiloyan, and Y. Shao-Horn, *Electrochem. and Solid State Lett.*, **13**, A69 (2010).
5. Y.-C. Lu, H. A. Gasteiger, E. Crumlin, R. McGuire Jr., and Y. Shao-Horn, *J. Electrochem. Soc.*, **157**, A1016 (2010).
6. J. Xiao, D. Wang, W. Xu, D. Wang, R. E. Williford, J. Liu, and J.-G. Zhang, *J. Electrochem. Soc.*, **157**, A487 (2010).
7. S. S. Zhang, D. Foster, and J. Read, *J. Power Sources*, **195**, 1235 (2010).
8. G. Q. Zhang, J. P. Zheng, R. Liang, C. Zhang, B. Wang, M. Hendrickson, and E. J. Plichta, *J. Electrochem. Soc.*, **157**, A953 (2010).
9. J. Read, *J. Electrochem. Soc.*, **149**, A1190 (2002).
10. Y.-C. Lu, D. G. Kwabi, K. P. C. Yao, J. R. Harding, J. Zhou, L. Zuin, and Y. Shao-Horn, *Energy Environ. Sci.*, **4**, 2999 (2011).
11. X.-H. Yang, P. He, and Y.-Y. Xia, *Electrochem. Comm.*, **11**, 1127 (2009).
12. A. Débart, J. Bao, G. Armstrong, and P. G. Bruce, *J. Power Sources*, **174**, 1177 (2007).
13. A. Débart, A. J. Paterson, J. Bao, and P. G. Bruce, *Angew. Chem.*, **47**, 4521 (2008).
14. Y.-C. Lu, Z. Xu, H. A. Gasteiger, S. Chen, K. Hamad-Schifferli, and Y. Shao-Horn, *J. Am. Chem. Soc.*, **132**, 12170 (2010).
15. J. Read, K. Mutolo, M. Ervin, W. Behl, J. Wolfenstine, A. Driedger, and D. Foster, *J. Electrochem. Soc.*, **150**, A1351 (2003).
16. F. Mizuno, S. Nakanishi, Y. Kotani, S. Yokoishi, and H. Iba, *Electrochemistry*, **78**, 403 (2010).
17. B. D. McCloskey, D. S. Bethune, R. M. Shelby, G. Girishkumar, and A. C. Luntz, *J. Phys. Chem. Lett.*, **2**, 1161 (2011).
18. S. A. Freunberger, Y. Chen, Z. Peng, J. M. Griffin, L. J. Hardwick, F. Bardé, P. Novak, and P. G. Bruce, *J. Am. Chem. Soc.*, **133**, 8040 (2011).
19. S. A. Freunberger, Y. Chen, N. E. Drewett, L. J. Hardwick, F. Bardé, and P. G. Bruce, *Angew. Chem. Int. Ed.*, **50**, 1 (2011).
20. M. Armand and J.-M. Tarascon, *Nature*, **451**, 652 (2008).
21. W. Xu, K. Xu, V. V. Viswanathan, S. A. Towne, J. S. Hardy, J. Xiao, Z. Nie, D. Hu, D. Wang, and J-G. Zhang, *J. Power Sources*, **196**, 9631 (2011).
22. http://www.goodfellow.com/E/Polychlorotrifluoroethylene.html http://www.goodfellow.com/E/Polytetrafluoroethylene.html.
23. K. Takechi, T. Shiga, and T. Asaoka, *Chem. Commun.*, **47**, 3463 (2011).
24. D. Linden and T. B. Reddy, *Handbook of Batteries* 3rd edition, ch. 38.46, McGraw-Hill, New York (2002).
25. G. Cohn, D. D. Macdonald, and Y. Ein-Eli, *Chem. Sus. Chem.*, **4**, 1124 (2011).
26. P. Albertus, G. Girishkumar, B. McCloskey, R. S. Sánchez-Carrera, B. Kozinsky, J. Christensen, and A. C. Luntz, *J. Electrochem. Soc.*, **158**, A343 (2011).
27. J. S. Hummelshøj, J. Blomqvist, S. Datta, T. Vegge, J. Rossmeisl, K. S. Thygesen, A. C. Luntz, K. W. Jacobsen, and J. K. Nørskov, *J. Chem. Phys.*, **132**, 071101 (2010).
28. K. Kinoshita, Carbon, John Wiley & Sons, New York (1988).
29. D. Aurbach, M. L. Daroux, P. Faguy, and E. Yeager, *J. Electroanal. Chem.*, **297**, 225 (1991).
30. L. G. Cota and P. De la Mora, *Acta Cryst.*, **B61**, 133 (2005).
31. C. O. Laoire, S. Mukerjee, E. J. Plichta, M. A. Hendrickson, and K. M. Abraham, *J. Phys. Chem. C*, **114**, 9178 (2010).
32. Z. Peng, S. A. Freunberger, L. J. Hardwick, Y. Chen, V. Giordani, F. Bardé, P. Novàk, D. Graham, J.-M. Tarascon, and P. G. Bruce, *Angew. Chem.*, **50**, 6351 (2011).
33. R. R. Mitchell, B. M. Gallant, C. V. Thompson, and Y. Shao-Horn, *Energy Environ. Sci.*, **4**, 2952 (2011).
34. E. L. Thompson, J. Jorne, W. B. Gu, and H. A. Gasteiger, *J. Electrochem. Soc.*, **155**, B625 (2008).

Downloaded 01 Feb 2012 to 138.246.2.183. Redistribution subject to ECS license or copyright; see http://www.ecsdl.org/terms_use.jsp

3.2 Effect of Carbon Surface Area on First Discharge Capacity of Li-O_2 Cathodes and Cycle-Life Behavior in Ether-Based Electrolytes

The paper entitled "Effect of carbon surface area on first discharge capacity of Li-O_2 cathodes and cycle-life behavior in ether-based electrolytes" is reported in the present section. This study is the natural continuation of the investigations reported and discussed in Section 3.1.

As the discharge of a Li-O_2 cell is limited by the electronic conductivity of the discharge product layer built on the electrode surface (Section 3.1) once a critical thickness is reached [47,49], a direct proportionality between surface and specific capacity is expected. By analyzing the surface properties and pore size distribution by BET method of several carbon blacks characterized by different total surface areas, namely in the range 70-1600 m^2/g, it was possible to estimate the surface area of those materials comprising mesoporosity, i.e. pores ≈2 nm wide or larger. The specific discharge capacity ([mAh/g_{carbon}]) of positive electrodes was found to be directly proportional to that external surface; the microporosity of those non-catalyzed electrodes (pores ≈2 nm wide or lower) is not utilized for oxygen reduction reaction, most probably because not accessible by the electrolyte solution.

The product selectivity of Li-O_2 cells using diglyme-based electrolyte solution was investigated by O_2 consumption measurements (Section 2.6). The main discharge product of our Li-O_2 cells using non-catalyzed carbon black electrodes is Li_2O_2, accounting for ≈80 % of the total in the first cycle (Table 3.1). However, our product selectivity data does not fully match with other scientific reports, wherein ≈100 % Li_2O_2 production was demonstrated [37]. The reason for that discrepancy is currently under investigation at TUM.

Table 3.1. Product selectivity data obtained with O_2 consumption measurements for two LITHion-bonded, non-catalyzed carbon black electrodes, namely Vulcan XC72 and Ketjen Black EC600J carbon blacks. Li-O_2 cells were built with lithium metal anode, and were cycled galvanostatically at 120 mA/g_{carbon} using 0.2 M LiTFSI in diglyme electrolyte solution in 101.3 kPa_{abs} O_2.

Cycle Number	e^-/O_2 Ratio on Vulcan XC72	Molar Li_2O_2/Li_2O on Vulcan XC72 [mol%/mol%]	e^-/O_2 Ratio on Ketjen Black EC600J	Molar Li_2O_2/Li_2O on Ketjen Black EC600J [mol%/mol%]
1	2.43	79/21	2.30	85/15
2	2.46	77/23	2.46	77/23
3	2.46	77/23	2.47	77/23
4	2.53	74/26	2.43	79/21
5	2.62	69/31	2.43	79/21

In order to simplify the evaluation of the product layer film thickness deposited atop the electrode surface, the approximation that Li_2O_2 was the *only* discharge product was done. Within that approximation, it was calculated that end of charge occurs when 1-2 monolayers of Li_2O_2, corresponding to a critical film thickness of ≈0.5 nm. Qualitatively, that result is in agreement with other similar studies in model systems, however the critical thickness of the insulating layer necessary to prevent ORR to occur was reported to be about one order of magnitude higher [47,49]. The very low critical thickness estimated by surface-capacity correlations translates in relatively low specific capacities (e.g. ≈200 mAh/g_{carbon} for Vulcan XC72 carbon black) and poor rate capability of the corresponding batteries.

Another topic discussed in this section is the cycle life of $Li-O_2$ cells using ether-based electrolyte solutions. Beyond the clear evidence that those systems are poorly reversible, that translates in the cell death after only several cycles, the study revealed that the degradation of the ether solvents is responsible for a strong increase in the discharge capacity in the first four cycles before cell failure. The apparent critical thickness of discharge products at which the ORR is stopped using degraded electrolyte solutions is much higher (2-3 nm) than in purified, water-free solutions, suggesting that the impurities introduced by decomposing the solvent (Section 3.3), as well as H_2O (Section 3.1), prevent the precipitation of the discharge products on the electrode surface by enhancing their solubility/mobility. As the reason for that at a molecular level is yet unclear, further effort should be invested in understanding the basic interactions of oxygen reduction reaction with impurities and H_2O, in order to design stable additives deliberately added to the electrolyte solution for improved capacity and rate capability. A thorough study on the role of impurities and ether solvents degradation products on capacity and cycle life is reported in Section 3.3.

Effect of Carbon Surface Area on First Discharge Capacity of Li-O_2 Cathodes and Cycle-Life Behavior in Ether-Based Electrolytes

S. Meini, M. Piana, H. Beyer, J. Schwämmlein, and H.A. Gasteiger

Journal of The Electrochemical Society, 2012, Volume 159, Issue 12,

Pages A2135-A214248

Permanent weblink:

http://dx.doi.org/10.1149/2.011301jes

Reproduced by permission of The Electrochemical Society

Journal of The Electrochemical Society, **159** (12) A2135-A2142 (2012) A2135
0013-4651/2012/159(12)/A2135/8/$28.00 © The Electrochemical Society

Effect of Carbon Surface Area on First Discharge Capacity of Li-O_2 Cathodes and Cycle-Life Behavior in Ether-Based Electrolytes

Stefano Meini,[*] Michele Piana,[,z] Hans Beyer, Jan Schwämmlein, and Hubert A. Gasteiger[***]**

Institute of Technical Electrochemistry, Technische Universität München, D–85748 Garching, Germany

---

In this study we report on the direct proportionality between cathode surface area and first discharge capacity of non-aqueous Li-O_2 cells using ether-based electrolytes. Seven different highly structured carbon blacks, characterized by different surface areas and porosities, were used to prepare non-catalyzed cathodes. Surface measurements and porosity analyzes were carried out on both raw materials and electrodes in order to estimate the fraction of cathode surface accessible by the electrolyte. The first specific discharge capacity of different cathodes was then normalized over its specific surface and a strong correlation between the two quantities was found. This result strongly supports a discharge mechanism for Li-O_2 batteries wherein the main factor limiting the capacity is the formation of a passivating layer of products on the surface of the cathode material, impeding ORR at carbon active sites. Also the cyclability of the cells was considered, demonstrating the effect of electrolyte degradation on the increased capacity upon cycling of ethereal electrolytes (e.g. DEGDME). The first discharge specific capacity and cyclability using TEGDME, commonly used in Li-air research, was found similar to reacting or degraded electrolytes, suggesting a much higher reactivity toward superoxide ion radical in comparison to its lighter homologues DEGDME and DME.
© 2012 The Electrochemical Society. [DOI: 10.1149/2.011301jes] All rights reserved.

Manuscript submitted August 24, 2012; revised manuscript received October 5, 2012. Published October 23, 2012.

Worldwide full electrification of the vehicular fleet is considered to be an important step toward the drastic reduction of fossil fuel consumption, with the objective of building a fully sustainable industrial society. In the field of energy storage research, lithium-air battery technology has drawn significant interest over the past decade.[1] The electrochemical couple Li^0/O_2 can operate both in aqueous and non-aqueous electrolytes, whereby reasonable rechargeability has been demonstrated in organic aprotic electrolytes.[2–6] The reaction between Li and O_2 could in principle lead to either lithium peroxide (Li_2O_2) or lithium oxide (Li_2O):[7]

$$2Li^+ + 2e^- + O_2 \leftrightarrow (Li_2O_2)_{solid} \quad ; E_{rev} = 2.96\ V_{Li} \qquad [1]$$

$$4Li^+ + 4e^- + O_2 \leftrightarrow 2(Li_2O)_{solid} \quad ; E_{rev} = 2.91\ V_{Li} \qquad [2]$$

Based on the above reactions, Li–air batteries with a metallic lithium anode and a carbon-based cathode can theoretically provide a 2- to 5-fold higher specific energy compared to the commonly used intercalation materials of the $LiMO_2$ (M = Mn, Ni, Co) type.[7,8]

Since the work by Mizuno et al.,[9] Freunberger et al.,[10] and McCloskey et al.[11] it is well known, however, that the oxygen reduction reaction (ORR) in alkyl carbonate–based electrolytes largely leads to the formation of Li_2CO_3, alkylcarbonates, and other electrolyte degradation species, caused by the high reactivity of superoxide ion radicals ($O_2^{-\bullet}$) which have been shown to be formed during the initial one-electron reduction of O_2 in Li-O_2 cathodes.[12] Accumulation of side products in the electrode porosity leads to cell failure.[10,11,13]

$$O_2 + e^- \rightarrow O_2^{-\bullet} \qquad [3]$$

$$O_2^{-\bullet} + \text{Solvent} \rightarrow Li_2CO_3, \text{AcOLi}, \text{HCOOLi}, \qquad [4]$$

Among the commonly available aprotic organic solvents and blends, only few showed acceptable stability toward superoxide attack. Examples of seemingly stable solvents are ethers like dimethoxy ethane (DME)[14] with which the desired Li_2O_2 was observed to be the main discharge product by XRD and in-situ spectroscopies (Raman, FTIR, and X–ray absorption).[11,15,16] Because Li-air batteries might be designed as open systems, non-volatile or very low vapor pressure electrolytes are required, which triggered the interest in ionic liquids like 1-butyl-1-methyl-pyrrolidinium bis(trifluoromethylsulfonyl)imide (Pyr_{14}TFSI)[17,18] and heavier ethers like diethylene glycol dimethyl ether (DEGDME) or tetraethylene glycol dimethyl ether (TEGDME),[19,20] although the stability of the latter toward superoxide radical is still controversial, with some studies suggesting instability[15] and others stability[20] of TEGDME toward ORR intermediates.

Discharge capacity, rate capability, and cyclability of Li-O_2 cells was shown to be influenced by many factors other than just electrolyte, the most important being electrode microstructure and thickness[21–23] that determine the rate of O_2 diffusion to the active sites where the ORR takes place,[24,25] O_2 partial pressure,[26,27] and electrode composition (binder, catalysts as well as support surface area and porosity).[16,28,29,30]

In our previous work[31] we reported that the use of a high-purity electrolyte with high stability toward $O_2^{-\bullet}$ (0.1 M $LiClO_4$ in DME) limits the discharge capacity of non-catalyzed carbon cathodes to much lower values (≈200 mAh/g_C) than those obtained with alkyl carbonates or heavy ethers reported in the literature (≈1000–2000 mAh/g_C). Early publications in the Li-air field proposed pore-clogging as main factor limiting Li-air cell capacity.[24,26] Later on, however, Albertus et al.[32] and Hummelshøj et al.[33] suggested the formation of a passivating layer of discharge products as the main factor limiting the discharge, imaging the formation of an electronically insulating 40–70 nm thick film during the discharge on a polished glassy carbon (GC) electrode in propylene carbonate (PC) based electrolyte[32] (note that the passivating film in this case must have consisted mostly of lithium carbonate and lithium alkyl carbonates). Later on, the same group showed that in non-reactive DME based electrolyte, an estimated film thickness of only 4–5 nm Li_2O_2 is sufficient to stop the discharge reaction,[24] which they modeled by the exponentially increasing electronic resistance through the deposited Li_2O_2 film which would prevent the further reduction of O_2 at the film/solution interface. While the passivating discharge film thickness of 4–5 nm reported for a glassy carbon electrode in their study is still significantly larger than the only several monolayer thick passivating film which we deduced from our data on high-surface area Vulcan-carbon electrodes,[31] the general concept that the formation of a passivating discharge product film is the major cause for the cathode discharge capacity limitation at relatively low current densities (10–100 mA/g_{carbon}) in Li–O_2 batteries is now widely accepted. At higher current densities, other factors are predominant in limiting the discharge specific capacity, e.g. O_2 diffusion through the electrode structure.[24,26]

The above described cathode surface passivation upon discharge would imply that the specific capacity of the first discharge cycle should be directly proportional to the carbon surface accessible to both O_2 and electrolyte, which in turn would suggest that the discharge capacities should increase with the specific carbon surface area used in lithium-air cathodes. Surprisingly, there are only a few reports in the literature which examine the effect of specific carbon surface area. For example, Yang et al. studied the influence of the cathode carbon material (different kinds of commercial carbon blacks and graphite) on the discharge capacity of Li–O_2 cells, but found no direct proportionality with carbon surface area; instead, the discharge capacity was observed to be proportional to the average pore diameter of the carbon structure.[30] Similarly, Kuboki et al. found that the discharge capacity increased with the mesopore volume in the carbon structure.[17] Unfortunately, both studies employed reactive alkyl carbonate blends as electrolytes, so that it is impossible to unambiguously interpret the lower capacity observed with microporous carbons.

---

[*] Electrochemical Society Student Member.
[**] Electrochemical Society Active Member.
[***] Electrochemical Society Fellow.
[z] E-mail: michele.piana@tum.de

In the present study, non-catalyzed carbon electrodes were prepared with several carbon blacks and examined in non-aqueous Li-O_2 cells with regards to their activity toward electrolyte decomposition at high potentials, their discharge capacity and their cyclability. We will thus compare the electrochemical behavior of commercial acetylene black for batteries and other commonly used carbon blacks like Vulcan XC72, Ketjenblack EC600JD, and Black Pearls 2000 in both their graphitized and non-graphitized modifications. The use of carbon blacks with different specific surface areas and different surface chemistries (graphitized and non-graphitized) serves to (i) experimentally prove the proposed direct proportionality between electrode surface area and first discharge capacity in non-reactive electrolytes, and to (ii) gain further insight into the Li-O_2 cell discharge mechanism, particularly with regards to differences observed between light (DME, DEGDME) and heavy ethers (TEGDME).

Experimental

Electrode design and testing: Seven carbon blacks were tested in this work as cathode material for Li-O_2 batteries. Timcal Super C65, Tanaka V-type (Vulcan XC72), Tanaka E-type (Ketjenblack EC600JD), Tanaka B-type (Black Pearls 2000), Tanaka VA-, EA- and BA-type (the nomenclature X**A**-type refers to graphitized versions of X-type carbon blacks); from now on the cathodes will be referred to by the above commercially used letter-code (e.g., "C" electrode for Super **C**65 or "BA" electrode for **BA**-type). The positive electrodes were prepared by Mayer-rod coating onto a Celgard C480 separator, using an ink composed of one of the above carbons, a solvent (isopropanol (IPA) for V, VA, and Super C65 or N-methyl pyrrolidone (NMP) for E, EA, B and BA -type carbons), and lithium-ion exchanged Nafion solution with a binder/carbon ratio of 0.5/1 g/g (LITHion with 10.6%wt. in IPA from Ion Power, USA). The ink was prepared by sonicating the carbon and the solvent (IPA Aldrich, for HPLC, 99.9% or NMP Aldrich, anhydrous 99.5%) for 20 minutes (Branson 250 probe-sonifier). Subsequently, LITHion solution was mixed into the ink with a spatula for half a minute. After coating and solvent evaporation (at room temperature for IPA or at 60°C for NMP inks), 15 mm diameter cathode electrodes were punched out, dried under dynamic vacuum at 95°C for 6 hours in a glass oven (Büchi, Switzerland), and transferred for cell assembly into an argon–filled glove box (O_2 < 0.1 ppm, H_2O < 0.1 ppm; MBraun, Germany) avoiding further exposure to ambient air. Table I shows average carbon loading (obtained by weighing at least 10 electrodes) and cathode thickness (mean value of at least 10 measurements on different electrodes, obtained using a Mitutoyo AbsOlute gauge with ± 2 μm accuracy).

Table I. Nomenclature, carbon loading, and thickness of non-catalyzed carbon electrodes used in this work. The LITHion-binder/carbon ratio is 0.5/1 g/g.

Electrode	Carbon type	Carbon loading ($mg_{carbon}/cm^2_{electrode}$)	Thickness (μm)
C	Timcal Super C65	0.34 ± 0.05	11 ± 2
VA	Tanaka VA-type	0.40± 0.05	14 ± 2
EA	Tanaka EA-type	0.41 ± 0.05	18 ± 2
V	Tanaka V-type	0.38 ± 0.05	11 ± 2
BA	Tanaka BA-type	0.22 ± 0.05	7 ± 2
E	Tanaka E-type	0.37 ± 0.05	13 ± 2
B	Tanaka B-type	0.34 ± 0.05	14 ± 2

Electrolytes: Ethers like dimethoxy ethane (DME) are reported to be very stable in a Li-O_2 cell environment, allowing the formation of essentially pure Li_2O_2 upon cell discharge.[11] Unfortunately, DME is not a convenient solvent for practical applications due to its very high vapor pressure. Therefore, heavier ethers like DEGDME and TEGDME were recently introduced as alternative electrolytes in Li-air research. However, Freunberger et al. demonstrated that in TEGDME the fraction of Li_2O_2 produced diminishes upon cycling, and concluded that TEGDME is slowly attacked by the superoxide ion radical via hydrogen extraction.[15] In this work, both DME and DEGDME were used for electrolyte preparation, yet DEGDME was preferred to DME due to its much lower vapor pressure (p_{vapor} (DEGDME) = 0.4 kPa vs. p_{vapor} (DME) = 6.4 kPa at 20°C). TEGDME was also used in order to test our cathodes using an ethereal electrolyte closer to a potential application (highest boiling point). Electrolytes were prepared with either $LiClO_4$ (Aldrich, battery grade, 99.99% trace metal basis) or LiTFSI (Aldrich, 99.95% metal basis), vacuum dried at 150°C for 24 hours before use. Anhydrous DME (Aldrich, $\geq$ 99.5%), DEGDME (Aldrich, $\geq$ 99%) and TEGDME (Aldrich, $\geq$ 99%) were dried for at least 24 hours over Sylobead MS 564C zeolites (3Å, Grace Division). The water content of the 0.2 M LiTFSI or 0.1 M $LiClO_4$ electrolytes was $\leq$10 ppm (Karl Fischer titration).

Cell design: The cell design was reported and extensively discussed in our previous work;[31] it consists of a 316Ti SS anode current collector and a cathode current collector separated by a Kel–F spacer. The sealing of the system is ensured by two Teflon O-rings, and the contact between cell components is made by a 316 SS compression spring.

Cell assembly: A 17 mm Ø lithium disk (0.45 μm thick, 99.9%; Chemetall, Germany) is placed onto the anode current collector, wetted with 40 μL of electrolyte, and covered with two Celgard C480 separators. The cathode is placed onto the separators before and after dropping 40 μL of electrolyte and then covered with a 21 mm Ø stainless steel (316SS) mesh (0.22 mm Ø wire, 1.0 mm openings, Spörl KG, Germany) cathode current collector. The cell is sealed with four screws at a torque of 6 Nm, then connected to an oxygen line (all 316SS tubing to avoid moisture intrusion) and purged with O_2 at 80 sccm for 35 seconds.

Background current measurements: anodic electrolyte decomposition currents for the different carbon cathodes were obtained from potentiostatic measurements in a Li–O_2 cell at 100 kPa O_2 without any prior discharge. Starting at 3.45 V_{Li} (OCV $\leq$ 3.30 V_{Li}), the potential was increased every hour by 0.15 V up to 4.50 V_{Li} and the current measured at the end of each potential and step, normalized by the mass of carbon, is reported in Figure 1. As expected, the electrolyte decomposition currents are higher for the high-surface area carbons (e.g. B-type) than for the low-surface area carbons (e.g., VA-type). Potential dependent electrolyte decomposition currents obtained for TEGDME are similar to those reported in Figure 1. Based on these data, the higher cutoff potential for the cycling experiments in DEGDME was chosen to be 4.5 V_{Li}, for which the background currents (A/g_{carbon}) are typically $\leq$ 10% of the applied charge/discharge current (120 mA/g_{carbon}).

Li-O_2 battery cycling: two cycling procedures were used in this work. *Regular cycling* consists of a galvanostatic discharge/charge at 120 mA/g_{carbon} between 2.0–4.5 V_{Li} (at room temperature) after 30 minutes rest at open circuit voltage (OCV). The second procedure, referred to as *controlled cycling*, consists of a galvanostatic discharge/charge with capacity and potential limitation: the cells are first discharged at 120 mA/g_{carbon}, limiting the absolute capacity to either 0.2 or 0.5 mAh, then charged at 120 mA/g_{carbon} until the potential of 4.2 V_{Li} is reached; that voltage is then held until the charge capacity reaches the discharge capacity. The experiments are stopped at the cycle that reaches during discharge the lower cutoff voltage of 2.4 V_{Li}

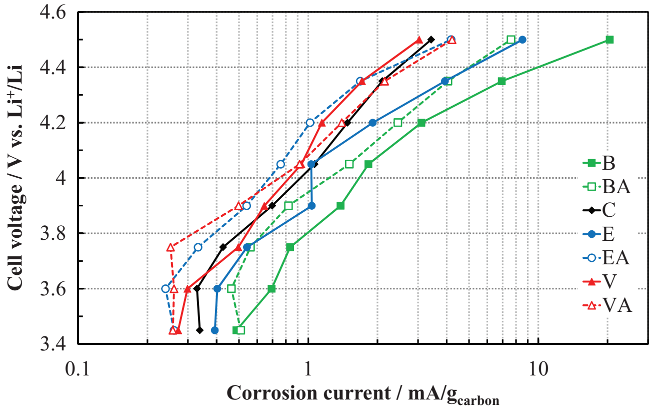

Figure 1. Potential-dependent electrolyte decomposition currents normalized to the carbon weight of the electrode obtained in Li-O_2 cells (100 kPa O_2) for non-catalyzed cathodes prepared with different non-graphitized and graphitized carbon blacks: Tanaka V-type (red –), E-type (blue –), B-type (green –), VA–type (red - - -), EA-type (blue - - -), BA-type (green - - -), and Timcal Super C65 (black –). Potentials were increased in 0.15 V increments every hour from 3.45 to 4.50 V_{Li} in 0.2 M LiTFSI in DEGDME; the reported currents are those obtained at the end of each potential step.

(note: similar cycling procedures were used in References 4 and 6). All electrochemical tests were performed using a multipotentiostat (VMP3, Bio-Logic, France).

Estimate of the carbon surface coverage by Li_2O_2 after Li-O_2 cell discharge: in order to find a correlation between Li-O_2 cell discharge limitations and surface passivation of the cathode, the number of monolayers of discharge products (assumed to be 100% Li_2O_2) produced at the carbon support/electrolyte interface was estimated using Eq. 5 the following formula:

$$N_{\text{monolayers Li2O2}} = Q_{\text{surface}} \cdot (260\,\mu C \cdot cm^{-2}_{\text{carbon}})^{-1} \qquad [5]$$

wherein Q_{surface} is the cell discharge normalized to the cathode surface area (S^{El}_{external}, see below for definition). The number $260\,\mu C \cdot cm^{-2}_{\text{carbon}}$ (used in our previous work[31]) is the estimated normalized discharge for 1 monolayer of Li_2O_2; that number is obtained by using the lattice parameters provided by Cota et al. for optimized, fully relaxed Föppl structures[35] ($a = 0.3183$ nm, $c = 0.77258$ nm) to calculate the *unit cell density* (i.e. number of unit cells per cm^2_{carbon}). We assumed that the unit cells lie with the c-axis parallel to the carbon surface, therefore we consider the thickness of *one monolayer* the "a" cell parameter (i.e. 0.3183 nm). Considering that each unit cell comprises two O_2^{2-} ions,[35] we can calculate from the geometric unit cell density the correspondent charge in $\mu C \cdot cm^{-2}_{\text{carbon}}$ involved in Li_2O_2 formation upon ORR. The choice on unit cell orientation (i.e. standing or lying) was in fact arbitrary, but a different choice wouldn't have significantly changed the results ($320\,\mu C \cdot cm^{-2}_{\text{carbon}}$, considering half height of standing unit cells, i.e. one layer of O_2^{2-} on the carbon surface). The corresponding charge can be calculated based on the ORR stoichiometry ($e^-/O_2 = 2$) for Li_2O_2 formation.

Analysis of cathode material surface and porosity: Surface area and porosity of pure carbons and final cathodes were determined by nitrogen physisorption at 77 K on a Quantachrome Autosorb–iQ instrument. The pure carbon powders were pretreated under vacuum at 350°C for 12 h prior to physisorption measurements. For the analysis of electrode coatings, inks were prepared as described above and coated on aluminum foil. The dry coatings were folded up and introduced into the instrument's sample tube. Electrode samples were pretreated under vacuum at 120°C for 18 h prior to analysis. This temperature was chosen to preserve the integrity of the binder. Adsorption and desorption isotherms of all samples were recorded in the relative pressure range of $10^{-5} \leq (p/p_0) \leq 0.995$. The adsorption branch was used to calculate BET surface areas (best fit within $0.01 \leq (p/p_0) \leq 0.25$). The surface area of micropores accessible to nitrogen was determined from the desorption branches of the isotherms using the t–method of Lippens and de Boer[36] (best linear fit in the range of $0.15 \leq (p/p0) \leq 0.40$). The data measured on electrode coatings were normalized to the amount of carbon present in the samples, assuming that neither the binder nor the aluminum foil makes a significant contribution to the surface area. External surface areas (S^C_{external}) were calculated by subtracting the t–plot micropore areas ($S^C_{\text{micropores}}$, i.e., the surface area of pores smaller than ~2 nm in diameter) from the BET areas (S^C_{total}, i.e., the total surface area).

Results and Discussion

An overview of the surface properties of different carbon blacks is given in Table II (left side). It is well known that high-structure carbon blacks, like the ones used in this work, consist of spherical primary particles (15–50 nm) that are fused together to form high-structure primary agglomerates (200–300 nm), the shape and porosity of which depend on the preparation process.[37] Generally, the so-called *acetylene blacks* (e.g., Timcal Super C65) are characterized by dense, graphitic primary particles with little or no microporosity, whereas the so-called *furnace blacks* (Vulcan XC72, Ketjenblack, and Black Pearls) are composed of partially graphitic microporous primary particles which have a significant coverage of oxygen-containing surface groups.[38] For non-porous materials like *acetylene blacks* or *graphitized furnace blacks* (i.e., furnace blacks heat treated at ≈3000 K in inert atmosphere[39]), the specific surface area can be estimated by the following equation (i.e., by the specific surface area of dense spheres):

$$S^C_{\text{external}} = 6/(\rho \cdot d) \qquad [6]$$

where ρ is the bulk density of carbon (≈2 g/cm^3) and *d* is the particle diameter. For *non-graphitized furnace blacks*, the specific surface area is substantially larger than that predicted by Eq. 6 due to their microporosity. Accordingly, for *graphitized furnace blacks* and *acetylene*

Table II. Surface area analysis data of carbon blacks used for cathode preparation and of cathodes coated on Al foil: all electrodes are composed of LITHion–binder and carbon black (1/0.5 g/g).

Carbon surface area analysis				Electrode surface area analysis		
Carbon type	Graphitized [yes/no]	S^C_{total} (BET) [m^2/g_{carbon}]	S^C_{external} [m^2/g_{carbon}]	Electrode name	S^{El}_{total} (BET) [m^2/g_{carbon}]	S^{El}_{external} [m^2/g_{carbon}]
Super C65	no	68	68	C	50	50
VA-type	yes	86	86	VA	82	82
EA-type	yes	143	143	EA	128	128
V-type	no	240	144	V	152	137
BA-type	yes	209	209	BA	193	193
E-type	no	834	713	E	533	432
B-type	no	1509	703	B	1123	513

$S_{\text{external}} = S_{\text{total}}\text{-}S_{\text{micropores}}$

black the *external* surface area ($S^C{}_{external}$, see experimental for definition) is essentially the same as their total surface area ($S^C{}_{total}$), which is clearly seen in Table II (left-hand-side) for Super C65, VA, EA, and BA-type. On the other hand, $S^C{}_{external}$ is significantly smaller than $S^C{}_{total}$ for the untreated surface blacks (i.e, V, E, and B-type; see left-hand-side of Table II) due to the fact that up to 50% of their total surface area is in micropores.

When preparing carbon-based electrodes, the necessary binder (in our case Li^+ exchanged Nafion) can affect the overall surface area of the electrode as well as physical-chemical properties (e.g., wettability, reactivity, etc.). To evaluate the effect of the electrode preparation procedure and the binder on the specific carbon surface area, surface and porosity analysis of the actual *electrodes* was performed. As long as the volume fraction of the binder is much less than the void volume fraction as in our case, the presence of the binder should only have a minor influence on the surface area of non-microporous carbons, since their surface is largely dependent on the primary particle diameter, which remains roughly unchanged even if it were coated with the binder as long as the binder will not deposit in nano-particular form. On the contrary, for microporous carbons we expect the binder to clog part of the micropores, resulting in significantly reduced micropore surface areas and, consequently, reduced total surface areas. These expectations agree very well with the experimental data obtained from electrode surface analysis (Table II, right-hand-side): electrodes prepared from graphitized carbons (Super C65, VA, EA, and BA-type) show only little decrease of total and external surface area compared to the pure carbons, whereas non-graphitized cathodes lose a significant fraction of their porosity, resulting in a drastic decrease of their micropore area, along with a moderate decrease of their external surface area, particularly in the case of B and E-type carbons.

Yang et al.[30] and Kuboki et al.[17] proposed that in high surface area cathodes, O_2 transport and carbon wettability are limited to carbon mesoporosity (i.e., no reaction would occur in micropores), thereby reducing the fraction of surface actually *accessible* to the reactants (O_2, Li^+) in highly microporous materials and thus limiting the discharge capacity. Inspired by the work of those authors, all surface–normalized discharge capacities in this work are calculated using the *external* surface areas of electrodes ($S^{El}{}_{external} = S^{El}{}_{total}$ - $S^{El}{}_{micropores}$, see last column of Table II), assuming that the ORR takes place exclusively on the external surface area.

Figure 2a shows the comparison between the specific discharge capacities in the first cycle of Li–O_2 cells using different carbons with 0.2 M LiTFSI in DEGDME as non-aqueous electrolyte. Each non-graphitized carbon (V-, E-, B-types) shows higher discharge capacities in comparison to its respective graphitized version (VA-, EA-, BA-types), as would be expected due to the higher specific carbon surface area of non-graphitized furnace blacks (s. Table II). The first-cycle specific discharge capacity for the different carbons using 0.2 M LiTFSI in DEGDME (Table III, 2nd column) increases ≈7-fold from low-surface area Super C65 (77 ± 3 mAh/g_{carbon}) to high-surface area B-type (517 ± 55 mAh/g_{carbon}), illustrating the strong effect of carbon surface area on discharge capacity which would be expected for the above discussed passivating-film model. Consequently, when the discharge capacity is normalized to the external carbon surface area of the cathode (i.e., to $S^{EL}{}_{external}$; s. right-most column in Table II) rather than to carbon mass, the resulting surface-normalized capacities are very similar for all the examined carbons (Table III, 3rd column), with an average of ≈480 $\mu C/cm^2{}_{C\text{-}external}$ ±20% in 0.2 M LiTFSI in DEGDME. While the graphitized carbons tend to yield slightly higher surface-normalized capacities, presumably related to their different surface chemistry, the first-discharge capacity is primarily proportional to the external specific carbon surface area, consistent with the passivating-film model. This holds also true for measurements in 0.1M $LiClO_4$ in DME (Table III, 3rd column). Thus, in DME and DEGDME electrolyte, the surface-normalized discharge capacities range within 350–580 $\mu C/cm^2{}_{C\text{-}external}$ for all the examined carbons.

These surface-normalized discharge capacities, $Q_{discharge}/S^{El}{}_{C\text{–}external}$, can be expressed in terms of Li_2O_2 film thickness, t_{film}, using the approach used by Viswanathan et al.:[34]

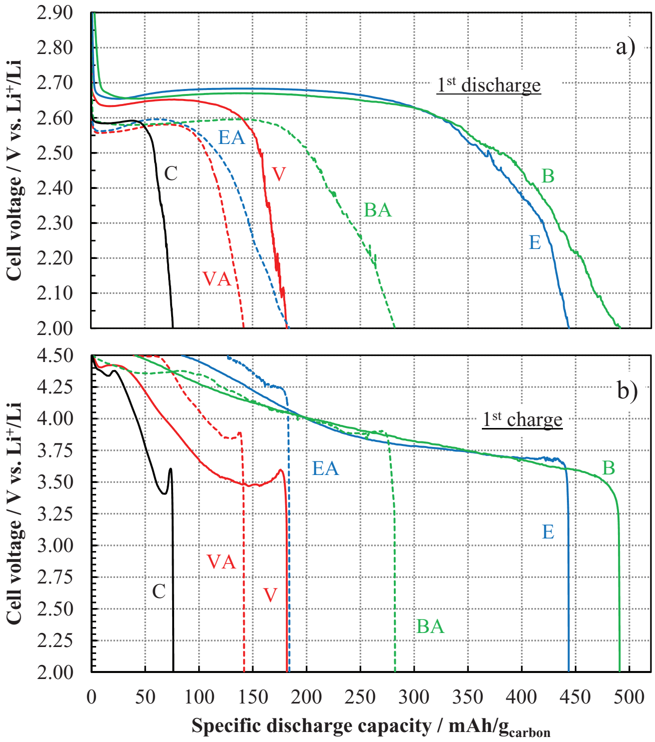

Figure 2. Comparison between a) discharge capacity (1st cycle) and b) charge capacity (1st cycle) of Li-O_2 cells with 0.2 M LiTFSI in DEGDME using non-catalyzed cathodes (s. Table I) prepared with different non-graphitized and graphitized carbon blacks (s. Table II): Tanaka V-type (red –), E-type (blue –), B-type (green –), VA–type (red - - -), EA-type (blue - - -), BA-type (green - - -), and Timcal Super C65 (black –). The cells are galvanostatically cycled at 120 mA/g_{carbon} after a 30 minutes rest period at OCV in pure 100 kPa_{abs} O_2.

$$t_{film} = Q_{discharge}/S^{El}{}_{external} \times M_{Li2O2}/(F \times \rho_{Li2O2}) \qquad [7]$$

where M_{Li2O2} (46 g/mol) and ρ_{Li2O2} (2.3 g/cm^3) are the molecular mass and the density of Li_2O_2, respectively. The resulting film thicknesses of ≈0.4–0.6 nm based on the surface area normalized discharge capacities in Table III are approximately 10–fold lower than the ≈5 nm reported by Viswanathan et al.[34] for a glassy carbon (GC) electrode. The higher t_{film}-values in the latter study could be related to the fact that the authors assumed a GC roughness factor of 1 $cm^2{}_{surface}/cm^2{}_{electrode}$ (i.e., equating the glassy carbon geometric surface area with $S^C{}_{external}$), even though mirror-polished glassy carbon typically has roughness factors on the order of 10 $cm^2{}_{surface}/cm^2{}_{electrode}$;[40] if the true roughness factor had indeed been higher than >1 $cm^2{}_{surface}/cm^2{}_{electrode}$, the calculated t_{film}-values would be proportionally smaller. While this ten-fold lower Li_2O_2 film thickness may seem inconsistent with the calculated electron-conduction-limiting Li_2O_2 film thickness of ≈5 nm in Ref. 34, it must be considered that the electron conductivity of the Li_2O_2 film in Ref. 34 was calculated by assuming zero vacancy scattering and by a subsequent fit of the resistance contribution by vacancy scattering (expected to be rather significant[41]) to the experimental data using the calculated film thickness based on a roughness factor of one. Due to this experimental fit of the vacancy scattering contribution of 0.1 V/nm,[34] the conductivity calculations are not entirely based on ab-initio calculations, which would explain the above described inconsistency.

The surface-normalized first discharge capacities reported in Table III can also be translated into an average number of Li_2O_2 monolayers (1 ML ≈ 260 $\mu C/cm^2$, assuming the predominant formation of Li_2O_2), equating to only 1–2 monolayers of Li_2O_2 for the first discharge cycle in 0.2 M LiTFSI in DEGDME

Table III. Carbon mass based discharge capacities (first cycle), surface area normalized discharge capacities (first cycle), and corresponding Li_2O_2-monolayer coverage of the external carbon surface for different high surface area carbon blacks using different non-aqueous electrolytes: 0.2 M LiTFSI in DEGDME, 0.1 M $LiClO_4$ in DME, and 0.2 M LiTFSI in TEGDME. All electrodes are composed of carbon black and LITHion as binder (1/0.5 weight ratio). The surface area *normalized discharge capacities* are obtained by dividing the discharge capacity with the external surface area of electrodes (last column of Table). The number of Li_2O_2 monolayers is obtained by dividing the surface area normalized discharge capacities by 260 $\mu C/cm^2_{carbon}$, corresponding to the surface normalized charge involved in the deposition of one monolayer of Li_2O_2 (see Eq. 5). The cells are galvanostatically cycled at 120 mA/g_{carbon} after a 30 minutes rest period at OCV in pure 100 kPa_{abs} O_2. The reported experimental measurement error is the standard deviation from a mean value obtained from at least 3 repeat experiments.

Electrode	1st cycle discharge [mAh/g_{carbon}]	Normalized discharge [$\mu C/cm^2_{external}$]	Li_2O_2 monolayers	Average discharge voltage [V_{Li}]	Normalized current [$\mu A/cm^2_{external}$]
0.2 M LiTFSI in DEGDME					
C	77 ± 3	554 ± 22	2.1 ± 0.1	2.48	0.240
VA	130 ± 20	571 ± 88	2.2 ± 0.3	2.50	0.146
EA	174 ± 19	489 ± 54	1.9 ± 0.2	2.51	0.094
V	183 ± 50	474 ± 130	1.8 ± 0.5	2.59	0.086
BA	290 ± 16	540 ± 30	2.1 ± 0.1	2.51	0.079
E	439 ± 61	359 ± 50	1.4 ± 0.2	2.59	0.027
B	517 ± 55	352 ± 38	1.4 ± 0.2	2.58	0.023
0.1 M $LiClO_4$ in DME					
V	202 ± 15	523 ± 39	2.0 ± 0.2	2.61	0.086
E	588 ± 49	481 ± 40	1.9 ± 0.2	2.63	0.027
B	587 ± 36	399 ± 25	1.5 ± 0.1	2.60	0.023
0.2 M LiTFSI in TEGDME					
V	772 ± 22	1999 ± 57	7.6 ± 0.2	2.54	0.086
E	1833 ± 91	1500 ± 75	5.8 ± 0.3	2.57	0.027
B	2168 ± 165	1475 ± 112	5.7 ± 0.4	2.57	0.023

(Table III, 4th column). The same passivating film thicknesses and monolayer coverages are observed for the first discharge cycle in 0.1 M $LiClO_4$ in DME (see Table III), as we had already reported previously for a Vulcan XC72 based cathode.[31] These data suggest, that in non-reactive electrolytes (i.e., for short-chain glymes), the formation of a very thin passivating film of Li_2O_2 limits the first-cycle discharge capacity.[31,34] Consequently, larger discharge capacities could be obtained if a stable electrolyte/additive were to be found that is able to solubilize the reaction intermediates ($O_2^{-\bullet}$, LiO_2) formed on the catalytic surface so that they could precipitate as Li_2O_2 away from the surface (as suggested in[31]); alternatively, higher discharge capacities could be obtained if the nature of the passivating film is changed (making it more conductive or more permeable) through reaction of the intermediates with the electrolyte[31] or other reactive species like CO_2[42] and water.[31]

Besides the dependence of the first discharge capacity on specific electrode surface area, a closer inspection of Fig. 2a also shows that that the discharge voltages on graphitized cathodes (Super C65 as well as VA, EA, and BA-type) of ≈2.5 V_{Li} are roughly 70–110 mV lower than those of the non–graphitized cathodes (≈2.6 V_{Li}) using DEGDME. Based on kinetic arguments, one would expect that the discharge voltage would decrease with increasing surface-normalized current density (last column in Table III), but a comparison of the V-type and BA-type electrode which have similar surface-normalized current densities but differ in discharge voltage by 80 mV suggests that the discharge voltage is highly dependent on the surface properties, tending to be lower for the graphitized carbons. Similarly, the charging voltages (s. Fig. 2b) are also clearly lower for the grapitized carbons, despite the fact that their surface-normalized charge current densities are higher than those of the non-graphitized carbons. The reason for this effect is not yet understood and is subject of current investigations.

Previously we found that much higher first-discharge capacities are obtained in mixtures of DME and propylene carbonate (PC) or in water-contaminated solvents if compared to pure DME[31] or DEGDME in the current study. Surprisingly, the discharge of Li-O_2 cells at 120 mA/g_{carbon} using non-graphitized cathodes and 0.2 M LiTFSI in TEGDME also yields ≈4–fold higher first-discharge capacities (see Table III and Figure 3a) that are consistent with the typically reported

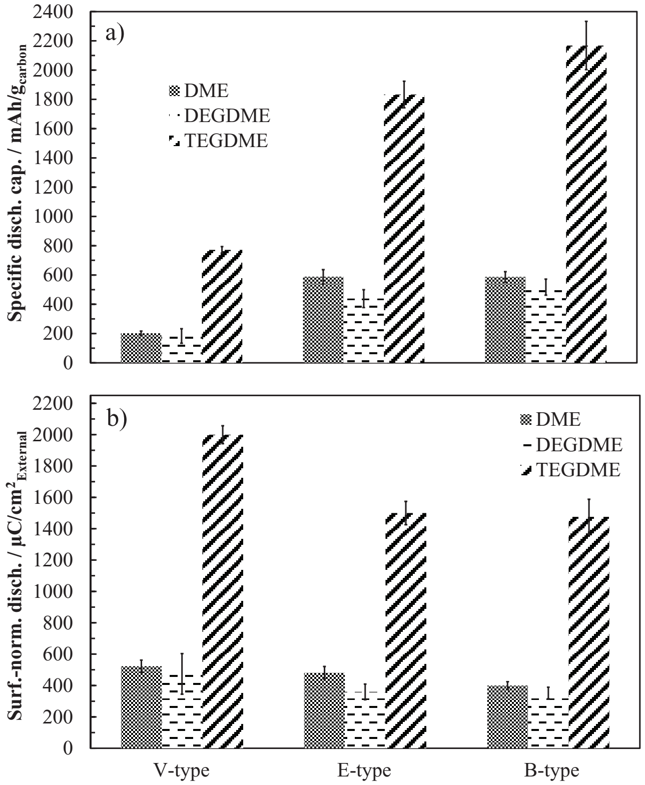

Figure 3. Comparison between discharge capacity (1st cycle) of Li-O_2 cells with non-graphitized carbon cathodes using different non-aqueous electrolytes: 0.1 M $LiClO_4$ in DME, 0.2 M LiTFSI in DEGDME and 0.2 M LiTFSI in TEGDME. a) Specific discharge capacity (mAh/g_{carbon}) and b) surface-normalized discharge expressed in $\mu C/cm^2{}_{S\ external}$. The cells are galvanostatically cycled at 120 mA/g_{carbon} after a 30 minutes rest period at OCV in pure 100 kPa_{abs} O_2. The error bars represent the standard deviation from at least 3 repeat experiments.

values for TEGDME in the literature.[15,19] If the discharge capacities are normalized to the electrode surface area (Table III, Figure 3b), values of ≈1500–2000 $\mu C/cm^2_{external}$ are obtained in TEGDME instead of ≈350–580 $\mu C/cm^2_{external}$ for DEGDME and DME; these values would equate to the formation of 6–8 monolayers of a hypothetical Li_2O_2 surface film (≈2–3 nm thick) in TEGDME instead of the above discussed 1–2 monolayers formed in DEGDME or DME. A similar behavior can be found when comparing the reported discharge film thicknesses on a glassy carbon electrode, reported to be ≈5 nm in DME by Viswanathan et al.[34] and ≈70 nm in PC by Albertus et al.[32] While the observed trend is analogous to that shown in Fig. 3b or Table III, the about ten–fold difference in film thickness in DME may in part be related to the above discussed uncertainty of the roughness factor of the glassy carbon electrode and to differences in the surface-normalized discharge current densities (≈1 $\mu A/cm^2_{surface}$ in[32] and[34] vs. those in our study, listed in Table III). In addition, the much higher product layer thickness obtained in PC by Albertus et al.[32] may also be related to the very high reactivity of PC with superoxide radicals in comparison with TEGDME, leading to a higher degree of slightly soluble reaction intermediates which can then react to the final product (e.g., via comproportionation of solubilized LiO_2 to Li_2O_2) either away from the electrode surface or in form of a "cracked" film.[31] Therefore, the formation of thicker product films on the electrode surface might be correlated with the degree of reactivity of the electrolyte with ORR intermediates (i.e, with $O_2^{-\bullet}$ and/or LiO_2).

The ≈4-fold capacity enhancement in TEGDME compared to DEGDME shown for non-graphitized carbon black electrodes (Figure 3, Figure 4a), is also observed for graphitized carbons as is shown in Figure 4b for a VA-type electrode. Furthermore, ≈500 mV lower initial charging potentials are observed in TEGDME on both carbon surfaces. This peculiar difference in the initial charging voltage would seem to be related to the formation of more easily oxidizable species in TEGDME compared to DEGDME, since the charging onset potentials in DEGDME for all carbons (≈3.5–3.7 V_{Li}, Figure 2b) agrees very well with the calculated overpotential of ≈ 0.6 V for solid Li_2O_2 oxidation in aprotic Li-O_2 systems.[33] The reactivity of TEGDME with ORR intermediates was already proposed by Freunberger et al.,[15] although Li_2O_2 was demonstrated to be the major discharge product; the authors proposed a reaction mechanism that proceeds via hydrogen extraction by the superoxide radical on the TEGDME molecule, with the formation of a soluble hydroperoxo-anion (HO_2^-) that in presence of Li^+ ions can react further to Li_2O_2 (see Figure 5), which then can precipitate in the electrode pores rather than on the carbon surface, thereby increasing the discharge capacity. The reaction mechanism proposed in Figure 5 (a revised version of the one proposed by Freunberger et al.[15]) illustrates how the slow but continuous electrolyte decomposition upon cycling can be consistent with the observed formation of Li_2O_2 as major solid discharge product (formed by reaction with the soluble HO_2^- intermediate) and, in fact, could even explain the enhanced discharge capacity through the TEGDME decomposition reaction which would lead to the formation of mobile peroxo-intermediates capable of diffusing away from the electrode surface and thus delay the formation of a passivating film. For this hypothesized mechanism, the lower initial charging potential in TEGDME (Fig. 4) would be explained by the higher reactivity for the oxidation of solubilized HO_2^- to O_2 and H^+ compared to the oxidation of solid Li_2O_2.

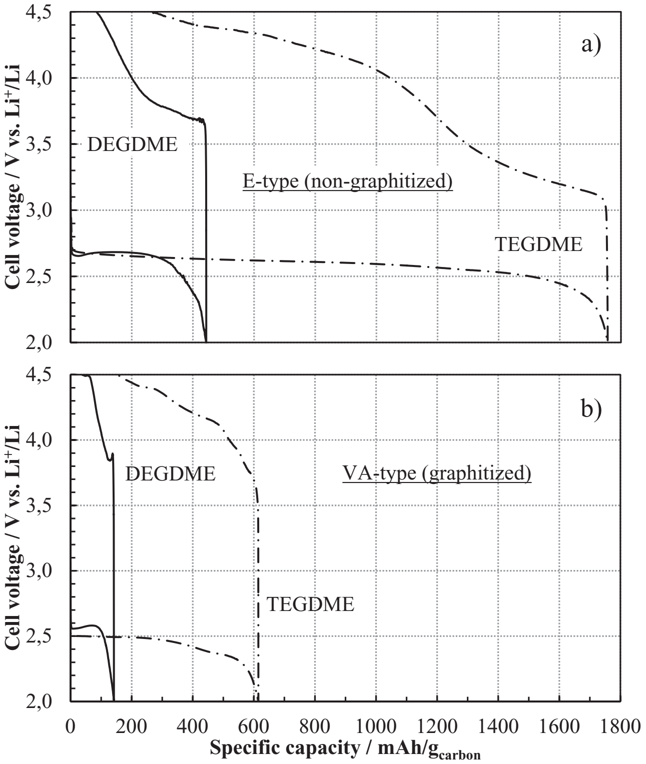

Figure 4. a) Comparison between the cell voltage profile (1st cycle) of Li-O_2 cells with E-type cathodes (non-graphitized) using different non-aqueous electrolytes with 0.2 M LiTFSI: in DEGDME (–) and in TEGDME(– · –). b) Comparison between the cell voltage profile (1st cycle) of Li-O_2 cells with VA-type cathodes (graphitized) using different non-aqueous electrolytes with 0.2 M LiTFSI: in DEGDME (–) and in TEGDME(– · –). The cells are galvanostatically cycled at 120 mA/g_{carbon} after a 30 minutes rest period at OCV in pure 100 kPa_{abs} O_2.

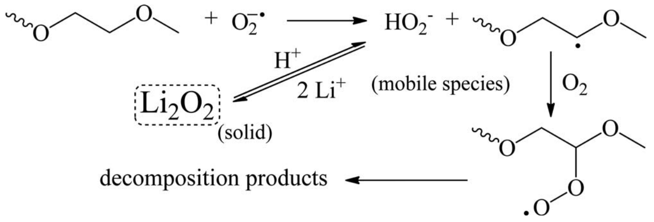

Figure 5. Revisited version of the reaction scheme proposed by Freunberger et al.[15] for Li_2O_2 formation reactions in parallel with electrolyte decomposition.

Regarding cell cyclability of all the carbon-based electrodes (Figure 7), DEGDME based electrolytes show an unusual behavior, i.e., the discharge capacity increases during the first 3–4 cycles and then fades in the subsequent 5 cycles. We tried to rationalize that curious behavior (occasionally found in the literature[3,29]) with two different hypotheses: one, considered less likely, might be the poor wettability of the carbon surface by the electrolyte, which could be improved by potential cycling; the other, considered more likely, could be the modification of the electrolyte composition by its decomposition at high potential during cell charging or even during repeated discharge. In order to examine the second hypothesis, Li-O_2 cells were assembled with fresh 0.2 M LiTFSI in DEGDME, that had been subjected to the electrolyte decomposition test (see Fig. 1 and Experimental Section). Subsequently, a cell with this pre-oxidized DEGDME was tested using the regular cycling procedure. Figure 6 shows the comparison between voltage profiles (1st cycle) of Li-O_2 cells with E-type based electrodes obtained using fresh (solid line) and pre-oxidized (dotted line) DEGDME. The pre-oxidized electrolyte provided about ≈3–fold capacity in comparison to the fresh electrolyte (Figure 6), approaching the results obtained with TEGDME (≈1800 mAh/g_{carbon}) and the charge profile resembles very well the one obtained using fresh TEGDME (compare Figure 6 with Figure 4a, dotted lines). The discharge curve is now composed of basically two voltage plateaus (Figure 6), both lower than the one observed with fresh DEGDME; a lower discharge voltage, already discussed above, was demonstrated in our previous work[31] to be a peculiar feature of unstable electrolytes toward ORR intermediates and could be rationalized by the presence of more easily oxidizable solubilized HO_2^- species. A ≈500 mV lower onset voltage for the charge process in degraded DEGDME

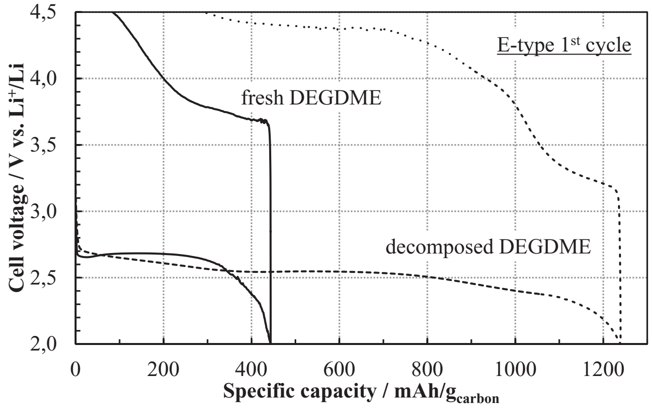

Figure 6. Comparison between cell voltage profile (1st cycle) of Li-O_2 cells with E-type cathodes using different non-aqueous electrolyte with 0.2 M LiTFSI: in fresh DEGDME (–) or in pre–oxidized DEGDME (- - -). The cells are galvanostatically cycled at 120 mA/g_{carbon} after a 30 minutes rest period at OCV in pure 100 kPa_{abs} O_2.

(Figure 6) suggests that the same feature observed in pure TEGDME (Figure 4) could be correlated to the electrolyte degradation, in one case produced voluntarily by means of a cell polarization procedure (pre-oxidized DEGDME), while in the other case produced upon cell discharge (TEGDME).

After electrolyte aging, the cyclability of a Li-O_2 cell with 0.2 LiTFSI in pre-oxidized DEGDME (Figure 7) loses its peculiar capacity increase in the first few cycles and resembles the profile obtained in fresh TEGDME, characterized by an abrupt capacity fading in the first 6 cycles. Comparing the cycling profile observed in DME (albeit with a different salt) and DEGDME where the capacity increases in the first 3–4 cycles with that of either pre-oxidized DEGDME or with TEGDME where the capacity fades continuosly with cycling suggests that reactive electrolyte components or more reactive electrolytes lead to higher first-cycle capacities.

In summary, the use of TEGDME, instead of lower molecular weight ethers, seems to delay the formation of a passivating film on the cathode surface upon cell discharge, delivering in this way ≈4-fold higher discharge capacity and the formation of apparent 6–8 monolayers of "Li_2O_2" instead of the 1–2 monolayers which were found to be sufficient to stop the ORR in less reactive electrolytes like DME and DEGDME. This result can be rationalized by the reactivity of TEGDME proposed by Freunberger et al.;[15] this hypothesis is further supported by the observation that both the discharge capacity (Figure 4a) and cycle behavior (Figure 7) of a TEGDME-based electrolyte resemble the behavior of pre-oxidized DEGDME-based electrolyte. We are aware of the presence of organic impurities in the solvents used and of their possible effect on the first-cycle discharge capacity, however the influence of chain length on the stability of glymes seems to be an acceptable explanation for higher capacities observed in TEGDME. First, differences in reactivity of various glymes were already shown in the supporting information of,[15] where triglyme was reported to decompose in larger extent than diglyme, despite their chemically similar structure. Second, the stability of carbon radicals in hydrocarbon molecules, as well as carbocations, is known to increase with the branching (i.e. tertiary radicals are more stable than primary) and chain length due to hyperconjugation,[43,44] thus justifying higher radical stability (i.e. higher instability toward superoxide) of longer chain glymes. The reaction of TEGDME with a fraction of the superoxide radicals created during discharge likely yields reaction products that allow ORR intermediates to leave the electrode surface, thereby delaying the formation of a passivating Li_2O_2 film. Similarly, pre-oxidized DEGDME-based electrolyte contains decomposition products (apparently produced also upon cycling) that show the very same effect on cell performance as intrinsically more reactive TEGDME.

The high specific capacity with TEGDME-based electrolytes, albeit most likely related to electrolyte decomposition, can be maintained over more than the 6 cycles shown in Fig. 7, when the discharge and charge capacity is limited to a fraction of the possible first-cycle capacity, a method which has been used in previous studies.[4,6] Figure 8 shows the cyclability of two Li-O_2 cells using TEGDME-based electrolyte for a cycling procedure, where discharge and charge capacity are limited to either 0.2 mAh (corresponding to ≈300 mAh/g_{carbon} or 17% of the maximum discharge capacity) or to 0.5 mAh (corresponding to ≈760 mAh/g_{carbon} or 42% of the maximum discharge capacity), with a lower cutoff voltage of 2.4 V_{Li}; the charging potential is limited here to 4.2 V_{Li}, i.e., charging is done potentiostatically once this upper limit is reached. The cycle life of the cells is improved in comparison with the regular galvanostatic cycling (Fig. 7), and up to 11 and 26 cycles are obtained for 0.5 and 0.2 mAh capacity, respectively (Figure 6). We do not believe that the improvements achieved by controlling the cycling protocol are due to the easiness of recharge of thinner Li_2O_2 layers on the cathode surface (≈nm range), since several authors have shown that the complete recharge of micrometric Li_2O_2 particles in non-catalyzed electrodes is possible; we think instead that the critical concentration of side products of electrolyte degradation (both

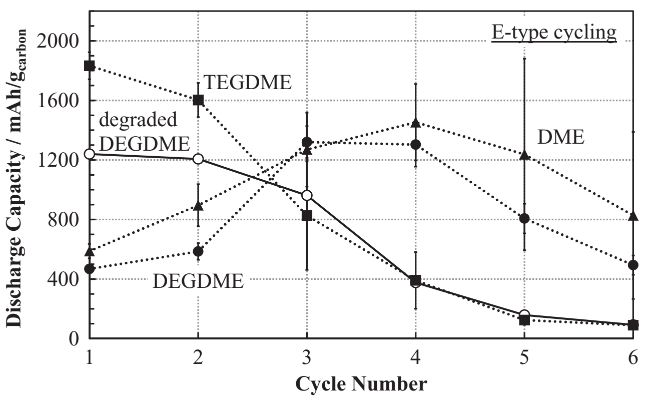

Figure 7. Comparison between discharge capacity behavior upon cycling of Li-O_2 cells with E-type cathodes using different non-aqueous electrolytes: 0.1 M $LiClO_4$ in DME, 0.2 M LiTFSI in fresh DEGDME (–), in 0.2 M LiTFSI in TEGDME (–·–), and in 0.2 M LiTFSI in pre-oxidized DEGDME (- - -). The cells are galvanostatically cycled at 120 mA/g_{carbon} after a 30 minutes rest period at OCV in pure 100 kPa_{abs} O_2. The error bars represent the standard deviation from at least 3 repeat experiments.

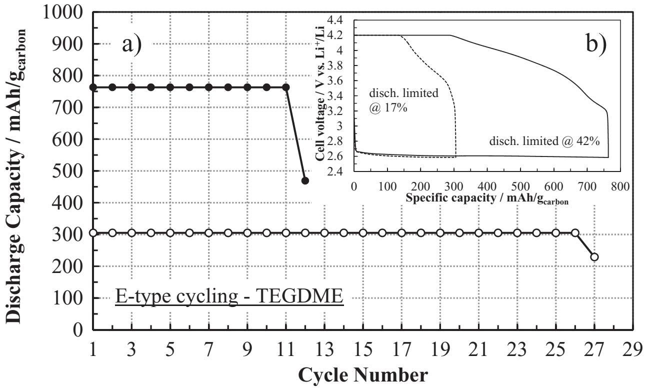

Figure 8. a) Potential and charge limited cycling of two Li-O_2 cells where the absolute capacity is limited to either 0.2 mAh (○) (corresponding to 17% of the maximum specific capacity) or to 0.5 mAh (●) (corresponding to 42% of the maximum specific capacity). b) Comparison between the voltage profile (1st cycle) of Li-O_2 cycled using the "controlled" procedure. The cells are first discharged at 120 mA/g_{carbon} limiting the capacity at an arbitrary value (lower cutoff 2.4 V_{Li}), then charged at 120 mA/g_{carbon} until 4.2 V_{Li}, then holding that voltage until the charge capacity reaches the discharge capacity.

upon charge and discharge) that bring to cell failure is reached after a longer number of cycles. Although it seems apparently possible to improve Li-O_2 cell cyclability by carefully controlling the cycling procedure, the continuous decomposition of the electrolyte is obviously an issue which needs to be resolved in the future. The latter is evidenced by the steeper potential increase during the first part of the charge (galvanostatic region, not shown) with each cycle, and was at least partially shown to be related to the increased formation of Li_2CO_3 from reaction with the carbon support,[45] and oxidation (e.g. formiate, acetate) or polymerization products from reaction with the electrolyte.[15] In conclusion, improved electrolytes and more stable electrode materials are needed for non-aqueous Li-air batteries.

Conclusions

In this article we used seven commercial carbon blacks, characterized by different degrees of microporosity and specific surface area, in order to demonstrate the direct correlation between the first discharge capacity in ether based electrolytes of non-catalyzed Li–air carbon cathodes and their accessible surface area. We found out that using DME and DEGDME based electrolytes, which are considered stable toward superoxide attack, the discharge capacity of Li–O_2 cells is proportional to the externally accessible surface area of non-catalyzed carbon-based electrodes: the surface normalized discharge (in terms of $\mu C/cm^2_{external}$) is similar for all the electrodes, corresponding to a passivating film of 1–2 monolayers of Li_2O_2 deposited on the cathode surface. Li–O_2 cells assembled with TEGDME based electrolyte deliver ≈4–fold higher intial discharge capacity in comparison to DME and DEGDME, corresponding to the formation of 6–8 monolayers of Li_2O_2 on the carbon surface. The impressive capacity enhancement given by TEGDME, together with the evidence that the cyclability obtained using that electrolyte resembles the one obtained using preoxidized DEGDME, suggests that TEGDME is much more reactive in comparison to its lighter homologues in a Li–O_2 cell.

Acknowledgments

Financial support of this research by BASF SE through the framework of its Scientific Network on Electrochemistry and Batteries is gratefully acknowledged by TUM. The TUM Graduate School (TUM-GS) is gratefully acknowledged by Stefano Meini for scholarly and financial support. Tanaka and TimCal are gratefully acknowledged for kindly providing the carbon blacks used in the paper. Nikolaos Tsiouvaras is gratefully acknowledged for fruitful discussions.

References

1. G. Girishkumar, B. McCloskey, A. C. Luntz, S. Swanson, and W. Wilcke, *J. Phys. Chem. Lett.*, **1**, 2193 (2010).
2. K. M. Abraham and Z. Jiang, *J. Electrochem. Soc.*, **143**, 1 (1996).
3. A. Debart, A. J. Paterson, J. Bao, and P. G. Bruce, *Angew. Chem. Int. Ed.*, **47**, 4521 (2008).
4. S. H. Oh and L. F. Nazar, *Adv. Energy Mater.*, **2**, 903 (2012).
5. Z. Peng, S. A. Freunberger, Y. Chen, and P. G. Bruce, *Science*, **337**, 563 (2012).
6. H.-G. Jung, J. Hassoun, J.-B. Park, Y.-K. Sun, and B. Scrosati, *Nature Chemistry*, **4**, 579 (2012).
7. Y.-C. Lu, H. A. Gasteiger, M. C. Parent, V. Chiloyan, and Y. Shao–Horn, *Electrochem. Solid–State Lett.*, **13**, A69 (2010).
8. J. Christensen, P. Albertus, R. S. Sanchez–Carrera, T. Lohmann, B. Kozinsky, R. Liedtke, J. Ahmed, and A. Kojic, *J. Electrochem. Soc.*, **159**, R1 (2012).
9. F. Mizuno, S. Nakanishi, Y. Kotani, S. Yokoishi, and H. Iba, *Electrochemistry*, **78**, 403 (2010).
10. S. A. Freunberger, Y. Chen, Z. Peng, J. M. Griffin, L. J. Hardwick, F. Bardé, P. Novàk, and P. G. Bruce, *J. Am. Chem. Soc.*, **133**, 8040 (2011).
11. B. D. McCloskey, D. S. Bethune, R. M. Shelby, G. Girishkumar, and A. C. Luntz, *J. Phys. Chem. Lett.*, **2**, 1161 (2011).
12. C. O Laoire, S. Mukerjee, K. M. Abraham, E. J. Plichta, and M. A. Hendrickson, *J. Phys. Chem. C*, **114**, 9178 (2010).
13. W. Xu, K. Xu, V. V. Viswanathan, S. A. Towne, J. S. Hardy, J. Xiao, Z. Nie, D. Hu, D. Wang, and J.–G. Zhang, *J. Power Sources*, **196**, 9631 (2011).
14. D. Aurbach, M. Daroux, P. Faguy, and E. Yeager, *J. Electroanal. Chem.*, **291**, 225 (1991).
15. S. A. Freunberger, Y. Chen, N. E. Drewett, L. J. Hardwick, F. Bardé, and P. G. Bruce, *Angew. Chem. Int. Ed.*, **50**, 1 (2011).
16. Y.-C. Lu, D. G. Kwabi, K. P. C. Yao, J. R. Harding, J. Zhou, L. Zuin, and Y. Shao-Horn, *Energy and Environ. Sci.*, **4**, 2999 (2011).
17. T. Kuboki, T. Okuyama, T. Ohsaki, and N. Takami, *J. Power Sources*, **146**, 766 (2005).
18. A. Garsuch, D. M. Badine, K. Leitner, L. H. Gasparotto, N. Borisenko, F. Endres, M Vracar, J. Janek, and E. Oesten, *Z. Phys. Chem.*, **255**, 1 (2011).
19. C. O Laoire, S. Mukerjee, E. J. Plichta, M. A. Hendrickson, and K. M. Abraham, *J. Electrochem. Soc.*, **158**, A302 (2011).
20. R. Black, S. Hyoung Oh, J–H. Lee, T. Yim, B. Adams, and L. F. Nazar, *J. Am. Chem. Soc.*, **134**, 2902 (2012).
21. G. Q. Zhang, J. P. Zheng, R. Liang, C. Xhang, B. Wang, M. Hendrickson, and E. J. Plichta, *J. Electrochem. Soc.*, **157**, A953 (2010).
22. S. D. Beattie, D. M. Manolescu, and S. L. Blair, *J. Electrochem. Soc.*, **156**, A44 (2009).
23. R. R. Mitchell, B. M. Gallant, C. V. Thompson, and Y. Shao-Horn, *Energy Environ. Sci.*, **4**, 2952 (2011).
24. S. S. Sandhu, J. P. Fellner, and G. W. Brutchen, *J. Power Sources*, **164**, 365 (2007).
25. S. S. Sandhu, G. W. Brutchen, and J. P. Fellner, *J. Power Sources*, **170**, 196 (2007).
26. J. Read, K. Mutolo, M. Wrvin, W. Behl, J. Wolfenstine, A. Driedger, and D. Forster, *J. Electrochem. Soc.*, **150**, A1351 (2003).
27. C. Tran, X.-Q. Yang, and D. Qu, *J. Power Sources*, **195**, 2057 (2010).
28. J. Xiao, D. Wang, W. Xu, D. Wang, J. Liu, and J. Zhang, *J. Electrochem. Soc.*, **157**, A487 (2010)
29. H. Cheng and K. Scott, *J. Power Sources*, **195**, 1370 (2010).
30. X.-H. Yang, P. He, and Y.-Y. Xia, *Electrochem. Commun.*, **11**, 1127 (2009).
31. S. Meini, M. Piana, N. Tsiouvaras, A. Garsuch, and H. A. Gasteiger, *Electrochem. Solid–State Lett.*, **15**, A45 (2012).
32. P. Albertus, G. Girishkumar, B. McCloskey, R. S. Sànchez–Carrera, B. Kozinsky, J. Christensen, and A. C. Luntz, *J. Electrochem. Soc.*, **158**, A343 (2011).
33. J. S. Hummelshøj, J. Blomqvist, S. Datta, T. Vegge, J. Rossmeisl, K. S. Thygesen, A. C. Luntz, K. W. Jacobsen, and J. K. Nørskov, *J. Chem. Phys.*, **132**, 071101 (2010).
34. V. Viswanathan, K. S. Thygesen, J. S. Hummelshøj, J. K. Nørskov, G. Girishkumar, B. D. MCloskey, and A. C. Luntz, *J.Chem. Phys.*, **135**, 214704 (2011).
35. L. G. Cota and P. de la Mora, *Acta Cryst.*, **B61**, 133 (2005).
36. B. C. Lippens and J. H. de Boer, *J.Catal.*, **4**, 349 (1965).
37. A. L. Dicks, *J. Power Sources*, **156**, 128 (2006).
38. M. Wissler, *J. Power Sources*, **156**, 142 (2006).
39. K. Kinoshita, *Carbon*, John Wiley & Sons, New York (1988).
40. Y.-C. Lu, H. A. Gasteiger, and Y. Shao-Horn, *J. Am. Chem. Soc.*, **133**, 19048 (2011).
41. J. Chen, J. S. Hummelshøj, K. S. Thygesen, J. S. G. Myrdal, J. K. Nørskov, and T. Vegge, *Catalysis Today*, **165**, 2 (2011).
42. K. Takechi, T. Shiga, and T. Asaoka., *Chem. Commun.*, **47**, 3463 (2011).
43. H. Togo, *Advanced Free Radical Reactions For Organic Synthesis*, p. 5–6, Elsevier, (2004).
44. J. Clayden and N. Greeves, *Organic Chemistry*, p. 406, Oxford University Press, Oxford (2001).
45. B. D. McCloskey, A. Speidel, R. Scheffler, D. C. Miller, V. Viswanathan, J. S. Hummelshøj, J. K. Nørskov, and A. C. Lunz, *J. Phys. Chem. Lett.*, **3**, 997 (2012).

3.3 Stability of Superoxide Radicals in Glyme Solvents for Non-Aqueous Li-O_2 Battery Electrolytes

In this paper, we reported a thorough study on the reactivity of superoxide ion radicals ($O_2^{-\bullet}$) with glyme solvents and their degradation products. This work enlightened the discrepancies in discharge capacity and cycling behavior discussed in the previous section for Li-O_2 cells using glymes of different chain length as electrolyte solvents.

Glymes were proved to be substantially more stable solvents compared to alkyl carbonates in presence of oxygen reduction reaction intermediates in Li-O_2 cells, allowing the precipitation of the desired product Li_2O_2 during Li-air battery discharge, and thus improved cycle life. However, discrepancies in terms of stability towards chemical sources of superoxide radicals (e.g. KO_2) were reported in the literature. More precisely, tetraglyme was previously reported to be slowly attacked by $O_2^{-\bullet}$ cycle after cycle in Li-air cells, that results in the formation of Li_2CO_3 and short chain (Li)carboxylates [11]. On the other hand, no noticeable degradation was observed on discharge for its smaller homologues monoglyme [37] (or dimethoxyethane, DME) and diglyme. Moreover, as shown in Section 3.2, by discharging Li-air cells using electrolyte solutions based on tetraglyme "as received", substantially higher capacities were obtained than with shorter glymes. As higher capacities were previously related to the reaction of ORR intermediates with the electrolyte solution's components (Section 3.1), those results suggested that despite the nearly identical chemical structure, glyme chain length should have an influence on their stability.

In order to clarify that point, K.U. Schwenke (main author of the paper) studied the stability of those solvents by exposing them to a commercial, chemical $O_2^{-\bullet}$ source, KO_2, and measuring the variation of the UV-vis absorption of $O_2^{-\bullet}$ as a function of time [74]. By mixing unstable solvents like propylene carbonate (PC) with $O_2^{-\bullet}$, a rapid drop in the UV-vis absorption of the latter was observed as the degradation reaction proceeded; on the other hand, a negligible reduction of absorption intensity could be noticed with monoglyme and diglyme in a time scale of about 15 hours. In contrast with the results with its smaller homologues, tetraglyme "as received" was found to be highly unstable.

However, nuclear magnetic resonance investigation of that solvent revealed several impurities, suggesting that the results previously obtained (both from the UV-vis method and by battery cycling) could have been affected. Indeed, after tetraglyme was purified by distillation over sodium, we were able to obtain stable UV-vis absorption profiles.

My role in that project was to understand the influence of impurities arising by solvent degradation (chemical and electrochemical) on the performance of Li-air batteries. Li-air cells were cycled between 2-4.5 V_{Li} using different electrolyte solvents; monoglyme, diglyme, tetraglyme "as received", purified tetraglyme, and electrochemically degraded tetraglyme. Monoglyme, diglyme and purified tetraglyme provided the same discharge capacities in the first cycle and similar cycle life behavior; more precisely, the discharge capacity increased from ≈200 mAh/g_{carbon} in the first cycle, up to a maximum of 1000-1500 mAh/g_{carbon} at the 3^{rd}/4^{th} cycles, and subsequently decayed. This behavior was previously observed (Section 3.2), and suggested the degradation of the electrolyte solvent and the introduction of impurities that, by reacting with ORR intermediates, delay the passivation of the electrode surface. That hypothesis was strongly supported by the results reported in this paper, whereby higher capacities can be achieved already in the first cycle by introducing those impurities deliberately (by using impure or electrochemically degraded tetraglyme).

In conclusion, we demonstrated that the chemical structure of glymes is very stable towards superoxide attack; the presence of impurities can reduce the apparent solvent stability and introduce artifacts in battery testing, thus great care must be taken to purify solvents prior to use for Li-air cell testing.

Stability of Superoxide Radicals in Glyme Solvents for Non-Aqueous Li-O_2 Battery Electrolytes

K.U. Schwenke, S. Meini, M. Piana, X. Wu, and H.A. Gasteiger

Physical Chemisty Chemical Physics, 2013, DOI: 10.1039/C3CP51531A

Permanent weblink:

http://dx.doi.org/10.1039/C3CP51531A

Reproduced by permission of The Royal Society of Chemistry

PCCP

RSC Publishing

PAPER

View Article Online
View Journal

Cite this: DOI: 10.1039/c3cp51531a

Stability of superoxide radicals in glyme solvents for non-aqueous Li–O_2 battery electrolytes†

K. Uta Schwenke,* Stefano Meini, Xiaohan Wu, Hubert A. Gasteiger and Michele Piana

Received 10th April 2013,
Accepted 14th May 2013

DOI: 10.1039/c3cp51531a

www.rsc.org/pccp

Glyme-based electrolytes were studied for the use in lithium–air batteries because of their greater stability towards oxygen reduction reaction intermediates (*e.g.*, superoxide anion radicals ($O_2^{\bullet-}$)) produced upon discharge at the cathode compared to previously employed carbonate-based electrolytes. However, contradictory results of glyme stability tests employing KO_2 as an $O_2^{\bullet-}$ source were reported in the literature. For clarification, we investigated the reaction of KO_2 with glymes of various chain lengths qualitatively using ^{1}H NMR and FTIR spectroscopy as well as more quantitatively using UV-Vis spectroscopy. During our experiments we found a huge impact of small quantities of impurities on the stability of the solvents. Therefore, we studied further the influence of impurities in the glymes on the cycling behavior of Li–O_2 cells, demonstrating the large effect of electrolyte impurities on Li–O_2 cell performance.

Introduction

The development of energy storage devices is gaining substantial importance in the process of replacing fossil fuels – in the past apparently inexhaustible and easily accessible – by variable renewable energy sources. Electrification of the vehicular fleet is believed to be an important step towards the set-up of a decentralized storage network and the significant reduction of fossil fuel consumption. However, the highest energy storage density of state-of-the-art lithium ion batteries is too low to meet consumer's demands.[1,2] One promising approach, which could lead up to a 4-fold increase in specific energy density, is the replacement of the lithium-intercalation compounds at the cathode of the lithium ion battery with an oxygen electrode.[3] While at the beginning of non-aqueous rechargeable Li–O_2 battery research lithium was expected to react with oxygen during discharge to yield Li_2O and Li_2O_2,[4] up to now the formation of Li_2O was never clearly verified.[5–10] However, also the rechargeable Li–O_2 battery based on the formation of Li_2O_2 does not provide a truly reversible oxygen chemistry, which is believed to be mainly due to the reactivity of currently used electrolytes with the discharge intermediates and products at the Li–O_2 cathode.[11]

Besides low viscosity, low volatility, and high oxygen solubility, the desired properties of a suitable electrolyte are anodic stability at high potentials, passivation of metallic lithium, and stability *versus* oxygen reduction reaction intermediates produced upon discharge at the cathode.[12] Initially, standard alkyl carbonate based electrolytes known from Li-ion batteries were employed.[4,13–15] But later it was shown using Fourier transform infrared (FTIR), nuclear magnetic resonance (NMR) and Raman spectroscopies, as well as using differential electrochemical mass spectrometry (DEMS) that the main discharge products at the cathode are $C_3H_6(OCO_2Li)_2$, Li_2CO_3, HCO_2Li, CH_3CO_2Li, CO_2, and H_2O rather than the desired Li_2O_2.[6,8,16] A theoretical study revealed as the dominant decomposition pathway the nucleophilic attack of superoxide radicals ($O_2^{\bullet-}$), produced during the reduction of O_2 upon discharge, on the *O*-alkyl carbon atom of organic carbonates.[17]

Hence, research was focused on ether-based electrolytes, which were judged to be more stable to $O_2^{\bullet-}$ attack[18,19] and attracted attention through high oxygen solubility and low viscosity to facilitate oxygen transport.[20] The high molecular weights of long glymes, such as tetraglyme, are correlated with their advantageous low volatility. In contrast to carbonate based electrolytes, Li_2O_2 was found to be the main discharge product when employing glyme-based electrolytes.[7,8,21] However, the selection of a suitable solvent requires the independent understanding of the different reactivity issues such as the degradation of the Li-anode,[7] the electrolyte including conducting salts,[22] the cathode materials like carbons,[23] binders and catalysts[24] as well as the influence of atmospheric components like

---

Institute of Technical Electrochemistry, Technische Universität München, Lichtenbergstr. 4, D-85748 Garching, Germany. E-mail: uta.schwenke@tum.de

† Electronic supplementary information (ESI) available. See DOI: 10.1039/c3cp51531a

H_2O[25] and CO_2.[26] To separate the various contributions to the reactivity, model systems must be developed. Rotating ring disc electrode voltammetry (RRDE) was recently successfully employed to quantify the stability of electrolytes against $O_2^{\bullet-}$.[27] As with the RRDE method reactions in the order of seconds are observed, it applies only to highly reactive electrolytes towards $O_2^{\bullet-}$ like propylene carbonate (PC). Therefore we investigated now further the long term stability of $O_2^{\bullet-}$ in the clearly more stable glymes, even though their long term stability is still controversially discussed in the literature.

While Freunberger *et al.* proposed a mechanism of $O_2^{\bullet-}$ induced decomposition of the glymes during discharge,[21] tests with chemically generated radicals, using KO_2 as a precursor, lead to the conclusion that DME (monoglyme) is stable against superoxide radical attack.[19] Testing tetraglyme, degradation products were once detected[28] and once not.[24] Due to these discrepancies in the literature, we decided to carefully repeat those qualitative experiments with glymes of various chain lengths, employing KO_2 as a superoxide radical source. Although KO_2 will be never present in a Li–O_2 cell its usage is a convenient experimental approach, as KO_2 is commercially available. Additionally, it was recently shown that the presence of a lithium salt in the KO_2 solution may increase the chemical reactivity of the superoxide radicals by forming LiO_2, but it did not change the stability ranking between different solvents.[29] Since the solubility of KO_2 varies in different solvents, it is mandatory to use for more quantitative results a stable solution of superoxide radicals to which the solvent under investigation can be added. DMSO was found to dissolve a maximum of KO_2 without reaction. Furthermore, several studies using DMSO as a solvent reported that the concentration of superoxide radicals can be observed using ultraviolet-visible spectroscopy (UV-Vis) as $O_2^{\bullet-}$ is absorbing UV-light with a maximum at 250–275 nm,[30–34] which allows the quantification of superoxide radical reactivity. During our investigations we noticed the necessity of purification of the examined solvents. The influence of impurities in the glymes on the cell cycling behavior was therefore also carefully studied.

Experimental

Solvents

Acetonitrile (Sigma-Aldrich, 99.8%), dimethyl sulfoxide (DMSO, Sigma Aldrich, 99.99%), diethylene glycol dimethyl ether (diglyme, Sigma Aldrich, ≥99.5%), monoethylene glycol dimethyl ether (monoglyme, Sigma Aldrich, 99.5%), propylene carbonate (PC, Sigma Aldrich, ≥99.5%), tetraethylene glycol dimethyl ether (tetraglyme, Sigma Aldrich, ≥99%) and triethylene glycol dimethyl ether (triglyme, Sigma Aldrich, 99%) were dried prior to use over Sylobead MS 564C zeolites (3 Å, Grace Davision) and stored in an argon-filled glovebox. All used solvents contained ≤5 ppm water, as determined by Karl Fischer titration (Titroline KF, Schott Instruments, Germany).

Tetraethylene glycol dimethyl ether was for reasons of comparison purified by fractional distillation (25 cm Vigreux column) over metallic sodium. The last fraction was collected at approximately 100 °C under vacuum and contained the in the following called "distilled tetraglyme" which was transferred into the glovebox without exposure to air. "Degraded tetraglyme" was obtained directly within fully assembled Li–O_2 cells by anodic oxidation of the distilled tetraglyme-based electrolyte at high potentials, increasing the cell voltage in one hour lasting incremental steps of 100 mV from 4.0 to 4.9 V. Further details can be found in our previous work.[35]

Qualitative investigation using ^1H NMR and FTIR spectroscopy

To investigate qualitatively the reactivity of the different solvents in contact with chemically generated $O_2^{\bullet-}$, an excess of 0.45 g potassium superoxide (KO_2, 96.5%, Alfa Aesar, used as received) was added to 5 g of the solvent under investigation in an argon-filled glovebox (Jacomex, Dagneux, France, <1 ppm of H_2O and O_2). We did not use crown ethers to facilitate the dissolution of KO_2 as decomposition products were detected after contact of KO_2 with 18-crown-6 (Sigma Aldrich, 99%). Even if this reactivity could have come from impurities in the crown ether, we decided to avoid any additional source of uncertainty. Additionally, it was recently stated that no qualitative difference exists between experiments with and without crown ether.[29] Due to very low solubility of KO_2 in the glymes, we stirred the dispersions for 8 days to ensure sufficient solid/liquid reaction time. Subsequently, we separated the liquid phase from the solid residue by centrifugation. Most of the remaining solvent was finally removed from the solid under vacuum: monoglyme at room temperature, diglyme at 50 °C, triglyme at 65 °C and tetraglyme at 80 °C. Both phases were analyzed by FTIR (diamond-ATR, Spectrum Two, Perkin Elmer, USA, located inside an argon-filled glovebox) and ^1H NMR (250 MHz, 128 scans, Avance I, Bruker Instruments, Germany). The solid residues were dissolved in D_2O (Sigma-Aldrich, 99.9 atom% D) and the liquid phases mixed with DMSO-d_6 (Sigma-Aldrich, 99.9%, water content ≤5 ppm). The signals of the deuterated solvents were used as reference for the ^1H NMR chemical shift.

Potassium acetate (Sigma Aldrich, ≥99%), potassium carbonate (K_2CO_3, Merck, puriss.), potassium formate (Sigma Aldrich, ≥99%) and potassium hydroxide (KOH, Merck, p.a.) were used without further purification for reference spectra.

Quantitative investigation using UV-Vis spectroscopy

For quantitative analysis, KO_2 in the right amount to obtain a 3 mM solution was stirred in DMSO for 90 min in an argon-filled glovebox (O_2 < 0.1 ppm, H_2O < 0.1 ppm; MBraun, Germany) to ensure complete dissolution. Furthermore, this time was sufficient for reaction of water traces in DMSO with the added KO_2. As two superoxide radicals react with one water molecule[31,32] the final $O_2^{\bullet-}$ concentration might be up to 20% lower, assuming a water content of 5 ppm in DMSO which corresponds to a concentration of 0.3 mM. 0.7 ml of the obtained KO_2 solution was filled into a quartz cuvette with a sealed screw cap (1/ST/C/Q/2 mm, Starna, USA) and a UV-Vis spectrum was recorded (Lambda35, Perkin Elmer, USA) to determine the initial absorbance which correlates with the $O_2^{\bullet-}$ concentration. Then, a 50-fold molar excess of the solvent under investigation (n(solvent)/n(KO_2) = 50, 8–23 μl depending on the solvent) was added to the solution in the glove box. Due to the large molar excess of solvent, the solvent degradation rate is expected to be pseudo-first-order with respect to $O_2^{\bullet-}$. Solvent addition was defined as the starting time of the reaction. Spectra were collected at constant temperature (25 °C) and corrected with a baseline of the corresponding mixture of DMSO and the solvent. To visualize the decay of the superoxide radical concentration, the absorbance at 270 nm was plotted *versus* time. The dilution of the KO_2 solution due to addition of different volumes of the examined solvents was arithmetically corrected.

Cycling of Li–O_2 battery cells

Cathodes were prepared as described previously[35] by Mayer-rod coating an ink composed of Vulcan XC72 carbon (Tanaka, Japan), isopropanol (IPA, Sigma Aldrich, 99.9%) and lithium-ion exchanged Nafion® solution (LITHion® with 10.6 wt% in IPA from Ion Power, USA) with a binder/carbon ratio of 0.5/1 g/g onto a Celgard C480 separator. The ink was prepared by sonicating carbon and solvent for 20 minutes (Branson 250 probe-sonifier). Subsequently, LITHion® solution was mixed into the ink with a spatula for half a minute. After coating, with a Mayer rod that provides 100 μm wet-film thickness, and solvent evaporation at room temperature, 15 mm diameter electrodes were punched out, dried under dynamic vacuum at 95 °C for 6 hours in a glass oven (Büchi, Switzerland) and transferred for cell assembly into an argon-filled glove box (O_2 < 0.1 ppm, H_2O < 0.1 ppm; MBraun, Germany) avoiding further exposure to ambient air. The average carbon loading was $0.38 \pm 0.05\ \text{mg}_{\text{carbon}}\ \text{cm}_{\text{electrode}}^{-2}$.

Electrolytes were prepared with lithium bis-(trifluoromethanesulfonyl)-imide (LiTFSI, Sigma Aldrich, 99.95% metal basis), which was vacuum dried at 150 °C for 24 hours before use.

The cell design and assembly used in our group were extensively described in previous work.[25] The used cells consist of a 316Ti SS anode current collector and a cathode current collector separated by a Kel-F spacer. The sealing of the system is ensured by two Teflon O-rings and the contact between the cell components is made by a 316 SS compression spring. The cells were assembled by placing a lithium disk (17 mm diameter, 0.45 μm thick, 99.9%, Chemetall, Germany) onto the anode current collector, wetting it with 40 μl of the electrolyte and covering it with two Celgard® C480 separators, which were afterwards wetted with additional 40 μl of the electrolyte. The cathode was placed onto the separators before adding further 40 μl of the electrolyte. Electrical contact was made with a stainless steel mesh (21 mm diameter, 0.22 mm diameter wire, 1.0 mm openings, Spörl KG, Germany). The cell was sealed with four screws at a torque of 6 Nm, then connected to an oxygen line and purged with O_2 at 80 sccm for 35 seconds.

Cycling consisted of a galvanostatic discharge/charge at 120 mA $\text{g}_{\text{carbon}}^{-1}$ between 2.0–4.5 V *vs.* Li/Li^+ at room temperature after minimum 30 minutes rest at open circuit voltage (OCV). All electrochemical tests were performed using a multi-potentiostat VMP3 from Bio-Logic, France.

Analysis of cathodes involved disassembling the cells in the glovebox, rinsing the electrodes with 1 ml acetonitrile and removing the solvent under dynamic vacuum at room temperature. The washed and dried electrodes were investigated using FTIR spectroscopy placing them directly on a MIRacle germanium ATR from Pike Technologies. Afterwards the electrodes were soaked for 30 min in 0.7 ml D_2O to collect ^1H NMR spectra. Lithium acetate (Sigma Aldrich, 99.95%), lithium carbonate (Li_2CO_3, Sigma Aldrich, ≥99%) and lithium formate monohydrate (Sigma Aldrich, 98%) were used for reference spectra.

Results and discussion

Qualitative investigation using ^1H NMR- and FTIR-spectroscopies

Previous studies, which investigated solvent stability against superoxide radicals generated from KO_2, showed only spectroscopic analysis of the solid reaction products but not of the remaining solution.[24,28] Although main decomposition products seem to be non-soluble salts,[6,21] we decided to check also the remaining solution. As expected, NMR-signals of the different investigated glymes with a chemical shift between 3 and 4 ppm did not vary due to contact of the solvents with KO_2 and also no new signals were detected after exposure to KO_2. However, the strongly enlarged NMR spectra of the glymes before and after contact with KO_2 (Fig. 1) revealed that impurities, which were present in tetraglyme and triglyme, showing NMR signals at around 4.5 ppm and 8.2 ppm, disappeared during reaction (marked by the boxes (orange) in Fig. 1c and d). Other impurity signals with low chemical shifts at around 0.5–2 ppm, which were observed in all spectra and which belong probably to alkyl groups, remained on the other hand unchanged. The amount of each of the different impurities was estimated to be at maximum 0.5–1%, integrating the different signals in comparison to the glyme signals set to 100% and using the assumption that each impurity signal would arise from only one hydrogen atom (actual concentration may be substantially lower). Identification of the impurities was more difficult than expected, as a gas chromatographic analysis coupled to mass spectrometry (GC-MS) of tetraglyme did not reveal any substance matching to the vanishing signals of the NMR spectra. We hypothesize that these impurities could be the result of the instability of glymes at high temperatures and/or in the presence of UV-radiation and oxygen, conditions possibly arising in an industrial plant during production, purification, and packing. The increase of impurities with the chain length of the glymes can probably be explained by the increasing boiling point with chain length, which complicates their purification as it requires higher temperatures in the distillation process so that additional decomposition processes may occur. Regarding the NMR spectra, most probable candidates for the reactive impurities are unsaturated-oxygenated hydrocarbons, such as vinyl ethers and vinyl esters. Those substances, *e.g.*, substituted vinyl-methyl ethers, exhibit ^1H NMR signals at around 4–5 ppm, in agreement with the experimental data reported in Fig. 1 for as-received triglyme and tetraglyme. The presence of

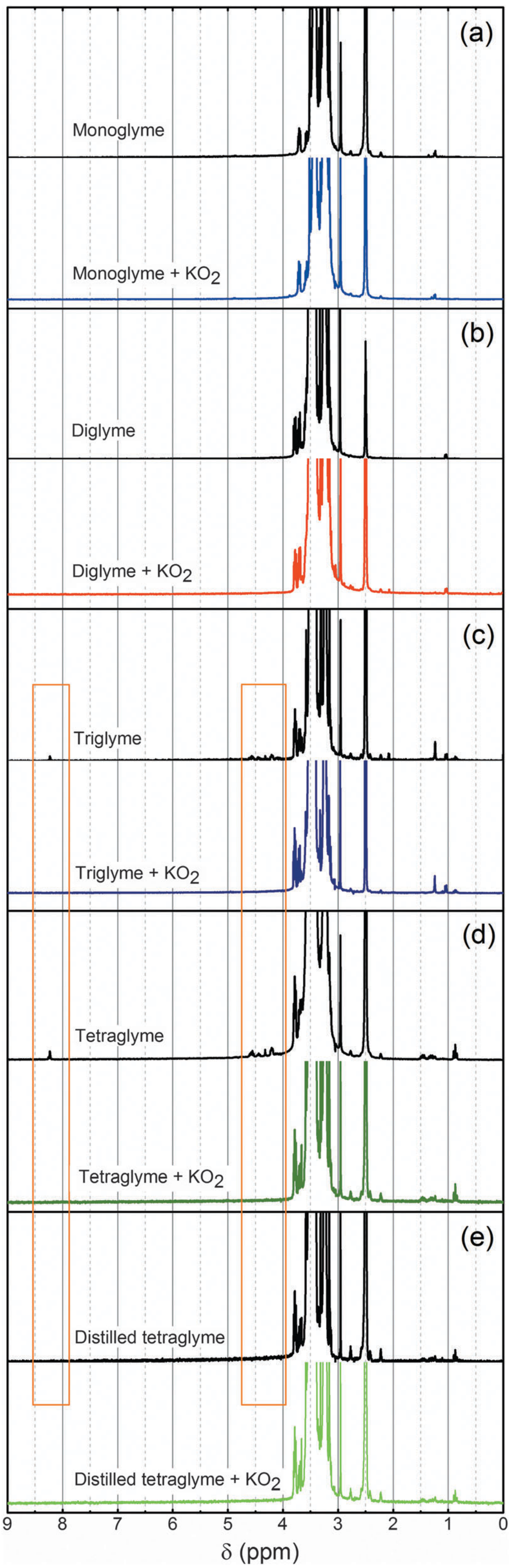

Fig. 1 ^{1}H NMR spectra (DMSO-d_6) of the liquid phase of the saturated KO_2-solution in (a) monoglyme, (b) diglyme, (c) triglyme, (d) tetraglyme as-received, and (e) distilled tetraglyme, compared with the solvent spectra prior to addition of KO_2. Signals around 3–4 ppm belong to the glymes, the signal at 2.5 ppm including satellite signals to the solvent. Impurity signals with low chemical shifts remain mainly unchanged after reaction with KO_2 whereas impurity signals highlighted by the boxes (orange) vanished.

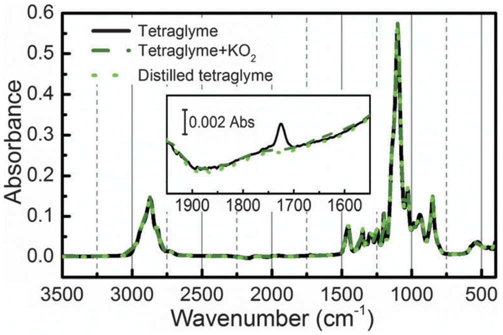

Fig. 2 FTIR spectra of the liquid phase of the saturated KO_2-solution with as-received tetraglyme after 8 days of exposure compared with the spectra of as-received and distilled tetraglyme prior to addition of KO_2. The inset shows the spectra enlarged.

impurities with C═O moieties is supported using FTIR-spectroscopy. Fig. 2 shows that the spectra of tetraglyme before and after stirring with KO_2 are almost identical (black and dark green lines in Fig. 2). The only difference consists of an absorption band at 1725 cm^{-1} which is typical for C═O stretching vibrations; it belongs to the reacting impurities, as it also vanished after distillation (a light green line in Fig. 2). It was therefore mandatory to compare the reactivity of purified and as-received tetraglyme, before assessing about the stability *versus* superoxide radicals. As can be seen in Fig. 1e, we succeeded to remove the reactive impurities by distillation.

The investigation of the solid residues confirmed our assumption that impurities in the different glymes affect their stability against superoxide radicals. While the residues in the distilled tetraglyme as well as in the more purely produced monoglyme and diglyme had a yellowish color like KO_2, the solid residues obtained from triglyme and tetraglyme contained a large white fraction. NMR spectra of the solid phases (Fig. 3) of the KO_2 suspensions with non-purified tetraglyme and triglyme show singlets of formate (8.5 ppm) and acetate (1.9 ppm) as well as some minor signals at around 3.8 ppm, which are consistent with previous work.[10,21] Integration of the NMR signals suggests a 5- to 10-fold excess of formate compared to acetate. Additionally, large amounts of carbonate were detected using FTIR spectroscopy, indicated by the characteristic bending out-of-plane vibration at 880 cm^{-1} (Fig. 4). Furthermore, formate was identified by the sharp absorption band at 760 cm^{-1}, whereas the vibration bands of acetate could only be seen by careful comparison. While tiny amounts of acetate were also detected in the NMR spectrum of the diglyme residue (not visible in the magnification of Fig. 3), none of the typical decomposition products were found in the residues of monoglyme and distilled tetraglyme. The FTIR spectra of the solid residues of distilled tetraglyme, monoglyme and diglyme are similar to the spectrum of the employed KO_2, which is dominated by the bands of carbonate impurity. These impurity bands remained unchanged during reaction. The very weak band of the superoxide bond stretching vibration at 1100 cm^{-1}[36,37] can be seen upon closer inspection. The solid residues from diglyme and much less pronounced monoglyme show additionally

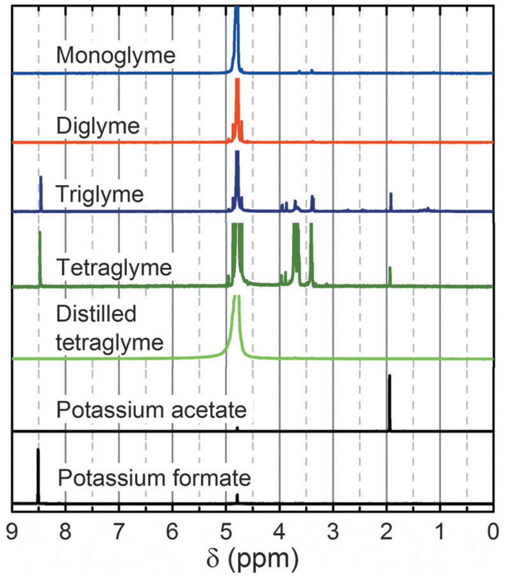

Fig. 3 ^{1}H NMR spectra (D_2O) of the solid residue of saturated KO_2-solutions in the different glymes compared with the spectra of potassium acetate and formate. The signal at 4.79 ppm belongs to HDO and was used as reference. Signals around 3.5 ppm belong to residues from the higher boiling glymes due to incomplete drying of the solid residues.

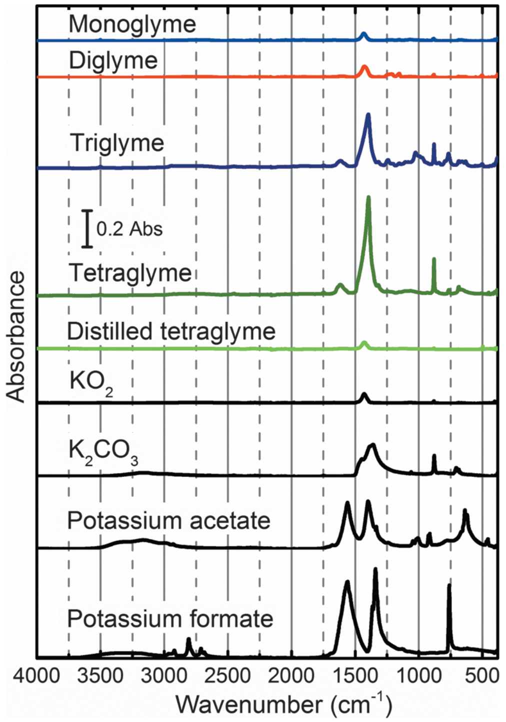

Fig. 4 FTIR spectra of the solid residue of the KO_2-suspension in the different glymes compared with reference spectra of potassium superoxide, potassium carbonate, potassium acetate and formate.

some vibrational absorption bands at 1150 and 1230 cm^{-1}. Freunberger *et al.* assigned vibrations between 1000 and 1300 cm^{-1} to polyethers/esters.[21] A definitive assignment, however, cannot be given. Most striking are the results of the solid residue from distilled tetraglyme as neither in the NMR (Fig. 3) nor in the FTIR spectrum (Fig. 4) any other compounds than D_2O, KO_2 (including its impurities), and very tiny amounts of tetraglyme were detected. Even vacuum drying at 80 °C for 7 hours to remove as much as possible of the latter to improve spectrum quality, did not lead to a reaction between KO_2 and the glyme, so that we believe that the glymes are not attacked by $O_2^{\bullet-}$. However, impurities, whose quantity increases with the chain length of the glymes, are reacting with $O_2^{\bullet-}$. The fact that Takechi *et al.* used the solvents as-received[28] whereas Black *et al.* distilled the solvents prior to the experiments,[24] can explain the discrepancies between their results.

Quantitative investigation using UV-Vis spectroscopy

To ensure that purified tetraglyme is intrinsically stable and that the difference in stability after purification is not simply due to a possibly better solubility of KO_2 by the impurities, we used DMSO to generate a defined amount of $O_2^{\bullet-}$. The absorbance band with a maximum at 255 nm allows us to quantify the initial concentration of superoxide radicals and to follow their rate of reaction with the added solvent. Fig. 5 shows that the superoxide radicals reacted with the non-purified tetraglyme as the absorbance decreases substantially after adding the solvent. For further evaluation, we plotted the absorbance at 270 nm, where DMSO does not yet absorb significantly, for the different reaction mixtures *versus* time (Fig. 6). As the $O_2^{\bullet-}$ starting concentration, indicated by absorbance, varied with a standard deviation of 5% due to the error of the balance and slightly fluctuating water content in DMSO, we normalized the measured values to the absorbance of the KO_2 solution prior to addition of the solvent under investigation. Fig. 6 confirms the qualitative results from the above NMR analysis: the $O_2^{\bullet-}$ concentration decreased considerably in the solutions with as-received tetraglyme and triglyme, while it remained essentially constant for monoglyme, diglyme and especially distilled tetraglyme (Fig. 6b). The "reactivity of the glymes" increased thereby with the amount of impurities and correlated with the amount of decomposition products found using FTIR and

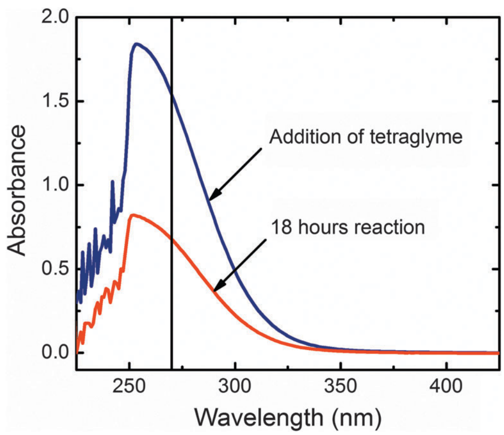

Fig. 5 Baseline corrected UV-Vis spectra of potassium superoxide in DMSO containing a 50 molar equivalent excess of tetraglyme at the beginning of the reaction and after 18 hours. The vertical line at 270 nm corresponds to the wavelength used for further evaluation.

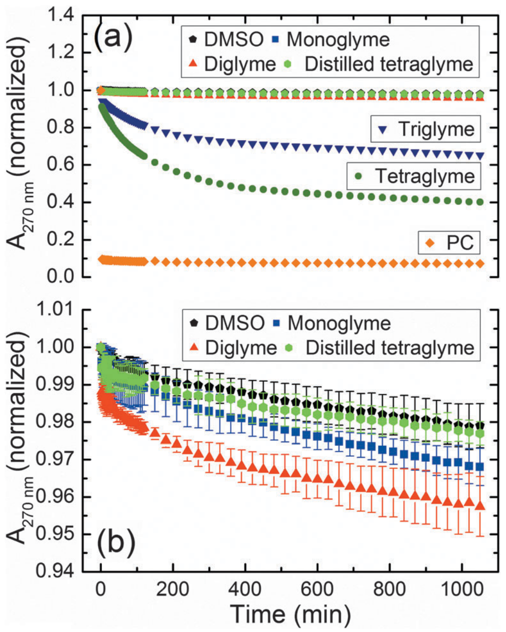

Fig. 6 (a) Plot of the absorbance at 270 nm *versus* time of KO_2 dissolved in pure DMSO and after addition of monoglyme, diglyme, triglyme, tetraglyme as-received and distilled, as well as PC, (b) *y*-axis zoom of Fig. 6a for a better distinction of the less reactive solvents. The error bars represent the standard deviation from three repeat experiments; absorbances are normalized to the absorbance of the starting solution of KO_2 in DMSO.

NMR. In the presence of a 50-fold excess of added solvent, we expected to be able to quantify the stability of $O_2^{\bullet-}$ by the pseudo first order reaction rate constant *k*. In the case of a first order reaction, *k* corresponds to the slope in a plot of the natural logarithm of the absorbance, which is directly proportional to the logarithm of the concentration, *versus* time.

To compare our method to previous results by RRDE, we examined a solution with PC. Due to a very high *k* of 78 min^{-1},[27] corresponding to a half-life of 0.53 s, the reaction was as expected ''completed'' before the collection of the first spectrum and, consequently, the absorbance was very low and did not change any more substantially with time (Fig. 6a). However, the absorbance did not drop to zero, which is most likely due to a changed DMSO/PC background caused by either the products formed from chain reactions initiated by the reaction of $O_2^{\bullet-}$ with PC or by the formation of hydrogen peroxide and dimethyl sulfone when water traces contained in the DMSO react during the 90 min stirring with KO_2.[31] The pseudo first order reaction rate constant could also not be determined for triglyme and tetraglyme, as $O_2^{\bullet-}$ reacted with impurities rather than with the glymes. We could, however, estimate *k* of the reactions with monoglyme, diglyme, and distilled tetraglyme from a semi-logarithmic plot between 2–18 h (the initial 2 hours were not used due to some deviation from linear behavior, most likely caused by trace water added with the solvents). All estimated *k*-values were in the order of 10^{-5} min^{-1}, which is well below the upper limit of 1.14 min^{-1} determined by RRDE for diglyme containing 0.8 M TBATFSI at 25 °C (determined by the RRDE method described in ref. 27). Since even the rate constant of the DMSO background was in the same order of magnitude, we believe that the slightly higher *k* of diglyme and monoglyme was also caused by small amounts of impurities, whereas distilled tetraglyme was found to be intrinsically stable against superoxide radical attack.

A similar method using UV-Vis spectroscopy to test $O_2^{\bullet-}$ stability in different ionic liquids can be found in the literature not related to battery science. Comparing the maximum rate constant of 10^{-5} min^{-1} determined for the clean glymes to the *k*-values reported for ionic liquids (1-*n*-butyl-2,3-dimethyl-imidazolium tetrafluoroborate, $[\text{BMMI}^+][\text{BF}_4^-]$: $k = 0.15\ \text{min}^{-1}$;[33] 1-hexyl-1-methyl-pyrrolidinium bis (trifluoromethylsulfonyl) imide, $[\text{HMPyrr}^+][\text{TFSI}^-]$: $k = 1.14 \times 10^{-3}\ \text{min}^{-1}$ [34]), the stability of glymes against superoxide radical attack is clearly superior. We thus confirm the theoretical predictions that glymes are not attacked by superoxide radicals.[19]

Cycling of Li–O_2 battery cells

Purifying tetraglyme did not only enhance the solvent resistance against superoxide radical attack, but also changed the Li–O_2 cell cycling behavior dramatically. Therefore, we discuss in the following paragraph the influence of impurities on the voltage profile of the first discharge–charge cycle, on the decomposition products found after discharge and charge in the cathode, and on the cycling behavior. Regarding the first cycle, electrolytes based on as-received tetraglyme (Fig. 7, dark green curve) delivered a *ca.* 3–4-fold higher discharge capacity in comparison to diglyme and monoglyme (Fig. 7, red and blue curves). As reported in our recent work,[35] an intrinsic instability of tetraglyme was given as one of the acceptable explanations for the observed higher capacities, possibly related to a decrease in glyme stability towards $O_2^{\bullet-}$ with increasing chain length. Nevertheless, we were aware of the presence of organic impurities in the as-received tetraglyme and their possible effect on discharge capacity. Indeed, the specific capacity in the first discharge of Li–O_2 cells using a distilled tetraglyme based electrolyte (Fig. 7, light green curve) resembles the ones obtained with the shorter homologues diglyme and monoglyme.

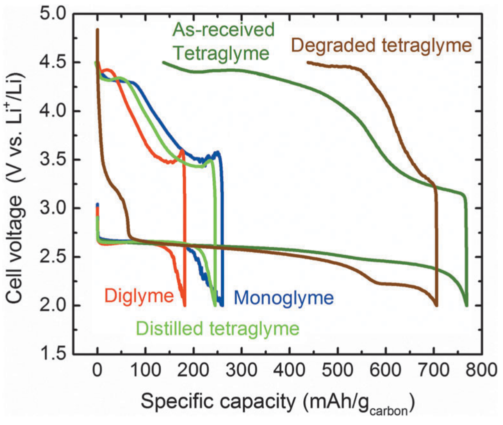

Fig. 7 First discharge–charge cycle between 2.0 and 4.5 V at 120 mA g_{carbon}^{-1} of Li–O_2 cells using a Vulcan carbon cathode and as electrolyte 0.2 M LiTFSI in monoglyme, diglyme, as well as as-received, distilled and degraded tetraglyme.

The correlation between the spectroscopic data and the electrochemical tests confirmed that impurities contained in the as-received glyme rather than the chain length were actually the cause of the different electrochemical behavior of as-received tetraglyme compared to monoglyme and diglyme. We reported earlier that the first discharge capacity is limited to a critical film thickness of 1–2 monolayers of Li_2O_2,[35] presumably due to the passivation of the cathode surface by the discharge products.[38] If, however, the superoxide radicals do not only form LiO_2, which then disproportionates to Li_2O_2 as desired,[39,40] but also react with electrolyte constituents leading to slightly soluble intermediates that leave the electrode surface, the discharge can be substantially prolonged. Furthermore, it does not seem to be important whether the solvent itself is reactive towards $O_2^{\bullet -}$ as in the case of PC[41] or whether reactive impurities are present in the electrolyte. The latter can also be introduced deliberately by electrooxidative degradation of the electrolyte (Fig. 7, brown line)[35] or can arise from water-contaminated oxygen.[25] As the reaction intermediates might diffuse away from the electrode, the discharge products can deposit elsewhere or form an inhomogeneous film, which would allow for higher discharge capacities. Interestingly, the discharge potential shows an inflection at around 550 mA h g_{carbon}^{-1} (after 70–80% of the full discharge) when using impure tetraglyme (either degraded or as-received), presumably related to impurities or oxidized impurities after reaction with $O_2^{\bullet -}$. This inflection is much more pronounced for the degraded electrolyte containing more impurities and also for electrolytes containing a clearly reactive solvent like PC.[25,41] Even though we have not yet fully understood the origin of this potential step, it is a useful indicator for reactive and impure electrolytes. Also, during charge two plateaus were observed (Fig. 7). The lower at around 3.5 V was previously assigned to the charge of Li_2O_2 and the higher close to 4.5 V to the decomposition of the electrolyte and the charge of products different from Li_2O_2.[11,41–44] Even though the second plateau is much more pronounced for the curve of the impure tetraglyme cells, it is also visible using the purified solvent, indicating formation of side products. However, it has to be noted that there is no evidence that the majority of products charged at this high voltage consist of carbonates as still lots of oxygen were detected *via* mass spectrometry[41] and salts different from Li_2O_2 do not yield O_2 during charge.[45]

To investigate when decomposition products are formed, we analyzed electrodes after the first discharge and after the first charge using NMR and FTIR spectroscopy. As expected, after discharge of the cell with as-received tetraglyme, we observed huge amounts of decomposition products like carbonate, acetate, and formate (Fig. 8c, d, 9c and d). Formate was the most important substance detectable by NMR, which is consistent with the reactivity study using KO_2 where formate was also found to be the main impurity detected by NMR (*cf.* Fig. 3). Surprisingly, lower amounts of reaction products were also detected after the discharge of the distilled tetraglyme cell (Fig. 9a). We believe that these products derive from the superoxide-mediated oxidation of hydroperoxides formed by the glymes in contact with oxygen and not of reaction of superoxide radicals with tetraglyme directly.[46]

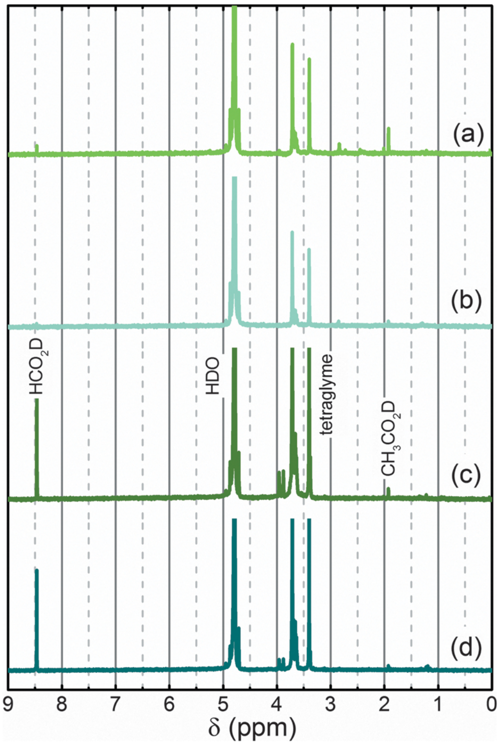

Fig. 8 ^{1}H NMR spectra of D_2O extracts of LITHion® bonded Vulcan cathodes cycled in 1 M LiTFSI in tetraglyme between 2.0 and 4.5 V at 120 mA g_{carbon}^{-1}, (a) 1st discharge distilled tetraglyme, (b) 1st recharge distilled tetraglyme, (c) 1st discharge as-received tetraglyme, (d) 1st recharge as-received tetraglyme.

This decomposition pathway was excluded in our investigations of glyme stability against superoxide radicals as all experiments were conducted under argon.

While no significant amount of the decomposition products from the cell with the as-received tetraglyme could be charged, it was possible to remove large parts of the side products during the first recharge using a cell with distilled tetraglyme (compare Fig. 8d with Fig. 8b). While the FTIR-spectrum after charge of the distilled tetraglyme cell (Fig. 9b) was without significant difference to the pristine electrode spectrum (Fig. 9e), some small traces of decomposition products could still be detected with NMR (Fig. 8b). As stated recently by Chen *et al.*,[47] small amounts of acetate formation seem to be less critical as most of it can be removed during charge below 4 V. However, in our study only small quantities of formate seemed to be decomposed during charge, probably due to the fact that the cell voltage did not stay sufficiently long at high values. These remaining discharge products as well as decomposition of the electrolyte during the end of charge[11,41] lead to an accumulation of impurities during cycling.

The influence of this growing amount of impurities was studied by continued cell cycling. Indeed, it was confirmed that the accumulated impurities inhibited the formation of a homogenous passivating Li_2O_2 film during the following discharges as the discharge capacity of the cells using the ''pure glymes'' increased during the first cycles (Fig. 10), presumably caused by the increase of reactive electrolyte impurities. The discharge capacities reached a maximum in the 3rd cycle before fading

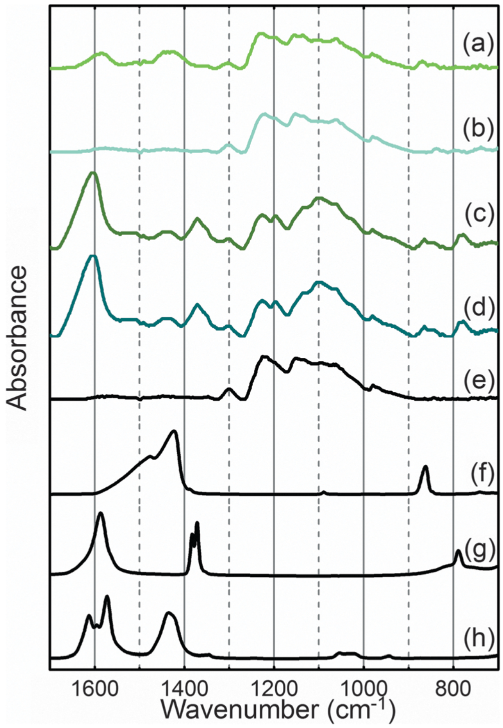

Fig. 9 FTIR spectra of LITHion® bonded Vulcan cathodes cycled in 1 M LiTFSI in tetraglyme between 2.0 and 4.5 V at 120 mA g_{carbon}^{-1}, (a) 1st discharge distilled tetraglyme, (b) 1st recharge distilled tetraglyme, (c) 1st discharge as-received tetraglyme, (d) 1st recharge as-received tetraglyme and for comparison (e) pristine electrode, (f) lithium carbonate, (g) lithium formate, (h) lithium acetate.

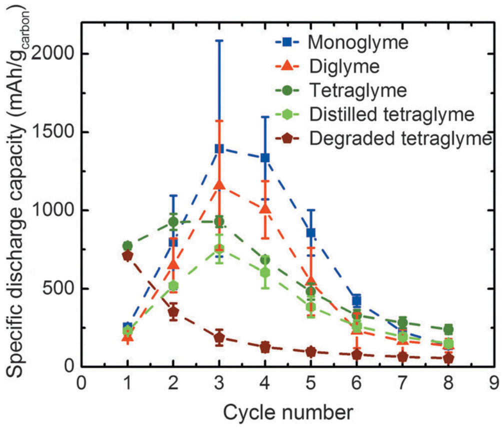

Fig. 10 Comparison of the change in specific discharge capacity upon cycling between 2.0 and 4.5 V at 120 mA g_{carbon}^{-1} of Li–O_2 cells using a Vulcan carbon cathode and as electrolyte 0.2 M LiTFSI in monoglyme, diglyme, as well as as-received, distilled and degraded tetraglyme. The error bars represent the standard deviation from three repeat experiments.

completely during the subsequent cycles. The correlation between maximum discharge capacity and chain length of glymes (shorter glymes yield higher maximum discharge capacity) could be caused by a higher oxygen solubility and lower viscosity of monoglyme compared with tetraglyme.[48] However, these factors seemed to play only a role if enhanced discharge capacity due to impurities was observed. The cyclability curve of as-received tetraglyme resembles the other glymes' curves from the 3rd cycle on, suggesting that the non-purified tetraglyme behaves like a degraded electrolyte. The amount of remaining side products on the cathode was too important to be significantly decomposed during charge (Fig. 8 and 9), so that the cathode blockage would lead in less cycles to complete cell failure. Electrooxidation of the distilled tetraglyme leads to discharge capacity behavior similar to PC,[41] which indicates more impurities in degraded than in as-received tetraglyme. In summary, we observed a continuous fading of capacity for reactive electrolytes (PC)[25] and electrolytes containing reactive impurities, while stable and pure electrolytes displayed a maximum discharge capacity during the third cycle.

Although distilled tetraglyme was found to be stable against superoxide radical attack, the differences in the voltage profiles of cells employing distilled and as-received tetraglyme vanished after the 3rd cycle, as shown in Fig. 11. The normalization of the cell voltage profiles to the respective discharge capacity as shown in Fig. 11 (non-normalized raw data can be found in the ESI† in Fig. S1) allows us to easily ascertain that the plateau near 3.5 V, associated with charging of Li_2O_2, decreased during cycling, while the plateau near 4.5 V, associated partially with carbonate species electrooxidation,[41,42,45] became increasingly dominant. Furthermore, the charging onset potential, which was characteristically high for the first cycle of the ''clean glyme electrolytes'' (*ca.* 3.5 V, Fig. 7, light green curve), approached the lower onset potential of the as-received glyme cells (*ca.* 3.1 V, Fig. 7, dark green curve) during the subsequent cycles. The change in this charging onset potential of the

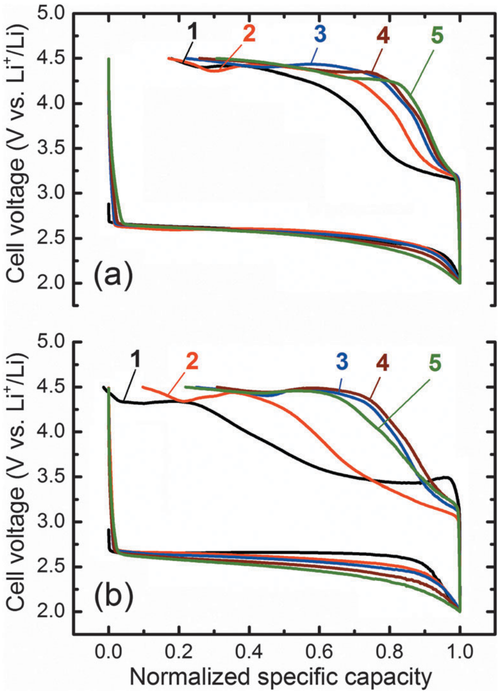

Fig. 11 Cell voltage profiles of the first five cycles of Li–O_2 cells using as electrolyte 0.2 M LiTFSI in (a) tetraglyme as-received and (b) distilled tetraglyme, normalized to the respective discharge capacity of each cycle.

distilled tetraglyme cell is comparable to that observed with diglyme cells, which were recently studied using on-line mass spectrometry.[41] There, O_2 evolution was detected at the expected rate of $2e^-/O_2$ at the beginning of each charging curve. This could suggest that impurities accumulated in the electrolyte evolve oxygen at the same rate as Li_2O_2 (*i.e.*, at $2e^-/O_2$) or more likely act as a mediator for peroxo-species at the electrode surface, which facilitate the charging reaction analogous to what was reported by Chase *et al.*[49] In fresh and pure electrolytes, the absence of impurities leads to solid, crystalline Li_2O_2 and thus to higher voltages at the beginning of the charge, indicated by the initial peak in the first-cycle charging voltage with monoglyme, diglyme and distilled tetraglyme (Fig. 7). As this feature is missing from the 2nd cycle on (see, *e.g.*, Fig. 11b), it can be concluded that the accumulation of electrolyte impurities during cycling as well as deposition of reaction products which block the cathode prevents reversible charge–discharge cycles for Li–O_2 cells using glyme-based electrolytes.

Conclusions

In this work we demonstrated that solvents of the glyme series are sufficiently stable against superoxide radical attack to be used as Li–O_2 battery solvents. No decomposition products were detected using ^{1}H NMR and FTIR spectroscopy after long-term exposure of the pure solvents to KO_2. We noticed that solvent purity is essential for assessing solvent reactivity and could clarify discrepancies in the literature with regard to the stability of glymes towards $O_2^{\bullet-}$. We proposed UV-Vis spectroscopy for more quantitative determination of the stability of various solvents towards superoxide radical attack. It was shown that the developed method is extremely sensitive to small amounts of reactive impurities present in the solvent under investigation. As impurities can change the cell-voltage profile dramatically, especially during the first cycle, we believe that the UV-Vis method is a simple tool for first screening of stable and pure Li–O_2 battery cell solvents.

Although the glymes do not react with superoxide radicals if they are sufficiently pure, the cycling behavior of pure glymes in Li–O_2 cells from the third cycle on does not differ any more from impure electrolytes. Furthermore, even after the first discharge in a distilled tetraglyme based electrolyte, decomposition products are observed by NMR and FTIR. The stability against superoxide radicals is therefore only the first step in the search of a suitable electrolyte. The electrolyte of a rechargeable Li–O_2 battery cell has also to be stable against autooxidation in oxygen and against electrooxidation, especially in the presence of Li_2O_2.

Acknowledgements

BASF SE is gratefully acknowledged by TUM for financial support of this research through the framework of its Scientific Network on Electrochemistry and Batteries and for GC-MS measurements of tetraglyme, in particular Arnd Garsuch for coordination and fruitful discussion. We thank Juan Herranz for proposing the UV-Vis method to investigate superoxide radical stability, for the RRDE measurement on diglyme, and for many fruitful discussions. Furthermore, we acknowledge Linda Nazar and Robert Black for suggestions concerning glyme distillation as well as Cüneyt Kavakli and Armin Siebel for their help in preparing the distillation set-up.

References

1 F. T. Wagner, B. Lakshmanan and M. F. Mathias, *J. Phys. Chem. Lett.*, 2010, **1**, 2204–2219.
2 P. G. Bruce, S. A. Freunberger, L. J. Hardwick and J.-M. Tarascon, *Nat. Mater.*, 2012, **11**, 19–29.
3 Y.-C. Lu, H. A. Gasteiger, M. C. Parent, V. Chiloyan and Y. Shao-Horn, *Electrochem. Solid-State Lett.*, 2010, **13**, A69–A72.
4 K. M. Abraham and Z. Jiang, *J. Electrochem. Soc.*, 1996, **143**, 1–5.
5 T. Ogasawara, A. Débart, M. Holzapfel, P. Novák and P. G. Bruce, *J. Am. Chem. Soc.*, 2006, **128**, 1390–1393.
6 S. A. Freunberger, Y. Chen, Z. Peng, J. M. Griffin, L. J. Hardwick, F. Barde, P. Novak and P. G. Bruce, *J. Am. Chem. Soc.*, 2011, **133**, 8040–8047.
7 C. Laoire, S. Mukerjee, E. J. Plichta, M. A. Hendrickson and K. M. Abraham, *J. Electrochem. Soc.*, 2011, **158**, A302–A308.
8 B. D. McCloskey, D. S. Bethune, R. M. Shelby, G. Girishkumar and A. C. Luntz, *J. Phys. Chem. Lett.*, 2011, **2**, 1161–1166.
9 Y.-C. Lu, E. J. Crumlin, G. M. Veith, J. R. Harding, E. Mutoro, L. Baggetto, N. J. Dudney, Z. Liu and Y. Shao-Horn, *Sci. Rep.*, 2012, **2**, 715.
10 D. Sharon, V. Etacheri, A. Garsuch, M. Afri, A. A. Frimer and D. Aurbach, *J. Phys. Chem. Lett.*, 2012, **4**, 127–131.
11 B. D. McCloskey, D. S. Bethune, R. M. Shelby, T. Mori, R. Scheffler, A. Speidel, M. Sherwood and A. C. Luntz, *J. Phys. Chem. Lett.*, 2012, **3**, 3043–3047.
12 R. Black, B. Adams and L. F. Nazar, *Adv. Energy Mater.*, 2012, **2**, 801–815.
13 J. Read, *J. Electrochem. Soc.*, 2002, **149**, A1190–A1195.
14 A. Débart, A. J. Paterson, J. Bao and P. G. Bruce, *Angew. Chem.*, 2008, **120**, 4597–4600.
15 P. Albertus, G. Girishkumar, B. McCloskey, R. S. Sánchez-Carrera, B. Kozinsky, J. Christensen and A. C. Luntz, *J. Electrochem. Soc.*, 2011, **158**, A343–A351.
16 F. Mizuno, S. Nakanishi, Y. Kotani, S. Yokoishi and H. Iba, *Electrochemistry*, 2010, **78**, 403–405.
17 V. S. Bryantsev and M. Blanco, *J. Phys. Chem. Lett.*, 2011, **2**, 379–383.
18 D. Aurbach, M. Daroux, P. Faguy and E. Yeager, *J. Electroanal. Chem. Interfacial Electrochem.*, 1991, **297**, 225–244.
19 V. S. Bryantsev, V. Giordani, W. Walker, M. Blanco, S. Zecevic, K. Sasaki, J. Uddin, D. Addison and G. V. Chase, *J. Phys. Chem. A*, 2011, **115**, 12399–12409.
20 J. Read, *J. Electrochem. Soc.*, 2006, **153**, A96–A100.
21 S. A. Freunberger, Y. Chen, N. E. Drewett, L. J. Hardwick, F. Barde and P. G. Bruce, *Angew. Chem., Int. Ed.*, 2011, **50**, 8609–8613.
22 G. M. Veith, J. Nanda, L. H. Delmau and N. J. Dudney, *J. Phys. Chem. Lett.*, 2012, **3**, 1242–1247.

23 M. M. Ottakam Thotiyl, S. A. Freunberger, Z. Peng and P. G. Bruce, *J. Am. Chem. Soc.*, 2012, 494–500.

24 R. Black, S. H. Oh, J.-H. Lee, T. Yim, B. Adams and L. F. Nazar, *J. Am. Chem. Soc.*, 2012, 2902–2905.

25 S. Meini, M. Piana, N. Tsiouvaras, A. Garsuch and H. A. Gasteiger, *Electrochem. Solid-State Lett.*, 2012, **15**, A45–A48.

26 K. Takechi, T. Shiga and T. Asaoka, *Chem. Commun.*, 2011, **47**, 3463–3465.

27 J. Herranz, A. Garsuch and H. A. Gasteiger, *J. Phys. Chem. C*, 2012, **116**, 19084–19094.

28 K. Takechi, S. Higashi, F. Mizuno, H. Nishikoori, H. Iba and T. Shiga, *ECS Electrochem. Lett.*, 2012, **1**, A27–A29.

29 V. S. Bryantsev, J. Uddin, V. Giordani, W. Walker, D. Addison and G. V. Chase, *J. Electrochem. Soc.*, 2013, **160**, A160–A171.

30 S. Kim, R. DiCosimo and J. San Filippo, *Anal. Chem.*, 1979, **51**, 679–681.

31 H. Gampp and S. J. Lippard, *Inorg. Chem.*, 1983, **22**, 357–358.

32 Y. Che, M. Tsushima, F. Matsumoto, T. Okajima, K. Tokuda and T. Ohsaka, *J. Phys. Chem.*, 1996, **100**, 20134–20137.

33 M. M. Islam, T. Imase, T. Okajima, M. Takahashi, Y. Niikura, N. Kawashima, Y. Nakamura and T. Ohsaka, *J. Phys. Chem. A*, 2009, **113**, 912–916.

34 M. Hayyan, F. S. Mjalli, M. A. Hashim, I. M. AlNashef, S. M. Al-Zahrani and K. L. Chooi, *J. Electroanal. Chem.*, 2012, **664**, 26–32.

35 S. Meini, M. Piana, H. Beyer, J. Schwämmlein and H. A. Gasteiger, *J. Electrochem. Soc.*, 2012, **159**, A2135–A2142.

36 L. Andrews, *J. Chem. Phys.*, 1971, **54**, 4935–4943.

37 B. Tremblay, L. Manceron, P. Roy, A.-M. LeQuéré and D. Roy, *Chem. Phys. Lett.*, 1994, **228**, 410–416.

38 V. Viswanathan, K. S. Thygesen, J. S. Hummelshoj, J. K. Norskov, G. Girishkumar, B. D. McCloskey and A. C. Luntz, *J. Chem. Phys.*, 2011, **135**, 214704–214710.

39 C. O. Laoire, S. Mukerjee, K. M. Abraham, E. J. Plichta and M. A. Hendrickson, *J. Phys. Chem. C*, 2010, **114**, 9178–9186.

40 Z. Peng, S. A. Freunberger, L. J. Hardwick, Y. Chen, V. Giordani, F. Barde, P. Novak, D. Graham, J.-M. Tarascon and P. G. Bruce, *Angew. Chem., Int. Ed.*, 2011, **50**, 6351–6355.

41 N. Tsiouvaras, S. Meini, I. Buchberger and H. A. Gasteiger, *J. Electrochem. Soc.*, 2013, **160**, A471–A477.

42 B. M. Gallant, R. R. Mitchell, D. G. Kwabi, J. Zhou, L. Zuin, C. V. Thompson and Y. Shao-Horn, *J. Phys. Chem. C*, 2012, **116**, 20800–20805.

43 Y.-C. Lu and Y. Shao-Horn, *J. Phys. Chem. Lett.*, 2012, 93–99.

44 R. Black, J.-H. Lee, B. Adams, C. A. Mims and L. F. Nazar, *Angew. Chem., Int. Ed.*, 2013, **125**, 410–414.

45 S. Meini, N. Tsiouvaras, K. U. Schwenke, M. Piana, H. Beyer, L. Lange and H. A. Gasteiger, *Phys. Chem. Chem. Phys.*, 2013, DOI: 10.1039/C3CP51112J.

46 V. S. Bryantsev and F. Faglioni, *J. Phys. Chem. A*, 2012, **116**, 7128–7138.

47 Y. Chen, S. A. Freunberger, Z. Peng, F. Barde and P. G. Bruce, *J. Am. Chem. Soc.*, 2012, **134**, 7952–7957.

48 J. Read, K. Mutolo, M. Ervin, W. Behl, J. Wolfenstine, A. Driedger and D. Foster, *J. Electrochem. Soc.*, 2003, **150**, A1351–A1356.

49 G. V. Chase, S. Zecevic, T. W. Wesley, J. Uddin, K. A. Sasaki, P. G. Vincent, V. Bryantsev, M. Blanco and D. D. Addison, *US Pat.*, 0028137 A1, 2012.

Supplementary Information

for

Stability of superoxide radicals in glyme solvents for non-aqueous Li-O_2 battery electrolytes

K. Uta Schwenke, Stefano Meini, Xiaohan Wu, Hubert A. Gasteiger and Michele Piana

Institute of Technical Electrochemistry, Technische Universität München,

Lichtenbergstr. 4, D-85748 Garching, Germany

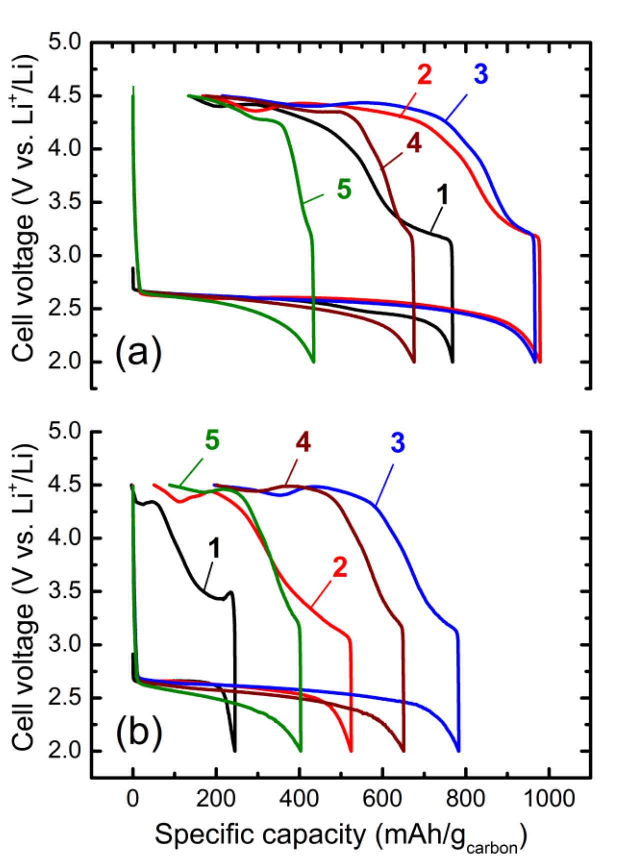

Figure S1. Cell voltage profiles of the first five cycles of Li-O_2 cells using as electrolyte 0.2 M LiTFSI in (a) tetraglyme as-received and (b) distilled tetraglyme.

3.4 Conclusions

In this chapter, some of the performance limitations of Li-O_2 batteries were studied with particular regard to the discharge. The oxygen reduction reaction carried out at the positive electrode surface using relatively high rates (≈100 mA/g_{carbon}) in purified ether-based non-aqueous electrolyte solutions leads to the deposition of a thin layer of discharge products that increases the resistivity at the electrode/solution interface. The critical thickness at which that passivation layer stops the ORR and thus the discharge process is on the order of ≈0.5 nm, accounting to 1-2 monolayers of Li_2O_2, assuming the latter as the only discharge product. As the discharge capacity is proportional to the external surface (average of ≈500 μC/$cm^2_{external}$), whereby external refers to surface comprising the mesoporosity of the electrode (pores >2 nm wide), the use of highly mesoporous electrode materials (e.g. Ketjen Black carbon black) results in higher capacities expressed as [mAh/g_{carbon}]. However, as the stored capacity is limited to surface, the full theoretical potential of Li-air technology consisting in filling electrode porosity with discharge products cannot be achieved at practical discharge rates.

The formation of a passivation layer of discharge products on the positive electrode active surface is however delayed by substances that react with ORR intermediates, enhancing their mobility or producing more soluble intermediates. This is the case when, for example, H_2O and alkyl carbonates are added to the electrolyte solutions. The sensitivity of Li-O_2 cells to impurities can lead to severe artifacts in the capacity measurements when solvents containing substantial amounts of them are used.

The poor cycle life obtained using electrolyte solutions based on glymes solvents (≈10 cycles) can be attributed to the continuous loss of rechargeability of the cells or, in other words, to the increasing charge overpotential that results in lower capacity recovery, cycle after cycle. The observed capacity fading can be explained by the accumulation of alternative discharge products (e.g. Li_2CO_3), resulting from electrolyte solvent degradation and carbon corrosion, in the electrode matrix. Limiting the discharge capacity to lower controlled values can apparently mitigate capacity fading, probably by limiting the accumulation of "inert" (i.e. not rechargeable below 4.5 V_{Li}) discharge products.

Chapter 4

Understanding the Charge Process of Li-Air Batteries: the Role of Electrolyte Solution and Electrode Material on Reversibility and Cycle Life

In the previous chapter, preliminary results on the cycle life of Li-O_2 cells using glyme-based electrolyte solutions were shown. Despite sporadic exceptions [75,76], the poor cycle life of Li-O_2 batteries with positive electrodes based on carbon (e.g. carbon blacks or carbon fibers, as well as carbon nanotubes) is an common feature in most scientific reports in the field [9]; for example, a maximum of 27 cycles could be obtained in our laboratories by limiting the discharge to 17 % of the total capacity of a Ketjen Black electrode (corresponding to ≈300 mAh/g_{carbon}) using tetraglyme solvent (Section 3.2). That number of cycles is insufficient for any application for which a rechargeable battery is required. But what are the fundamental reasons that cause capacity fading in a Li-O_2 battery? In order to answer that question, it is important to obtain further knowledge of the mechanisms governing the recharge (i.e. electrooxidation of discharge products) of a Li-O_2 cell.

The discharge of a Li-O_2 cell involves the consumption of O_2 from the gas phase producing Li_2O_2; accordingly, the *charge* should theoretically yield O_2 gas as the electrooxidation of Li_2O_2 proceeds, at a rate of 2 e^-/O_2 according to the reaction:

$$Li_2O_2 \longrightarrow O_2 + 2Li^+ + 2e^- \qquad \text{(Re. 4.1)}$$

The electrooxidation of Li_2O_2 on carbon surfaces can be carried out at cell voltages below 4.5 V_{Li}, using convenient charge currents of 50-100 mA/g_{carbon} [71,77]. On the other hand, the poor capacity retention of Li-O_2 cells suggests the production of non-Li_2O_2 species arising from the degradation of the electrolyte solution or carbon black corrosion. As the higher cut-off voltage in our cycling experiments is 4.5 V_{Li}, those non-Li_2O_2 species should start to be electroactive only at higher potentials, and they accumulate in the electrode matrix; that leads to pore clogging and permanent passivation of the electroactive surface [13].

In this chapter, the rechargeability of Li-O_2 batteries is studied by comparing the electrochemical behavior and the gases evolved from both discharged electrodes (Section 4.1) and *pre-filled* with possible discharge products (Section 4.2), namely Li_2O, Li_2CO_3 and LiOH; those studies revealed in which conditions those species would accumulate upon cycling, determining the observed capacity fading. Secondly, a fundamental study on the reactivity of Li_2O_2 with carbon and electrolyte solution upon charge, as well as the nature of the oxygen species evolved during Li_2O_2 electrooxidation (Section 4.3). Based on the collected data, several strategies for enhancing rechargeability and cycle life of Li-O_2 batteries were proposed.

4.1 A Novel On-Line Mass Spectrometer Design for the Study of Multiple Charging Cycles of a Li-O_2 Battery

In this paper, we presented a novel mass spectrometer design for the quantitative determination of volatile substances in the headspace of a Li-O_2 cell. The paper reports on the construction features and capability of the On-line Electrochemical Mass Spectrometer developed by Dr. Nikolaos Tsiouvaras, main author of the manuscript, as well as the experimental details that complete the brief description reported in Section 2.7.

As previously discussed, the technical novelty of that setup consists in the connection between the battery cell hardware and the mass spectrometer. A calibrated capillary leak of ≈1 μl/min allows the sampling of the battery headspace and, differently to more common DEMS setups, the one-stage pressure reduction from ambient pressure (battery) to the high vacuum of the mass spectrometer. This allows the continuous determination of the concentration of gases as they are evolved from the electrodes and accumulate in the electrochemical cell headspace. The low sample rate used permits in-situ measurements in completely sealed cell configuration for up to 30 hours, without substantially changing the inner pressure of the cell.

The path for obtaining reliable results with OEMS was sprinkled with many issues, mostly regarding the reproducibility of the discharge capacity values of Li-air cells discharged in the same conditions. More precisely, Li-O_2 cells cycled at the OEMS often provided 2-5 fold higher capacities than equivalent cells cycled using a regular potentiostat available in our laboratory. It was already known that water contaminated O_2 feed results in discharge capacities up to one order of magnitude higher than water-free cells (Section 3.1), however, no substantial amounts of H_2O were detected by the Mass Spectrometer in the gas phase.

My role at that point was to optimize non-catalyzed carbon black (Vulcan XC72) electrodes and support Dr. Tsiouvaras in troubleshooting those reproducibility issues. With our combined strength we were able to understand that traces of H_2O in the O_2 supply line were transported by the O_2 flow into the electrochemical cell (all cells were purged with O_2 for 5 minutes before discharging), wherein they were absorbed by the electrolyte solution and enhanced discharge capacity. That artifact was simply removed by flushing the O_2 supply line for at least one hour before connecting to the electrochemical cell. A systematic coordinated study of several parameters revealed that by using separators of different chemical nature, i.e. glass fiber instead of the most common porous polymeric membranes, the discharge capacity also increased by a factor of ≈3 with diglyme as electrolyte solvent. This effect is not yet fully understood, but we strongly believe that adsorbed species on the glass surface (e.g., H^+ or alkali metal ions K^+, Na^+) could play a major role, as we noticed that the effect is strongly mitigated by Li^+ exchanging the material in a Li^+ containing electrolyte solution prior to cell assembly.

The reliability of the OEMS setup was subsequently proved by determining the gases and their current normalized evolution rates upon charge of previously discharged non-catalyzed carbon electrodes; by comparing an electrolyte solvent (propylene carbonate, PC) known to be highly unstable towards oxygen reduction reaction intermediates with the stable diglyme (Section 3.3), we could benchmark the system and characterize evolved gases (mostly CO_2 with PC, mostly O_2 with diglyme, in accord with the literature [37]). Based on the nature of diglyme solvent fragments detected by the OEMS when cell voltage is increased at values >4.5 V_{Li}, I proposed a possible degradation mechanism of that electrolyte solvent on carbon surfaces, included in the discussion of the paper.

Despite diglyme was revealed to be a stable and reliable electrolyte solvent as discharge is concerned (Section 3.3), this paper pointed out that O_2 recovery by charging a discharged electrode (i.e., by electrooxidizing Li_2O_2) is not complete (overall O_2 evolution efficiency ≈75 %). Substantial amounts of CO_2 evolved at the end of the charge suggested that parasitic reactions of O_2 or Li_2O_2 (sort of "combustive agents") occur with either the electrolyte solvent or the carbon electrode (reduced species and thus "combustible"). That evidence, corroborated by several reports from other groups in the field [58-60], triggered two other fundamental studies on rechargeability of Li-O_2 cells reported in Sections 4.2 and 4.3 respectively.

Analysis of evolved gases of multiple cycles with diglyme solvent revealed that the specific amount of O_2 evolved ([mol_{O2}/mAh]) decreases with cycle number, in accord with the decreasing amount of Li_2O_2 produced on Vulcan XC72 electrodes upon cycling (Table 3.1). That evidence suggests that discharge products alternative to Li_2O_2 such as Li_2O, whose formation is indicated by product selectivity measurements (Table 3.1), cannot be recharged below 4.7 V_{Li}, and accumulate in the electrode matrix upon cycling.

A Novel On-Line Mass Spectrometer Design for the Study of Multiple Charging Cycles of a Li-O_2 Battery

N. Tsiouvaras, S. Meini, I. Buchberger, and H.A. Gasteiger

Journal of The Electrochemical Society, 2013, Volume 160, Issue 3,

Pages A471-A477

Permanent weblink:

http://dx.doi.org/10.1149/2.042303jes

Reproduced by permission of The Electrochemical Society

Journal of The Electrochemical Society, **160** (3) A471-A477 (2013) A471
0013-4651/2013/160(3)/A471/7/$31.00 © The Electrochemical Society

A Novel On-Line Mass Spectrometer Design for the Study of Multiple Charging Cycles of a Li-O_2 Battery

N. Tsiouvaras,*,z S. Meini, I. Buchberger, and H. A. Gasteiger*****

Institute of Technical Electrochemistry, Technische Universität München, D-85748 Garching, Germany

---

In this work we present a novel on-line electrochemical mass spectrometer design, which enables quantitative gas evolution analysis with a sealed battery design, applied to the study of the charging processes in a Li-O_2 battery. Successive charge/discharge cycles were performed using Vulcan-carbon based positive electrodes in electrolytes composed of 0.2 M LiTFSI and two different solvents: *i)* propylene carbonate (PC), and, *ii)* bis(2-methoxyethyl) ether (diglyme). Results on the PC based electrolyte reveal a strong potential dependence of the evolved gaseous products which is maintained throughout subsequent cycles, consisting predominantly of O_2 below 3.7 V and of predominantly CO_2 above 3.7 V. The observed capacity fading is most likely caused by the gradual accumulation of discharge products which can only be oxidized at high anodic potentials. With diglyme electrolyte, the predominant gas during charging is O_2. However, while the number of electrons/O_2 closely corresponds to the oxidation of Li_2O_2 at the beginning of each charging cycle (2 e^-/O_2), it increases with potential and with the number of cycles, suggesting the gradual formation of other oxygen-containing discharge products which can only be oxidized at high potential with the parallel formation of CO_2.
© 2013 The Electrochemical Society. [DOI: 10.1149/2.042303jes] All rights reserved.

Manuscript submitted November 5, 2012; revised manuscript received December 20, 2012. Published January 10, 2013.

Li-O_2 batteries, promising a significant increase in energy density over conventional lithium-ion batteries,[1–4] have been attracting much attention over the past years. Originally, it was assumed that Li_2O_2 would be the predominant discharge product at the positive electrode (generally referred to as cathode) of Li-O_2 batteries based on aprotic organic electrolytes, formed either directly at the electrode surface[5] or through superoxide intermediates ($O_2^-$and/or LiO_2);[1,6,7] also, early experiments with Li_2O_2-filled electrodes showed that O_2 is evolved during charging of Li_2O_2.[8]

These first studies in the field employed the standard alkyl carbonate based electrolytes used for Li-ion batteries,[1,7–11] but later on it was shown that alkyl carbonates are susceptible to nucleophilic attack by superoxide radicals, leading to the formation of Li_2CO_3 and lithium alkyl carbonates, and are thus unsuitable for Li-O_2 batteries.[12–16] Attention has thereafter been shifted to ether-based electrolytes, particularly the glymes, which are more stable in the presence of superoxide radicals.[17,18] Consequently, Li_2O_2 was found to be the predominant product during the initial discharge of Li-O_2 cathodes,[13,19–21] even though their stability is nowadays also believed to be compromised upon cycling.[13,20,22] While the decomposition mechanism of ether-based electrolytes is not as easily understood as in the case of alkyl carbonates, there is evidence that ether-based electrolytes gradually degrade during both the discharge and the charge process.[20]

In several of the above mentioned studies[13,20] as well as in many other recent publications,[23–25] mass spectrometry is employed as a means to determine the electrolyte decomposition products as well as the products produced during battery charging. Most mass spectrometry systems rely upon differential pumping[26–29] (hence the name differential electrochemical mass spectrometry or DEMS), and the first systems of this kind appeared in the mid-80s.[29] Differential pumping refers to a two-stage pressure reduction, whereby a continuously sampled ambient pressure gas stream is first expanded into low vacuum (ca. 0.1-1 mbar) through a properly sized aperture or capillary pumped with a roughing pump, and then expanded into the high vacuum (ca. 10^{-6} mbar) of the mass spectrometer recipient. The advantage of this two-stage expansion is that gas fractionation can be avoided, thereby simplifying quantitative analysis. While this approach is ideal when gas sample flow rates on the order of 1 mL/min can be provided, as is the case for open flow systems (e.g., flow-cells[30]), its use is less straightforward in the case of closed systems like batteries where the sample gas volume is limited. In the latter case, it is therefore necessary to either use a carrier gas which is continuously purging through the battery cell,[27] or to intermittently purge the gas head-space of the battery cell into the differentially pumped inlet of the mass spectrometer.[13] The disadvantage of these approaches, apart from their complexity, is the fact that there is no longer a sealed volume from which the sampling is performed; instead there is a dynamic flow system that is more prone to contamination, particularly when considering that the necessary gas flow rates of ≈1 mL/min are large compared to the typical electrolyte volume in a small-area battery cell (≈10–100 µL for a ≈1 cm^2 cell).

In the present work, we are introducing a new type of on-line electrochemical mass spectrometer (OEMS) system, which to our knowledge has not been used in battery testing so far, permitting continuous gas head-space sampling from a sealed volume over extended periods of time. The main components of the system can be seen in Figure 1, whereby the connection between the sealed gas head-space (9.0 mL) of the battery cell (left-hand-side of Fig. 1) and the mass spectrometer (right-hand-side of Fig. 1) is made through a calibrated crimped-capillary leak which limits the gas flow rate to ≈1 µL/min while still providing response times on the order of 1 second. Thus, gas evolution from anodic/cathodic electrolyte decomposition or during charging of Li-O_2 battery cathodes can be monitored continuously over approximately 10 hours with only minor changes in gas head-space pressure. Despite gas fractionation caused by the one-step expansion into high vacuum, the mass spectrometer signals can be quantified by means of calibration gases. Using this OEMS system, we will examine the anodic stability of an alkyl carbonate and an ether based electrolyte as well as the gas product evolution during the first and subsequent charging cycles of Li-O_2 cathodes.

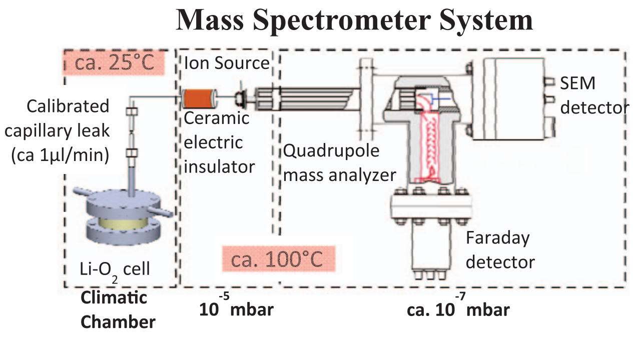

Figure 1. On-line electrochemical mass spectrometer (OEMS) system with a Li-O_2 battery cell (internal gas head space of 9 mL) connected directly through a calibrated crimped-capillary leak (≈1 µL/min) to a mass spectrometer with a closed ionization cage at a pressure of ≈10^{-6} mbar. All gas products evolved in the battery cell are continuously sampled,

---

*Electrochemical Society Active Member.
**Electrochemical Society Student Member.
***Electrochemical Society Fellow.
zE-mail: nikos.tsiouvaras@tum.de

Experimental

Electrode and Electrolyte Preparation: Positive electrodes were prepared by coating a carbon/binder ink onto a glass fiber (GF) separator (Fioroni Filters 259 grade) using a Mayer-rod (100μm wet film thickness). The ink, with a binder/carbon ratio of 0.5/1 g/g was prepared by first sonicating Vulcan XC72 carbon (Tanaka, Japan) and isopropanol (Sigma-Aldrich, 99.9%) for 10 minutes with a Branson 250 digital probe-sonicator. Subsequently, the appropriate amount of LITHion solution (10.6%wt. Li-exchanged Nafion in isopropanol from Ion Power, USA) was stirred into the ink with a spatula for ca. half a minute. The solvent was left to evaporate from the coating at room temperature and then 15 mm diameter electrodes (1.77 cm^2 area) were punched out from the dry coating. Finally, the electrodes were dried under dynamic vacuum at 95°C for 6 hours in a glass oven (Büchi, Switzerland) prior to use and directly transferred to an Ar filled glove box without any further contact with ambient air. The carbon loading of the electrodes was obtained by weighing the electrodes in the glove box and subtracting the weight of the GF separator; the carbon loadings ranged from 0.57 to 1.11 mg_{carbon}/cm^2 (corresponding to 1.0 to 1.96 mg_{carbon} for the various cathode electrodes) and the actual loading for each experiment is given in the figure captions. When trying to compare the anodic electrolyte oxidation currents usually recorded on glassy carbon electrodes with those measured on high-surface area carbon electrodes (see below), it is useful to estimate their actual carbon surface area: the specific carbon surface area available outside of micropores obtained from BET measurements on these electrodes is $\approx$140 m^2/g_{carbon},[31] which equates to an electrode roughness factor of 800 to 1500 $cm^2{}_{carbon}/cm^2{}_{electrode}$.

Electrolytes used were prepared with battery grade LiTFSI (Sigma-Aldrich, 99.99% trace metal basis) as lithium salt; prior to use, the salt was vacuum dried at 150°C for 24 h in a Büchi oven. Anhydrous bis(2-methoxyethyl) ether ("diglyme": Aldrich, 99.5%) and propylene carbonate ("PC": Aldrich, 99.7%) were dried over Sylobead MS 564C zeolites (3Å, Grace Division) and stored in an Ar-filled dry box. Each of the solvents was mixed with LiTFSI to yield a 0.2 M LiTFSI electrolyte with a water content of below 4 ppm (Karl Fischer titration).

Battery cell assembly.— The cell used for the experiments was the one designed by our group and already described in the literature,[32] the only modification being the additional port for connecting the crimped-capillary leak to the mass spectrometer (see Fig. 1). Cells were assembled in an Argon-filled glove box: *i)* placing a 17 mm diameter lithium foil onto the lower part of the cell (negative electrode); *ii)* covering the lithium foil with a 28 mm diameter binder-free glass fiber separator (Fioroni Filters 259 grade); *iii)* adding 120 μL of electrolyte; and, *iv)* covering the separator with the above described 15 mm diameter carbon electrode (GF side of the electrode facing the 28 mm diameter GF separator); electrical contact is made with a stainless steel mesh (see[32]).

OEMS set-up.— The mass spectrometer in the OEMS system is a Pfeiffer Vacuum QMA 410 with a closed cross-beam ionization chamber, attached to a high-vacuum recipient with a 300 l/s turbomolecular pump (Pfeiffer). The gas from the head-space of the battery cell is sampled at a flow rate of $\approx$1 μL/min through a calibrated crimped-capillary leak (Ar leak rate of 1.8 10^{-8} mbar · mL/s at 24°C; from VTI Technologies, USA) and is guided through a tube directly into a differentially pumped cross-beam ionization chamber. The resulting pressure in the ionization chamber is $\approx 1 \cdot 10^{-6}$ mbar and $\approx 1 \cdot 10^{-7}$ mbar at the off-axis secondary electron multiplier (SEM) of the mass spectrometer, allowing for quantification of ppm-level gas constituents (detection limit of $\approx 10^{-14}$ mbar). The SEM voltage was optimized by determining the highest potential for which the ratio between the Argon isotopes remained constant (1400 V in our system) without producing ion currents that would deteriorate the detector (typically below 10^{-7} A).

The advantage of using a crimped-capillary leak is its very low leak rate combined with a fast response time (on the order of 1 second). However, like all single stage pressure reduction inlets and contrary to differentially pumped gas inlets, crimped-capillaries do cause mass fractionation of the sampled gas due to the fact that the flow at the high-pressure side of the capillary is viscous and changes to Knudsen diffusion toward the low-pressure side.[33] As the objective of this work is a quantitative study of the gases evolved during the anodic oxidation of electrolyte and during the charging of Li-O_2 batteries, the signals of the components of interest must be calibrated using calibration gas mixtures with the same background matrix. Considering that all mass-spectrometric analysis was done with an argon filled battery head-space (see below), a calibration gas with low concentrations of oxygen and carbon dioxide in argon was used (2000 ppm each of O_2, CO_2, CO, and H_2 in argon; Westfalen AG, Germany). The detection limits of the system have been approximately calculated assuming that a real signal increase is one that is above 10% of the background. By this approximation the detection limits for O_2, CO_2, and CO should be placed in the range of tenths of ppm, whereas for H_2 and H_2O (H_2O calibration was done by leaking air into the system) should be placed in the scale of hundredths of ppm.

During all experiments the battery cell is connected to a Gamry Series G300 potentiostat and placed in a climatic chamber (KB 20, from Binder, Germany) programmed to maintain a temperature of 25°C. All potentials are reported with respect to the Li/Li^+ potential.

As Li-O_2 batteries are assembled in a charged state, the system was first discharged in the presence of O_2 at ambient pressure. Once the discharge was completed (discharge rate of 120 mA/g_{carbon} to a cutoff potential of 2 V), the cell was purged with Ar until the mass spectrometer detected no more O_2. Subsequently, calibration was performed by filling the cell with the calibration gas; after calibration of the mass spectrometer signals, the gas head-space in the cell was replaced with pure argon prior to starting the charging cycle (charging rate of 120 mA/g_{carbon} to a cutoff potential of 4.7 V), during which the evolved products were followed with the mass spectrometer, recording currents at mass/charge-ratios (m/z) ranging from 1 to 90. An example of the analysis of a typical charging experiment can be seen in Figure 2. Figure 2a shows the first charging curve of a discharged Li-O_2 battery cell with the PC based electrolyte together with the concentration of the only products registered by the mass spectrometer during charging, namely O_2 and CO_2 (Fig. 2b); here, the mass spectrometer detector currents for a given m/z-ratio (averaged over 1.2 s) were converted into concentrations by means of the above determined calibration factors (note that the relevant m/z ratio for each compound was referenced to the m/z = 36 argon isotope signal to minimize the effect of minor variations in the base pressure of the mass spectrometer recipient). The molar gas evolution rates (see Fig. 2c), which correspond to the time derivative of the gas concentrations, are obtained by first smoothing the concentration vs. time data with a Savitzky-Golay smoothing routine, then using a central finite difference method (order of h^4) to obtain the evolution rate in ppm/s, and finally converting them into the molar gas evolution rate (in nmol/s) using the cell volume (9.0 mL) and the ideal gas law.

To analyze gas evolution rates during Li-O_2 battery charging, particularly when only one product is detected at a given time, it is often convenient to express the molar evolution rate (in [nmol/s]) in terms of current-normalized molar flow rates (in [μmol/(As)]), since a 2-electron oxidation process (e.g., the oxidation of Li_2O_2 to O_2 and 2 Li^+) would correspond to a rate of 5.18 μmol/(As) independent of the applied current. The later corresponds to $(2 \cdot F)^{-1}$, where F is the Faraday constant (96485 As/mol), so that experiments conducted at different absolute currents can be compared easily (e.g., electrodes with different carbon loadings charged at equal carbon-mass normalized currents). Molar flow rate (in μmol/s) can be calculated from the here current-normalized flow rates shown in Figs. 5–8 by multiplication with the total current given in the Figure captions

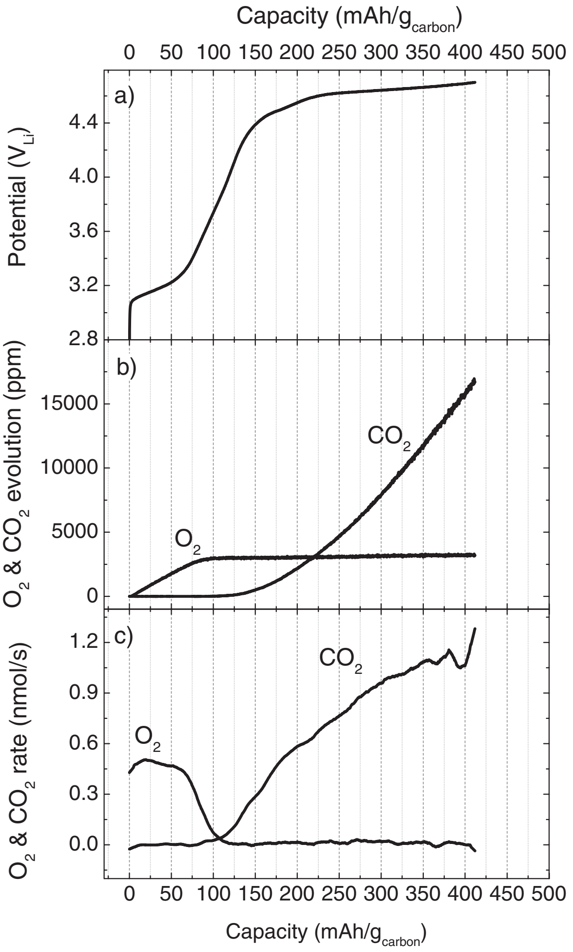

Figure 2. OEMS data processing example for the galvanostatic charging of a discharged Li-O_2 cell with a Vulcan carbon // GF cathode (0.57 mg_{carbon}/cm^2) and 0.2 M LiTFSI in PC electrolyte: a) cell voltage vs. charging capacity at 120 mA/g_{carbon} (corresponding to 122 μA total current) after a first discharge a the same rate; b) mass spectrometer signals for O_2 and CO_2 (in ppm) obtained from the calibration coefficients derived from calibration gas mixtures; c) time derivative of the concentration signal in (b) and conversion into a molar gas evolution rates.

Results and Discussion

Electrolyte stability investigation.— Prior to conducting Li-O_2 battery charge/discharge experiments, the anodic stability of the PC and diglyme based electrolytes was determined. Figure 3a presents the anodic current versus potential curves obtained from potential-step experiments on as-prepared Vulcan carbon cathodes under argon (i.e., prior to any discharge reaction under oxygen). The anodic oxidation currents in Figure 3a are given in terms of carbon mass normalized currents in order to provide a straightforward comparison with the charge/discharge currents used in Li-O_2 battery testing (120 mA/g_{carbon} in our study). For both PC and diglyme based electrolytes, anodic oxidation currents of 20–25 mA/g_{carbon} are reached at a potential of 4.7 V, which we have set as the positive voltage cutoff for all subsequent Li-O_2 battery tests. Essentially identical anodic electrolyte decomposition currents were obtained under O_2 on non-discharged Vulcan carbon cathodes, so that the maximum parasitic current during Li-O_2 battery charging will be $\leq$20% based on our charging current of 120 mA/g_{carbon}.

Studies on the anodic stability of electrolytes can be found in the literature for several aprotic solvents and salts.[34–38] The reported anodic stability of PC based electrolytes obtained from experiments with low surface area glassy carbon electrodes ranges from 5.3 V (with $LiClO_4$ [34]) and 6.0 V (with Et_3MeNPF_6 [38]) all the way up to 6.3 V (with LiTFSI[36,37]), whereby the electrolyte stability potential limit is usually defined at a current density between 0.1 and 1.0 mA/cm^2. Based on these values, one might have expected much lower electrolyte corrosion currents below 5 V for the PC based electrolyte than those shown in Fig. 3a ($\approx$0.1 mA/cm^2 at 4.95 V in Fig. 3a). This apparent discrepancy, however, is due to the fact that the active carbon surface area of high surface area carbon electrodes (roughness factor of $\approx$1250 $cm^2_{carbon}/cm^2_{electrode}$ for the electrodes shown in Fig. 3) will obviously lead to higher anodic electrolyte decomposition currents than on low surface area glassy carbon electrodes, as was discussed previously for high surface area carbon or oxide electrodes.[34,38] Therefore, the interference from anodic electrolyte decomposition must always be evaluated on the actual working electrodes, particularly in the case of Li-O_2 battery experiments, where the geometric current densities are usually only on the order of 0.1 mA/cm^2 (e.g., $\approx$100 mA/g_{carbon} for $\approx$1 $mg_{carbon}/cm^2_{electrode}$). Assuming that the anodic stability of 1,2-dimethoxy ethane (DME) is comparable to diglyme, most of the literature would predict a lower anodic stability for glymes than for propylene carbonate.[34,36] This is different from our findings, which suggest similar anodic stability for PC and diglyme up to 4.8 V; our data are thus more consistent with the similar anodic stability of DME and PC reported by Tobishima and Okada.[39]

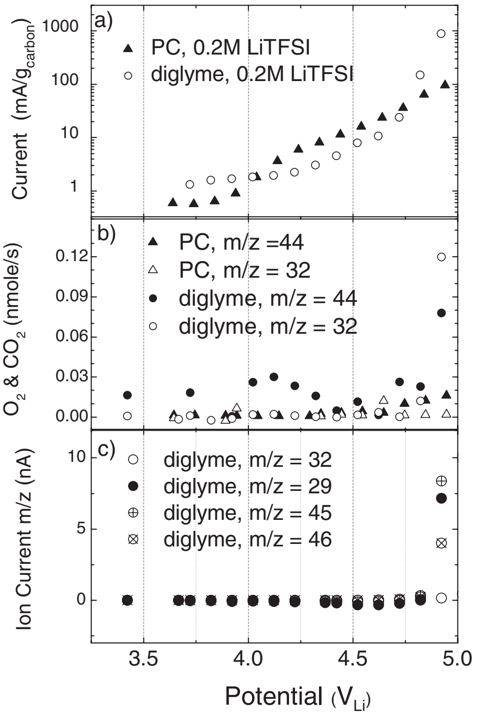

Figure 3. Anodic stability of PC and diglyme based electrolytes with 0.2 M LiTFSI on a Vulcan carbon // GF cathode (1.12 mg_{carbon}/cm^2) working electrode under argon: a) Electrolyte oxidation currents versus potential; b) O_2 and CO_2 evolution rates at each potential; c) highest mass spectrometer ion current signals recorded for diglyme. Experiments were performed potentiostatically in steps of 0.1 V from 3.6 to 5 V (20 minutes per step).

Figure 3b shows the O_2 and CO_2 evolution rates versus cathode potential. In the case of PC, the highest signal is observed for CO_2 in accordance with earlier reports by McCloskey et al.[13] However, this CO_2 evolution rate is extremely low and at potentials below 4.9 V, the number of electrons consumed per evolved CO_2 molecule is close to 100, which suggests that other non-detected (i.e., non-volatile) decomposition product/intermediates are formed. While CO_2 was also observed as the main anodic decomposition product of PC with 1 M $LiPF_6$ by Ufheil et al.,[40] we did not observe the additional formation of minor amounts of acetone as suggested in their study (i.e., we observed no signals at m/z values 43 and 58). In the case of diglyme, mass spectrometric signals are not detected up to 4.8 V, even though high oxidation currents of up to ≈100 mA/g_{carbon} (corresponding to ≈0.1 mA/$cm^2_{electrode}$) are observed, clearly indicating the formation of non-volatile decomposition products or of surface film formation. Volatile products are only detected above 4.8 V, consistent with the behavior of DME reported by McCloskey et al.[13] Next to very low formation rates of oxygen and carbon dioxide (see Fig. 3b), the formation of dimethyl ether is indicated by ion currents at m/z values of 46, 45, and 29 (see Fig. 3c), with intensity ratios as expected for dimethyl ether (see NIST database CAS 115-10-6); unfortunately, due to a lack of the corresponding calibration gas, its evolution rate could not be quantified. Mechanistically, the formation of dimethyl ether suggests an oxidative scission of the carbon-carbon bonds in diglyme; one possible reaction path could be a process analogous of the Kolbe electrolysis reaction in which a β-cleavage reaction produces dimethyl ether and radicals:

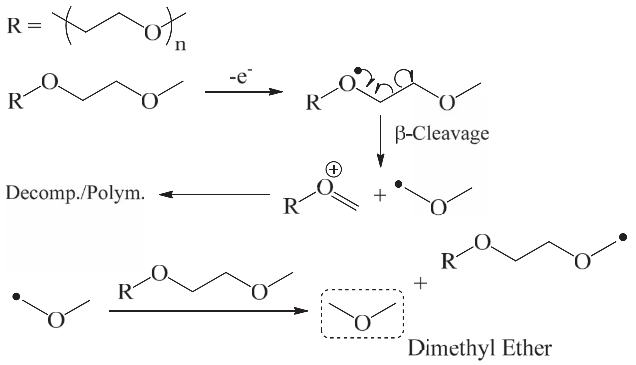

Li-O_2 battery charge/discharge behavior.— The first five charge/discharge cycles of Li-O_2 cells with the different electrolytes are presented in Figure 4. The first discharge capacity in pure PC (Fig. 4a) is similar to what we had reported previously for PC/DME (1/2 and 1/4),[32] and the subsequent strong capacity fading is consistent with other literature reports.[3,41] On the other hand, the discharge capacity of the diglyme cell is increasing over the first few cycles, reaching a maximum at the third cycle. The same behavior was observed for DME and diglyme electrolyte,[31] which is likely related to the formation of electrolyte decomposition products during the first discharge and charge cycle. Here, it should be noted that glyme based electrolytes are considered significantly more stable toward superoxide radical attack during discharge compared to alkyl carbonates,[19,42] even though recent data by Freunberger et al.[20] indicate some decomposition of glyme based electrolytes already during the first charge. One of the suggested decomposition products in the latter study is water, in which case the observed increased discharge capacity in subsequent cycles could be explained based on the previously observed capacity enhancing effect of water.[32] For further insight, the OEMS is used to evaluate the evolution of volatile products during subsequent charging cycles.

In the first charging cycle of a cell with PC-based electrolyte, the only gaseous products detected are O_2 and CO_2 (see Fig. 5), in accordance with other literature results with PC/DME-based electrolyte.[13,43] Analogous to these previous works, small amounts of O_2 are evolved at low potentials, corresponding to approximately ≈2.6 e^-/O_2. The fact that this value is rather close to the theoretical value for the oxidation of Li_2O_2 suggests that small amounts of Li_2O_2 are formed even in PC-based electrolyte, consistent with previous measurements[13,44] but contrary to the observations by Freunberger et al.[45] As the potential increases, the O_2 evolution rate vanishes (Fig. 5b) and CO_2 evolution initiates, reaching rates of ≈1.2 e^-/CO_2 toward the end of discharge at the positive cutoff potential of 4.7 V. When the positive cutoff potential is reached, the CO_2 evolution rate still amounts to ≈1.1 nmol/s (or ≈1.1 μmol/(g_{carbon} · s) when normalized to the carbon mass), which is two orders of magnitude higher than the CO_2 evolution rate from the electrolyte shown in Fig. 3b (≈0.016 nmol/s or ≈0.008 μmol/(g_{carbon} · s)), indicating that 4.7 V is not sufficient to oxidize all the products formed during the first discharge. This is consistent with the charge/discharge data in Fig. 4a, where the discharge capacities are always larger than the corresponding charging capacities. Therefore, the observed capacity fading shown in Fig. 4a is clearly related to the inability to completely remove the discharge products during charging up to 4.7 V. Unfortunately, owing to the excessive electrolyte oxidation currents above 4.7 V (see Fig. 3a), a higher positive cutoff potential is not feasible. During subsequent charging cycles, the O_2 and CO_2 evolution patterns and rates do not change significantly (Fig. 5b), despite the substantial loss of capacity; in addition, O_2 evolution rates at low potential still suggest the presence of minor amounts of Li_2O_2 (albeit strongly diminished).

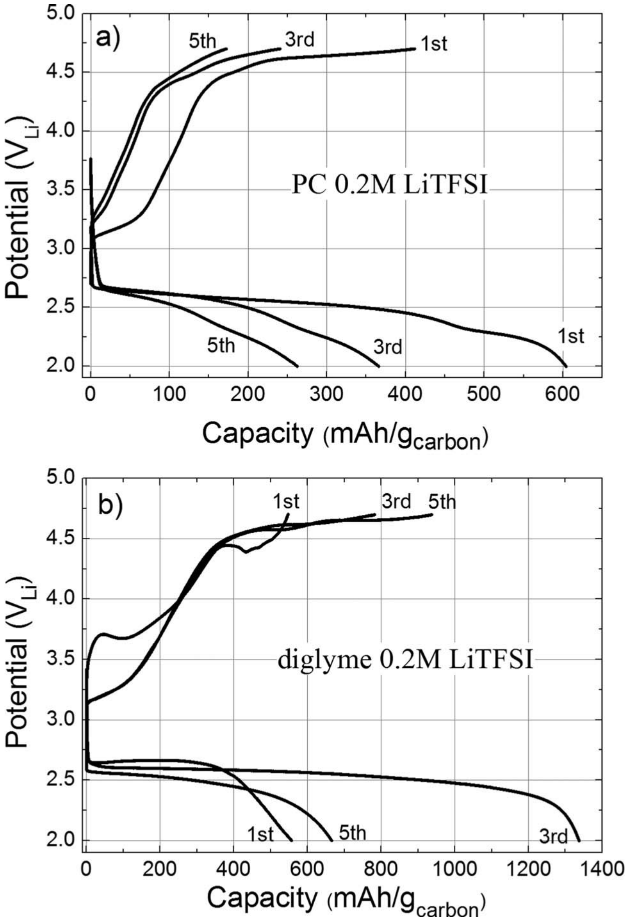

Figure 4. Li-O_2 battery charge discharge cycles between 2.0 and 4.7 V on a Vulcan carbon // GF cathode at 120 mA/g_{carbon} in 0.2 M LiTFSI electrolyte based on: a) PC (0.57 mg_{carbon}/cm^2) and b) diglyme (1.11 mg_{carbon}/cm^2). The cell was connected to the mass spectrometer and discharged in ambient pressure O_2 and charged in Ar (see Experimental).

Further insight into the nature of the discharge products evolution during charge/discharge cycling can be gained by plotting the gas evolution rates versus potential, as is shown in Fig. 6a. Interestingly, despite the significant capacity fading, the O_2 evolution rates are only a function of potential, vanishing at ≈3.7 V independent of cycle number. On the other hand, CO_2 evolution initiates at a higher potential in the first charging cycle than in subsequent cycles, which is likely related to the effect of electrolyte degradation products formed in the first charging cycle. Since the evolution of O_2 and CO_2 occurs in different potential ranges (exclusively O_2 below ≈3.7 V and exclusively CO_2 above this potential), the average number of electrons per mol of evolved gas can be determined and is shown in Fig. 6b. For CO_2, this value is near ≈2 e^-/CO_2, for the first charging cycle and ≈1.5 e^-/CO_2 for all subsequent cycles, suggesting the decomposition of Li_2CO_3 and alkyl carbonate species as was suggested by

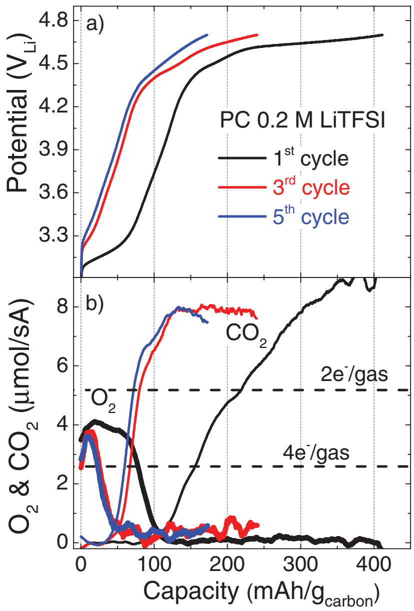

Figure 5. Li-O_2 battery data from Fig. 4a (0.2 M LiTFSI in PC electrolyte; Vulcan carbon // GF cathode with 0.57 mg_{carbon}/cm^2): a) charging potential profiles under Ar (at a current of 120 mA/g_{carbon} corresponding to 120 μA); b) current-normalized evolution rates of O_2 and CO_2 during cell charging, whereby a 2-electron oxidation process would correspond to a rate of 5.18 μmol/(As) if only one product is formed (2.59 μmol/(As) for a 4-electron process).

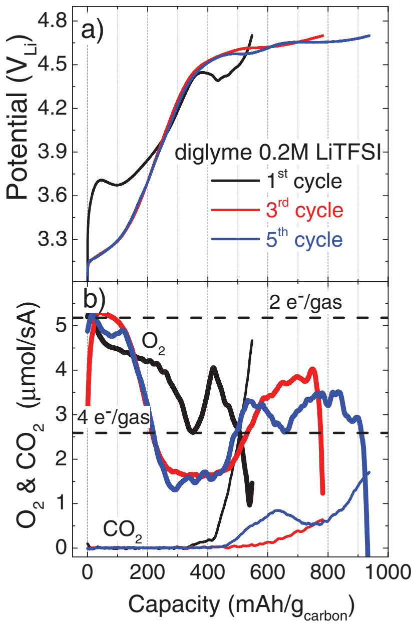

Figure 7. Li Li-O_2 battery data from Fig. 4b (0.2 M LiTFSI in diglyme electrolyte; Vulcan carbon // GF cathode with 1.11 mg_{carbon}/cm^2): a) charging potential profiles under Ar (120 mA/g_{carbon} corresponding to 236 μA); b) current-normalized evolution rates of O_2 and CO_2 during cell charging, whereby a 2-electron oxidation process would correspond to a rate of 5.18 μmol/(As) if only one product is formed (2.59 μmol/(As) for a 4-electron process).

other authors.[8,45] On the other hand, the average number of electrons per evolved O_2 varies between 3 to 4 e^-/O_2 over all cycles, suggesting that even if some small amounts of Li_2O_2 are formed during discharge as was proposed previously.[13,44] Although H_2O and H_2 are also reported as products produced during the charging of cells with PC-based electrolyte,[45] we did not observe any potential-dependent changes in the corresponding mass spectrometric current signals at m/z-values of 18 and 2, respectively. Since the baseline values of H_2O and H_2 in most mass spectrometer set-ups are usually rather high, it is not clear whether the signals in the study by Freunberger et al.[45] have been sufficiently above the background to be meaningful.

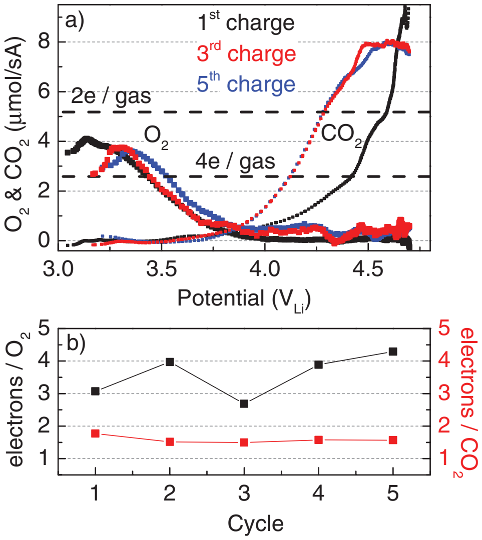

Figure 6. a) Potential dependent O_2 and CO_2 gas evolution rates (current-normalized) for 0.2 M LiTFSI electrolyte based on PC, as derived from Fig. 5b; b) Average number of electrons consumed per evolved O_2 or CO_2, integrated over the potential region below 3.7 V for O_2 and above 3.7 V for CO_2.

In contrast to cells with PC-based electrolyte, O_2 is the main charging product in cells with diglyme-based electrolyte, with CO_2 only being formed toward the end of the charge as shown in Fig. 7. In the first charging cycle, the O_2 evolution rate continuously decreases with increasing potential, analogous to what has been observed for pure DME-based electrolytes.[13,43,46] As is shown in Fig. 7b, the initial O_2 evolution rate corresponds to ≈2 e^-/O_2, consistent with the oxidation of Li_2O_2 and in agreement with what was shown for DME-based electrolytes[13,43,46] for which Li_2O_2 formation was demonstrated by XRD and Raman.[13] Similarly, the predominant formation of Li_2O_2 was also shown by FTIR during the first discharge cycle in tetraglyme.[20] At the end of the first charging cycle, however, the CO_2 evolution rate reaches ≈1.1 nmol/s (≈0.5 $\mu mol/(g_{carbon} \cdot s)$), which is more than an order of magnitude higher than the CO_2 evolution rate from diglyme electrooxidation inferred from Fig. 3b (≈0.02 nmol/s or ≈0.01 $\mu mol/(g_{carbon} \cdot s)$). This could be explained taking into account the observation by Freunberger et al.[20] that a small fraction of difficult-to-oxidize species other than Li_2O_2 are produced during the first discharge in glyme-based electrolytes. An alternative explanation could be that in a parallel to the fuel cell process, amounts of H_2O produced in the cell during the discharge[20] trigger the carbon corrosion resulting in CO_2 evolution. As the CO_2 evolution decreases with each subsequent cycle, although the H_2O concentration should be increasing, the first hypothesis seems to be more probable which would unfortunately imply, as in the case of PC-based electrolyte, that not all discharge products can be oxidized at our cutoff potential of 4.7 V on non-catalyzed carbon electrodes (again, higher positive cutoff potentials are not feasible due to excessive electrolyte oxidation currents).

In the subsequent discharge cycles, there is a striking inflection in the O_2 evolution rates, with the O_2 evolution rates increasing again at the onset of CO_2 evolution (Fig. 7b). Currently, our only explanation for this phenomenon is that this might correspond to the kinetically hindered oxidation of Li_2O_2 (partially) covered by other discharge

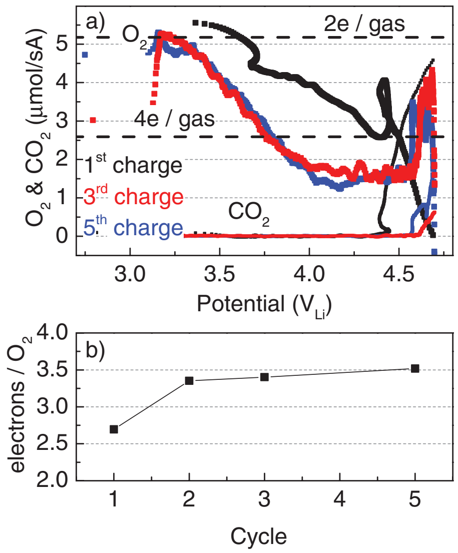

Figure 8. a) Potential dependent O_2 and CO_2 gas evolution rates (current-normalized) for 0.2 M LiTFSI electrolyte based on diglyme, as derived from Fig. 5b; b) Average number of electrons consumed per evolved O_2 over the first five charging cycles, based on the data shown in Figs. 7b.

products like Li_2CO_3 (as proposed by McCloskey et al.[46] and consistent with recent data by Gallant et al.[47]) or by lithium formate, lithium acetate or polyether/ester species (as proposed by Freunberger et al.[20]). This is also based on our observation, that no O_2 evolution occurs during oxidation of other oxygen-containing lithium species when using electrodes pre-filled with Li_2O (oxidative decomposition on a non-catalyzed cathode ca. 4.9 V_{Li}), LiOH(at 4.9 V_{Li}, removal confirmed by FTIR), or Li_2CO_3 (at 4.8 V_{Li}, removal confirmed by FTIR).[48] The fact that this increased O_2 evolution rate at high potentials becomes more pronounced after several charge/discharge cycles is consistent with the observation of an increasing fraction of non-Li_2O_2 species in discharged electrodes (in tetraglyme) with increasing cycle number.[20] Finally, it may be noted that the initial high-potential peak during the galvanostatic charging of Li_2O_2 pre-filled electrodes (see Fig. S10 in[49]) is probably also related to a surface-film contamination of Li_2O_2 particles.

Examining the potential dependence of the O_2 and CO_2 evolution rate in Fig. 8a, one can discern maybe more clearly that the first cycle is distinctly different from the subsequent cycles, probably due to the contamination of the electrolyte by decomposition species formed during the first charging process (analogous to the case with PC-based electrolyte, Fig. 6a). Figure 8b shows the average electrons per O_2 evolved over each charging cycle with diglyme-based electrolyte. The value of ≈2.6 e^-/O_2 for the first cycle is somewhat lower than reported for DME-based electrolyte on either carbon-fiber paper (≈3.2 e^-/O_2 [13]) or on a Vulcan-carbon electrode (≈3.0 e^-/O_2 [43]). This value increases with the number of cycles, reaching ≈3.5 e^-/O_2 for the fifth charging cycle, thus differing more and more from the ideal of 2 e^-/O_2 for pure Li_2O_2. This behavior is consistent with the reported gradual buildup of other discharge products with cycle number observed by FTIR in tetraglyme-based electrolyte,[20] reflecting the instability of glyme-electrolytes over lithium-O_2 battery charge/discharge cycles.

Effect of the separator.— Glass fiber separators are widely used in Li-ion batteries, providing a porous and mechanically stable substrate for the electrolyte. In this work, they were used as electrode substrate and as separator between anode and cathode due to their excellent wettability with PC, which precluded the use of polypropylene/polyethylene separators (e.g., Celgard) as they are not sufficiently wettable with PC. When comparing the initial discharge rates of nominally identical Vulcan-carbon based electrodes coated either on glass fiber separator ("GF") or on Celgard ("CG") in diglyme based electrolyte, however, we noted that 3- to 5-fold higher discharge capacities were obtained for the former (see Fig. 9). Previously, we had observed these higher initial discharge capacities for Vulcan-carbon electrodes coated on Celgard and using a Celgard separator could be obtained if PC/DME (≈500 mAh/g_{carbon}[32]) or tetraglyme based electrolytes (≈800 mAh/g_{carbon}[31]) were used, a phenomenon which we had associated with the reactivity of the electrolyte with superoxide radicals and/or contaminants in the electrolyte.[31] If this were true, one would conclude that the glass fiber separator interacts in some way with the electrolyte, either introducing small levels of impurities or scavenging electrolyte components as has been reported in the literature.[50] The observed higher capacity when using glass fiber separators (s. Fig. 9) could in principle also be related to different electrode morphologies, but preliminary experiments with Vulcan-carbon electrodes coated on Celgard but assembled into a cell with a glass fiber separator show high capacities, suggesting that it is indeed the glass fiber separator interaction with the electrolyte and not any differences in electrode morphology which is responsible for the higher capacities. Although the exact reasons for the capacity-enhancing effect of the glass fiber separator are not fully understood at this point, the gas evolution behavior during charging in diglyme electrolyte with carbon electrodes coated on glass fiber separator (Fig. 7) is the same as that obtained for carbon electrodes coated on Celgard (data not shown). Therefore, the conclusions based on the carbon electrodes coated on glass fiber separator apply to all non-catalyzed carbon electrodes, despite the differences in first discharge capacity.

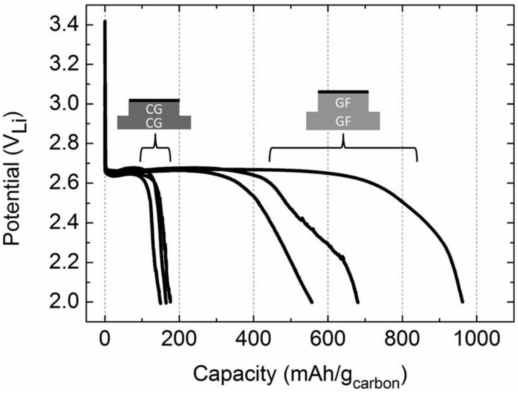

Figure 9. Li-O_2 battery first discharge to 2.0 V at 120 mA/g_{carbon} in diglyme with 0.2 M LiTFSI. Cells were assembled with two different types of electrodes/separators: *i)* Vulcan cathodes coated on glass fiber separator ("GF") and using an additional glass fiber separator between anode and cathode (0.95 ± 0.15 mg_{carbon}/cm^2); or, *ii)* Vulcan cathodes coated on Celgard ("CG") and using an additional Celgard separator between anode and cathode (0.40 ± 0.05 mg_{carbon}/cm^2).

Conclusions

We presented a new on-line mass spectrometer design, which enables the quantitative analysis of the charging product in lithium-air battery cells. Experiments on the anodic stability of diglyme and PC showed that electrolyte oxidation currents and gas evolution rates on Vulcan-carbon electrodes are sufficiently small up to 4.7 V. Above these potentials, the very low evolution rates of predominantly CO_2 are observed for PC, whereas significant evolution rates of CO_2, O_2, and dimethylether are observed for diglyme.

Over successive charge and discharge cycles in a PC electrolyte, the charging processes are characterized by the exclusive evolution of small amounts of O_2 at potentials below 3.7 V and the evolution of large amounts of CO_2 above 3.7 V. These small amounts of O_2 suggest that some Li_2O_2 is produced in every discharge cycle, whereas the CO_2 evolved originates from the dominant discharge products in PC, viz., Li_2CO_3 and alkyl carbonates. The remaining high CO_2 evolution rates at the end of the charging cycle (i.e., at the positive cutoff voltage of 4.7 V) and the fact that the charging capacity is always lower than the associated discharge capacity clearly indicate the incomplete decomposition of the discharge species during charge, leading to their gradual accumulation in the cathode, which is the most likely cause of the observed capacity fading.

While O_2 is the main charging product in diglyme electrolyte, its evolution rate only corresponds to the theoretical $2e^-/O_2$ for Li_2O_2 during the initial part of each charging cycle, and then increases in value. At ≈4.5 V, however, the oxygen yield increases again, accompanied by the onset of CO_2 evolution, suggesting the oxidation of other oxygen-containing discharge products which can only be oxidized at high potential. The average number of e^-/O_2 during charging increases with the number of charge/discharge cycles, indicating a decrease in the Li_2O_2 yield during discharge. The incomplete oxidation of these species for a cutoff potential of 4.7 V again are the most likely cause for the observed capacity fading.

Acknowledgments

The financial support for this work by BASF SE through the framework of its Scientific Network on Electrochemistry and Batteries is gratefully acknowledged. We would also like to thank Michele Piana (TUM) and Arnd Garsuch (BASF SE) for sharing valuable scientific insight and for discussion of the data. The TUM Graduate School (TUM-GS) is gratefully acknowledged by Stefano Meini for scholarly and financial support. Nikolaos Tsiouvaras gratefully acknowledges the Alexander von Humboldt Foundation for his scholarship.

References

1. Y.-C. Lu, H. A. Gasteiger, E. Crumlin, J. R. McGuire, and Y. Shao-Horn, *Journal of The Electrochemical Society*, **157**(9), A1016 (2010).
2. M. Armand and J. M. Tarascon, *Nature*, **451**(7179), 652 (2008).
3. J. Christensen, P. Albertus, R. S. Sanchez-Carrera, T. Lohmann, B. Kozinsky, R. Liedtke, J. Ahmed, and A. Kojic, *Journal of The Electrochemical Society*, **159**(2), R1 (2012).
4. G. Girishkumar, B. McCloskey, A. C. Luntz, S. Swanson, and W. Wilcke, *The Journal of Physical Chemistry Letters*, **1**(14), 2193 (2010).
5. J. S. Hummelshoj, J. Blomqvist, S. Datta, T. Vegge, J. Rossmeisl, K. S. Thygesen, A. C. Luntz, K. W. Jacobsen, and J. K. Norskov, *The Journal of chemical physics*, **132**(7), 071101 (2010).
6. C. O. Laoire, S. Mukerjee, K. M. Abraham, E. J. Plichta, and M. A. Hendrickson, *The Journal of Physical Chemistry C*, **113**(46), 20127 (2009).
7. K. M. Abraham and Z. A. Jiang, *Journal of The Electrochemical Society*, **143**(1), 1 (1996).
8. T. Ogasawara, A. Debart, M. Holzapfel, P. Novak, and P. G. Bruce, *Journal of the American Chemical Society*, **128**(4), 1390 (2006).
9. J. Read, *Journal of The Electrochemical Society*, **149**(9), A1190 (2002).
10. Y.-C. Lu, H. A. Gasteiger, M. C. Parent, V. Chiloyan, and Y. Shao-Horn, *Electrochemical and Solid-State Letters*, **13**(6), A69 (2010).
11. A. Garsuch, D. M. Badine, K. Leitner, L. H. S. Gasparotto, N. Borisenko, F. Endres, M. Vracar, J. Janek, and R. Oesten, *Zeitschrift für Physikalische Chemie*, **226**, 107 (2012).
12. J. Herranz, A. Garsuch, and H. A. Gasteiger, *The Journal of Physical Chemistry C*, **116**(36), 19084 (2012).
13. B. D. McCloskey, D. S. Bethune, R. M. Shelby, G. Girishkumar, and A. C. Luntz, *The Journal of Physical Chemistry Letters*, **2**(10), 1161 (2011).
14. S. A. Freunberger, Y. Chen, Z. Peng, J. M. Griffin, L. J. Hardwick, F. Barde, P. Novak, and P. G. Bruce, *Journal of American Chemical Society*, **133**(20), 8040 (2011).
15. F. Mizuno, N. Shinji, K. Yukinari, Y. Shoji, and I. Hideki, *Electrochemical Communications*, **78**, (2010).
16. V. S. Bryantsev and M. Blanco, *The Journal of Physical Chemistry Letters*, **2**(5), 379 (2011).
17. V. S. Bryantsev, V. Giordani, W. Walker, M. Blanco, S. Zecevic, K. Sasaki, J. Uddin, D. Addison, and G. V. Chase, *The Journal of Physical Chemistry A*, **115**(44), 12399 (2011).
18. D. Aurbach, M. Daroux, P. Faguy, and E. Yeager, *Journal of Electroanalytical Chemistry and Interfacial Electrochemistry*, **297**(1), 225 (1991).
19. R. Black, S. H. Oh, J. H. Lee, T. Yim, B. Adams, and L. F. Nazar, *Journal of the American Chemical Society*, **134**(6), 2902 (2012).
20. S. A. Freunberger, Y. Chen, N. E. Drewett, L. J. Hardwick, F. Barde, and P. G. Bruce, *Angewandte Chemie International Edition*, **50**(37), 8609 (2011).
21. Y.-C. Lu, E. J. Crumlin, G. M. Veith, J. R. Harding, E. Mutoro, L. Baggetto, N. J. Dudney, Z. Liu, and Y. Shao-Horn, *Scientific Reports*, **2**(715), (2012).
22. H. Wang and K. Xie, *Electrochimica Acta*, **64**, 29 (2012).
23. Z. Peng, S. A. Freunberger, Y. Chen, and P. G. Bruce, *Science*, **337**(6094), 563 (2012).
24. Y. Chen, S. A. Freunberger, Z. Peng, F. Bardé, and P. G. Bruce, *Journal of American Chemical Society*, **134**(18), 7952 (2012).
25. W. Xu, V. V. Viswanathan, D. Wang, S. A. Towne, J. Xiao, Z. Nie, D. Hu, and J.-G. Zhang, *Journal of Power Sources*, **196**(8), 3894 (2011).
26. M. Holzapfel, A. Würsig, W. Scheifele, J. Vetter, and P. Novák, *Journal of Power Sources*, **174**(2), 1156 (2007).
27. P. Novak, D. Goers, L. Hardwick, M. Holzapfel, W. Scheifele, J. Ufhiel, and A. Wursig, *Journal of Power Sources*, **146**(1–2), 15 (2005).
28. P. Novák, J. C. Panitz, F. Joho, M. Lanz, R. Imhof, and M. Coluccia, *Journal of Power Sources*, **90**(1), 52 (2000).
29. G. Eggert and J. Heitbaum, *Electrochimica Acta*, **31**(11), 1443 (1986).
30. H. Baltruschat, *Journal of the American Society for Mass Spectrometry*, **15**(12), 1693 (2004).
31. S. Meini, M. Piana, H. Beyer, J. Schwämmlein, and H. A. Gasteiger, *Journal of The Electrochemical Society*, **159**(12), A2135 (2012).
32. S. Meini, M. Piana, N. Tsiouvaras, A. Garsuch, and H. A. Gasteiger, *Electrochemical and Solid-State Letters*, **15**(4), A45 (2012).
33. H. T. Bach, B. A. Meyer, and D. G. Tuggle, *Journal of Vacuum Science & Technology A*, **21**(3), 806 (2003).
34. F. Ossola, G. Pistoia, R. Seeber, and P. Ugo, *Electrochimica Acta*, **33**(1), 47 (1988).
35. D. Aurbach, in *Nonaqueous Electrochemistry* (CRC Press, 1999).
36. M. Ue, M. Takeda, M. Takehara, and S. Mori, *Journal of The Electrochemical Society*, **144**(8), 2684 (1997).
37. K. Xu, *Chemical Reviews*, **104**(10), 4303 (2004).
38. K. Xu, S. P. Ding, and T. R. Jow, *Journal of The Electrochemical Society*, **146**(11), 4172 (1999).
39. S.-i. Tobishima and T. Okada, *Electrochimica Acta*, **30**(12), 1715 (1985).
40. J. Ufheil, A. Würsig, O. D. Schneider, and P. Novák, *Electrochemistry Communications*, **7**(12), 1380 (2005).
41. A. Débart, J. Bao, G. Armstrong, and P. G. Bruce, *Journal of Power Sources*, **174**(2), 1177 (2007).
42. C. O. Laoire, S. Mukerjee, K. M. Abraham, E. J. Plichta, and M. A. Hendrickson, *The Journal of Physical Chemistry C*, **114**(19), 9178 (2010).
43. B. D. McCloskey, R. Scheffler, A. Speidel, D. S. Bethune, R. M. Shelby, and A. C. Luntz, *J. Am. Chem. Soc.*, **133**(45), 18038 (2011).
44. J. Xiao, J. Hu, D. Wang, D. Hu, W. Xu, G. L. Graff, Z. Nie, J. Liu, and J.-G. Zhang, *Journal of Power Sources*, **196**(13), 5674 (2011).
45. S. A. Freunberger, Y. Chen, Z. Peng, J. M. Griffin, L. J. Hardwick, F. Bardé, P. Novák, and P. G. Bruce, *Journal of the American Chemical Society*, **133**(20), 8040 (2011).
46. B. D. McCloskey, A. Speidel, R. Scheffler, D. C. Miller, V. Viswanathan, J. S. Hummelshøj, J. K. Nørskov, and A. C. Luntz, *The Journal of Physical Chemistry Letters*, **3**(8), 997 (2012).
47. B. M. Gallant, R. R. Mitchell, D. G. Kwabi, J. Zhou, L. Zuin, C. V. Thompson, and Y. Shao-Horn, *The Journal of Physical Chemistry C*, **116**(39), 20800 (2012).
48. S. Meini, M. Piana, N. Tsiouvaras, H. Beyer, and H. A. Gasteiger, manuscript in preparation.
49. J. R. Harding, Y.-C. Lu, Y. Tsukada, and Y. Shao-Horn, *Physical Chemistry Chemical Physics*, **14**(30), 10540 (2012).
50. R. Sharabi, E. Markevich, V. Borgel, G. Salitra, D. Aurbach, G. Semrau, M. A. Schmidt, N. Schall, and C. Stinner, *Electrochemistry Communications*, **13**(8), 800 (2011).

4.2 Rechargeability of Li-Air Cathodes Pre-Filled with Discharge Products Using an Ether Based Electrolyte Solution

The paper entitled "Rechargeability of Li-air cathodes pre-filled with discharge products using an ether based electrolyte solution: implications for cycle-life of Li-air cells" is reported in this section. The electrooxidation of several possible discharge products, namely Li_2O_2, LiOH, Li_2CO_3 and Li_2O was investigated by charging model carbon electrodes *pre-filled* with those commercially available compounds. Those electrodes were galvanostatically charged and characterized by XRD or IR spectroscopy at different state of charge (SOC), in order to understand to which extent those products can be removed by electrooxidation and thus the electrodes can be recharged. Furthermore, the gases evolved upon charging were quantitatively determined by On-line Electrochemical Mass Spectrometry (OEMS).

Li_2O_2 electrodes charged galvanostatically provided a characteristic cell voltage profile with a defined electrooxidation plateau at $\approx 4.1\ V_{Li}$ and a defined end of charge. O_2 was the only gas evolved until the theoretical capacity of the electrode for the expected reaction $Li_2O_2 \rightarrow O_2 + 2\ e^-$ is reached. At that point, substantial amounts of CO_2 were detected, suggesting a parasitic reaction of Li_2O_2, mild oxidant, with the carbon electrode [58-60] (Section 4.3). Despite some degree of irreversibility, Li-air electrodes containing only Li_2O_2 are rechargeable.

On the other hand, electrooxidation of LiOH and Li_2CO_3 (proposed as possible discharge products when a H_2O and CO_2 contaminated O_2 feed is used) was possible on non-catalyzed carbon at high potentials ($>4.8\ V_{Li}$), however at the expense of electrolyte solution's stability (no O_2 was evolved as it would be expected). XRD studies at different state of charge revealed that Li_2O cannot be electrooxidized on carbon surfaces, however charge of Pt-catalyzed Li_2O electrode is feasible. Similarly to LiOH and Li_2CO_3 electrodes, the process is highly irreversible and no O_2 is evolved.

Those results have the implication that Li_2O_2 can be the only acceptable discharge product of rechargeable, non-aqueous Li-air batteries. As other products do not evolve O_2, the drop of O_2 evolution upon cycling discussed in the previous section can be explained by the accumulation of those in the electrode matrix, leading to capacity fading and cell failure.

Rechargeability of Li-air Cathodes Pre-Filled with Discharge Products Using and Ether Based Electrolyte Solution: Implications for Cycle-Life of Li-air Cells

S. Meini, N. Tsiouvaras, K.U. Schwenke, M. Piana, H. Beyer, L. Lange,

and H.A. Gasteiger

Physical Chemistry Chemical Physics, 2013, DOI: 10.1039/c3cp51112j

Permanent weblink:

http://dx.doi.org/10.1039/c3cp51112j

Reproduced by permission of Royal Society of Chemistry

PCCP

RSCPublishing

PAPER

View Article Online
View Journal

Cite this: DOI: 10.1039/c3cp51112j

Rechargeability of Li–air cathodes pre-filled with discharge products using an ether-based electrolyte solution: implications for cycle-life of Li–air cells†

Stefano Meini, Nikolaos Tsiouvaras,* K. Uta Schwenke, Michele Piana, Hans Beyer, Lukas Lange and Hubert A. Gasteiger

Received 13th March 2013,
Accepted 9th May 2013

DOI: 10.1039/c3cp51112j

www.rsc.org/pccp

The instability of currently used electrolyte solutions and of the carbon support during charge–discharge in non-aqueous lithium–oxygen cells can lead to discharge products other than the desired Li_2O_2, such as Li_2CO_3, which is believed to reduce cycle-life. Similarly, discharge in an O_2 atmosphere which contains H_2O and CO_2 impurities would lead to LiOH and Li_2CO_3 discharge products. In this work we therefore investigate the rechargeability of model cathodes pre-filled with four possible Li–air cell discharge products, namely Li_2O_2, Li_2CO_3, LiOH, and Li_2O. Using Online Electrochemical Mass Spectrometry (OEMS), we determined the charge voltages and the gases evolved upon charge of pre-filled electrodes, thus determining the reversibility of the formation/electrooxidation reactions. We show that Li_2O_2 is the only reversible discharge product in ether-based electrolyte solutions, and that the formation of Li_2CO_3, LiOH, or Li_2O is either irreversible and/or reacts with the electrolyte solution or the carbon during its oxidation.

1. Introduction

Li–air battery technology promises to overcome the limitations of the state-of-the-art storage systems for automotive applications.[1] Due to their ≈4-fold higher theoretical specific energy compared to Lithium ion batteries (LiBs) based on $LiMO_2$ (M = Mn, Ni, Co) intercalation materials,[2] non-aqueous Li–air technology could allow the full electrification of the vehicular fleet, considered to be a promising path for drastically reducing CO_2 emissions from fossil fuel combustion.

Unfortunately, Li–air cells still suffer from poor round-trip efficiency and poor rate capability;[3–6] furthermore, many of the commonly used non-aqueous electrolyte solutions react with superoxide radical ($O_2^{-\bullet}$) intermediates produced during the oxygen reduction reaction (ORR),[7–9] so that the charge–discharge behavior of Li–O_2 cells is strongly influenced by the choice of electrolyte solution.[9] For example, alkyl carbonate blends were shown to be unstable in the presence of ORR intermediates,[8–13] leading to cell failure due to the irreversible formation of decomposition products (*e.g.*, Li_2CO_3 and Li-alkyl carbonates) that, unlike the desired Li_2O_2, can be oxidized only at very high potentials.[8] Since glymes are very stable in the presence of superoxide radicals,[11,12,14–16] they have been studied extensively as Li–air battery electrolyte solutions in recent years.[9,17–19] In these electrolyte solutions, Li_2O_2 was determined to be the predominant discharge product using a variety of characterization techniques,[8,9,20,21] but after several charge–discharge cycles, the Li_2O_2 fraction in the electrode was found to decrease.[17,20,22] The gradual formation of discharge products other than Li_2O_2 was recently suggested to be due to the reactivity of the carbon materials commonly used for Li–air electrodes,[23–25] and to the instability of ether solvents.[17,18,20,23,26,27] In a recent report by Thotiyl *et al.*, Li–O_2 cell cycling using ^{13}C-labeled electrodes allowed the distinction between degradation of the carbon or of the solvent. Severe carbon corrosion leading to Li_2CO_3 was observed only during charge above 3.5 V_{Li} and on the other hand, solvent degradation was observed during both discharge and charge.[28] Both processes are responsible for the accumulation of Li_2CO_3 upon cycling.

Thermodynamically, the electrochemical reaction between Li and O_2 can lead to Li_2O_2 and Li_2O (Table 1, reactions (1) and (2)). However, Li–air battery operation in H_2O and CO_2 contaminated oxygen (*e.g.*, atmospheric air contains H_2O (up to ≈3%) and CO_2 (≈400 ppm), would thermodynamically favor LiOH and Li_2CO_3 formation (see Table 1 for the thermodynamics of the different possible reactions during discharge and charge).

Institute of Technical Electrochemistry, Technische Universität München, Lichtenbergstr. 4, 22 D-85748, Garching, Germany.
E-mail: nikos.tsiouvaras@tum.de

† Electronic supplementary information (ESI) available. See DOI: 10.1039/c3cp51112j

Table 1 Gibbs free energy (standard conditions), reversible potential, and theoretical capacity of electrochemical and chemical reactions expected upon discharge and recharge of a *Li–air* device, assuming no parasitic reactions involving electrolyte solution or electrode materials take place. The theoretical capacity values are calculated assuming material/carbon weight ratios of 1/1. The theoretical capacity for Li_2O_2 electrooxidation is calculated considering that the as received active material is guaranteed as 90% pure (technical grade)

No	Possible discharge reactions	ΔG°/ kJ mol^{-1}	E_{rev}/ V_{Li}	Capacity/ mA h g_{carbon}^{-1}
1	$2Li^+ + 2e^- + O_2 \rightarrow Li_2O_2$	−570.2	2.96	1168
2	$4Li^+ + 4e^- + O_2 \rightarrow 2Li_2O$	−561.2	2.91	1794
3	$4Li^+ + 4e^- + 2H_2O_{(vap)} + O_2 \rightarrow 4LiOH$	−654.4	3.39	2238
4	$4Li^+ + 4e^- + O_2 + 2CO_2 \rightarrow 2Li_2CO_3$	−737.7	3.82	718
5	$Li_2O + H_2O_{(vap)} \rightarrow 2LiOH$	−93.2	—	—
6	$2LiOH + CO_2 \rightarrow Li_2CO_3 + H_2O$	−83.3	—	—
7	$2Li_2O_2 + 2H_2O_{(vap)} \rightarrow 4LiOH + O_2$	−168.3	—	—

No	Possible charging reactions	ΔG°/ kJ mol^{-1}	E_{rev}/ V_{Li}	Capacity/ mA h g_{carbon}^{-1}
8	$Li_2O_2 \rightarrow 2Li^+ + O_2 + 2e^-$	570.2	2.96	1051
9	$2Li_2CO_3 \rightarrow 4Li^+ + 2CO_2 + O_2 + 4e^-$	737.7	3.82	718
10	$4LiOH \rightarrow 4Li^+ + O_2 + 2H_2O_{(vap)} + 4e^-$	654.4	3.39	2238
11	$2LiOH \rightarrow 2Li^+ + O_2 + 2H^+ + 4e^-$	883.0	4.57	2238
12	$LiOH \rightarrow Li^+ + {}^\bullet OH + e^-$	425.7	4.41[a]	1119
13	$2Li_2O \rightarrow 4Li^+ + O_2 + 4e^-$	561.2	2.91	1794

[a] ΔG_f value of the $^\bullet$OH radical refers to the gas phase.[32] All other thermodynamic data were extracted from ref. 33. For more details on the thermodynamic calculations, refer to the supporting information of our previous work (ref. 25).

Water was demonstrated to be a strong capacity enhancer for Li–air batteries in our previous work.[29]

The reproducibly higher discharge voltage of a $Li–O_2$ cell operated with water contaminated oxygen suggested the electrochemical formation of LiOH rather than Li_2O_2 as a discharge product, consistent with the higher reversible potential of the former process (Table 1, reactions (3) and (1)). Similarly, Takechi *et al.*[30] and Gowda *et al.*[31] demonstrated that Li_2CO_3 is indeed formed during discharge products in CO_2 contaminated oxygen. In addition to the formation of discharge products other than Li_2O_2 caused by impurities in the oxygen feed, the above discussed reactivity of the carbon support and of the electrolyte solution during charging will likely lead to the accumulation of discharge products other than Li_2O_2 upon cycling. Therefore, the rechargeability of a Li–air cell will depend on whether Li_2O_2, Li_2O, Li_2CO_3, and LiOH can be reversibly electrooxidized to Li, O_2, CO_2, and H_2O (reactions (8)–(13) in Table 1) within the operating potential window of a Li–air cathode.

Model electrodes assembled in the discharged state, *i.e.*, pre-filled with a defined discharge product were shown to be useful tools for investigating the basic principles of rechargeability and catalysis in Li–air battery research. Lu *et al.*[34] and recently Harding *et al.*[35] performed basic studies on the Li_2O_2 decomposition kinetics in non-catalyzed and noble metal catalyzed carbon cathodes, demonstrating the effectiveness of Au and Pt as catalysts for Li_2O_2 electrochemical decomposition in non-aqueous electrolyte solution. Giordani *et al.* determined the oxygen evolution activity for carbon and transition-metal catalysts, out of which α-MnO_2 showed the highest activity and dramatically lowered ($\approx$0.7 V) the charging potential of a Li_2O_2 pre-filled electrode at 70 mA g_{carbon}^{-1}.[36] DEMS studies carried out by Xu *et al.* confirmed O_2 as the main gas evolved during the charge of a Fe_2O_3 catalyzed Li_2O_2 electrode,[37] as expected from reaction (8) (see Table 1) and as was observed in our own work.[25]

The chargeability of lithium (alkyl)carbonate pre-filled electrodes was first studied by Freunberger *et al.*, who observed the electrochemical decomposition of those compounds at potentials near $\approx$4.0 V_{Li} in α-MnO_2 nanowire catalyzed carbon electrodes.[8] In their work, α-MnO_2 showed interesting catalytic activity for Li_2CO_3 decomposition, whereas non-catalyzed carbon electrodes[38] or Fe_2O_3-catalyzed carbon electrodes[36] had a very low activity for the oxidation of Li_2CO_3 in pre-filled electrodes. As expected from Table 1, reaction (9), CO_2 was the main gas being evolved during the anodic oxidation of lithium (alkyl)carbonates; however, in contrast to reaction (9), no evolved O_2 could be detected, which was hypothesized to be due to the reaction of oxygen evolution reaction (OER) intermediates with the electrolyte solution.[8,36,38]

Despite the variety of studies on Li_2O_2, not many reports examined the rechargeability of LiOH, Li_2CO_3, and Li_2O pre-filled electrodes; the latter possible discharge product was recently claimed on platinum electrodes.[39] McCloskey *et al.* reported on potential scans of Li_2O and Li_2CO_3 electrodes in a DME-based electrolyte solution, detecting at potentials $\geq$4.6 V_{Li} H_2 and CO_2 as main gaseous products evolved respectively.[38]

Most of the literature studies using pre-filled electrodes, except the recent paper by Harding *et al.* who used Lithion® binder,[35] are based on the poly vinylidene difluoride (PVdF) binder and NMP solvent, but as reported by Xu *et al.*,[40] PVdF and NMP react with Li_2O and LiOH and, to a lesser degree even with Li_2O_2 during electrode preparation (*e.g.*, PVdF is dehydrofluorinated through a mechanism analogous to that reported for the reaction of PVdF and NaOH by Wootthikanokkhan and Changsuwan[41]). Nonetheless, Xu *et al.* carried out galvanostatic charge experiments on Li_2O pre-filled electrodes (Fe_2O_3 catalyzed) in alkyl carbonate electrolyte solutions; although the measurements were unfortunately compromised by the corrosion of the cathode current collector, no O_2 was detected using on-line mass spectrometry during charging to 4.5 V_{Li}.[37] Similarly, no oxygen evolution was observed from Li_2O pre-filled electrodes when charged to 5.0 V_{Li} in dimethoxy ethane (DME) based electrolyte solutions.[9]

Further investigations on Li_2O and LiOH electrooxidation therefore require alternative electrode preparation procedures in order to exclude parasitic reactions with the electrode binder and the solvent used for electrode preparation. In particular, alternatives to NMP–PVdF should (i) be resilient to the attack of strong bases such as LiOH and Li_2O and (ii) properly wet and disperse the carbon matrix. Unfortunately, alcohol-based solutions of Li^+-exchanged Nafion® (*i.e.*, Lithion®) used in our previous work are also not suitable due to their typically relatively high water content ($\approx$1%). In this work, we chose polyethylene oxide (PEO) and toluene as an alternative binder–solvent pair, since neither ethers like PEO nor hydrocarbons such as toluene are attacked by strong bases like LiOH and Li_2O, thereby preserving the integrity/purity of both compounds during electrode preparation.

The aim of this work is to examine the rechargeability of Li–air cathodes when, due to contaminations and/or parasitic reactions, Li_2O_2 is not the only discharge product. To pursue that objective, model electrodes pre-filled with Li_2O_2, Li_2CO_3, LiOH, and Li_2O were prepared using the PEO binder dissolved in toluene. The compositional integrity of the as-prepared pre-filled electrodes was verified using thermogravimetric analysis coupled with mass spectrometry (TGA-MS), X-ray diffraction (XRD), and Fourier transform infrared spectroscopy (FTIR). Subsequently, the rechargeability of pre-filled non-catalyzed electrodes in a diglyme-based non-aqueous electrolyte solution was studied using an on-line electrochemical mass spectrometry (OEMS) system,[17] supported by *ex situ* XRD and FTIR analysis. Furthermore, we investigated the influence of a platinum catalyst on the electrooxidation processes during the charging of pre-filled electrodes, which was particularly striking in the case of Li_2O. We believe that the data reported in this paper will serve as a useful tool for further understanding rechargeability issues and cycle-life limitations of non-aqueous Li–air batteries.

2. Experimental

2.1. Electrode preparation

Li_2O_2 powder (Aldrich, 90%) was used as received with no further milling/grinding due to its low particle size ($\approx$1 μm). Vulcan carbon (VC) electrodes pre-filled with Li_2O_2 (Li_2O_2/VC) look uniform, and the salt is barely distinguishable from the carbon support. On the other hand, Li_2CO_3 (Aldrich, 99% purity), LiOH (Aldrich, 98% purity), and Li_2O (Aldrich, 97%) powders are composed of $\approx$100–200 μm large particles, therefore we reduced their particle size by ball-milling prior to electrode preparation. After ball-milling it was possible to obtain a uniform distribution of all active materials in the electrode matrix; only $\approx$1 μm particles are observed by SEM in the final coatings (agglomerates >1 μm are mostly dispersed during sonication, see Fig. S1, ESI†). PEO-bonded non-catalyzed Li_2O_2 and Li_2CO_3 electrodes with a binder/carbon ratio of 0.2/1 g/g were prepared by coating an ink composed of a 1/1 g/g mixture of each lithium compound and Vulcan XC72 carbon (VC), of toluene (Aldrich, 99.5%, <1 ppm water), and of PEO (Aldrich, M_w = 400 000 g mol^{-1}) onto a Celgard® C480 separator. The same procedure was used for Li_2O and LiOH electrodes, but the binder/carbon ratio was reduced to 0.1/1 g/g due to strong agglomeration during ink preparation. The Pt-catalyzed electrodes were prepared using a similar procedure, adjusting the amount of catalyst (Pt/VC, 37% Pt on Vulcan XC72, Tanaka, Japan) to maintain the same active material/carbon ratio as in the non-catalyzed pre-filled electrodes and using a 0.3/1 g/g binder/carbon ratio. The compositions of all the electrodes prepared in this study are summarized in Table 2.

The inks were prepared using the following procedure: 1/1 wt mixtures of carbon (or Pt/VC equivalent to get a 1/1 active material/carbon ratio) and each lithium compound (mixed by hand in a mortar for 15 min) were added to a PEO–toluene solution, and sonicated under an Ar atmosphere for 10 minutes using a Branson 250 digital probe-sonifier. The ink was coated in an Ar-filled glove box (O_2 < 1 ppm, H_2O < 1 ppm; Jacomex, France) onto a Celgard® C480 separator using a Mayer-Rod. After evaporation of the solvent at room temperature in the glove-box, 15 mm diameter cathode electrodes were punched out. The electrodes were dried under dynamic vacuum overnight at 50 °C in a glass oven (Büchi, Switzerland) prior to cell assembly. During the entire electrode preparation process, any exposure to ambient air was carefully avoided.

Table 2 Target composition and measured carbon loadings of all electrodes used in this work. The abbreviations VC and Pt/VC stand for Vulcan XC72 carbon and 37 wt% Pt/Vulcan XC72, respectively

Electrode	Catalyst/support	Target composition/% (C/cat/Li-compound/PEO)	Carbon loading/mg cm^{-2}
VC	Vulcan XC72	83/0/0/17	0.38
Li_2O_2/VC	Vulcan XC72	45/0/45/10	0.39
Li_2CO_3/VC	Vulcan XC72	45/0/45/10	0.39
LiOH/VC	Vulcan XC72	47/0/47/6	0.38
Li_2O/VC	Vulcan XC72	47/0/47/6	0.38
Pt/VC	37.5% Pt/Vulcan XC72	51/34/0/15	0.41
Li_2O_2/Pt	37.5% Pt/Vulcan XC72	34/22/34/10	0.30
Li_2CO_3/Pt	37.5% Pt/Vulcan XC72	34/22/34/10	0.51
LiOH/Pt	37.5% Pt/Vulcan XC72	34/22/34/10	0.57
Li_2O/Pt	37.5% Pt/Vulcan XC72	34/22/34/10	0.47

2.2. X-ray diffraction (XRD) analysis

X-ray powder diffraction data of the electrode coatings and of the Li_2O pre-filled electrodes were collected using a Stadi MP diffractometer (STOE, Germany) equipped with a one dimensional silicon strip detector Mythen 1K (Dectris, Switzerland) and monochromatized Mo(Kα_1) radiation (λ = 0.7093 Å, 50 kV, 40 mA) in Debye–Scherrer or transmission geometry. The silicon strip detector allowed to simultaneously collect data in an angle range of 18.84° 2θ and the high energy Mo(Kα_1) X-ray radiation roughly halved the values of the 2θ reflection positions compared with the commonly used Cu(Kα_1) radiation; the combination of these two features allowed us to collect the most intense part of the diffraction patterns in stationary mode (*i.e.*, without moving the detector or the sample), avoiding the loss of data-collection time due to goniometer movement, thereby maximizing the signal to noise/ratio. The detector was centered for Li_2O samples at 20.395° 2θ (getting a 2θ range between 10.975° and 29.815° with a step of 0.015°) and for all the other samples at 18.455° 2θ (getting a 2θ range between 9.035° and 27.875° with a step of 0.015°); if not specified otherwise, the data-collection times were 15 minutes, 40 minutes or 2 hours, depending on the type of sample used.

For as-prepared pre-filled electrodes, XRD patterns were collected for 40 minutes in Debye–Scherrer geometry by scratching the electrodes off the Celgard® separator, transferring them into a 0.7 mm diameter glass capillary for XRD, and sealing the capillary (all done in an Ar-filled glove-box). This method allowed us to enormously improve the signal/noise ratio of the diffracted beam and to avoid any possible reaction between the lithium oxides or hydroxides and the ambient atmosphere (see Fig. 4).

Regarding the direct analysis of the Li_2O pre-filled electrodes before and after charge, the above glass-capillary technique cannot be applied, since scratching-off electrode coatings from a used electrode and transferring it into the capillary is very difficult and introduces the risk of contamination. On the other hand, using electrodes supported on the Celgard® separator in an XRD transmission cell is difficult due to the low amount of active material loading (0.38–0.57 mg cm^{-2}, see Table 2) and due to the high reactivity of LiOH and Li_2O with CO_2 and water vapor in ambient air. This is illustrated by the XRD patterns collected on a Li_2O pre-filled electrode for 15, 30, and 80 minutes, using a standard sample holder for transmission (STOE, Germany), where a single electrode was sandwiched between two 10 μm thick cellulose acetate foils. The results, shown in Fig. 1a, demonstrate that Li_2O reacts very quickly to form monohydrated LiOH with water permeating from the ambient through the cellulose acetate foils: both Li_2O and $LiOH{\cdot}H_2O$ have their main reflection peak at 15.3° 2θ, and its increase in intensity from 15 to 80 min evidences the increased amount of diffracting atoms due to reaction and incorporation of water into the structure; in addition, a new reflection for $LiOH{\cdot}H_2O$ appears at $\approx$16.8° 2θ after 30 min, increasing after 80 min of exposure of the sample holder to ambient air. The permeation of water through the cellulose acetate film is due to the high water permeability of the cellulose acetate foils (>4000 × 10^{-13} cm^3_{STP} cm cm^{-2} s^{-1} Pa^{-1} at 25 °C[42]). Indeed, when the cellulose acetate foils are replaced with 15 μm thick aluminum foils (practically impermeable to gases), the diffusion of water into the electrode and its subsequent reaction with Li_2O is much decreased (see Fig. 1b). In this case, the formation of LiOH is still observed by its main reflection at $\approx$14.8° 2θ for acquisition times of >2 hours, which is due to the diffusion of water from the edge of the foil to the electrode.

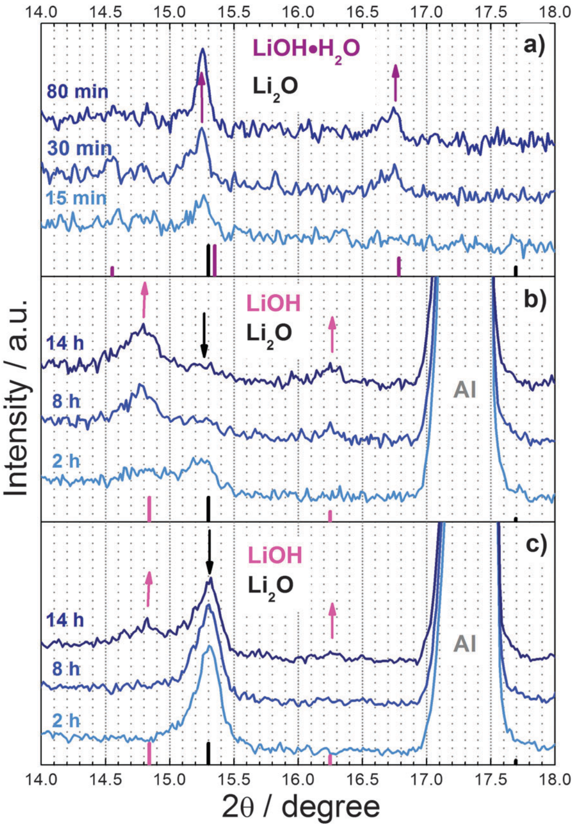

Fig. 1 X-ray diffraction patterns collected in stationary mode on the Celgard®-supported Li_2O/VC pre-filled electrode after various times of exposure to an ambient atmosphere. (a) Electrode placed between two 10 μm cellulose acetate foils in a standard sample holder for transmission (15 min data acquisition); (b) electrode placed between two 15 μm Al foils in the same sample holder (2 hours data acquisition); (c) electrode cut into four pieces, stacked on top of each other between two 15 μm Al foils PTFE gasket sealed sample holder (2 hours data acquisition). The strong reflection between 17 and 17.7° 2θ in (b) and (c) is due to the Al foils. The expected reflections from the ICDD database for Li_2O (PDF 12-0254), $LiOH{\cdot}H_2O$ (PDF 25-0486) and LiOH (PDF 85-1064) are indicated by the ticks on the *x*-axis.

To overcome this problem, we designed a custom-made sample holder using a thin PTFE gasket between the Al foils of the transmission cell to improve the sealing; in addition, in order to increase the signal-to-noise ratio, we also cut the electrode into four pieces which we then stacked inside the transmission cell sample holder. The resulting diffraction patterns are shown in Fig. 1c, demonstrating not only the expected four-fold increase of the signal-to-noise ratio (compare the patterns after 2 h acquisition time in Fig. 1b and c), but also the excellent sealing of the cell, which prevents the intrusion of water from the ambient for more than 8 hours (LiOH formation becomes only detectable after 14 h). This XRD transmission cell design and this measurement methodology were used to collect *ex situ* data for the Li_2O pre-filled electrodes after charging in a Li–O_2 cell (see Fig. 9c and 13c).

2.3. Thermal analysis (TA)

Quantitative analysis of electrode compositions is crucial to verify the preservation of lithium compounds during the electrode preparation process. Simultaneous thermogravimetric (TGA) and calorimetric (DSC) analyses of final electrode coatings were performed on a Mettler Toledo TGA/DSC 1 instrument coupled to a Pfeiffer Vacuum Thermostar Mass Spectrometer for evolved gas analyses (EGA). Electrode samples for TA were obtained by scraping pre-filled electrode coatings off the support followed by grinding the mixtures in a mortar for 5 minutes. All samples were prepared in an Ar-filled glovebox and directly transferred to the TA furnace in covered sapphire crucibles. After sample insertion, the furnace was purged with Ar at 120 mL min^{-1} for 10 min at 25 °C to minimize trace amounts of ambient air during measurements. Subsequently, the samples were heated from 25 °C to 925 °C at 10 K min^{-1} in Ar (60 mL min^{-1}) and then held at 925 °C in 67 vol% O_2/Ar for 60 min in order to combust the organic components (Vulcan XC72 and PEO). Under these conditions, only Li_2O and the Pt-catalyst are left as residues, and the original electrode composition can be back calculated from the total weight loss. Reference measurements of pure Li compounds or mixed with carbon are reported and extensively discussed in our previous work.[25]

2.4. FTIR-ATR analysis

Li_2CO_3 and LiOH electrodes at different state-of-charge (SOC) were analyzed using an FTIR spectrometer (Perkin–Elmer Spectrum Two) equipped with a MIRacle germanium ATR (Pike Technologies) and housed in an argon glove box. Li_2CO_3 is characterized by its asymmetric stretching ($\approx$1450 cm^{-1}) and out-of-plane bending ($\approx$850 cm^{-1}) vibrations; LiOH can be characterized by its O–H stretching ($\approx$3700 cm^{-1}) vibration (Fig. 2). Li_2CO_3 and LiOH electrodes were studied at different state-of-charge, namely 0% (referred to as "2 h OCV", whereby electrodes were built into an electrochemical cell and disassembled after a 2 h rest at OCV), 50%, and 100% charged, in order to monitor the electrooxidation of the active materials. After charging to the desired SOC, electrochemical cells were disassembled, and the cathodes were dried overnight at 40 °C in a glass oven under dynamic vacuum.

Fig. 2 shows the IR spectra of electrodes immersed in electrolyte solution (0.2 M LiTFSI in diglyme) and dried overnight; since the new absorptions between 1300 and 1000 cm^{-1} due to LiTFSI do not superimpose with Li_2CO_3 and LiOH signals, no further handling of the electrodes was performed (*i.e.*, electrodes were not washed with solvents). All spectra obtained using that procedure are normalized to the TFSI anion absorption band at 1200 cm^{-1}.

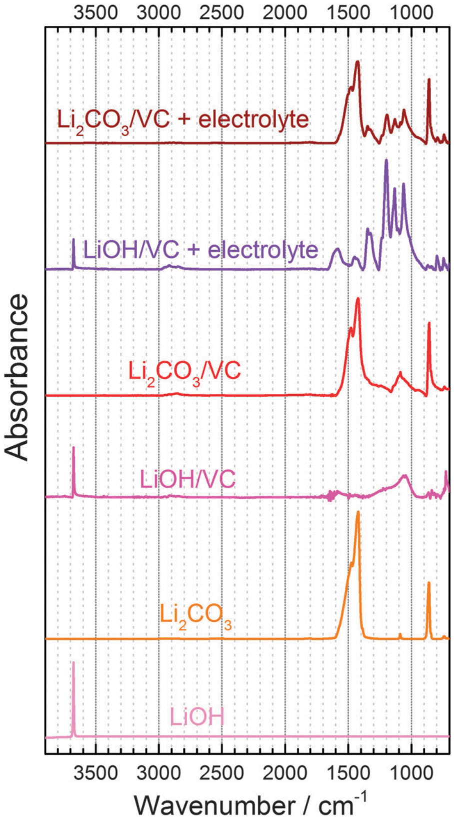

Fig. 2 FTIR-ATR spectra from bottom to top of: (i) LiOH (light magenta line) and Li_2CO_3 (orange line); (ii) PEO-bonded LiOH/VC electrode (magenta line) and PEO-bonded Li_2CO_3/VC electrode (red line); (iii) LiOH/VC electrode (violet line) and Li_2CO_3/VC electrode (wine line) both after immersion in a 0.2 M LiTFSI in diglyme electrolyte solution followed by vacuum drying overnight at 40 °C (these are used as reference for all other FTIR-ATR measurements).

2.5. Electrochemical measurements

0.2 M LiTFSI in diglyme was used as non-aqueous electrolyte solution. LiTFSI (Aldrich, 99.95% metal basis) was vacuum dried at 150 °C for 24 hours before use. Anhydrous diglyme (Aldrich, $\geq$99%) was stored for at least 24 hours over Sylobead MS 564C zeolites (3 Å, Grace Division) before use. The water content of the final electrolyte solution was below 8 ppm (Karl Fischer titration).

The electrochemical cell design was extensively discussed in our previous work[29] and it consists of a 316Ti SS anode current collector and a cathode stainless steel mesh current collector separated by a Kel-F spacer. The sealing of the system is ensured by two Teflon O-rings, and the contact between cell components is made by a 316 SS compression spring. For on-line mass spectrometry measurements, the cells were equipped with a capillary leak to the mass spectrometer.[17]

A 17 mm ∅ lithium disk (0.45 μm thick, 99.9%; Chemetall, Germany) is placed onto the anode current collector, wetted with 40 μL of electrolyte solution, and covered with two Celgard® C480 separators. The cathode is placed onto the separators before and after dropping 40 μL of electrolyte solution and then covered with a 21 mm ∅ stainless steel (316 SS) mesh (0.22 mm ∅ wire, 1.0 mm openings, Spörl KG, Germany) cathode current collector. The cell is sealed with four screws at a torque of 6 N m.

The anodic stability of the electrolyte solution was tested by applying a series of 30 min long potential steps from OCV ($\approx$3 V_{Li}) to 5.5 V_{Li} in 0.1 V increments using Vulcan (VC) and Pt/Vulcan (Pt/VC) electrodes without active material in an Ar atmosphere using a Bio-Logic VMP3 multipotentiostat. The mean of the 10 last current values at the end of each potential step were normalized to the mass of carbon and plotted in Fig. 3a. Additional background experiments were performed by galvanostatically charging VC and Pt/VC electrodes (no active material) at the same rate which was used for OEMS studies (*i.e.*, at 120 mA $g_{carbon}{}^{-1}$; see Fig. 3b).

The gases evolved upon charging of all pre-filled electrodes were analyzed using an on-line mass spectrometer.[17] It consists of a Pfeiffer Vacuum QMA 410 mass spectrometer connected to the closed electrochemical cell through a calibrated capillary leak with a leak rate of approximately 1 μL min^{-1}, and allows the detection of masses between 1 and 128 amu. To quantify gas evolution rates, a calibration gas with oxygen and carbon dioxide in argon was used (2000 ppm each; Westfalen AG, Germany), allowing to convert the mass spectrometer signals into concentrations (note that the relevant m/z ratio for each compound was referenced to the m/z = 36 argon isotope signal to minimize the effect of minor variations in cell and mass spectrometer base pressure). The time derivatives of the gas concentrations then yield the molar gas evolution rates (in [nmol s^{-1}]). Particularly when predominantly one gas species is produced at a given time, the interpretation of the data is more straightforward if the molar evolution rates are converted to current-normalized gas evolution rates (in [μmol A^{-1} s^{-1}]),

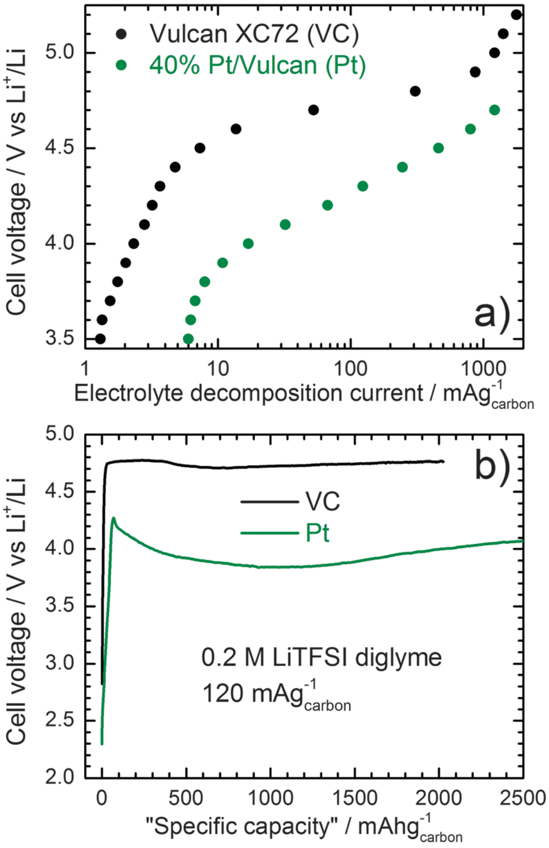

Fig. 3 (a) Anodic stability of 0.2 M LiTFSI in diglyme *versus* potential on Vulcan (PEO-bonded VC electrode, 0.38 mg_{carbon} cm^{-2}, black dots) and Pt/VC (PEO-bonded Pt/VC electrode, 0.41 mg_{carbon} cm^{-2}, green dots), obtained by measuring the current at the end of 30 minute long potential steps. (b) Background of a galvanostatic charge at 120 mA g_{carbon}^{-1} for both Vulcan (VC, 80.7 μA, black line) and Pt (Pt/VC, 87.1 μA, green line) PEO-bonded electrodes (no active material) using 0.2 M LiTFSI in diglyme. While the *x*-axis is simply a time axis (120 mA h $g_{carbon}^{-1} \equiv 1$ hour), it is expressed in terms of "specific capacity" in order to allow better comparison with the other galvanostatic charging curves reported in this work.

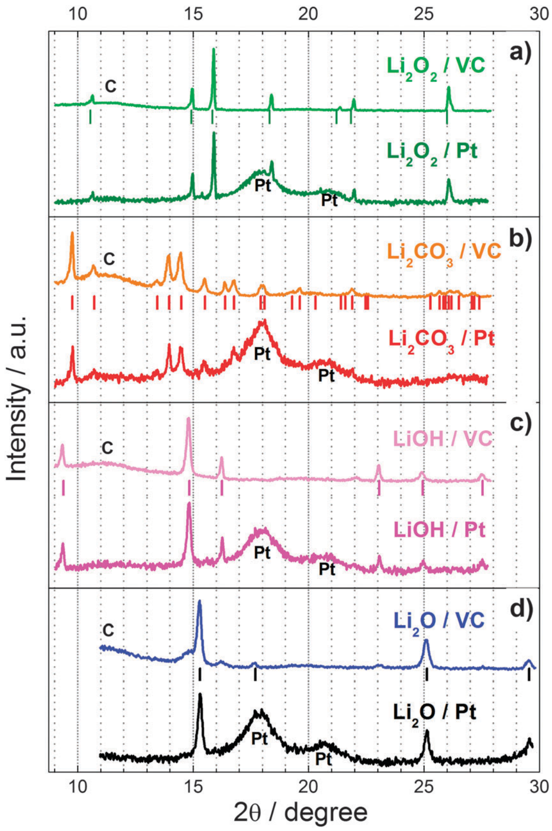

Fig. 4 X-ray diffraction patterns of final PEO-bonded non-catalyzed and Pt-catalyzed pre-filled electrodes using 0.7 mm diameter glass capillaries as sample holders. The expected reflections from the ICDD database are shown by the ticks between the two data of each compound (a: Li_2O_2, PDF 73–1640; b: Li_2CO_3, PDF 22–1141; c: LiOH, PDF 85–1064; d: Li_2O, PDF 12–0254). The broad reflections centered at $2\theta \approx 18°$ and $2\theta \approx 21°$ observed for all catalyzed samples are due to the Pt nanoparticles of the catalyst, while the broad reflection at about 11.5° 2θ is due to the carbon support.

since a 2-electron oxidation process (*e.g.*, the oxidation of Li_2O_2 to O_2 and 2 Li^+) would correspond to a rate of 5.18 μmol A^{-1} s^{-1}, independent of the applied current (equating to $(2F)^{-1}$, where F is the Faraday constant (96 485 A s mol^{-1}).

3. Results and discussion

3.1. Characterization of pre-filled electrodes

In order to assure that the lithium compounds for pre-filled electrodes have not undergone reaction during the electrode processing steps (*e.g.*, Li_2O tends to become LiOH very quickly if exposed to traces of water), we will first examine the as-prepared pre-filled electrodes by XRD and TGA-MS. Fig. 4 shows the XRD patterns of all as-prepared pre-filled electrode coatings, both catalyzed with platinum and non-catalyzed.

Besides the broad diffraction signals of Pt nanoparticles centered at $2\theta \approx 18°$ and $\approx 21°$ observed for catalyzed electrodes, each coating provides the characteristic pattern of the different active materials (see the ticks between the non-catalyzed and Pt-catalyzed data in Fig. 4a–d), demonstrating that our novel electrode preparation method for pre-filled electrodes indeed enables to preserve the integrity of all active materials. Only in the case of Li_2O pre-filled electrodes, the presence of LiOH contamination is observed (indicated by the small shoulder at $2\theta = 14.82°$ as well as the weak reflections at $2\theta = 16.25°$ and 23.06°). Regardless of its origin, the quantity of the LiOH contamination in Li_2O must be determined in order to understand whether it might impact the charging studies with Li_2O pre-filled electrodes.

The total amount of active materials in the pre-filled electrodes can be determined by TGA-MS analysis as was outlined in detail in our previous work.[25] We will briefly illustrate the basic principles of this method by discussing the TGA-MS analysis data for a non-catalyzed and a Pt catalyzed Li_2O pre-filled electrode shown in Fig. 5. Increasing the temperature of a non-catalyzed Li_2O pre-filled electrode under argon, the first observed process is the thermal decomposition of the binder (starting at ≈300 °C), producing H_2O which subsequently converts Li_2O into LiOH. The latter then reacts with carbon between 400 and 600 °C, leading to the formation of Li_2CO_3, which decomposes above 600 °C by reacting with the carbon

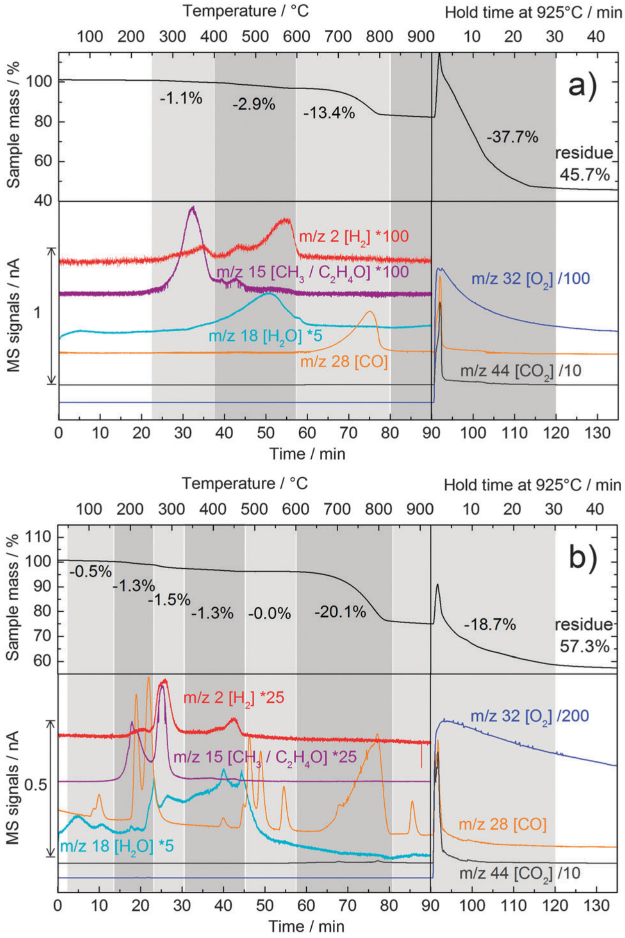

Fig. 5 TGA-MS analysis of as-prepared pre-filled electrode coatings: (a) PEO-bonded Li_2O/VC coating and (b) PEO-bonded Li_2O/Pt coating. The coatings are scraped off the Celgard® support in an Ar-filled glovebox and introduced in the TGA furnace within sapphire crucibles. After a linear temperature scan at 10 K min^{-1} up to 925 °C in an Ar atmosphere, the gas is switched to 67 vol% O_2 in Ar and the temperature is held at 925 °C to combust all organic components, leaving a residue of Li_2O and Pt.

support into Li_2O and CO (for a detailed discussion see ref. 25). Once a temperature of 925 °C is reached, the gas atmosphere is switched from argon to a mixture of 67 vol% O_2 in Ar, which leads to the combustion of all organic species and of the carbon support, leaving Li_2O as the only residue, so that its weight fraction in the as-prepared pre-filled electrode can be determined. The already complex reaction sequence for a non-catalyzed Li_2O pre-filled electrode becomes more complicated when Pt is added as an electrocatalyst (see MS traces in Fig. 5b). Nevertheless, the final decomposition residues at the end of the above described TGA program is always Li_2O (residue) plus platinum in the case when Pt-catalyzed pre-filled electrodes were used.

Since, analogous to Li_2O, all the other active materials (*i.e.*, Li_2CO_3, LiOH, Li_2O_2) convert into Li_2O at the end of the above TGA program, a match between the theoretical and the measured Li_2O residue (plus Pt in the case of catalyzed electrodes) provides an indication about the integrity of the active material after the whole electrode preparation procedure.

Table 3 Theoretical and measured Li_2O (+Pt) residues for as-prepared electrode coatings obtained by TGA-MS analysis. The active material/carbon weight ratio in the pre-filled electrodes is calculated assuming that the chemical composition of the active material in the as-prepared electrode was unchanged during the electrode preparation process. Pt-catalyzed Li_2O_2 electrodes violently decompose at $T > 250$ °C, making it impossible to obtain a reliable residue value

Electrode	Theoretical residue (Pt + Li_2O)/%	Measured residue/%	Active material/ carbon weight ratio from measured residue/g/g
Li_2O_2/VC	29.2	30.5	0.99
Li_2CO_3/VC	18.2	19.1	1.07
LiOH/VC	29.3	30.9	1.07
Li_2O/VC	47.0	45.7	0.95
Li_2O_2/Pt	44.1	N.D.	N.D.
Li_2CO_3/Pt	35.8	36.8	1.31
LiOH/Pt	43.2	45.9	1.35
Li_2O/Pt	56.0	57.3	1.05

If the residue mass deviates significantly from that calculated for the design composition (active material to carbon weight ratio of 1 g/1 g), the chemical nature of the active material must have been changed during the electrode preparation process. For example, a lighter than expected residue for Li_2O_2, LiOH, and Li_2O electrodes would indicate a reaction with H_2O/CO_2 during electrode preparation. A comparison of theoretical *vs.* measured residues is given in Table 3, together with a calculated active material to carbon weight ratio assuming that no reaction had taken place during electrode preparation.

The calculated active material to carbon weight ratios for non-catalyzed pre-filled electrodes (see right-hand-side of Table 3) are within ±10% of the target value, which validates our electrode preparation process. In the case of Pt catalyzed electrodes the deviation is somewhat larger, but this is likely related to the oxidation of the Pt nanoparticles to PtO_2 at the end of the TGA program. The lighter than expected residue of Li_2O/VC ($\approx -1.3\%$) confirms the XRD results, suggesting that Li_2O/VC electrodes are slightly contaminated with LiOH. However, that deviation corresponds to only ≈2–2.5% of LiOH in the final electrode, *i.e.*, ≤5% if normalized to the active material mass. Considering that Li_2O employed in this work was 97% pure (see Experimental section), the impurity mostly being LiOH,[25] the added contamination is negligible, and in fact the back-calculated Li_2O/carbon ratio of 0.95 (Table 3) matches the theoretical value of 1. In general, both TGA and XRD confirm that the integrity of even the most reactive Li compounds is indeed preserved during the whole electrode preparation and characterization processes.

3.2. OEMS analysis of non-catalyzed pre-filled electrodes

3.2.1. Charge of the Li_2O_2/VC electrode. Fig. 6 shows the galvanostatic charge of a non-catalyzed Li_2O_2/VC electrode coupled with evolved gas analysis by OEMS.

At first the charge process starts with a high potential peak at ≈4.65 V_{Li} (first 100 mA h $g_{carbon}{}^{-1}$). This phenomenon was already shown in a recent publication by Harding *et al.*,[35] but it has no unambiguous explanation yet. The authors hypothesize a surface coating of LiOH (detected by XRD[35]) on Li_2O_2 particles that must be removed (*i.e.* oxidized) before Li_2O_2 oxidation can

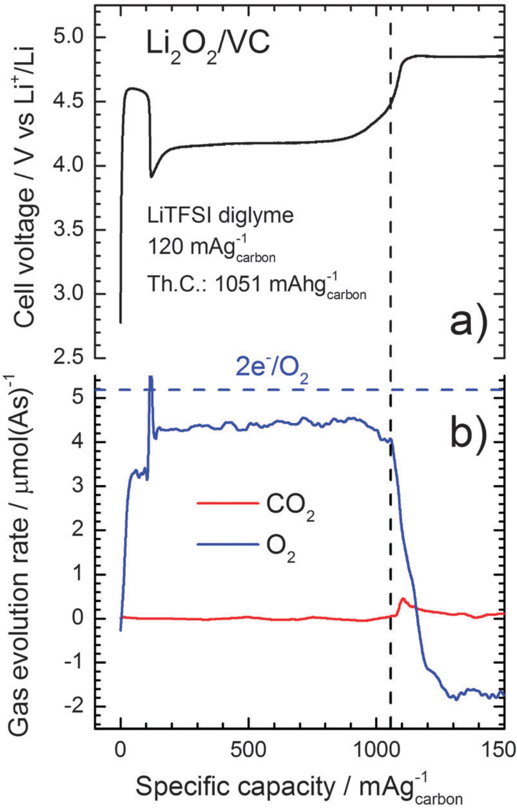

Fig. 6 (a) Galvanostatic charge of non-catalyzed the Li_2O_2 pre-filled electrode (0.39 mg_{carbon} cm^{-2}) at 120 mA $g_{carbon}{}^{-1}$ (corresponding to 82.8 μA) using 0.2 M LiTFSI in diglyme, and (b) gas evolution rates for CO_2 and O_2 (O_2 only gas expected from Li_2O_2 electrooxidation: no other gas but CO_2 was detected in significant amounts). The black dotted line indicates the specific capacity of 1051 mA h $g_{carbon}{}^{-1}$ for the expected reaction $Li_2O_2 \rightarrow 2\ Li^+ + O_2 + 2e^-$, whereas the blue dotted line indicates the expected evolution rate corresponding to $2e^-/O_2$.

start. Thermal analysis performed in our lab on Li_2O_2 indeed revealed LiOH and Li_2CO_3 as impurity in the as-received batch, comprising ≈5% of the total Li_2O_2 mass.[25] This hypothesis is apparently confirmed by the much lower oxygen evolution rate observed in the high voltage region, very close to the $4e^-/O_2$ line (a $4e^-/O_2$ process is expected for LiOH electrooxidation, see reactions (10) and (11) in Table 2): we will discuss that more in detail after the charge of LiOH is presented. The remaining part of the charge of a Li_2O_2 electrode is performed at ≈4.15 V_{Li}, whereby O_2 is the only gas evolved in agreement with reaction (8) in Table 2. Interestingly, also in this region the oxygen evolution rate doesn't fully match with the theoretical value of 2 e^-/O_2, but rather on the order of $2.3e^-/O_2$, as previously shown by McCloskey *et al.* for discharged Li–air electrodes in DME.[22] The electrolyte solution decomposition current at 4.15 V_{Li} for 0.2 M LiTFSI in diglyme lies at ≈3 mA $g_{carbon}{}^{-1}$ (Fig. 3a), ≈2.5% of the 120 mA $g_{carbon}{}^{-1}$ drawn during the charge experiment. Since the deviation in the O_2 evolution rate is more on the order of ≈15% of the theoretical value, electrolyte solution corrosion at high potentials cannot *directly* explain the mismatch between theory and experiments. The integral O_2 evolved through the whole measurement corresponds to 1.06×10^{-5} moles, to be compared with the expected 1.39×10^{-5} moles introduced as Li_2O_2 in the electrochemical cell, corresponding to an O_2 recovery efficiency of 77%. Those values allow us to calculate an *overall* experimental e^-/O_2 value of 2.6 that excellently matches the *overall* value obtained for the charge of discharged carbon cathodes reported in our previous work (also $2.6e^-/O_2$).[17]

If we continue to apply a current after the end of Li_2O_2 electrooxidation (*i.e.* at $C > C_{theor}$), the potential raises up to the electrolyte solution decomposition potential of ≈4.75 V_{Li}, typical for the rate applied (Fig. 3b). After the potential reached that value, a small but significant CO_2 evolution is detected from the electrode, related to the electrooxidation of Li_2CO_3 originating by the reaction of Li_2O_2 with the carbon support at potentials >3.5 V_{Li}.[28] As reported in our previous work,[17] CO_2 is detected at the end of the charge of a previously discharged Li–air cathode also, but in much higher quantities; that is probably due to the much higher contact area between a Li_2O_2 coating on the carbon support.[27]

The strong *negative* O_2 evolution rate, *i.e.* the oxygen *consumption* observed in the whole high potential region at $C > C_{theoretical}$ agrees with the overall e^-/O_2 value higher than the theoretical (2.6 instead of 2.0) value integrated over the entire capacity range $C \leq C_{theoretical}$, and with the actual deviation observed in the low potential region (≈$0.3e^-/O_2$). In fact, an oxygen consumption superimposed to the OER would lead to lower oxygen evolution values, therefore introducing a systematic artifact in all our measurements, in particular for those performed at high potential. The deviation of the experimental O_2 evolution rate from the theoretical value could have in principle three possible explanations, namely; (i) oxygen consumption at the lithium metal anode, (ii) the direct reaction of "nascent oxygen" (*alias* atomic "O") with the carbon support,[25] and (iii) the thermal reaction of molecular oxygen with electrolyte solution fragments (free radicals) produced as a result of electrolyte solution corrosion.[17] On the other hand, the strong oxygen consumption, *after* Li_2O_2 is quantitatively electrooxidized, can be reasonably attributed to the thermal reaction of molecular oxygen with the free radicals produced by electrolyte solution corrosion, and it is in a way potential-dependent. As it will be discussed later, this phenomenon could play a major role in determining the oxygen evolution rate for the other discharge products explored (namely Li_2CO_3, LiOH and Li_2O) since their electrooxidation takes place at cell voltages ≥4.8 V_{Li}, leading to systematic artifacts of the OEMS data regarding O_2 evolution.

3.2.2. Charge of the Li_2CO_3/VC electrode.

Fig. 7 shows the galvanostatic charge of a non-catalyzed Li_2CO_3/VC electrode using an ether-based electrolyte solution.

The development of the cell voltage can be rationalized as three different charging phases. At $0 < C < 400$ mA h $g_{carbon}{}^{-1}$ a plateau at ≈4.8 V_{Li} with a concomitant CO_2 evolution at ≈2 e^-/CO_2 expected for Li_2CO_3 electrooxidation (reaction (9), Table 2) is observed. This is the region where nearly a pure Li_2CO_3 electrooxidation takes place. Comparing the voltages at which Li_2CO_3 and Li_2O_2 electrodes are charged on carbon with the OEMS study of the charge of a discharged Vulcan electrode,[17] it seems reasonable to estimate the overpotential observed for the charge of pre-filled electrodes related to the much higher particle size at ≈0.5 V. In fact, as Li_2O_2/VC electrodes are charged at 4.1–4.2 V_{Li} and the Li_2CO_3/VC electrode charge onset lies at 4.8 V_{Li}, typical features of the charge voltage of a discharged Vulcan electrode are a plateau at 3.6–3.7 V_{Li}, where Li_2O_2 is electrooxidized, and a plateau at ≈4.3 V_{Li}, at which CO_2 evolution starts to take place;[17] thus, the potential difference between *model* and *real* electrodes (*i.e.* the "particle size effect") is ≈0.5 V, and we expect it to be similar for LiOH and Li_2O electrooxidation as well.

At $400 < C < 1500$ mA h g_{carbon}^{-1} the cell voltage raises to ≈5 V_{Li}; in this region the CO_2 evolution rate shows a constant decay. Interestingly, according to the background experiments presented in Fig. 3, the current density that one can sustain on carbon at that potential is on the order of ≈1000 mA g_{carbon}^{-1}, definitely higher than the 120 mA g_{carbon}^{-1} set. Finally, at $C > 1500$ mA h g_{carbon}^{-1}, the cell voltage decays to the value of ≈4.75 V_{Li} typical for the electrolyte solution decomposition potential at the applied rate.

The total CO_2 evolved throughout the charging process is 8.10×10^{-6} moles, to be compared to the 9.23×10^{-6} moles introduced as Li_2CO_3 in the electrochemical cell, corresponding to a ≈88% CO_2 recovery efficiency. Despite the much higher potentials needed for the electrooxidation of Li_2CO_3 in comparison with Li_2O_2 (Fig. 6), thus probably triggering a larger set of parasitic reactions, the recovered CO_2 fraction is always much higher than the recovered O_2 fraction in Li_2O_2 electrodes charging. This is also true for catalyzed electrodes (Fig. 10 and 11), and it seems to come along very well with the different chemical reactivity of those gases (*i.e.* reactivity $O_2 \gg CO_2$, evolved fraction of $O_2 < CO_2$). Based on reaction (9), Table 2, O_2 would also be expected as a gaseous product, however, no O_2 evolution was observed during the whole charging process. Characterization of the electrodes at different state of charge (SOC), namely 0% (OCV), 50% and 100% (wherein the percentages refer to the specific capacity corresponding to the end of CO_2 evolution, Fig. 7b) shows a decay in the intensity of the typical absorption bands of the CO_3^{2-} anion, suggesting that Li_2CO_3 is indeed being consumed, and thus its electrooxidation rather than electrolyte solution decomposition is indeed the origin of the CO_2 detected with the OEMS. Unfortunately the absorbance of CO_3^{2-} bands is not fully proportional to the SOC, possibly due to inhomogeneity of the electrode surface (Fig. S1f, ESI†).

Freunberger *et al.* proposed a mechanistic hypothesis for the "*missing oxygen*", based on several intermediates typical of CO_3^{2-} electrooxidation in aqueous systems. Carbonate (CO_3^{2-}) electrooxidation in aqueous systems on Pt electrodes proceeds through the formation of an intermediate, peroxidicarbonate $C_2O_6^{2-}$, characterized by an O–O bond.[8] In presence of H_2O peroxidicarbonate ions are unstable, thus they are hydrolyzed leading to H_2O_2 and CO_2 ($2e^-/CO_2$). At the potentials where CO_3^{2-} oxidation takes place on Pt surfaces (*i.e.* > 1.6 V_{SCE}), H_2O_2 from peroxidicarbonate hydrolysis is simultaneously electrooxidized to O_2[43] (overall $4e^-/O_2$, $C_2O_6^{2-}$-to-products). In the assumed analogy between aqueous and non-aqueous systems in the paper by Freunberger *et al.* arises a doubt on how from peroxodicarbonate ions, $C_2O_6^{2-}$, one can obtain CO_2, since a hydrolysis step cannot take place in water-free non-aqueous electrolyte solutions. The authors elegantly overcame that by hypothesizing an intermediate electrooxidation step to $C_2O_4^{-\bullet}$, subsequently decomposed to CO_2 and $O_2^{-\bullet}$. Since the experiments were performed in alkyl carbonate-based electrolyte solutions, the missing O_2 evolution was explained with the well characterized reactivity of the superoxide ion radical with the electrolyte solution solvent.[8] However, this explanation cannot be applied to the electrolyte solutions used in this paper, since, as reported in one of our recent publications, glymes were

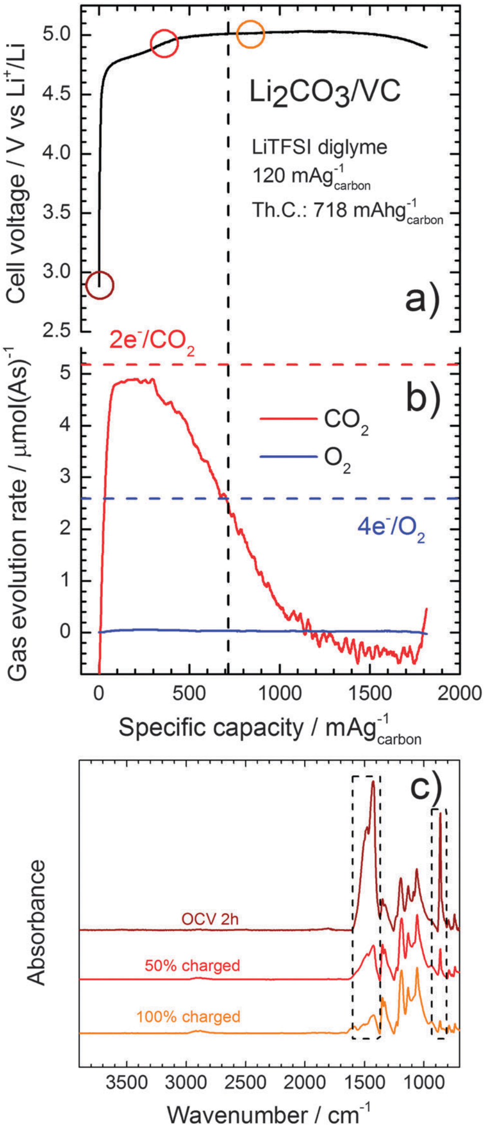

Fig. 7 (a) Galvanostatic charge of the non-catalyzed Li_2CO_3 pre-filled electrode (0.39 mg_{carbon} cm^{-2}) at 120 mA g_{carbon}^{-1} (corresponding to 82.8 μA) using 0.2 M LiTFSI in diglyme, and (b) gas evolution rates for CO_2 and O_2 (expected from Li_2CO_3 electrooxidation: no other gas was detected in significant amounts). The black dotted line indicates the specific capacity of 718 mA h g_{carbon}^{-1} for the expected reaction $2Li_2CO_3 \rightarrow 4Li^+ + 2CO_2 + O_2 + 4e^-$, whereas the red and blue dotted lines indicate the expected evolution rate corresponding to $2e^-/CO_2$ and $4e^-/O_2$ ratios respectively. (c) IR characterization of the cathodes at different state of charge: after 2 h OCV, at 50% and 100% of the theoretical capacity.

demonstrated to be very stable towards superoxide attack.[15] The charging of isotopically labeled Li_2CO_3 (produced by reaction of Li_2O_2 obtained during a Li-O_2 discharge in DME electrolyte solutions with isotopically labeled CO_2) reported in a recent study by Gowda *et al.* also confirms that no O_2 is detected during the electrooxidation of Li_2CO_3 at potentials $\geq 4.5\ V_{Li}$ in DME-based electrolyte solutions.[31]

The complete lack of O_2 evolution could be the result of several mechanisms: (i) if, unlike the aqueous case, recombination into $C_2O_6^{2}$ of CO_3^{2-} was not possible due to the lack of mobility of the latter anion in electrolyte solutions where its solubility is little or none (as in our case), one could expect that electrooxidation proceeds on a single CO_3^{2-} unit, and a "nascent O" unit is involved in parasitic reactions with the carbon support. (ii) If, however, recombination takes place and molecular oxygen is formed, its reactivity with free radicals produced at high potential (please refer to Fig. 7 for $C > C_{theor}$) would result in a continuous O_2 uptake by the electrolyte solvent, and correspondingly no O_2 would be detected in the gas phase. The same interpretation can be applied for all other pre-filled electrodes, in both non-catalyzed and catalyzed forms, reported in the following sections.

3.2.3. Charge of the LiOH/VC electrode. Fig. 8 shows the galvanostatic charge of a non-catalyzed LiOH/VC electrode.

Similar to the Li_2CO_3/VC electrode, the cell voltage remains higher ($\approx 5\ V_{Li}$) than the electrolyte solution decomposition potential during the first ≈ 2000 mA h g_{carbon}^{-1}, about the theoretical capacity expected (reactions (10) and (11) in Table 2, both thermodynamically possible within the potential window explored). Once the theoretical capacity value is reached, a neat decay in cell voltage is observed, after which a relatively constant plateau typical for the electrolyte solution decomposition at the applied current density is reached.

The potential step in the proximity of the theoretical capacity for the expected LiOH electrooxidation reactions seem to serve as indication of the completion of the charge process. In order to confirm that the potential profile observed is somehow related to LiOH electrooxidation and not to parasitic reactions involving the electrolyte solution, IR spectra were registered on different electrodes after 2 h OCV (in a fully assembled electrochemical cell), 50% and 100% of the theoretical capacity (Fig. 8c); the decrease in the O–H stretching absorption at $\approx 3700\ cm^{-1}$ confirms that the potential profile measured is related to LiOH electrooxidation. Another time the total absence of oxygen and other gases raises doubts on the reaction mechanism.

A few paragraphs before we discussed about the possible origins of the high voltage peak with the corresponding $4e^-/O_2$ evolution rate at the beginning of the charge of Li_2O_2/VC electrodes (Fig. 6). Although the oxygen evolution rate would theoretically correspond to LiOH electrooxidation (reactions (10) and (11) in Table 2), hypothesized to be in the form of a coating on the surface of Li_2O_2 particles by Harding *et al.*, the data reported in Fig. 8 seem to exclude it to be the only process in those first 100 mA h g_{carbon}^{-1}. We rather believe that during that period a mixed electrooxidation of solvent/Li_2O_2 or LiOH/Li_2O_2 is taking place, at a reasonable mixed potential value of $\approx 4.65\ V_{Li}$ for both eventual processes. Unfortunately, that question cannot yet be unambiguously answered.

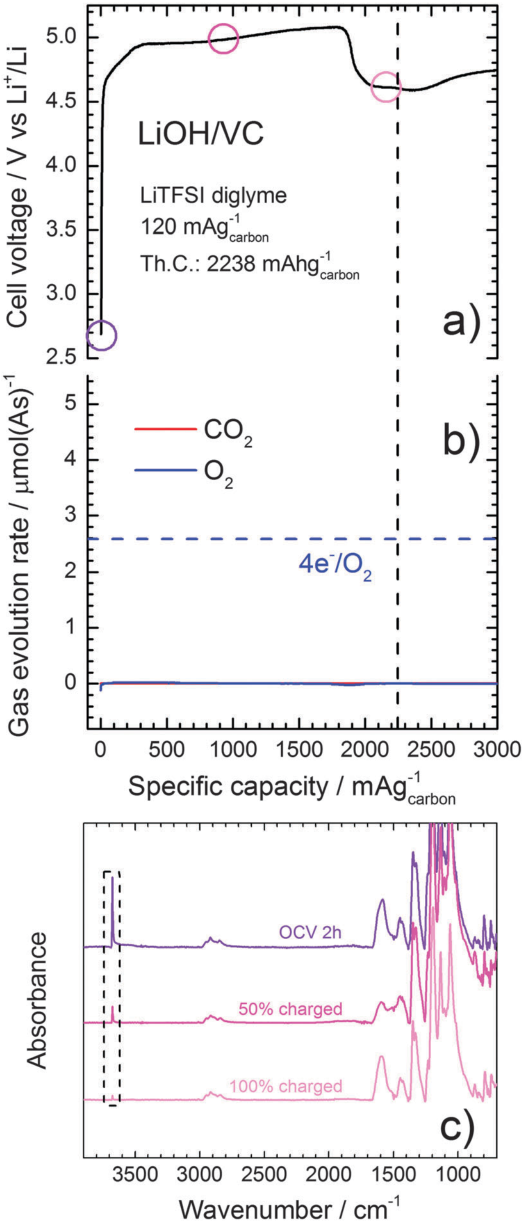

Fig. 8 (a) Galvanostatic charge of the non-catalyzed LiOH pre-filled electrode (0.38 $mg_{carbon}\ cm^{-2}$) at 120 mA g_{carbon}^{-1} (corresponding to 80.7 μA) using 0.2 M LiTFSI in diglyme, and (b) gas evolution rates for O_2 and CO_2 (expected gas from LiOH electrooxidation and common decomposition product respectively: no other gas was detected in significant amounts). The black dotted line indicates the specific capacity of 2238 mA h g_{carbon}^{-1} for the expected reaction $2LiOH \rightarrow 2Li^+ + 2H^+ + O_2 + 4e^-$, whereas the blue dotted line indicates the expected evolution rate corresponding to the $4e^-/O_2$ ratio. (c) IR characterization of the cathodes at different state of charge: after 2 h OCV, at 50% and 100% of the theoretical capacity.

3.2.4 Charge of the Li_2O/VC electrode. Fig. 9 shows the galvanostatic charge of a non-catalyzed Li_2O/VC electrode.

Similar to LiOH, the Li_2O galvanostatic charge also (Fig. 9a) proceeds at cell voltages ($\approx 5\ V_{Li}$) much higher than the electrolyte solution decomposition potential, with the difference that no potential feature (*i.e.* potential steps) indicates the end of charge, thus suggesting that Li_2O cannot be electrooxidized on carbon surfaces. Also in this case, the total absence of O_2 evolution raises doubts on the correct interpretation of the potential profile, thus the characterization of the electrode at different state of charge being mandatory. Since Li_2O doesn't absorb MIR radiation due to the absence of a truly covalent bond in its structure, XRD had to be the technique of choice. Indeed, XRD at different SOC (Fig. 9c) confirms that Li_2O (reflection at $2\theta = 15.3°$) is unchanged after several hours of charging (the difference between the pristine and the charged electrodes can arise from some detaching of the coating from the Celgard® during manipulation). Only a LiOH impurity of the pristine electrode (detected by XRD and TGA as discussed in Section 3.1) (shoulder at $2\theta = 14.82°$) is removed at the end of the galvanostatic process, another time confirming the electroactivity of LiOH on carbon.

3.3 OEMS analysis of Pt-catalyzed pre-filled electrodes

One can summarize the results reported up to now with two main points: (i) the galvanostatic charge of Li_2CO_3, LiOH and Li_2O pre-filled carbon electrodes takes place at very high potentials, definitely higher ($\approx$300 mV) than the electrolyte solution decomposition potential at the same rate. (ii) For the same compounds, *i.e.* for compounds whose oxygen atoms are not bonded in some peroxo-unit (O–O), no molecular O_2 is detected in the headspace upon recharge. As discussed above, a substantial O_2 *consumption* can be observed after the charge of a Li_2O_2/VC is finished and electrolyte solution decomposition takes place at $C > C_{\text{theoretical}}$ (Fig. 6b); under these conditions, a stable O_2 consumption rate of ≈ -2 μmol A^{-1} s^{-1} is observed, corresponding to a substantial ($\approx$40% of the theoretical) O_2 evolution rate of 5.18 μmol A^{-1} s^{-1} (corresponding to $2e^-/O_2$). As reported in our previous work,[25] that O_2 consumption seems to be somehow potential dependent (or rather dependent on the fraction of anodic current that is involved in electrolyte solution corrosion). We therefore believed that an OER catalyst could enhance O–O recombination and substantially lower the charge voltage, thus improving the reversibility and efficiency of the electrooxidation reactions. In the following sections, the galvanostatic charge of Pt-catalyzed pre-filled electrodes will be presented.

Although the role of catalysis in Li–air is nowadays a controversial topic, we decided anyway to investigate the influence of catalysts on the charge performance of pre-filled electrodes. The commercial catalyst 40% Pt on Vulcan XC72 provided by Tanaka appeared to be the right choice, since Pt was/is extensively studied in aqueous systems (*e.g.* PEMFC), and it was demonstrated in several reports to be one of the most active catalyst for Li_2O_2 electrooxidation in non-aqueous systems.[35] Furthermore, we had the hope that a catalyst like Pt could trigger Li_2O electrooxidation also. Finally, the higher oxygen binding energy of Pt compared to that of carbon[44,45] could stabilize reactive oxygen species on its surface, therefore enhancing O–O coupling and O_2 evolution. Unfortunately, Pt also appears to be a fairly good decomposition catalyst for organic electrolyte solutions; in fact, the electrolyte solution decomposition potential for Pt-catalyzed electrodes at 120 mA g_{carbon}^{-1} is $\approx$4 V_{Li}, *i.e.* $\approx$0.7 V lower than on non-catalyzed electrodes (Fig. 3b).

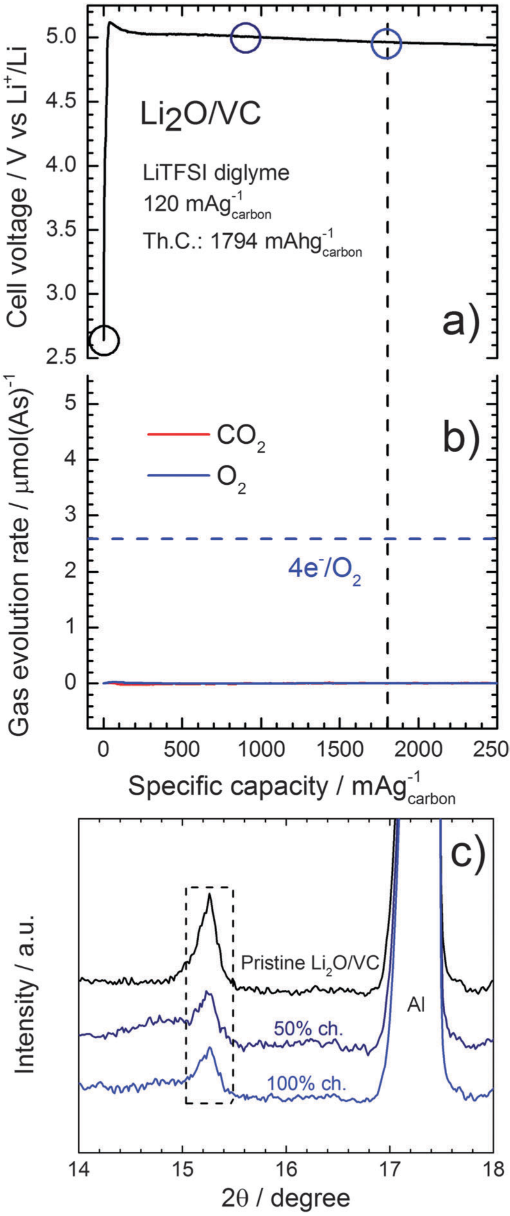

Fig. 9 (a) Galvanostatic charge of the non-catalyzed Li_2O pre-filled electrode (0.38 mg_{carbon} cm^{-2}) at 120 mA g_{carbon}^{-1} (corresponding to 80.7 μA) using 0.2 M LiTFSI in diglyme, and (b) gas evolution rates for O_2 and CO_2 (expected gas from Li_2O electrooxidation and common decomposition product respectively: no other gas was detected in significant amounts). The black dotted line indicates the specific capacity of 1794 mA h g_{carbon}^{-1} for the expected reaction $2Li_2O \rightarrow 4Li^+ + O_2 + 4e^-$, whereas the blue dotted line indicates the expected evolution rate corresponding to the $4e^-/O_2$ ratio. (c) XRD characterization of the cathodes at different state of charge: pristine (0% charged), at 50% and 100% of the theoretical capacity. The dotted rectangles encircle the strongest Li_2O reflection ($2\theta = 15.30°$). The shoulder at $2\theta = 14.82°$ belongs to LiOH, contained as impurity. The strong reflection between 17 and 17.7° 2θ is due to the Al foils used to protect the sample.

3.3.1. Charge of the Li_2O_2/Pt electrode. Fig. 10a shows the galvanostatic charge of a Li_2O_2/Pt catalyzed electrode; similar to the non-catalyzed case, O_2 and CO_2 are evolved substantially during the charge, the latter being observed only at high potentials after O_2 evolution stops. Although the outstanding catalytic activity of Pt on Li_2O_2 electrooxidation reported in the literature[35] doesn't seem to be fully confirmed in our laboratory, a Li_2O_2 electrode can be completely charged at potentials $\leq 4\ V_{Li}$. In comparison to a non-catalyzed electrode, no high potential peak in the first 100 mA h g_{carbon}^{-1} is observed.

The O_2 evolution rate at low potentials (Fig. 10b) shows a stronger deviation ($\approx 30\%$) from the theoretical value than on non-catalyzed electrodes: this corresponds to an integral O_2 evolution of 67% of the expected value (0.74×10^{-5} moles of the 1.12×10^{-5} moles introduced in the cell as Li_2O_2), *alias* 3.0 e^-/O_2. However, the lower O_2 consumption rates at high potentials for $C > C_{theoretical}$, about one half of that observed on carbon, goes in the direction of mitigating the artifact of concurrent oxygen consumption and thus of enhancing the O_2 evolved/consumed ratio also for LiOH and Li_2O electrooxidation reactions: if the consumption of O_2 was indeed the reason for the "*missing oxygen*" from non-catalyzed electrodes, that would allow to detect substantial O_2 evolution on Pt for all other lithium compounds.

The lower O_2 consumption rate at the electrolyte solution decomposition potential on Pt than on carbon could in principle allow us to increase the O_2 evolved/consumed ratio also for the remaining electrooxidation reactions: if the consumption of O_2 was indeed the reason for the "*missing oxygen*" from non-catalyzed electrodes, substantial O_2 evolution on Pt for all other lithium compounds should be detected.

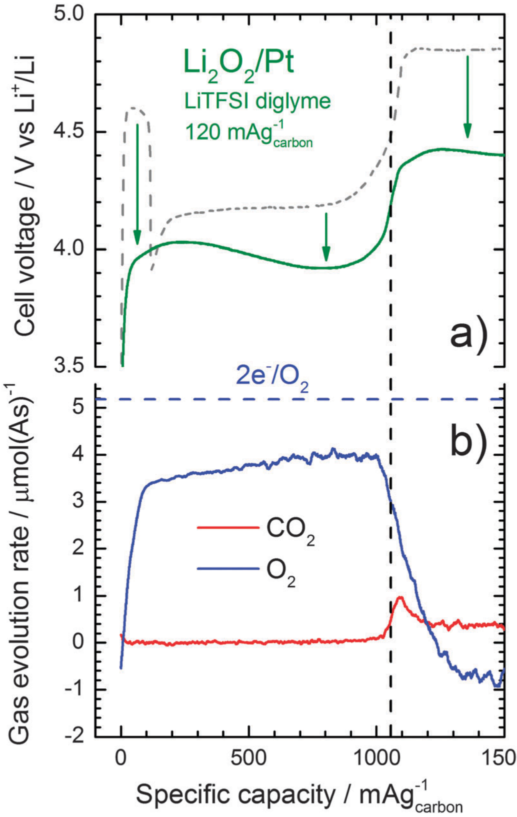

Fig. 10 (a) Galvanostatic charge of the Pt-catalyzed Li_2O_2 pre-filled electrode (0.30 $mg_{carbon}\ cm^{-2}$) at 120 mA g_{carbon}^{-1} (corresponding to 63.7 μA) using 0.2 M LiTFSI in diglyme, and (b) gas evolution rates for CO_2 and O_2 (O_2 only gas expected from Li_2O_2 electrooxidation: no other gas but CO_2 was detected in significant amounts). The black dotted line indicates the specific capacity of 1051 mA h g_{carbon}^{-1} for the expected reaction $Li_2O_2 \rightarrow 2Li^+ + O_2 + 2e^-$, whereas the blue dotted line indicates the expected evolution rate corresponding to $2e^-/O_2$.

3.3.2. Charge of the Li_2CO_3/Pt electrode. The very high voltages needed to electrooxidize Li_2CO_3 on carbon (4.8–5.0 V_{Li}) drop to a nearly constant plateau at $\approx 4.2\ V_{Li}$ on Pt (Fig. 11a), also in this case higher (≈ 0.2 V) than the electrolyte solution decomposition potential at the same rate.

In this respect, Pt doesn't seem to act differently than pure carbon, thus providing similar potential profiles just shifted 0.5–0.7 V down in the potential scale. Interestingly, a potential step indicating end of charge appears this time also for Li_2CO_3 in the proximity of the theoretical capacity. In fact, the potential drop corresponds pretty well to the end of CO_2 evolution from the electrode (Fig. 11b). After the discussed step, further overcharging the electrode determines a cell voltage of $\approx 4\ V_{Li}$, in accord with the electrolyte solution decomposition potential on Pt (Fig. 3b). The constant fading of the strong CO_3^{2-} IR absorption bands at $\approx 1450\ cm^{-1}$ and $\approx 850\ cm^{-1}$ by advancing the state of charge (Fig. 11c) confirms another time that the CO_2 evolution observed is indeed the result of Li_2CO_3 electrooxidation/removal. Despite that the CO_2 recovery efficiency on Pt is even higher than on carbon (1.15×10^{-5} mol/1.23×10^{-5} mol, corresponding to $\approx 94\%$, to be compared to the 88% on carbon, Fig. 7), O_2 evolution is still missing.

3.3.3. Charge of the LiOH/Pt electrode. Fig. 12a shows the galvanostatic charge of a catalyzed LiOH/Pt electrode. Also in this case the charge voltage is drastically lowered by ≈ 1 V to $\leq 4\ V_{Li}$. In analogy with the LiOH/VC electrode, the charge process is characterized by a neat voltage drop, however in this system that potential feature is observed at about one half of the theoretical capacity expected for the possible reactions (reactions (10) and (11) in Table 2). This "alternative" theoretical capacity of LiOH electrodes set by the use of Pt was therefore used as reference for the IR characterization (Fig. 12c), therefore the state of charge was *corrected* on the basis of 1119 mA h g_{carbon}^{-1} considered as "fully charged". The rough inverse proportionality between the absorbance related to the O–H stretching and the *corrected* state of charge (Fig. 13c) confirms that the LiOH electrooxidation reaction on Pt is indeed completed when the voltage drop appears.

What has been discussed until now suggests that the electrooxidation of LiOH on carbon and Pt proceeds over different *intermediates*, wherein on Pt only one electron per OH^- unit is extracted, leading to the formation of highly reactive oxygen species such as •OH adsorbed on the catalyst surface (reaction (12) in Table 2):

$$\mathrm{Pt + LiOH \rightarrow Pt\text{-}(^{\bullet}OH) + Li^+ + 1e^-} \quad C_{theor} = 1119\ \mathrm{mA\ h\ g_{carbon}^{-1}}$$

$$\mathrm{Pt\text{-}(^{\bullet}OH) + Solv. \rightarrow Cat + Oxidized\ Solvent}$$

The higher strength of the Pt–O bond compared to the C–O bond[44,45] should be a substantial driving force for that process to occur. This mechanism is further supported by the substantial amounts of CO_2 detected by OEMS (Fig. 12b), particularly intense between 500 and 1100 mA h g_{carbon}^{-1}, most probably

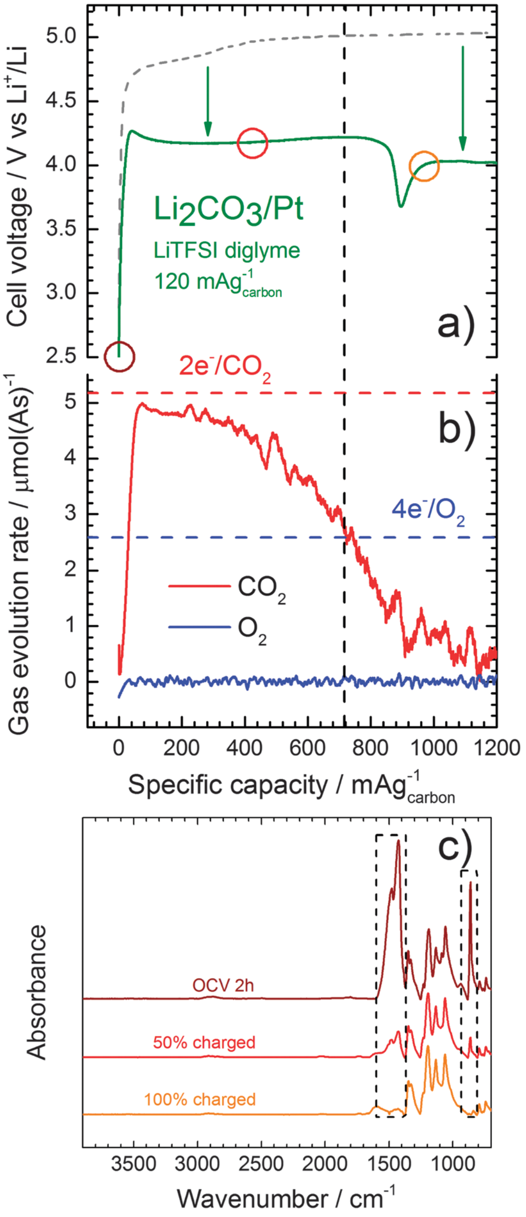

Fig. 11 (a) Galvanostatic charge of the Pt-catalyzed Li_2CO_3 pre-filled electrode (0.51 mg_{carbon} cm^{-2}) at 120 mA $g_{carbon}{}^{-1}$ (corresponding to 108.3 μA) using 0.2 M LiTFSI in diglyme, and (b) gas evolution rates for CO_2 and O_2 (expected from Li_2CO_3 electrooxidation: no other gas was detected in significant amounts). The black dotted line indicates the specific capacity of 718 mA h $g_{carbon}{}^{-1}$ for the expected reaction $2Li_2CO_3 \rightarrow 4Li^+ + 2CO_2 + O_2 + 4e^-$, whereas the red and blue dotted lines indicate the expected evolution rate corresponding to $2e^-/CO_2$ and $4e^-/O_2$ ratios respectively. (c) IR characterization of the cathodes at different state of charge: after 2 h OCV, at 50% and 100% of the theoretical capacity.

related to the *chemical* oxidation of the organic components of the cell (electrolyte solution, carbon) by relatively adsorbed oxygen species (the total absence of O_2 *and* CO_2 during oxidation of LiOH/VC, Li_2O/VC and Li_2O/Pt suggests that the *electrochemical* co-electrooxidation of solvent and carbon proceeds with no concomitant gas evolution).

3.3.4. Charge of the Li_2O/Pt electrode.

Pt shows a strong catalytic activity on the electrooxidation of Li_2O (Fig. 13a).

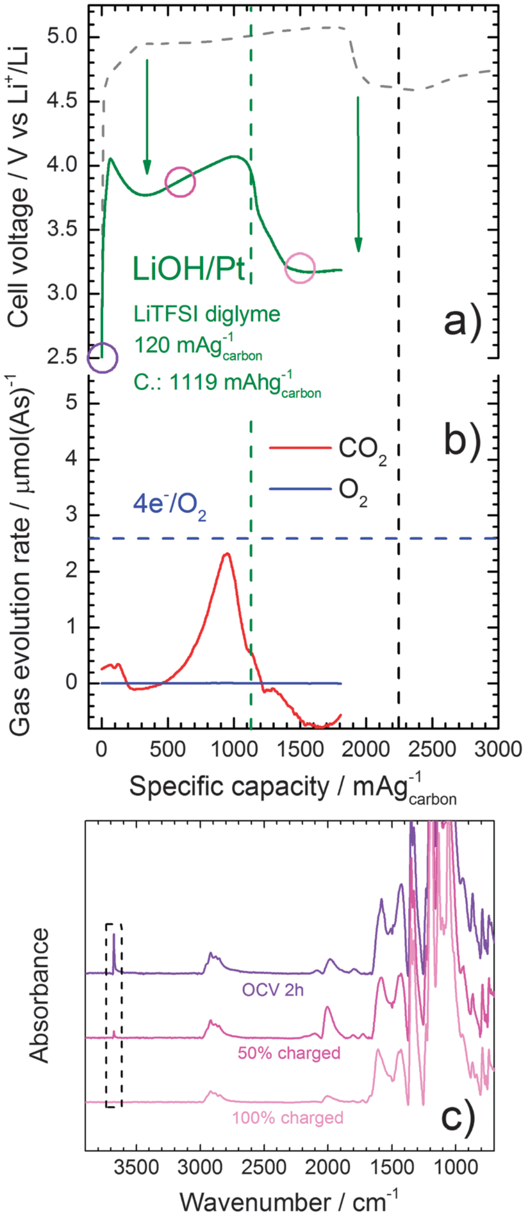

Fig. 12 (a) Galvanostatic charge of the Pt-catalyzed LiOH pre-filled electrode (0.57 mg_{carbon} cm^{-2}) at 120 mA $g_{carbon}{}^{-1}$ (corresponding to 121.1 μA) using 0.2 M LiTFSI in diglyme, and (b) gas evolution rates for O_2 and CO_2 (expected gas from LiOH electrooxidation and common decomposition product respectively: no other gas was detected in significant amounts). The black dotted line indicates the specific capacity of 2238 mA h $g_{carbon}{}^{-1}$ for the expected reaction $2LiOH \rightarrow 2Li^+ + 2H^+ + O_2 + 4e^-$, whereas the blue dotted line indicates the expected evolution rate corresponding to the $4e^-/O_2$ ratio. (c) IR characterization of the cathodes at different state of charge: after 2 h OCV, at 50% and 100% of the theoretical capacity.

Different than for pure carbon, a neat voltage drop of ≈1 V is observed when the theoretical capacity of 1794 mA h $g_{carbon}{}^{-1}$ is reached, similar to what happens with LiOH/VC and LiOH/Pt electrodes. The ability of Pt catalysts to enhance Li_2O electrodes rechargeability is unambiguously confirmed by XRD, showing a fairly good inverse proportionality between Li_2O reflexes intensity ($2\theta = 15.25^\circ$ and $2\theta = 25.16^\circ$) and state of charge (Fig. 13c).

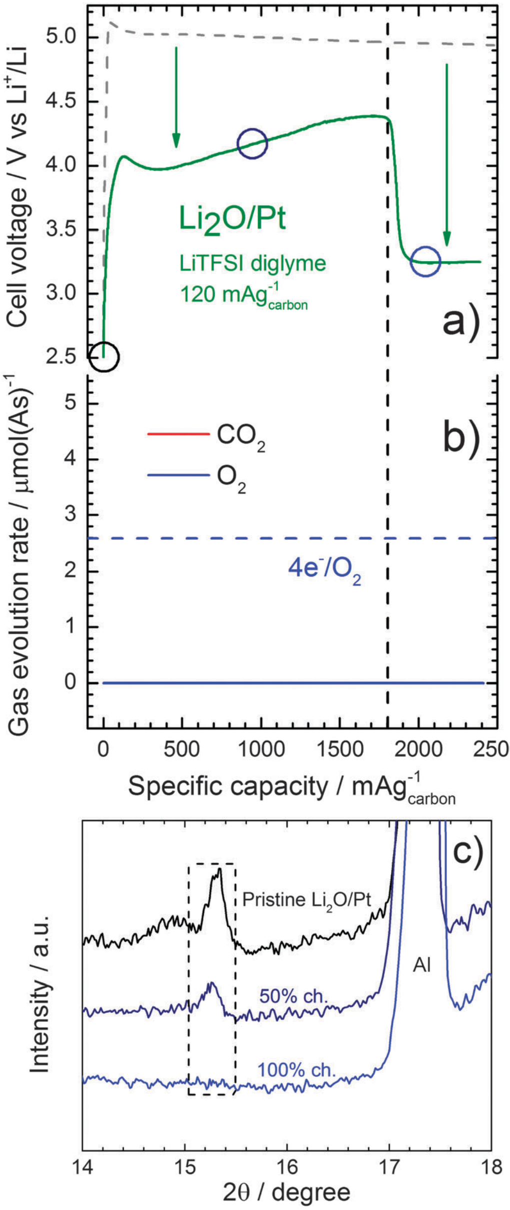

Fig. 13 (a) Galvanostatic charge of the non-catalyzed Li_2O pre-filled electrode (0.47 mg_{carbon} cm^{-2}) at 120 mA g_{carbon}^{-1} (corresponding to 99.8 μA) using 0.2 M LiTFSI in diglyme, and (b) gas evolution rates for O_2 and CO_2 (expected gases from Li_2O electrooxidation and common decomposition product respectively: no other gas was detected in significant amounts). The black dotted line indicates the specific capacity of 1794 mA h g_{carbon}^{-1} for the expected reaction $2Li_2O \rightarrow 4Li^+ + O_2 + 4e^-$, whereas the blue dotted line indicates the expected evolution rate corresponding to the $4e^-/O_2$ ratio. (c) XRD characterization of the cathodes at different state of charge: pristine (0% charged), at 50% and 100% of the theoretical capacity. The dotted rectangles encircle the strongest Li_2O reflection ($2\theta = 15.30°$). The shoulder at $2\theta = 14.82°$ belongs to LiOH, contained as impurity. The strong reflection between 17 and 17.7° 2θ is due to the Al foils used to protect the sample.

However, similar to LiOH, electrooxidation of Li_2O on Pt doesn't lead to recovery of molecular O_2 (Fig. 13b), suggesting another time its involvement in parasitic reactions with the electrolyte solution.

3.3.5. General consideration on the charge of pre-filled electrodes. LiOH/Pt and Li_2O/Pt electrodes are charged with very similar voltage profiles, although the capacities are different and most probably also the reactions, as extensively discussed above. In fact, when overcharged both electrodes exhibit a very low electrolyte solution decomposition potential, ≈1 V lower than the background (Fig. 14b). We believe that during the charging process of LiOH and Li_2O (to a minor extent Li_2CO_3), the *missing oxygen* originally contained on the active material is reacted with the organic electrolyte solution leading to the formation of highly polar decomposition products that can be oxidized at much lower potential than the diglyme molecules on Pt.

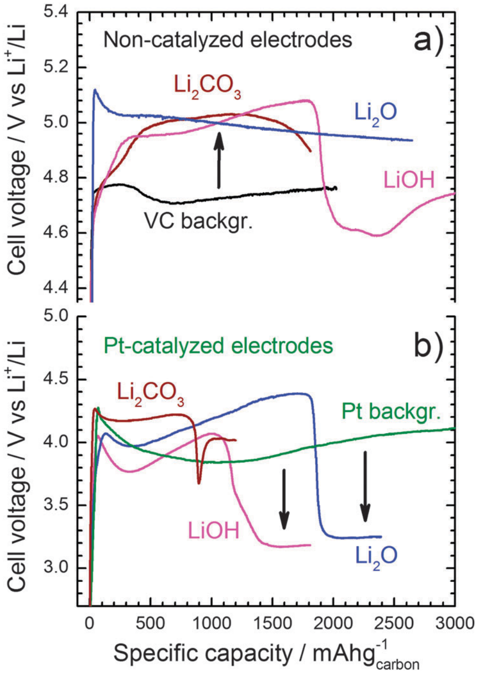

Fig. 14 (a) Comparison between galvanostatic charge profiles at 120 mA g_{carbon}^{-1} of PEO-bonded Li_2CO_3 (wine line), LiOH (magenta line) and Li_2O (blue line) pre-filled electrodes with a Vulcan XC72 (VC) electrode using 0.2 M LiTFSI in diglyme as non-aqueous electrolyte solution (data from Fig. 4b, 8a, 9a, and 10a). (b) Comparison between galvanostatic charge profiles at 120 mA g_{carbon}^{-1} of PEO-bonded, Pt-catalyzed Li_2CO_3 (wine line), LiOH (magenta line), and Li_2O (blue line) pre-filled electrodes with a Pt-catalyzed Vulcan XC72 (Pt) electrode using 0.2 M LiTFSI in diglyme as non-aqueous electrolyte solution (data from Fig. 4b, 12a, 13a, and 14a). (c) Schematic summary of the main reactions taking place at the electrode surface when Li_2O_2, Li_2CO_3, LiOH, or Li_2O are charged in an ether-based electrolyte solution. The carbon cathode is illustrated as black branched particles.

Post-mortem NMR analysis performed on the electrolyte solution after a full charge of LiOH/Pt and Li_2O/Pt did not however reveal significant amounts of any particular degradation product except formates and acetates, common oxidative products of glymes at high potentials in presence of an oxygen source.[15,19] Even IR spectroscopy doesn't reveal any interesting absorption more than already observed in a pristine electrode (PEO as a binder limits the detection polyethers eventually produced as electrolyte solution decomposition products). However, the peculiar low voltage when LiOH/Pt and Li_2O/Pt electrodes are overcharged could also be merely due to the much higher "missing O"/diglyme mole ratio for LiOH and Li_2O cells in comparison to Li_2CO_3 cells ($\gg 2\times$) due to the much higher molecular weight (and thus much fewer moles) of the

Table 4 Mass of active material actually contained in pre-filled electrodes and corresponding ''missing O''/diglyme mole ratio. The amount of diglyme in mol is constant in every cell (120 μL of electrolyte solution are always systematically added to our Li–air cells)

Electrode	Mass of active material in cell/mg	''Missing O''/diglyme ratio/mol%
Li_2CO_3/VC	0.69	1.1
LiOH/VC	0.67	3.3
Li_2O/VC	0.67	2.7
Li_2CO_3/Pt	0.90	1.5
LiOH/Pt	1.01	5.0
Li_2O/Pt	0.83	3.3

latter (Table 4), leading to a higher concentration of decomposition products and thus preferable electrooxidation of those instead of diglyme in the LiOH and Li_2O cases. Unfortunately, a clear answer to that cannot be given yet.

Another interesting common feature of all but Li_2O_2 pre-filled electrodes studied in this work is the charge voltage higher or equal than the electrolyte solution decomposition potential (Fig. 14a and b). A possible reason for that could be the hindered mass-transport of electrolyte solution at the electrode active surface offered by the presence of a non-conductive material (*e.g.* LiOH) in the electrode matrix; that would cause a slower diffusion of electrolyte solution molecules to the carbon active sites, leading to a mixed potential between electrolyte solution decomposition and electrooxidation of the active material and thus to an ''apparent stabilization'' of the non-aqueous electrolyte solution at high potential.

4. Conclusions

In this work we investigated the rechargeability of non-catalyzed and catalyzed Li–air cathodes pre-filled with the possible products arising from a discharge of a Li–air battery performed in H_2O and CO_2 contaminated oxygen, namely Li_2O_2, Li_2CO_3, LiOH and Li_2O. The galvanostatic charge of Li_2O_2 electrodes, both non-catalyzed and catalyzed, with concomitant O_2 evolution suggests that if Li_2O_2 was the only product of a Li–air battery discharge, one could indeed obtain a reversible cycling. The data showed in this paper support the widespread accepted idea that a co-oxidation of the electrolyte solution upon recharge is unavoidable. The irreversible chemistry associated with the charge of Li_2CO_3, LiOH or Li_2O seems to close the door to a full *Li–air* device, *i.e.* operated in *atmospheric air*. On non-catalyzed carbon surfaces, Li_2CO_3 and LiOH could be electrooxidized, although at high potentials, whereas Li_2O is electrochemically active only on catalyzed surfaces like Pt. However, even using Pt as a catalyst, the recovery of the starting reactants (*e.g.* O_2 for Li_2CO_3) seems to be a major challenge. The high potentials needed for the removal of LiOH and Li_2CO_3 and thus their constant accumulation in the cathode matrix, in addition to the parasitic chemistry associated with their electrooxidation, are most probably the reason for the poor rechargeability and cycle-life of Li–air cells, whereby those products could be the result of contaminants produced upon cell cycling (*e.g.* refer to the recent work of Gallant *et al.*, where >100 ppm H_2O was found in a DME electrolyte solution after cycling of a carbon nanotube electrode). Moreover, the results presented in this work suggest that any reaction of Li_2O_2 with the carbon support leading to Li_2CO_3, more than only gradually *consume* the electrode during cycling, will necessarily have consequences on the electrolyte solution stability, since one oxygen unit of the CO_3^{2-} ion is never recovered. Therefore, future Li–air batteries should preferably be engineered as *closed systems*, preferably using cathodes and electrolyte solutions that are stable in contact with and upon oxidation of Li_2O_2, only acceptable discharge product of a non-aqueous Li–air (or rather Li–O_2) battery.

Acknowledgements

Financial support of this research by BASF SE through the framework of its Scientific Network on Electrochemistry and Batteries is gratefully acknowledged by TUM. Dr Arnd Garsuch is gratefully acknowledged for fruitful discussions. The TUM Graduate School (TUM-GS) is gratefully acknowledged by Stefano Meini for scholarly and financial support. Tanaka is gratefully acknowledged for kindly providing carbon materials and catalyst samples. Nikolaos Tsiouvaras gratefully acknowledges the Alexander von Humboldt foundation for financial support.

Notes and references

1 G. Girishkumar, B. D. McCloskey, A. C. Luntz, S. Swanson and W. Wilcke, *J. Phys. Chem. Lett.*, 2010, **1**, 2193–2203.

2 J. Christensen, P. Albertus, R. S. Sanchez-Carrera, T. Lohmann, B. Kozinsky, R. Liedtke, J. Ahmed and A. Kojic, *J. Electrochem. Soc.*, 2012, **159**, R1–R30.

3 K. M. Abraham and Z. Jiang, *J. Electrochem. Soc.*, 1996, **143**, 1–5.

4 S. D. Beattie, D. M. Manolescu and S. L. Blair, *J. Electrochem. Soc.*, 2009, **156**, A44–A47.

5 T. Kuboki, T. Okuyama, T. Ohsaki and N. Takami, *J. Power Sources*, 2005, **146**, 766–769.

6 X.-H. Yang, P. He and Y.-Y. Xia, *Electrochem. Commun.*, 2009, **11**, 1127–1130.

7 F. Mizuno, S. Nakanishi, Y. Kotani, S. Yokoishi and H. Iba, *Electrochemistry*, 2010, **78**, 403–405.

8 S. A. Freunberger, Y. Chen, Z. Peng, J. M. Griffin, L. J. Hardwick, F. Bardé, P. Novàk and P. G. Bruce, *J. Am. Chem. Soc.*, 2011, **133**, 8040–8047.

9 B. D. McCloskey, D. S. Bethune, R. M. Shelby, G. Girishkumar and A. C. Luntz, *J. Phys. Chem. Lett.*, 2011, **2**, 1161–1166.

10 J. Herranz, A. Garsuch and H. A. Gasteiger, *J. Phys. Chem. C*, 2012, **116**, 19084–19094.

11 V. S. Bryantsev, V. Giordani, W. Walker, M. Blanco, S. Zecevic, K. Sasaki, J. Uddin, D. Addison and G. V. Chase, *J. Phys. Chem. A*, 2011, **115**, 12399–12409.

12 D. Aurbach, M. Daroux, P. Faguy and E. Yeager, *J. Electroanal. Chem.*, 1991, **297**, 225–244.

13 F. Mizuno, N. Shinji, K. Yukinari, Y. Shoji and I. Hideki, *Electrochem. Commun.*, 2010, **78**, 403–405.

14 R. Black, S. H. Oh, J.-H. Lee, T. Yin, B. Adams and L. F. Nazar, *J. Am. Chem. Soc.*, 2012, **134**, 2902–2905.

15 K. U. Schwenke, S. Meini, M. Piana, X. Wu and H. A. Gasteiger, *Phys. Chem. Chem. Phys.*, DOI: 10.1039/C3CP51531A.

16 Y.-C. Lu, H. A. Gasteiger and Y. Shao-Horn, *J. Am. Chem. Soc.*, 2011, **133**, 19048–19051.

17 N. Tsiouvaras, S. Meini, I. Buchberger and H. A. Gasteiger, *J. Electrochem. Soc.*, 2013, **160**, A471–A477.

18 R. Black, J.-H. Lee, B. Adams, C. A. Mims and L.F. Nazar, *Angew. Chem., Int. Ed.*, 2012, **51**, 1–6.

19 S. A. Freunberger, Y. Chen, N. E. Drewett, L. J. Hardwick, F. Bardé and P. G. Bruce, *Angew. Chem., Int. Ed.*, 2011, **50**, 1–6.

20 B. M. Gallant, R. R. Mitchell, D. G. Kwabi, J. Zhou, L. Zuin, C. V. Thompson and Y. Shao-Horn, *J. Phys. Chem. C*, 2012, **116**, 20800–20805.

21 Y.-C. Lu, D. G. Kwabi, K. P. C. Yao, J. R. Harding, J. Zhou, J. L. Zuin and Y. Shao-Horn, *Energy Environ. Sci.*, 2011, **4**, 2999–3007.

22 B. D. McCloskey, D. S. Bethune, R. M. Shelby, T. Mori, R. Scheffler, A. Speidel, M. Sherwood and A. C. Luntz, *J. Phys. Chem. Lett.*, 2012, **3**, 3043–3047.

23 B. S. McCloskey, A. Speidel, R. Scheffler, D. C. Miller, V. Viswanathan, J. S. Hummelshoj, J. K. Norskov and A. C. Luntz, *J. Phys. Chem. Lett.*, 2012, **3**, 997–1001.

24 Z. Peng, S. A. Freunberger, Y. Chen and P. G. Bruce, *Science*, 2012, **337**, 563–566.

25 H. Beyer, S. Meini, N. Tsiouvaras, M. Piana and H. A. Gasteiger, *Phys. Chem. Chem. Phys.*, DOI: 10.1039/C3CP51056E.

26 K. R. Ryan, L. Trahey, B. J. Ingram and A. K. Burrell, *J. Phys. Chem. C*, 2012, **116**, 19724–19728.

27 S. Meini, M. Piana, H. Beyer, J. Schwaemmlein and H. A. Gasteiger, *J. Electrochem. Soc.*, 2012, **159**, A2135–A2142.

28 M. M. Ottakam Thotiyl, S. A. Freunberger, Z. Peng and P. G. Bruce, *J. Am. Chem. Soc.*, 2013, **135**, 494–500.

29 S. Meini, M. Piana, N. Tsiouvaras, A. Garsuch and H. A. Gasteiger, *Electrochem. Solid-State Lett.*, 2012, **15**, A45–A48.

30 K. Takechi, T. Shiga and T. Asaoka, *Chem. Commun.*, 2011, **47**, 3463–3465.

31 S. R. Gowda, A. Brunet, G. M. Wallraff and B. D. McCloskey, *J. Phys. Chem. Lett.*, 2013, **4**, 276–279.

32 http://webbook.nist.gov/cgi/cbook.cgi?ID = C3352576&Units = SI.

33 D. R. Lide, *CRC Handbook of Chemistry and Physics*, CRC Press, Boca Raton (FL), USA, 2004, 85th edn, ch. 5, pp. 5–60.

34 Y.-C. Lu, H. A. Gasteiger, M. C. Parent, V. Chiloyan and Y. Shao-Horn, *Electrochem. Solid-State Lett.*, 2010, **13**, A69–A72.

35 J. R. Harding, Y.-C. Lu, Y. Tsukada and Y. Shao-Horn, *Phys. Chem. Chem. Phys.*, 2012, **14**, 10540–10546.

36 V. Giordani, S. A. Freunberger, P. G. Bruce, J.-M. Tarascon and D. Larcher, *Electrochem. Solid-State Lett.*, 2010, **13**, A180–A183.

37 W. Xu, V. V. Viswanathan, D. Wang, S. A. Towne, J. Xiao, Z. Nie, D. Hu and J.-G. Zhang, *J. Power Sources*, 2011, **196**, 3894–3899.

38 B. D. McCloskey, D. S. Bethune, R. M. Shelby, G. Girishkumar and S. C. Luntz, *J. Phys. Chem. Lett.*, 2011, **2**, 1161–1166, supp. info.

39 D. Sharon, V. Etacheri, A. Garsuch, M. Afri, A. A. Frimer and D. Aurbach, *J. Phys. Chem. Lett.*, 2013, **4**, 127–131.

40 W. Xu, K. Xu, V. V. Viswanathan, S. A. Towne, J. S. Hardy, J. Xiao, Z. Nie, D. Hu, D. Wang and J.-G. Zhang, *J. Power Sources*, 2011, **196**, 9631–9639.

41 J. Wootthikanokkhan and P. Changsuwan, *J. Met., Mater. Miner.*, 2008, **18**, 57–62.

42 http://www.goodfellow.com.

43 J. Zhang and C.W. Oloman, *J. Appl. Electrochem.*, 2005, **35**, 945–953.

44 B. Hammer and J. K. Nørskov, *Adv. Catal.*, 2000, **45**, 71.

45 D. C. Sorescu, K. D. Jordan and P. Avoruris, *J. Phys. Chem. B*, 2001, **105**, 11227–11232.

Supplementary Information

for

Rechargeability of Li-air cathodes pre-filled with discharge products using an ether-based electrolyte solution: implications for cycle-life of Li-air cells.

Stefano Meini[a], Nikolaos Tsiouvaras[a]*, K. Uta Schwenke[a], Michele Piana[a], Hans Beyer[a],

Lukas Lange[a] and Hubert A. Gasteiger[a]

[a] *Institute of Technical Electrochemistry, Technische Universität München,*
Lichtenbergstr. 4, 22 D-85748 - Garching - Germany

Ball-milling of active materials powders and SEM investigation of final electrodes (non-catalyzed carbon).

LiOH, Li_2CO_3 and Li_2O powders were ball-milled prior to electrode preparation to reduce particle size. In order to avoid parasitic reactions and thus contamination of the electrodes, LiOH and Li_2O were ball-milled without solvent using 3 mm ∅ ZrO_2 balls at 700 rpm in dry Ar atmosphere for one hour (Pulverisette 7 planetary ball-mill, Fritsch, Germany); the material/balls ratio was always 1/6 g/g. Using this procedure (Figure S1 shows Li_2O and LiOH ball-milled powders), it was indeed possible to obtain a uniform distribution of the active material in the electrode matrix for both LiOH and Li_2O powders and only ≈1 μm particles of LiOH and Li_2O are observed by SEM in the respective electrodes; apparently, agglomerates > 1 μm are mostly dispersed during sonication.

Due to its chemical stability, making parasitic reactions with most solvents highly unlikely, Li_2CO_3 was wet-milled in NMP in order to try to obtain even smaller particles. A 2/3 g/g suspension of Li_2CO_3 in NMP (Aldrich, anhydrous, 99.5 %) was ball-milled for one hour at 700 rpm with 3 mm ∅ diameter ZrO_2 balls. The Li_2CO_3/balls ratio was ≈1/5 g/g. Despite the quite smaller primary particles of wet-milled Li_2CO_3 compared to, for instance, dry milled LiOH (compare Figure S1 e) and g)), agglomeration seems to occur during ink sonication since relatively large agglomerates (up to several micrometer) can be observed in the electrodes by SEM. Nevertheless, the differences in terms of particle size and distribution between Li_2CO_3, LiOH, and Li_2O pre-filled electrodes are relatively minor, and we therefore expect comparable electrical contact between the active materials and the carbon support.

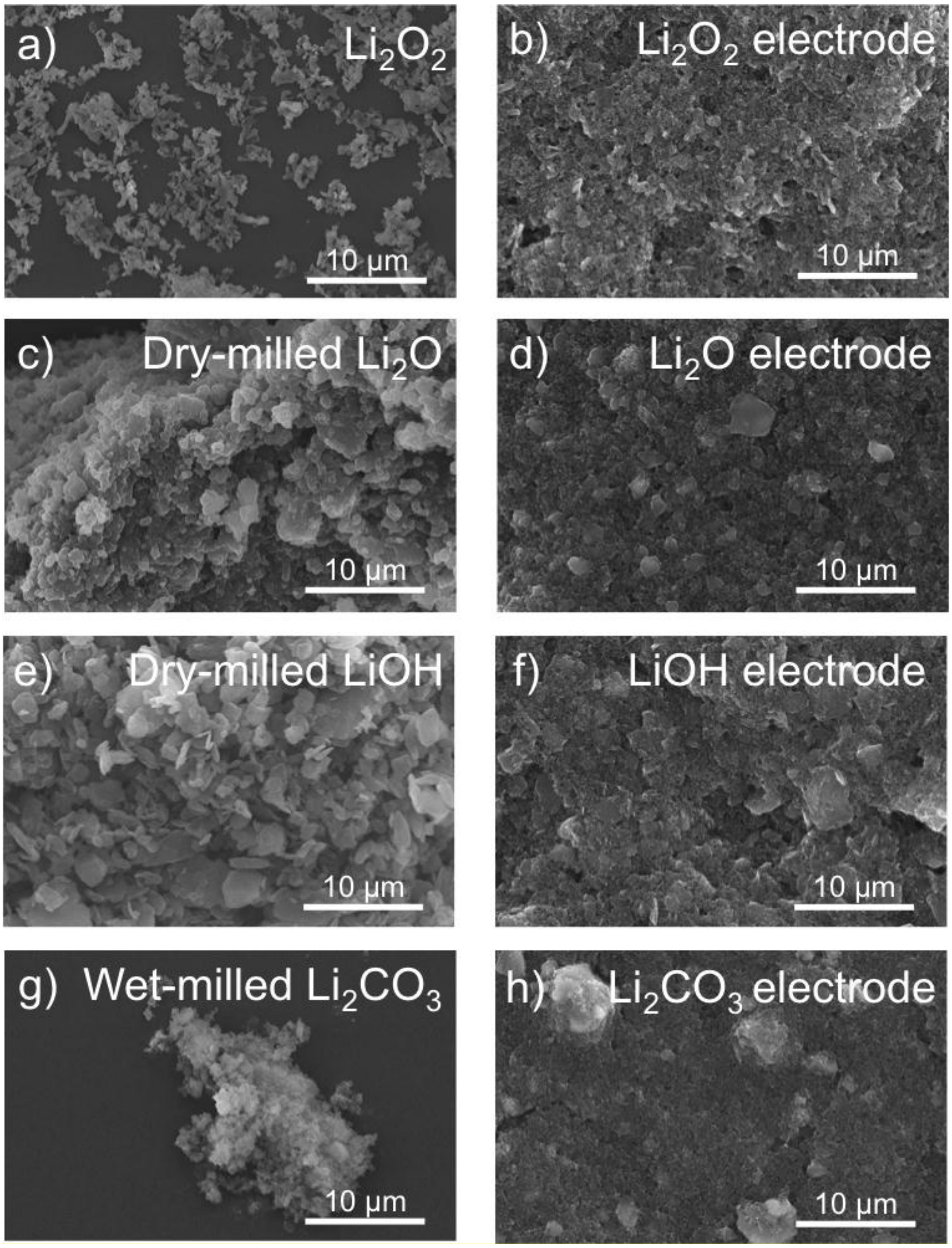
a)
Li_2O_2
10 µm
b)
Li_2O_2 electrode
10 µm
c)
Dry-milled Li_2O
10 µm
d)
Li_2O electrode
10 µm
e)
Dry-milled LiOH
10 µm
f)
LiOH electrode
10 µm
g)
Wet-milled Li_2CO_3
10 µm
h)
Li_2CO_3 electrode
10 µm

Figure S1: SEM micrographs of active material and final pre-filled electrodes based on Vulcan carbon and PEO binder: a) Li_2O_2 as received; b) Li_2O_2 final electrode; c) dry-milled Li_2O sample; d) Li_2O final electrode; e) dry-milled LiOH sample; and, f) LiOH final electrode; g) wet-milled Li_2CO_3 sample; and, h) Li_2CO_3 final electrode

4.3 Thermal and Electrochemical Decomposition of Lithium Peroxide in Non-Catalyzed Carbon Cathodes for Li-Air Batteries

In this paper, the (electro)chemical and thermal reactions of Li_2O_2 with the electrolyte solvent and the air electrode was investigated. The work here presented was edited by Dr. Hans Beyer, and served to get further understanding of the reactivity of electrolyte solution and carbon black with both oxygen and Li_2O_2 via thermo gravimetric analysis (TGA) and On-line Electrochemical Mass Spectrometry (OEMS). The results obtained provided further insight on the rechargeability of Li-air cathodes by identifying the main parasitic reactions and degradation processes.

As previously discussed in Section 4.2, the charge of *pre-filled* Li_2O_2 and discharged electrodes using ether based electrolyte solutions leads to an overall O_2 evolution efficiency lower than 80 %. Those evidences are in agreement with other reports in the literature [73].

Li_2O_2 decomposes into O_2 and Li_2O when heated in a TGA furnace at temperatures >300 °C. When mixed with carbon black in a 1/1 mass ratio, Li_2O_2 thermal decomposition proceeds as a violent reaction in the temperature range 300-400 °C, and CO is the main gas evolved. As reference experiments performed in 67% vol. O_2/Ar atmosphere revealed, the combustion of carbon black (the only source of C) with dioxygen O_2 is not possible at temperature <600 °C; for that reason, our data suggest that Li_2O_2 thermal decomposition proceeds via a "nascent oxygen" (or atomic O) intermediate, known to be strongly reactive with carbon materials, leading to CO evolution before recombination into O_2 can take place [78]. That "nascent oxygen" can be quenched by polyethers (in our case, poly(ethyleneoxide) PEO, used as binder), and the use of lower temperature scan rates substantially slows down the reaction (<10 K/min, whereby TGA analysis was commonly performed at 10 K/min); in both cases, the thermal reactions of Li_2O_2 with carbon and binder lead to Li_2CO_3 and LiOH respectively.

By heating a Li_2O_2 electrode coating made of Vulcan XC72 carbon black, Li_2O_2 and PEO (binder) up to 925 °C, Li_2O_2 reacts via solid-state reaction yielding LiOH in the 250-400 °C range, and subsequently Li_2CO_3 in the 400-600 °C range, whereby the latter is the most stable inorganic Li compound. Li_2CO_3 particles are finally converted into Li_2O and CO at temperatures >600 °C. That complex reaction path was fully disclosed by analyzing the mass weight loss and the evolved gases of the samples, and confronting them with the results obtained from reference experiments performed on 1/1 $Li_xC_yO_z$/carbon mixtures.

On the other hand, charge experiments carried out on discharged Li-O_2 cell cathodes and pre-filled Li_2O_2 electrodes revealed that 20-25% of the O_2 expected by the electrooxidation of the amount of Li_2O_2 stored in the electrode matrix cannot be recovered, and it is thus consumed by parasitic processes. The net O_2 consumed by processes that cannot be ascribed to measurement artifacts (electrolyte corrosion, reaction of freshly plated Li on the Li metal anode with the evolved O_2) accounts for ≈5 % of the total "missing oxygen". Based on the discussed TGA results, we hypothesize that electrooxidation of Li_2O_2 on carbon surfaces proceeds partially via a "nascent oxygen" intermediate. Such a reactivity was previously proposed [29], and leads to the irreversible consumption of O_2, thus to degradation of the materials and cell death.

My role in this work was to support Dr. Beyer's TGA investigation by preparing Li_2O_2 pre-filled electrodes coatings, and by designing the electrochemical/OEMS measurements that support the connection between thermal reactions and electrochemistry. Moreover, I concentrated my efforts in studying the thermodynamics of carbon in presence of CO_2, H_2O, O_2, O and the solid Li compounds Li_2O_2, LiOH, Li_2CO_3 and Li_2O, in order to determine the values of Gibb's free energy of thermal decomposition reactions as a function of temperature. That allowed us to disclose the complex reaction paths typical of the thermal decomposition of a "discharged" air electrode when heated at high temperature.

The experimental part of the paper completes the brief introduction of Section 2.8.5 with further experimental details.

Thermal and Electrochemical Decomposition of Lithium Peroxide in Non-Catalyzed Carbon Cathodes for Li-air Batteries

H. Beyer, S. Meini, N. Tsiouvaras, M. Piana, and H.A. Gasteiger

Physical Chemistry Chemical Physics, 2013, DOI: 10.1039/c3cp51056E

Permanent weblink:

http://dx.doi.org/10.1039/c3cp51056E

Reproduced by permission of Royal Society of Chemistry

PCCP

RSC Publishing

PAPER

View Article Online
View Journal

Cite this: DOI: 10.1039/c3cp51056e

Thermal and electrochemical decomposition of lithium peroxide in non-catalyzed carbon cathodes for Li–air batteries†

H. Beyer,* S. Meini, N. Tsiouvaras, M. Piana and H. A. Gasteiger

Received 11th March 2013,
Accepted 9th May 2013

DOI: 10.1039/c3cp51056e

www.rsc.org/pccp

The decomposition of lithium peroxide during the charging process of lithium–air batteries is investigated. A novel preparation method for electrodes in the discharged state, *i.e.*, prefilled with Li_2O_2 using polyethylene oxide as a binder, is presented. The composition and reactivity of Li_2O_2-prefilled electrodes are examined by thermal analysis coupled with on-line mass spectrometry. Voltage profiles and gas evolution during the charging process of Li_2O_2-prefilled electrodes in battery cells are correlated with the thermal decomposition process of Li_2O_2 and its impact on other electrode compounds. It is found that both thermal Li_2O_2 decomposition and the electrochemical decomposition of Li_2O_2 during charging enhance the oxidation of the electrolyte, the binder, and/or carbon, which is suggested to be due to the formation of ''nascent'' oxygen during Li_2O_2 decomposition into O_2 and Li_2O (thermally) or into O_2 and lithium ions (electrochemically).

1. Introduction

1.1. Background

The need for sustainable transportation has triggered the research on electrochemical energy storage and conversion devices with high energy density. Current electric vehicle range limitations imposed by the maximum projected specific energy of lithium-ion batteries of $\sim$200 $Wh_{net}\ kg_{pack}^{-1}$ (ref. 1) could be overcome by non-aqueous lithium–air batteries, which promise a 4-fold higher specific energy[2] while maintaining rechargeability.

However, the development of rechargeable Li–air cells is facing major challenges such as low rate capability,[3] low round trip efficiency[4,5] and poor cycle life.[6] These issues have been discussed extensively in several excellent review articles.[7,8] It is widely accepted that the cycle life fundamentally depends on the reversible formation/decomposition of lithium peroxide *via* the following cathode reaction:[2]

$$2Li^+ + 2e^- + O_2 \leftrightarrows Li_2O_2, \quad \Delta E^0 = 2.96\ V \qquad (1)$$

Although Peng *et al.*[9] recently reported a highly reversible Li–O_2 cell where Li_2O_2 formation on discharge prevailed even after 100 cycles, this result could only be achieved by using dimethyl sulfoxide as an electrolyte and a gold cathode of presumably limited potential for practical applications due to its high cost. For the more practical carbon cathodes, the discharge process is often dominated by side reactions due to electrolyte decomposition occurring during discharging and/or charging of lithium–air batteries, leading to the formation of Li_2CO_3 and lithium alkyl carbonates rather than the formation of Li_2O_2. This applies particularly for alkyl carbonate electrolytes which react readily with the oxygen superoxide radicals (O_2^-) produced during the discharge reaction (*i.e.*, the oxygen reduction reaction), as was shown by online mass spectrometry and by *ex situ* FTIR[5,10–14] as well as by the rotating ring disk electrode method.[15] After this discovery, ether based electrolytes, which are stable towards O_2^-,[16–20] were shown to lead to the predominant formation of Li_2O_2 in the first discharge cycles,[5,11,21] but their stability over the entire discharge–charge cycle still appears to be insufficient.[22,23] This is suggested to be related to the reaction of Li_2O_2 with the carbon support, the binder and/or the electrolyte,[24] predominantly during the charging reaction.[23,25–28] Although carbon free electrodes have been suggested to exclude the corrosion of the electrode support,[8] a deeper understanding of the interplay between the degradation of different cell materials has to be achieved. In a recent publication, Thotiyl *et al.*[28] have used ^{13}C-labeled electrodes to distinguish between the degradation of the electrolyte and carbon. Electrolyte oxidation was seen during discharge and charge, whereas the carbon support was found to be

---

Institute of Technical Electrochemistry, Technische Universität München, Lichtenbergstr. 4, D-85748, Garching, Germany. E-mail: hans.beyer@tum.de; Fax: +49 8928913674; Tel: +49 8928913658

† Electronic supplementary information (ESI) available: Contains an additional charging experiment of a Li_2O_2-prefilled electrode using an LFP counter electrode, additional TGA-MS measurements of Vulcan carbon, PEO–C, Li_2CO_3–C and LiOH–C mixtures, and a compilation of the thermodynamic data used for the calculation of all ΔG^R values presented in this work. See DOI: 10.1039/c3cp51056e

oxidized only during charge above 3.5 V. Both processes lead to the accumulation of Li_2CO_3 upon cycling.

For a more detailed study of the charging process, lithium–air cathodes have been prepared in the discharged state, *i.e.*, either prefilled with Li_2O_2 or with other possible discharge products.[10,29–33] However, most experiments were conducted using a poly-vinylidene fluoride (PVDF) binder,[10,29–31] which may affect the charge–discharge stability due to the reported reactivity of Li_2O_2 with PVDF–NMP (*n*-methyl-2-pyrrolidinone) solutions during electrode preparation[31] and due to the instability of PVDF towards O_2^-.[19]

1.2. Aim and motivation

In this study, we report a novel preparation procedure for Li_2O_2-prefilled electrodes, using ink-processing solvents and binders which are stable in the presence of Li_2O_2. This allows us to preserve the chemical composition of Li_2O_2 and to avoid possible artifacts deriving from the reaction of Li_2O_2 with the binder/solvent during electrode preparation and/or electrochemical measurements.[19,30,31] All electrode compositions are characterized using thermogravimetric analysis coupled with online mass spectrometry (TGA-MS), seeking to: (i) verify the chemical integrity of Li_2O_2 during the preparation of Li_2O_2-filled electrodes; (ii) determine the quantity and nature of impurities in Li_2O_2; and (iii) study the chemical stability and reactivity of various electrode components over a wide temperature range.

The aim of this work is to study the thermal (*via* TGA-MS) and electrochemical (*via* charging of Li_2O_2 prefilled electrodes) decomposition of Li_2O_2 as well as the effect of thermal/electrochemical Li_2O_2 decomposition on the other Li–air cathode constituents like the Vulcan carbon, the poly-ethylene oxide (PEO) binder, and the diethylene glycol dimethyl ether (DEGDME) based electrolyte. The reactivity of Li_2O_2-prefilled electrodes under thermal stress is correlated with their electrochemical charging behaviour. Charge–discharge voltage profiles of Li–O_2 cells are accompanied by the continuous analysis of gases in the cells' headspace *via* an online electrochemical mass spectrometer (OEMS) developed by our group,[12] which permits the assignment and quantification of evolved gases during the charging of discharged Li–air electrodes or Li_2O_2 prefilled electrodes.

We show that TGA-MS can not only be used to probe the reactivity of single electrode compounds such as Vulcan carbon,[34] lithium peroxide[35,36] and PEO,[37] but can also be used to gain insight into possible reaction pathways between all these compounds under thermal stress and, importantly, provides further insight into the processes occurring during the charging of Li–air cathodes. Thermal analysis has already been successfully applied to battery research, though it has mostly been used for electrolyte stability tests[37] or the determination of metal oxide loadings on carbon-based electrodes,[38] but, to our knowledge, never with focus on the reactivity of lithium salts in Li–air battery electrodes.

2. Experimental

2.1. Electrode preparation

Li_2O_2 (technical grade, >90% purity), LiOH (98% purity), Li_2CO_3 (99% purity) and Li_2O (97% purity) were purchased from Aldrich and stored in an argon-filled glovebox ($c(O_2) < 1$ ppm, $c(H_2O)$ <1 ppm, Jacomex, France). Toluene (Aldrich, anhydrous, 99.5% purity) was stored in the glovebox over Sylobead MS 564C zeolites (3 Å, Grace Division) and contained <1 ppm water. PEO (Aldrich, M_V = 400 000 g mol^{-1}) and carbon (Vulcan XC-72, Tanaka) were dried under dynamic vacuum for 48 h at 50 °C (PEO) or 70 °C (carbon) in a glass oven (Büchi, Switzerland) before use. LiOH, Li_2CO_3, and Li_2O were ground in a Pulverisette 7 planetary ball-mill (Fritsch, Germany) with 3 mm ∅ ZrO_2 balls prior to use. Li_2CO_3 was suspended in NMP (Aldrich, anhydrous, 99.5%) at a 2/3 w/w ratio and wet-milled for 1 h at 700 rpm (*viz.*, 12 milling/rest periods of 5/25 minutes). LiOH and Li_2O were dry-milled for 1 h at 700 rpm in an argon atmosphere (*viz.*, 30 milling/rest periods of 2/28 minutes) to exclude any reactions with solvents or ambient air. Li_2O_2 was used without milling due to the low average particle diameter of ~1 μm of the as-received material.[39]

Li_2O_2-prefilled electrodes were prepared according to the following procedure: each lithium salt was hand-mixed with carbon (1/1 wt/wt ratio) in a mortar. Electrode inks were prepared by adding this mixture to a solution of 0.67 wt% PEO in toluene and sonicating the slurry for 10 minutes under an argon atmosphere using a Branson 250 digital probe-sonifier. The PEO–carbon weight ratio was 0.2/1. Electrode inks were coated onto Celgard® C480 separators in the glovebox using the Mayer-Rod technique. After evaporation of the solvent at room temperature, 15 mm ∅ electrodes (1.77 cm^2) were punched out. The electrodes were dried under dynamic vacuum overnight at 50 °C in the glass oven and directly transferred to the glove box for cell assembly without any exposure to ambient air. Both the carbon and Li_2O_2 loadings of the prefilled electrodes were 0.39 mg cm^{-2}. Non-filled Vulcan carbon electrodes (carbon loading of 0.38 mg cm^{-2}) were prepared in the same manner.

2.2. Electrochemical measurements

Electrolyte. Lithium bis(trifluoromethanesulfonyl)imide (LiTFSI) (Aldrich, 99.95%) was vacuum dried at 150 °C for 24 hours before use. Anhydrous DEGDME (Aldrich, ≥99%) was stored for at least 24 hours over Sylobead MS 564C zeolites (3 Å, Grace Division) before use, resulting in a water content below 10 ppm (determined by Karl Fischer titration). Electrolytes were prepared by dissolving 0.2 M LiTFSI in DEGDME.

Cell design. The battery cell design has been reported and extensively discussed in our previous work.[40] It consists of a 316Ti SS anode current collector and a cathode current collector separated by a Kel-F spacer. The system is sealed by two Teflon O-rings, and the contact between cell components is ensured by a 316 SS compression spring. All battery charging experiments presented in this work make use of that cell design, with modifications added for the connection of external devices (*e.g.*, pressure transducer or mass spectrometer[12]).

Cell assembly. A 17 mm ∅ lithium disk (0.45 μm thick, 99.9%; Chemetall, Germany) was placed onto the anode current collector, wetted with 40 μl of electrolyte, and covered with two Celgard® C480 separators. Another 40 μl of electrolyte were added, then the cathode was placed onto the wetted separators.

After dripping another 40 μl of the electrolyte onto the cathode, it was covered by a 21 mm ∅ stainless steel mesh cathode current collector (316SS, 0.22 mm ∅ wire, 1.0 mm openings, Spörl KG, Germany). The cell was sealed with four screws at a torque of 6 N m.

Cell test and online electrochemical mass spectrometry. Evolved gas analysis upon Li–O_2 cell charging was performed using our OEMS system, extensively described in our previous work.[12] It consists of a closed Li–O_2 cell which is connected to a Pfeiffer Vacuum HiQuad Mass Spectrometer through a calibrated capillary leak of approximately 1 μl min^{-1}, and allows the detection of masses between 1–128 amu. After 2 hours rest at OCV, all Li–O_2 cells were cycled galvanostatically at 120 mA $g_{carbon}{}^{-1}$ between 2.0–4.7 V_{Li} in a temperature-controlled chamber (Binder KB series) at 25 °C using a Gamry Series G300 potentiostat. Before every charging process, the cell was purged with Ar for 10 minutes in order to allow for O_2 quantification during charge, whereas before every discharge process, the cell was purged with O_2 at 101.3 kPa_{abs}. When charging Li_2O_2-prefilled electrodes which were assembled into the electrochemical cell in the glove box, the cell's head space was also filled with Ar.

To quantify gas evolution rates, a calibration gas with oxygen and carbon dioxide in argon was used (2000 ppm each; Westfalen AG, Germany), allowing to convert the mass spectrometer signals into concentrations (note that the relevant m/z ratio for each compound was referenced to the $m/z = 36$ argon isotope signal to minimize the effect of minor variations in cell and mass spectrometer base pressure). The time derivatives of the gas concentrations then yield the molar gas evolution rates (in nmol s^{-1}). Particularly when predominantly one gas species is produced at a given time, the interpretation of the data is more straightforward if the molar evolution rates are converted to current-normalized gas evolution rates (in μmol/(As)), since a 2-electron oxidation process (*e.g.*, the oxidation of Li_2O_2 to O_2 and $2Li^+$) would correspond to a rate of 5.18 μmol/(As), independent of the applied current (equating to $(2F)^{-1}$, where F is the Faraday constant (96 485 As mol^{-1})).

2.3. Thermal analysis (TA)

Differential scanning calorimetry (DSC) of lithium peroxide was conducted on a Mettler Toledo DSC 1 instrument equipped with a cryostat using nitrogen as carrier gas (flow rate 50 ml min^{-1}). In an argon-filled glovebox, samples were densely packed into aluminum crucibles, which were then sealed by cold-welding and directly transferred to the DSC furnace. Samples were held isothermal at 5 °C, then heated to 45 °C at 20 K min^{-1} and finally held isothermal at 45 °C. The heat capacity, $c_{p(T_0)}$, of Li_2O_2 was calculated from the baseline-corrected heat flow integrals between 15 and 35 °C (average of 3 measurements).

Thermogravimetric analysis of electrode materials was performed on a Mettler Toledo TGA/DSC 1 instrument coupled to a Pfeiffer Vacuum Thermostar mass spectrometer for evolved gas analysis. Electrode samples for TGA-MS were obtained by scraping electrode coatings off the Celgard substrate. Samples of lithium salt–carbon or PEO–carbon were prepared by grinding the mixtures in a mortar for 5 minutes. All samples were prepared in an argon-filled glovebox and directly transferred to the TGA furnace. After sample insertion, the furnace was purged with an Ar flow of 120 ml min^{-1} for 10 min at 25 °C to minimize trace amounts of ambient air during measurements. Pure Li salt samples were heated from 25 °C to 1250 °C at 10 K min^{-1} in Ar (flow rate = 60 ml min^{-1}) in open alumina crucibles. Samples of pure carbon were heated from 25 °C to 925 °C at 10 K min^{-1} in 67 vol% O_2–Ar (flow rate = 60 ml min^{-1}) in alumina crucibles with perforated alumina lids to avoid sample spills during carbon burn-off. Samples containing mixtures of Li_2O_2–C or Li_2O_2–PEO–C were heated from 25 °C to 550 °C at 10 K min^{-1} or 50 K min^{-1} in Ar or 67 vol% O_2–Ar (flow rate = 60 ml min^{-1}) in aluminum crucibles sealed with perforated aluminum lids by cold-welding to avoid sample spills in case of vigorous reaction. Samples containing mixtures of PEO–C, LiOH–C, Li_2CO_3–C, and Li_2O_2–PEO–C under conditions where very vigorous reactions can be excluded were heated from 25 °C to 925 °C at 10 K min^{-1} in Ar (flow rate = 60 ml min^{-1}) and subsequently held at 925 °C in 67 vol% O_2–Ar for 60 min in sapphire crucibles covered with perforated sapphire lids to avoid sample spills during measurements.

2.4. X-ray diffraction (XRD)

All X-ray powder diffraction data (in transmission geometry) have been collected using a STOE Stadi MP diffractometer equipped with a Dectris Mythen 1 K one-dimensional silicon strip detector and using monochromatized Mo($K\alpha_1$) radiation (λ = 0.7093 Å, 50 kV, 40 mA). The silicon strip detector allowed us to simultaneously collect data in a 2θ-range of 18.84°. Electrode samples were held between two cellulose acetate foils with low X-ray absorption and diffraction, and the data were collected in stationary mode for 40 min with a 2θ range between 9.035–27.875° and steps of 0.015° in 2θ.

3. Results and discussion

3.1. Electrode binder considerations

The reactivity of Li_2O_2 with solutions of PVDF in NMP, which are commonly used for electrode preparation in battery research, as reported by Xu *et al.*,[31] necessitates the investigation of alternative binder–solvent mixtures. In this work, PEO is used as a binder for electrodes prefilled with lithium peroxide. Unlike PVDF, PEO has no electron-withdrawing fluoride groups. Therefore, the C–H bonds in PEO are less prone to nucleophilic attack by aggressive lithium compounds (Li_2O_2, LiOH, and Li_2O) as well as by O_2^- radicals compared to those in PVDF. Also, PEO has no functional groups except end-chain OH functionalities, the concentration of which in the final electrode, however, is negligible compared to the concentration of Li_2O_2. Furthermore, since PEO is soluble in toluene, electrodes can be prepared with toluene rather than NMP, so that the reactivity of Li_2O_2 with NMP[31] during electrode preparation can be avoided.

Thermal analysis shows that Li_2O_2 is well preserved during the entire electrode preparation procedure. Starting from commercial Li_2O_2 of 95% purity (the major impurity being LiOH,

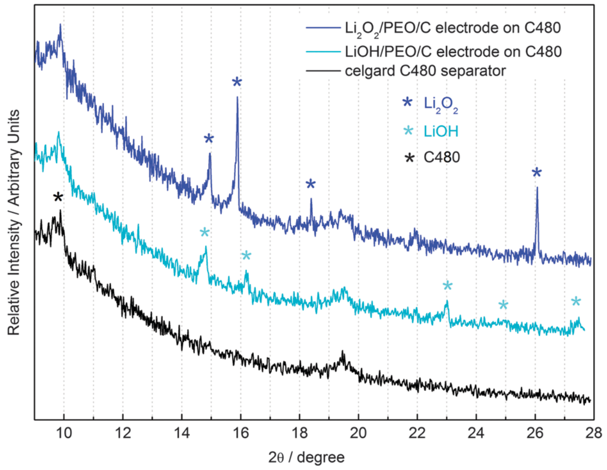

Fig. 1 X-ray (Mo Kα_1) diffraction patterns of Celgard substrates and prefilled electrodes (from top to bottom): (i) Li_2O_2-prefilled electrode (Li_2O_2–PEO–C; dark blue line); (ii) LiOH-prefilled electrode (LiOH–PEO–C; light blue line); (iii) pure Celgard separator (black line). The asterisks in the figure mark the reflections for Li_2O_2 (dark blue), LiOH (light blue), and Celgard (black); the diffraction peak at $2\theta \approx 19.56°$ seen in all three diffractograms is an instrumental artifact caused by the sample holder.

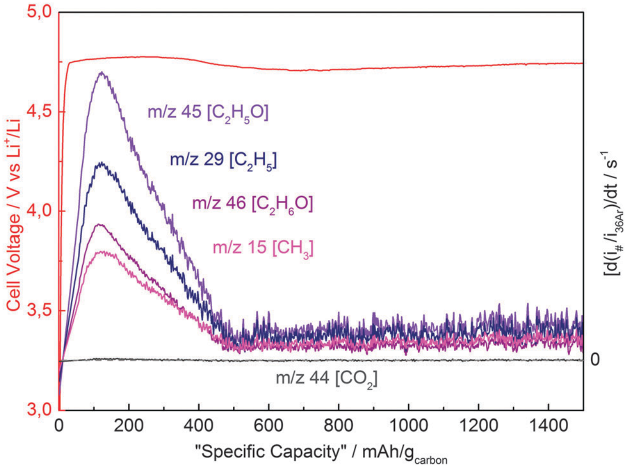

Fig. 2 Galvanostatic ''charging'' of a pure carbon cathode (PEO–C with 0.38 mg_{carbon} cm^{-2}) under argon at 120 mA g_{carbon}^{-1} in DEGDME with 0.2 M LiTFSI, showing the evolution rates for all significant *m*/*z* mass spectrometer signals, corresponding to the time derivative of the ion current, $di_\#/dt$ (note that the evolution rates in our OEMS set-up are proportional to the time derivative of the ion currents as explained in ref. 12). The signals at *m*/*z* of 45, 20, 46, and 15 correspond to the mass spectrum reported for dimethyl ether.[41] While the *x*-axis is simply a time axis (120 mA h g_{carbon}^{-1} ≡ 1 hour), it is expressed in terms of ''specific capacity'' in order to allow better comparison with the galvanostatic charging curves shown in Fig. 3 and 4.

see Section 3.3), at least 88% Li_2O_2 purity is confirmed by TGA-MS for the final prefilled electrodes (see Section 3.5).

This is consistent with the XRD analysis of Li_2O_2-prefilled electrodes (Li_2O_2–PEO–C) shown in Fig. 1, which reveals no diffraction peaks other than those which can be clearly assigned to Li_2O_2 (dark blue asterisks in Fig. 1) or to the Celgard separator (gray asterisk in Fig. 1). Also, no XRD signals are observed for LiOH (the absence of LiOH peaks which do not overlap with Li_2O_2 peaks, *viz.*, those at 2*θ* values of 16.25° and 23.06°), which would be a likely degradation product of Li_2O_2 in the presence of water impurities during ink processing. In summary, both TGA-MS and XRD analysis confirm that Li_2O_2 is essentially quantitatively preserved in the Li_2O_2-prefilled electrodes prepared here.

3.2. Electrochemical oxidation of Li_2O_2 in prefilled and discharged electrodes

For all electrochemical measurements in this work, an online electrochemical mass spectrometer was coupled to the headspace of the battery cell to detect any gases evolved during experiments.[12] Since electrolyte degradation could play a significant role in the galvanostatic charging of Li–O_2 or Li_2O_2-prefilled electrodes, we first determine the DEGDME electrolyte stability window and the gases evolved during its anodic oxidation. Thus, the galvanostatic "charging" of a Li_2O_2-free cell containing only carbon and the PEO binder (PEO–C), *i.e.*, the degradation of the electrolyte and/or the binder during anodic oxidation, is shown in Fig. 2. At a charging current of 120 mA g_{carbon}^{-1}, the degradation of the DEGDME electrolyte and/or the PEO binder of the cathode proceeds at a potential of ≈4.75 V. The observed mass trace pattern demonstrates that the electrolyte and/or the binder are predominantly decomposed to organic C_2 fragments, as a result of C–C bond scission in the parent molecules; it is noteworthy that no evolution of CO_2 is observed. As was discussed in detail in our previous work,[12] the observed *m*/*z*-signals are consistent with the anodic oxidation of DEGDME to dimethyl ether[41] *via* the intermediate formation of methoxy methyl radicals ($^\bullet CH_2$–O–CH_3) by scission of the carbon–carbon bonds. The evolution rates of the decomposition products increase until a "specific capacity" of 150 mA h g_{carbon}^{-1} is reached (*i.e.*, during the initial 1.25 hours) and then gradually decrease to a steady-state value (Fig. 2). Considering the very similar nature of DEGDME and PEO, the above suggested anodic oxidation decomposition pathway would be expected to be identical for both compounds. In summary, the anodic oxidation of the electrolyte, which becomes significant at ≈4.5 V (see Fig. 3 in ref. 12), leads to the formation of dimethyl ether, most likely *via* $^\bullet CH_2$–O–CH_3 radicals, but does not result in CO_2 formation at potentials below 4.9 V. This result suggests that during the charging of a Li_2O_2-prefilled cathode, any simultaneous decomposition of the electrolyte and/or the binder would be expected to occur without the evolution of CO_2.

Galvanostatic charging of a Li_2O_2-prefilled cathode (Li_2O_2–PEO–C) under argon at 120 mA g_{carbon}^{-1} is shown in Fig. 3, exhibiting an initial voltage peak of up to ≈4.6 V (red line in Fig. 3), which has also been observed by Harding *et al.* (using Lithion®-bonded electrodes in the DME based electrolyte, see Fig. S10 (ESI†) in ref. 32), who attributed this to a thin layer of other compounds covering the surfaces of Li_2O_2 particles which would delay the onset for Li_2O_2 electrooxidation. Thereafter, a voltage plateau at ≈4.15 V is observed that represents the electrochemical decomposition of Li_2O_2, followed by a rapid increase of the cell potential at a capacity near the theoretical value for the Li_2O_2-prefilled cathode (marked by the vertical dashed line in Fig. 3). Subsequently, the voltage stabilizes at ≈4.8 V, where the applied current is consumed for the

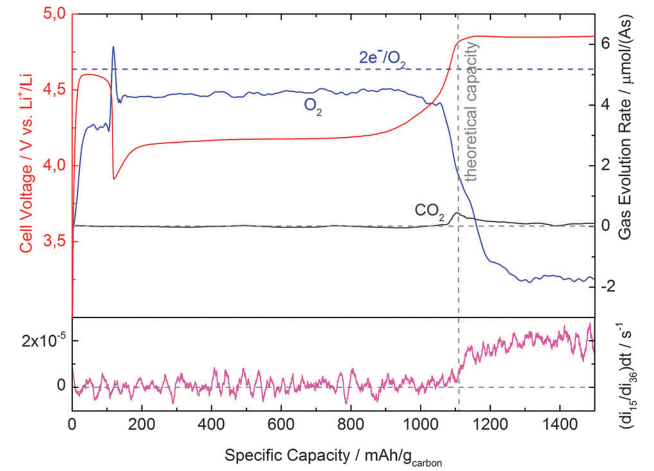

Fig. 3 Galvanostatic charging of a Li_2O_2-prefilled electrode (Li_2O_2–PEO–C with 0.39 mg_{carbon} cm^{-2}) under argon at 120 mA g_{carbon}^{-1} (≡83 μA) in DEGDME with 0.2 M LiTFSI: (i) red line: galvanostatic voltage profile; (ii) blue and black lines: current-normalized molar gas evolution rates of O_2 and CO_2; (iii) ion current derivative of the *m*/*z* 15 trace representative of the dimethyl ether formation rate from anodic oxidation of DEGDME–PEO (for clarity, the observed traces for *m*/*z* 29, 45 and 46 are not shown). The dotted blue line shows the theoretical O_2 evolution rate corresponding to the desired oxygen evolution rate of $2e^-$ per O_2 (according to eqn (1)); the vertical dashed gray line marks the theoretical charging capacity of 1110 mA h g_{carbon}^{-1} (based on a Li_2O_2–C weight ratio of 1/1 and 95% Li_2O_2 purity).

continuous oxidative degradation of the DEGDME electrolyte and/or the PEO binder. Proof for this can be seen in Fig. 3, indicated both by the essentially identical decomposition potential (red line) and by the evolution of the same ion fragments (magenta line in the lower panel of Fig. 3) as was observed for the anodic oxidation in the absence of Li_2O_2 (see Fig. 2). No CO_2 evolution (black line in Fig. 3) is observed during charging of the Li_2O_2-prefilled electrode; only once the theoretical charging capacity is reached and once the electrode potential increases beyond ≈4.7 V, where Li_2CO_3 can be oxidized to CO_2,[39] a small amount of CO_2 is evolved. Considering its magnitude, it is most likely due to the minor Li_2CO_3 contamination of the Li_2O_2 (≈1.7% wt, see Section 3.3). The O_2 evolution rate remains below the expected $2.0e^-$ per O_2 rate (dashed blue line in Fig. 3) throughout the entire charging process, but decreases rapidly as expected once the theoretical capacity (dashed gray line in Fig. 3) is reached. During most of the charging process (with exception of the initial part which will be discussed later), the O_2 evolution rate corresponds to ≈4.45 μmol/(As) (*i.e.*, ≈$2.3e^-$ per O_2), whereas the theoretical oxygen evolution rate equates to 5.18 μmol/(As), which suggests that ≈14% oxygen is consumed in one or more of the following side reactions: (i) oxygen consumption on the lithium electrode; (ii) oxygen consumption from reaction of O_2 with electrolyte oxidation fragments; and/or (iii) reaction of "nascent" highly-reactive oxygen species produced during Li_2O_2 electro-oxidation with the electrolyte and/or carbon.

(i) Although it has been reported that the O_2 yield during charging of discharged Li–O_2 cells is independent of whether the anode is based on lithium metal or on lithium iron phosphate (LFP) (the latter cannot reduce O_2 and does not chemically react with it),[23] we conducted an additional charging experiment using a LFP anode and a solid electrolyte diffusion barrier (see Fig. S1 in the ESI†) to verify if anodic oxygen consumption can be discarded under the experimental conditions used in this work. Indeed, it is found that the O_2 evolution rate in Fig. S1 (ESI†) corresponds to ≈4.70 μmol/(As) (*i.e.*, effectively ≈$2.2e^-$ per O_2 for the cathode reaction). Given the O_2 evolution rate of ≈4.45 μmol/(As) in Fig. 3, oxygen is assumed to be reduced at the Li metal anode at a rate of ≈0.25 μmol/(As) (≈5% of the theoretical oxygen evolution), so that another ≈0.48 μmol/(As) must be consumed in other side reactions.

(ii) In order to determine whether O_2 can react with electrolyte decomposition fragments, we measured the oxygen consumption rate during the anodic oxidation on a carbon electrode (PEO–C) in a mixture of 10% O_2 in argon (Fig. 4). Quite clearly, in the presence of significant DEGDME oxidation, *i.e.*, at 4.8 V and at 120 mA h g_{carbon}^{-1}, O_2 gets consumed at a substantial rate.

Considering the above proposed electrolyte decomposition *via* C–C bond scission through intermediate $^{\bullet}CH_2–O–CH_3$ radical formation in conjunction with the large negative free energy for the reaction of O_2 with carbon radicals[42] (*i.e.*, O_2 + $^{\bullet}CH_2–O–CH_3$ → $^{\bullet}O–O–CH_2–O–CH_3$), the oxygen consumption during anodic electrolyte oxidation is not surprising. At the same time, since the anodic oxidation of DEGDME at 4.15 V is very small (≈1 mA g_{carbon}^{-1}, see Fig. 1 in ref. 22), the oxygen consumption rate at this potential is accordingly more than one order of magnitude smaller. It should be noted that the oxygen consumption rate based on this mechanism might be smaller by a factor of up to three under the conditions in Fig. 3, since the O_2 concentration for the experiments in Fig. 4 (10% O_2 in Ar) was about 3-fold higher than the effective O_2 concentration

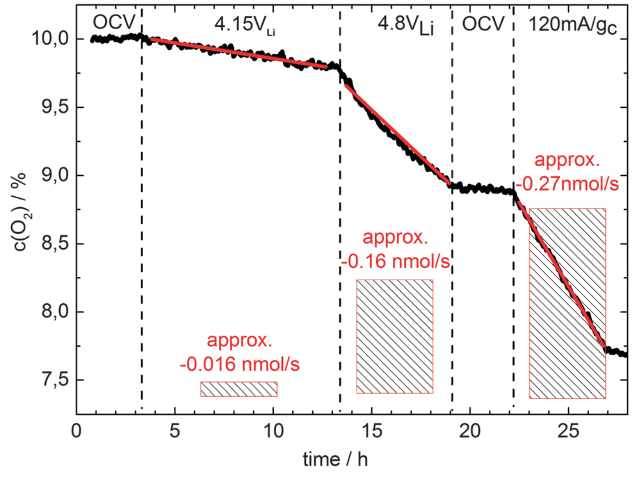

Fig. 4 Oxygen concentration variation *versus* time during OCV (open circuit potential) and during the anodic oxidation on a carbon electrode (PEO–C; 0.42 mg_{carbon} cm^{-2}) in a 10% O_2/Ar atmosphere in DEGDME with 0.2 M LiTFSI. Shown are the initial O_2 concentration at OCV, followed by potentiostatic oxidation at 4.15 and 4.80 V_{Li}, an intermediate OCV period, and a final galvanostatic oxidation at 120 mA g_{carbon}^{-1}. The values of dc_{O_2}/dt in each segment were obtained by linear regression fits, equating to ≈−0.016 nmol s^{-1} at 4.15 V_{Li}, ≈−0.16 nmol s^{-1} at 4.80 V_{Li}, and ≈−0.27 nmol s^{-1} at 120 mA h g_{carbon}^{-1}. The O_2 consumption rate at OCV is negligible (<0.002 nmol s^{-1}).

after the complete charging of the Li_2O_2-prefilled electrode. Comparing the above findings with the charging of a Li_2O_2-prefilled electrode, it becomes obvious that the negative O_2 evolution rate at the end of charge (≈ -1.8 μmol/(As); see blue line at >1300 mA h g_{carbon}^{-1} in Fig. 3) is due to the reaction of O_2 with the anodic oxidation products from DEGDME (again, the slightly lower negative value is most likely due to the roughly 3-fold lower O_2 concentration). Now we can determine whether the remaining ≈ 0.48 μmol/(As) of "missing oxygen" during the voltage plateau at ≈ 4.15 V in Fig. 3 (after consideration of (i)) may be consistent with the reaction of O_2 with oxidation products of DEGDME. For the conditions in Fig. 3, the value of ≈ 0.48 μmol/(As) of "missing oxygen" equates to ≈ 0.040 nmol s^{-1}. This amount is significantly larger than what could be explained by the O_2 consumption caused by the anodic electrooxidation of DEGDME (at most ≈ 0.016 nmol s^{-1}, corresponding to $\approx 4\%$ of the theoretical oxygen evolution).

(iii) Since the side reactions (i) and (ii) together can only account for $\approx 9\%$ missing oxygen, the only feasible explanation for the observed amount of $\approx 14\%$ missing oxygen is that the oxidation of DEGDME, PEO and/or carbon may be accelerated by "nascent" oxygen which is released during the oxidative decomposition of Li_2O_2. The nature of "nascent" oxygen released during Li_2O_2 oxidation may be singlet oxygen, as was proposed by McCloskey *et al.*,[23] or atomic oxygen. The latter has been demonstrated to react with carbon at high rates with minimal activation energy already at room temperature to yield CO (and CO_2 *via* consecutive reaction with CO),[43] but since we do not observe CO or CO_2 during the main charging voltage plateau, and since the overall amount of released CO_2 near the theoretical capacity line (see Fig. 3), which is presumably from the charging of Li_2CO_3, would be too small to account for the "missing" O_2, the reaction of DEGDME (and PEO) with highly reactive species produced during the oxidative decomposition of Li_2O_2 is the most likely hypothesis. We will try to substantiate this hypothesis later on by comparing these observations on the electrochemical oxidation of Li_2O_2 with those of the thermal decomposition of Li_2O_2 (in Sections 3.3 and 3.5). On the basis of the above findings, the substantially lower O_2 evolution rate in the initial stage of the charging of a Li_2O_2-prefilled electrode (see blue line between 0 and 100 mA h g_{carbon}^{-1} in Fig. 3) can now easily be rationalized by the already substantial anodic oxidation rates of DEGDME at ≈ 4.6 V (see Fig. 3 in ref. 12), leading to the consumption of oxygen through reaction with $^{\bullet}CH_2–O–CH_3$ radicals.

In the following we will compare the above findings on the charging behavior of a Li_2O_2-prefilled electrode with the galvanostatic charging (120 mA g_{carbon}^{-1}) of a Vulcan carbon electrode (PEO–C) which was discharged under oxygen in DEGDME with 0.2 M LiTFSI, yielding a specific capacity of ≈ 200 mA h g_{carbon}^{-1} (identical to the discharge capacities we reported previously[22]). As shown in Fig. 5, the charging potential (red line) increases gradually from ≈ 3.5 to ≈ 4.4 V, at which point a sharp potential increase and a sudden drop in the oxygen evolution rate (blue line) at the expected charging capacity of ≈ 200 mA h g_{carbon}^{-1} mark the end of the charging process. Quite obviously, for up to $\approx 70\%$ of the charging capacity, the voltage remains below the ≈ 4.15 V charging plateau which was observed for a Li_2O_2-prefilled electrode (Fig. 3). The lower charging potential on a discharged electrode could be rationalized, if one was to assume that electron transport between the carbon and the Li_2O_2 phase is rate-limiting, since the contact area between the electron conducting carbon phase and the insulating Li_2O_2 phase (illustrated in Fig. 6) is orders of magnitude larger for Li_2O_2 formed on carbon during discharge in O_2 (see Fig. 6b) compared to the contact area between carbon particles and micrometer-sized Li_2O_2 particles (see Fig. 6a). This is consistent with the reported lowering of the charging potential of a Li_2O_2-prefilled electrode (≈ 0.5 V!), in the presence of a redox mediator serving as an electron shuttle between the carbon and the Li_2O_2 phase.[33,44]

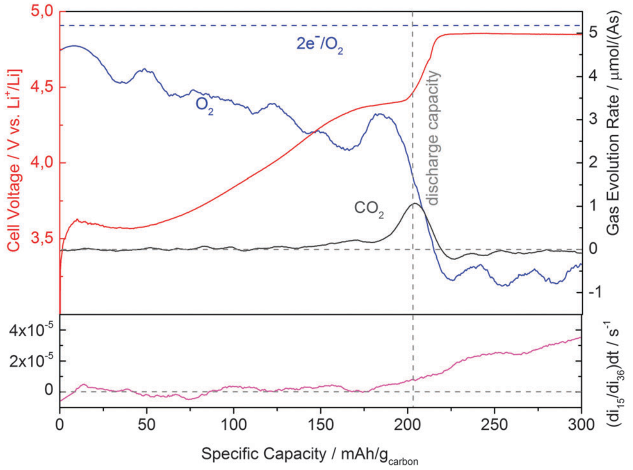

Fig. 5 Galvanostatic charging of a previously discharged Li–O_2 cathode (PEO–C with 0.38 mg_{carbon} cm^{-2}; discharge capacity of ≈ 200 mA h g_{carbon}^{-1}, indicated by the vertical gray line) under argon at 120 mA g_{carbon}^{-1} ($\equiv 81$ A) in DEGDME with 0.2 M LiTFSI: (i) red line: galvanostatic voltage profile; (ii) blue and black lines: current-normalized molar gas evolution rates of O_2 and CO_2; (iii) ion current derivative of the m/z 15 trace, representative of the dimethyl ether formation rate from anodic oxidation of DEGDME–PEO (for clarity, the signals for m/z 29, 45 and 46 are not shown). The dotted blue line shows the theoretical O_2 evolution rate corresponding to the desired oxygen evolution rate of $2e^-$ per O_2 (according to eqn (1)).

During the initial charging of the discharged carbon electrode, the oxygen evolution rate of ≈ 4.5 μmol/(As) ($\approx 2.3e^-$ per O_2; see blue line in Fig. 5) is similar to that obtained for a Li_2O_2-prefilled electrode (blue line in Fig. 3), but continuously decreases towards a value of ≈ 2 μmol/(As) ($\approx 5e^-$ per O_2) at the end of discharge. While the oxygen yield of the discharged electrode averaged over the charging process (≈ 3.2 μmol/(As) $\equiv$ $\approx 3.0e^-$ per O_2) is consistent with other reports in the literature ($\approx 3.2e^-$ per O_2[11] and $\approx 2.6e^-$ per O_2[23] in DME as well as $\approx 2.7e^-$ per O_2[12] in the DEGDME electrolyte), it is surprisingly much lower than that obtained for the Li_2O_2-prefilled electrode (≈ 4.5 μmol/(As) $\equiv$ $\approx 2.3e^-$ per O_2). Thus, the much higher fraction of "missing" O_2 during charging of a discharged carbon electrode ($\approx 30\%$, based on the average O_2 yield of ≈ 3.2 μmol/(As) *vs.* 5.18 μmol/(As) according to eqn (1)), compared to $\approx 14\%$ for the Li_2O_2-prefilled electrode, points towards an enhanced reactivity with carbon and/or the electrolyte. We hypothesize again that highly reactive "nascent" oxygen, released during Li_2O_2 oxidation, enhances the

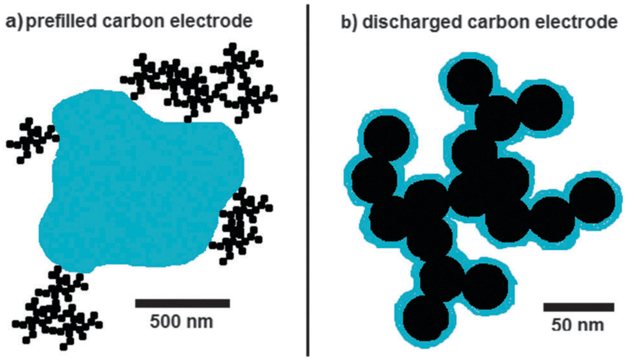

Fig. 6 Sketch of the morphology of Vulcan carbon based electrodes, illustrating the approximate distribution of the carbon (black) and the Li_2O_2 (blue) phases: (a) Li_2O_2-prefilled electrode (Li_2O_2–PEO–C) using ≈1 μm-sized Li_2O_2 particles; (b) Vulcan carbon electrode (PEO–C) discharged under oxygen, leading to nm-thick Li_2O_2 surface deposits on the carbon.[22] Vulcan carbon is depicted as ≈30 nm ∅ spherical primary particles that form highly structured ≈200–300 nm ∅ primary agglomerates.[46,47]

oxidative decomposition of the electrolyte at potentials below 4.5 V, *i.e.*, at potentials where DEGDME is otherwise stable against anodic oxidation (see Fig. 4 as well as Fig. 1 in ref. 22). This explains the "missing" O_2 during charge as oxygen would be consumed for both the oxidative decomposition of the electrolyte and the reaction with thereby produced $^\bullet CH_2–O–CH_3$ radicals, as discussed above.

To rationalize the proposed higher electrolyte decomposition rates on the discharged electrode compared to the Li_2O_2-prefilled electrode, one needs to consider the differences in the electrolyte/Li_2O_2 interface for ≈1 μm-sized Li_2O_2 particles in prefilled electrodes *vs.* nanometer-sized Li_2O_2 films in discharged carbon electrodes, with reported Li_2O_2 film thicknesses of ≈0.5 nm[22] up to ≈5 nm,[22,45] as is illustrated in Fig. 6. Therein, Vulcan carbon is depicted as ≈30 nm ∅ spherical primary particles that form highly structured ≈200–300 nm ∅ primary agglomerates.[46,47] Based on this, ≈1 μm-sized Li_2O_2 particles in the prefilled electrode[39] with a Li_2O_2–C weight ratio of 1/1 have a maximum interface area with the electrolyte corresponding to ≈3 $m_{Li_2O_2}{}^2$ per g_{carbon} (*i.e.*, for a Li_2O_2–C weight ratio of 1/1, the specific surface area of Li_2O_2 per gram carbon can be estimated *via* a spherical approximation as $m_{Li_2O_2}{}^2$ per g_{carbon} ≈ $6/(d_{Li_2O_2} \times \rho_{Li_2O_2})$). This is ≈30-fold lower than the value of ≈100 $m_{Li_2O_2}{}^2$ per g_{carbon} estimated for nm-thick Li_2O_2 films on a Vulcan carbon electrode (again, estimating $m_{carbon}{}^2$ per g_{carbon} ≈ $6/(d_{carbon} \times \rho_{carbon})$ with d_{carbon} ≈ 30 nm (see Fig. 6b) and equating carbon surface area with the Li_2O_2 surface area). Thus, assuming the formation of highly reactive "nascent" oxygen during the oxidative decomposition of Li_2O_2, the ≈30-fold higher electrolyte/Li_2O_2 interface area of the discharged carbon electrode compared to the Li_2O_2-prefilled electrode would indeed explain the higher electrolyte decomposition rates observed with the former.

Finally, the higher rate of CO_2 evolution during the end of charge of the discharged carbon electrode (black line in Fig. 5) is again consistent with its several orders of magnitude larger carbon/Li_2O_2 interface area compared to a Li_2O_2-prefilled electrode (illustrated in Fig. 6), leading to the formation of Li_2CO_3. According to Thotiyl *et al.*,[28] a minor fraction of Li_2CO_3 might already have formed during discharge due to electrolyte degradation, whereas the major fraction is assumed to be formed because of electrolyte and carbon corrosion during charge, as was also proposed previously.[25,26] In summary, all of the above observations support our hypothesis that oxidative decomposition of Li_2O_2 during charging leads to enhanced electrolyte and carbon degradation *via* the formation of highly reactive "nascent" oxygen. Further evidence for the highly reactive oxygen species produced during the electrochemical oxidation of Li_2O_2 will be provided in the following by comparing it with the thermal decomposition of Li_2O_2 in detailed TGA-MS analyses.

3.3. TA of lithium salts

TGA-MS data of pure Li_2O_2, Li_2O, LiOH, and Li_2CO_3 samples are shown in Fig. 7 to determine the purity of the commercial Li_2O_2 used in this work, as well as to provide a reference for the upcoming analysis on the thermal decomposition pathways of more complex mixtures (Li_2O_2–C and Li_2O_2–PEO–C).

During their thermal decomposition, Li_2O_2, LiOH, and Li_2CO_3 are all converted into the thermodynamically most stable Li_2O (in the absence of CO_2 and H_2O), as indicated by the evolved gases and the excellent match of the measured mass losses (Δ*m* meas) with the expected mass losses (Δ*m* theo) according to the reaction stoichiometries (see Table 1). Li_2O itself is stable over the measured temperature range. As all conversions take place in discrete temperature windows, the analysis of lithium salt mixtures is feasible. For the decomposition of LiOH and Li_2CO_3, a sudden increase in the reaction rate is seen at the melting points of those salts (given in Table 1). Though the reported melting point of Li_2O_2 is not consistent in the literature, Li_2O_2 is commonly reported to decompose upon melting.[48] Furthermore, the change in Gibbs free energy (ΔG^R) at the onset and endset temperature of each reaction is given in Table 1,

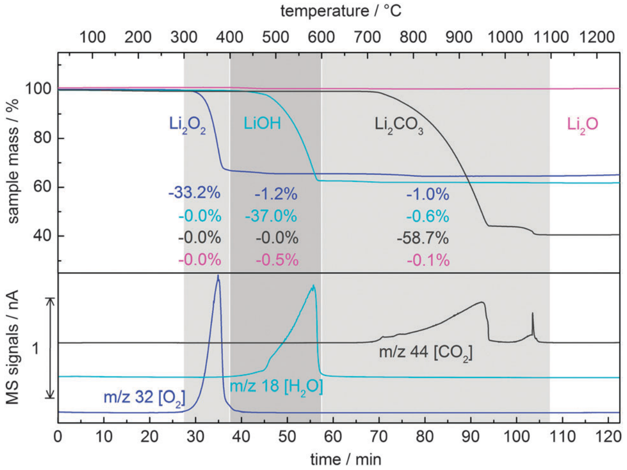

Fig. 7 TGA of Li_2O_2, LiOH, Li_2CO_3, and Li_2O (sample mass *vs.* temperature) and on-line MS of evolved gases (mass traces with *m*/*z* of 32, 18, and 44 attributed to O_2, H_2O, and CO_2, respectively). The percentage values given next to the TGA curves represent the measured mass losses, Δ*m* meas, for each of the observed transitions. Samples were heated from 25 °C to 1250 °C at 10 K min^{-1} in Ar.

Table 1 Reactions of lithium salts observed during thermal analysis

No.	T range [°C]	Atmosphere	Reaction	Δm theo/meas [% of LiX]	Evolved(↑) gases	ΔG^{R} at T_{onset}/T_{endset} [kJ mol^{-1}]	m.p. (reactant) [°C]
(–)	25–1250	Ar	Li_2O does not react	—	—	—	1570
(2)	280–400	Ar	$Li_2O_2 \rightarrow Li_2O + \frac{1}{2}O_2$	−34.9/−33.2	$O_2\uparrow$	−24/−44	~340
(3)	400–600	Ar	$2LiOH \rightarrow Li_2O + H_2O$	−37.6/−37.0	$H_2O\uparrow$	+42/+16	471
(4)	700–1100	Ar	$Li_2CO_3 \rightarrow Li_2O + CO_2$	−59.6/−58.7	$CO_2\uparrow$	+72/+12	723

calculated assuming a temperature independence of the change in heat capacity over the reaction (*i.e.*, $\Delta c^{R}_{p(T_0)} \neq f(T)$):

$$\Delta G^{R}_{(T)} = \Delta G^{R}_{(T_0)} - \Delta S^{R}_{(T_0)}(T - T_0) - \Delta c^{R}_{p(T_0)}[(T\ln(T/T_0) - (T - T_0)]$$

$\Delta G^{f}_{(T_0)}$, $S_{(T_0)}$ and $c_{p(T_0)}$ of reactants and products are generally taken from ref. 49 except for $c_{p(T_0)}$ of Li_2O_2, for which different values are reported in the literature. We therefore determined it by DSC, resulting in $c_{p(T_0)}$ (Li_2O_2) = 71 ± 7 J (mol K)$^{-1}$ (errors taking into account Li_2O_2 purity, weighting, and measurement errors). This agrees reasonably well with the only two sets of literature data, *viz.*, $c_{p(T_0)}$ of 76 J (mol K)$^{-1}$ extrapolated from measurements at $T > 300$ K published in 1979[50] and c_v of 66 J (mol K)$^{-1}$ measured at 300 K in a vacuum.[51] All the required thermodynamic data are listed in Table S3 of the ESI.† For ΔG^{R} calculations, the solid state is always assumed for Li salts, which is not expected to cause significant errors unless the reaction temperature is far above the melting point (m.p.) of any involved salt. The melting points of all relevant lithium salts given in Table 1 are adapted from ref. 52 except for Li_2O_2 (see above).

Gibbs free energy changes are calculated under the assumption that the partial pressures of all gaseous reaction products are at their standard reference pressure, p_{ref}, of 101.3 kPa. However, due to the continuous removal of gaseous products by the TGA carrier gas flow, their real partial pressures are expected to be far below 101.3 kPa, which may result in the calculation of positive $\Delta G^{R}_{(T)}$ values for some reactions that are actually thermodynamically feasible under the conditions present in the TGA. Considering the correction for actual partial pressures, p_{actual}, which are below the reference partial pressure due to dilution *via* $RT \ln(p_{actual}/p_{ref})$, the water vapor concentration below which the ΔG^{R} values in reaction No. 3 (Table 1) would become negative is ≈500 ppm and ≈11% at T_{onset} and T_{endset}, respectively, which is reasonably consistent with expectations. Similarly, the CO_2 concentration below which the ΔG^{R} values in reaction No. 4 (Table 1) would become negative is ≈100 ppm and ≈35% at T_{onset} and T_{endset}, respectively.

After having clarified the various reaction sequences through which the examined lithium compounds decompose with increasing temperature, the amount and nature of impurities present in the commercial Li_2O_2 used for electrode preparation can now be determined from the TGA curve of Li_2O_2 in Fig. 7 (dark blue line). The fraction of each lithium salt in the Li_2O_2 sample is calculated by dividing the measured weight loss in its specific decomposition range by the stoichiometric weight loss of the pure substance. The following contents are found in the Li_2O_2 sample: 95.1% Li_2O_2, 3.2% LiOH, and 1.7% Li_2CO_3. These three compounds add up to 100.0%, indicating the absence of Li_2O and other impurities.

3.4. TA of Li_2O_2–C

The thermal analyses of a Li_2O_2–C mixture in Ar and 67 vol% O_2–Ar are shown in Fig. 8.

In an argon atmosphere (Fig. 8a), similar to pure Li_2O_2, the onset of O_2 evolution (blue line in Fig. 8a) initiates in between 280 and 340 °C, indicating the onset of Li_2O_2 decomposition. However, at 340 °C a very rapid and highly exothermic reaction between Li_2O_2 and carbon occurs (DSC results not shown for clarity), with CO being the only gaseous product. An essentially instantaneous mass loss of 29.0% suggests the formation of Li_2O as the only solid product *via* reaction No. 5 (see Table 2). The fact that CO is exclusively formed (despite CO_2 being the thermodynamically more stable product of carbon oxidation in this temperature range) suggests that the decomposition of Li_2O_2 produces highly reactive "nascent" oxygen which instantly reacts with nearby carbon atoms, approximately 200 °C below the temperature where carbon reacts with gas phase oxygen (see Fig. S2 in the ESI†). As mentioned before, the nature of these oxygen species could be either singlet oxygen or atomic oxygen. The latter seems to be the more likely hypothesis, since the primary product of the reaction between atomic oxygen and carbon is CO.[43] In this case, CO_2 would only be formed in a consecutive reaction between CO and atomic oxygen, which is unlikely to happen in the TGA due to the localized oxygen formation at Li_2O_2 surfaces and the constant product removal by the gas flow.

When the measurement is performed in 67 vol% oxygen in argon (Fig. 8b), this very rapid and highly exothermic reaction occurs already at 320 °C. Apparently, the presence of gas-phase oxygen shortens the reaction onset phase needed to build up the oxygen level and/or oxygen release rate that is necessary to trigger the reaction between Li_2O_2 and carbon. During the reaction, a significant amount of oxygen from the gas-phase is consumed ("negative" peak in the m/z 32 trace, the baseline level of which represents 67 vol% oxygen), and 75.9% of the sample mass is lost. This value far exceeds the calculated mass loss for reaction No. 5 in Table 2, indicating that carbon is not only oxidized by "nascent" oxygen from the decomposition of Li_2O_2, but also by oxygen from the gas phase. This is confirmed by the detection of a huge amount of CO_2 (black line in Fig. 8b; see also Table 2, reaction No. 6) in addition to an amount of CO that is similar to the one released in an argon atmosphere (orange lines in Fig. 8a and b). As the total oxidation of pure

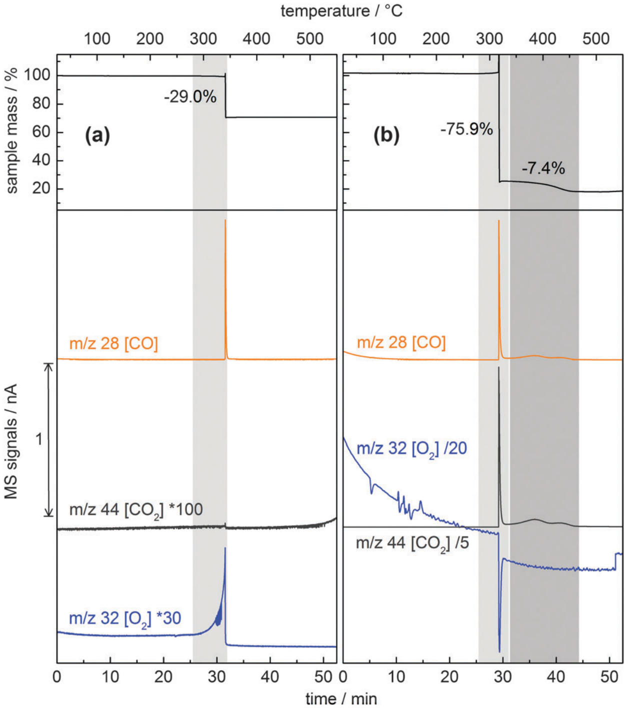

Fig. 8 TGA (sample mass *vs.* temperature) and on-line MS of evolved gases (mass traces with *m*/*z* of 32, 28, and 44 attributed to O_2, CO, and CO_2, respectively) of Li_2O_2–C (mixing ratio 1/1). The percentage values given next to the TGA curves represent the measured mass losses, Δm meas, for each of the observed transitions. The multipliers/divisors in the mass trace labels represent the amplification factors used on the relative intensities of the respective signals. Samples were ramped from 25 to 550 °C at 10 K min^{-1} in (a) Ar and (b) 67 vol% O_2/Ar.

Vulcan carbon by gaseous oxygen does not occur at temperatures below 500 °C (see Fig. S2, ESI†), it is assumed that the initial rapid and highly exothermic reaction of carbon with "nascent" oxygen from the decomposition of Li_2O_2 leads to a large local temperature increase, driving the reaction with gas-phase oxygen. The fact that the measured mass loss of 75.9% exceeds the combined calculated losses from reactions No. 5 and No. 6 (67.5%) is explained by an obvious sample spill that is inevitable when such a rapid and highly exothermic reaction occurs in an open system, although precautions have been made to minimize this effect (see Section 2.3 for details).

Another noteworthy feature of the TGA profile in Fig. 8b is an additional weight loss of 7.4% between 360 and 470 °C, accompanied by the release of CO and CO_2 (weak MS signals compared to the previous reaction). To explain this, it has to be considered that in the course of the preceding reaction caused by Li_2O_2 decomposition, small fractions of the products Li_2O and CO_2 are instantly converted to Li_2CO_3 (Table 2, reaction No. 7). The retention of CO_2 by Li_2O at $T > 190$ °C is in agreement with literature results.[53] At higher temperature, Li_2CO_3 decomposes again, resulting in the mentioned weight loss. However, unlike the decomposition of pure Li_2CO_3 under argon (Fig. 7 and Table 1, reaction No. 4), carbon is now also involved in the reaction: in argon, this reaction occurs at 650–900 °C and yields Li_2O and CO (Table 3, reaction No. 14), as confirmed by a reference measurement of Li_2CO_3–C in argon (see Fig. S4 in the ESI†); in an O_2–Ar atmosphere (as in Fig. 8b), the reaction already takes place at 360–470 °C, and both CO and CO_2 are detected in the off-gas (Table 2, reaction No. 8). The exact stoichiometry of this reaction cannot be determined by means of TGA-MS, so the proposed stoichiometry of reaction No. 8 (Table 2) is an estimate that allows us to demonstrate the thermodynamic feasibility of such a reaction in this temperature range. As reactions No. 5 and No. 6 have already taken place at this point of the TA, only trace amounts of carbon should be left in the sample, suggesting that just enough carbon is participating in the reaction to allow the detection of trace amounts of CO. It has to be mentioned that due to sample spills, comparing theoretical mass losses to measured ones does not provide conclusive results for this particular experiment.

In summary, in the absence of gas-phase oxygen, the thermal decomposition of Li_2O_2 in the presence of carbon leads to the rapid and highly exothermic evolution of CO near ≈300 °C according to reaction No. 5 (see Fig. 8a). Since carbon does not react with gas-phase oxygen below ≈500 °C (see Fig. S2, ESI†) due to kinetic limitations, we believe that highly reactive "nascent" oxygen produced during Li_2O_2 decomposition causes this very rapid reaction with carbon and Li_2O_2 at already ≈300 °C. Due to the high exothermicity of this reaction, a substantial local temperature rise is very likely, which would explain the observed complete oxidation of carbon at ≈300 °C in the presence of gas-phase oxygen (Fig. 8b). While this high reactivity between *thermally* decomposing Li_2O_2 and carbon at ≈300 °C might allow us to hypothesize a similar reactivity during the *electrochemical* oxidation of Li_2O_2 in a Li–air battery, one first needs to consider the effect of the presence of the electrolyte. For this reason, we next examine the effect of the addition of PEO to Li_2O_2–C, since PEO is chemically very similar to the commonly used glyme electrolytes and is also the binder which we have used in the electrochemical experiments in Sections 3.2 and 3.3.

3.5. TA of Li_2O_2-prefilled electrodes

The results of the TGA-MS measurements performed on Li_2O_2–C–PEO electrode samples are shown in Fig. 9.

Table 2 Reactions of Li_2O_2–C (mixing ratio 1/1) observed during thermal analysis

No.	T range [°C]	Atmosphere	Reaction	Δm(total) theo/meas [% sample]	Δm(LiX) theo/meas [% sample]	Δm(C) theo/meas [% sample]	Evolved(↑) or consumed(↓) gases	ΔG^R at T_{onset}/T_{endset} [kJ mol^{-1}]
(5)	280–340	Ar/O_2	$Li_2O_2 + C \rightarrow Li_2O + CO$	−30.6/−29.0	−17.5/−16.6	−13.1/−12.4	CO↑	−173/−183
(6)	320 + Q^R	O_2	$C + O_2 \rightarrow CO_2$	≤−36.9/−46.9	0/0	≤−36.9/−46.9	CO_2↑	−394
(7)	320	O_2	$Li_2O + CO_2 \rightarrow Li_2CO_3$	≤+47.9/+5.8	≤+47.9/+5.8	0/0	CO_2↓	−130
(8)	340–470	O_2	$Li_2CO_3 + C + \frac{1}{2}O_2 \rightarrow Li_2O + CO + CO_2$	≤−61.0/−7.4	≤−47.9/−5.8	≤−13.1/−1.6	CO↑, CO_2↑	−39/−72

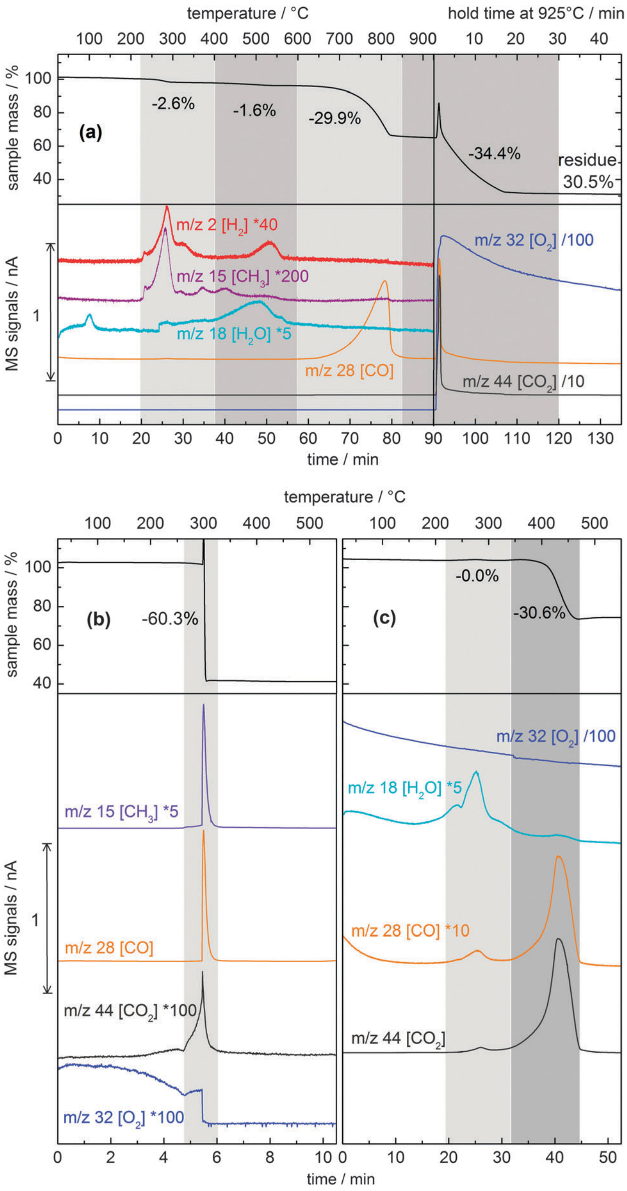

Fig. 9 TGA (sample mass *vs.* temperature) and on-line MS of evolved gases (mass traces with *m*/*z* of 32, 18, 28, 44, 15, and 2 attributed to O_2, H_2O, CO, CO_2, CH_3, and H_2, respectively) of Li_2O_2–C–PEO (mixing ratio 1/1/0.2). The percentage values given next to the TGA curves represent the measured mass losses, Δm meas, for each of the observed transitions. The multipliers/divisors in the mass trace labels represent the amplification factors used on the relative intensities of the respective signals. Samples were ramped (a) from 25 to 925 °C in Ar at a heating rate of 10 K min^{-1} and subsequently held isothermal at 925 °C in 67 vol% O_2–Ar, (b) from 25 to 550 °C in Ar at a heating rate of 50 K min^{-1}, and (c) from 25 to 550 °C in 67% O_2–Ar at a heating rate of 10 K min^{-1}.

When the analysis is performed in argon at a heating rate of 10 K min^{-1} (left panel of Fig. 9a), no vigorous reaction of the sample at 340 °C (which would be expected from the results on Li_2O_2–C mixtures) is seen. Instead, a weight loss of only 2.6% accompanied by the release of organic fragments from PEO decomposition (identified by the *m*/*z* 15 trace, see Fig. S3 in the ESI†) and hydrogen is detected in the temperature range of 220 to 400 °C. As the presence of PEO in the sample is the only difference to the TA of Li_2O_2–C in Fig. 8a, it is assumed that PEO acts as a scavenger for "nascent" oxygen originating from the decomposition of Li_2O_2, preventing the buildup of the oxygen concentration necessary for the vigorous reaction with carbon (described in the discussion of Fig. 8).

This observation is highly relevant for the understanding of the electrochemical charging behavior of Li–O_2 cells with Li_2O_2-prefilled electrodes, as our cell tests in Section 3.2 indicate a similar reaction of DEGDME and PEO with "nascent" oxygen. Interestingly, the extent of this reaction during the charging of a Li_2O_2-prefilled battery cell is so small that the evolution of volatile organic decomposition products is below the OEMS detection limit, whereas both the increase of Li_2O_2 specific surface area (*i.e.*, charging a previously discharged battery cell) and the increase of the reaction temperature (*i.e.*, the TA of a Li_2O_2-prefilled electrode) lead to an increased reaction rate that allows the unambiguous *in situ* identification of volatile organic products (TA) or of oxygen consumption (charging a previously discharged cell).

The hypothesis that PEO acts as a scavenger for "nascent" oxygen is supported by the results of a TA conducted at a heating rate of 50 K min^{-1} (Fig. 9b). In this case, "nascent" oxygen is evolved by Li_2O_2 decomposition at a higher rate than it is consumed by the subsequent reaction with PEO. Thus, the oxygen level necessary for the vigorous reaction with the carbon fraction is reached at 300 °C. Upon this rapid reaction, mainly CO, but also organic fragments that are ascribed to PEO decomposition and marginal amounts of CO_2 are detected in the off-gas. This experiment also demonstrates that the amount of PEO present in a Li_2O_2-prefilled electrode can reduce, but not eliminate the inherent risk of a vigorous reaction under thermal stress.

A third TA in 67% oxygen atmosphere at a heating rate of 10 K min^{-1} is shown in Fig. 9c. Analogous to Fig. 9a, no vigorous reaction occurs. The less rapid mass loss between 360 and 470 °C is ascribed to the decomposition of Li_2CO_3 *via* reaction No. 8 in Table 2, as indicated by CO_2 and minimal CO evolution (slightly higher intensity of *m*/*z* 28 then expected for pure CO_2 fingerprint). As in the previously discussed TA of Li_2O_2–C in oxygen (Fig. 8b), Li_2CO_3 is initially formed from the Li_2O_2 reduction product Li_2O and the CO_2 that derives from the oxidation of PEO triggered by the decomposition of Li_2O_2. This experiment clearly confirms that the vigorous reaction of Li_2O_2–C mixtures with or without PEO is not just due to the evolution of regular triplet oxygen, but due to the formation of an extremely reactive "nascent" oxygen species during Li_2O_2 decomposition.

The feasibility of a TA of Li_2O_2-prefilled electrodes without triggering a vigorous reaction under specific conditions (*i.e.*, low heating rate) permits us to quantify the results precisely, extend the TA temperature range up to 925 °C, and add an isothermal step at 925 °C while switching the atmosphere from argon to 67% oxygen in argon to oxidize all organic fractions of the sample so that Li_2O remains as the only residue. This extended TA procedure is shown in Fig. 9a. Please refer to the Experimental section for further details on the TA procedures. In the following, this extended TA is discussed in more detail.

Table 3 Reactions of Li_2O_2–C–PEO electrodes observed during thermal analysis

No.	T range [°C]	Atmos-phere	Reaction	Δm(total) theo/meas [% sample]	Δm(LiX) theo/meas [% sample]	Δm(C) theo/meas [% sample]	Evolved(↑) or consumed(↓) gases	ΔG^R at T_{onset}/T_{endset} [kJ mol^{-1}]
(9)	220–450	Ar	$[C_2H_4O]_n$ decomposition[a]	−9.1/−2.6 overlap with (13)	−9.1/−2.6 overlap with (13)	0/0	$CH_3\uparrow$, $C_2H_4O\uparrow$, $C_4H_8O_2\uparrow$, $CO\uparrow$, $H_2O\uparrow$	n.d.
(10)	220–400	Ar	$5nLi_2O_2 + [C_2H_4O]_n \rightarrow 5nLi_2O + 2nH_2O + 2nCO_2$	Compensated by (11,12)	Compensated by (11,12)	0/0	$H_2O\uparrow$, $CO_2\uparrow$	n.d.
(11)	220–400	Ar	$Li_2O + H_2O \rightarrow 2LiOH$	Compensated by (10)	Compensated by (10)	0/0	$H_2O\downarrow$	−66/−42
(12)	220–400	Ar	$Li_2O + CO_2 \rightarrow Li_2CO_3$	Compensated by (10)	Compensated by (10)	0/0	$CO_2\downarrow$	−146/−118
(13)	220–600	Ar	$4LiOH + C \rightarrow Li_2CO_3 + Li_2O + 2H_2$	≤−2.0/−1.6 overlap with (9,3)	≤+4.0/+3.2 overlap with (9,3)	≤−6.0/−4.8 overlap with (9,3)	$H_2\uparrow$	+18/−51
(3)	400–600	Ar	$2LiOH \rightarrow Li_2O + H_2O$	≤−17.9/−1.6 overlap with (13)	≤−17.9/−1.6 overlap with (13)	0/0	$H_2O\uparrow$	+42/+16
(14)	600–850	Ar	$Li_2CO_3 + C \rightarrow Li_2O + 2CO$	≤−55.6/−29.9	≤−43.7/−23.5	≤−11.9/−6.4	$CO\uparrow$	+101/+15
(6)	925	O_2	$C + O_2 \rightarrow CO_2$	−45.5 −$\Delta m(C)$ of (13,14)/−34.4	0/0	−45.5 −$\Delta m(C)$ of (13,14)/−34.4	$CO_2\uparrow$	−387
(7)	925	O_2	$Li_2O + CO_2 \rightarrow Li_2CO_3$	Overlap with (6)	Overlap with (6)	0/0	$CO_2\downarrow$	−38
(4)	925	O_2	$Li_2CO_3 \rightarrow Li_2O + CO_2$	Overlap with (6)	Overlap with (6)	0/0	$CO_2\uparrow$	+38

[a] See Fig. S2 in the ESI.

As mentioned before, in the temperature range of 220 to 400 °C, Li_2O_2 reacts with Li_2O and "nascent" oxygen which is taken up by PEO. Thereby PEO is decomposed to yield water, CO_2 and organic fragments. These combined reactions are summarized in Table 3, reaction No. 10. However, only minor amounts of organic fragments and neither water nor CO_2 are released. This indicates that the water formed during this process is instantly taken up by Li_2O, yielding LiOH (Table 3, reaction No. 11). Concurrently, all formed CO_2 is taken up by Li_2O, yielding Li_2CO_3 (Table 3, reaction No. 12). All these processes take place during the already mentioned 2.6% mass loss in the temperature range of 220 to 400 °C. In these subsequent reactions lies a major difference in the electrochemical charging of a Li_2O_2-prefilled electrode. As the electrochemical process does not produce any Li_2O, LiOH and Li_2CO_3 cannot be formed *via* reactions No. 11 and No. 12 (otherwise the OEMS data in Fig. 3 would show a much more pronounced CO_2 release once the charging voltage increases beyond ≈4.7 V, where Li_2CO_3 can be oxidized to CO_2).[39]

The additional hydrogen release monitored between 220 and 400 °C is now discussed together with the subsequent 1.6% mass loss between 400 and 600 °C, which is also accompanied by hydrogen release. Both H_2 peaks indicate that the previously formed LiOH (see above) reacts with carbon to form Li_2CO_3, Li_2O and hydrogen *via* reaction No. 13 in Table 3. This reaction pathway has been confirmed by a reference TA of LiOH–C (see Fig. S5 in the ESI†). In the 220 to 400 °C range, LiOH decomposition takes place solely *via* reaction No. 13, whereas from 400 to 600 °C, reactions No. 13 and No. 3 are both seen (No. 3 evidenced by minor H_2O release). In summary, the 2.6% mass loss between 220 and 400 °C is attributed to overlapping reactions No. 9 and No. 13, whereas the 1.6% mass loss from 400 to 600 °C is due to reactions No. 13 and No. 3. The additional reactions No. 10, No. 11 and No. 12, all taking place between 220 and 400 °C, do not contribute to any net change in sample mass.

Between 650 and 900 °C, another weight loss of 29.9% is seen and carbon monoxide is released. This points out that Li_2CO_3 (product of the previous reactions No. 12 and No. 13) is decomposed to give Li_2O *via* reaction No. 14 in Table 3 (see also Fig. S4, ESI† for reference).

At the final temperature of 925 °C, the gas atmosphere is switched from pure argon to a mixture of 67% oxygen in argon. This results in the total oxidation of the complete carbon fraction (Table 3, No. 6). This combustion temporarily leads to a partial pressure of CO_2 that is high enough to trigger the formation of Li_2CO_3 from Li_2O (Table 3, No. 7). However, as CO_2 is quickly removed by the TGA carrier gas, the reaction is reversed and all Li_2CO_3 is again converted to Li_2O (Table 3, No. 4). This reaction results in the sharp peak in the TGA curve directly after switching to the oxidizing atmosphere. For thermodynamic considerations, please refer to the discussion in Section 3.3 about the calculation of ΔG^R and its dependency on the partial pressure of gaseous reactants and products. After the decomposition of this transient Li_2CO_3 and the total oxidation of carbon are complete, a residue of 30.5% is left, which consists of pure Li_2O. This amount of Li_2O is equivalent to an initial Li_2O_2 fraction of 46.9%, an excellent match of the 45.5% Li_2O_2 content of the electrode ink used for synthesis. This confirms that Li_2O_2 is well preserved during electrode preparation. For example, if 12% of the initial Li_2O_2 had reacted with Li_2CO_3 during preparation, the expected Li_2O residue would be 28.5%, whereas if 12% had reacted with Li_2O, the residue would be 31.8%. As the weight span between 28.5 and 31.8% exceeds the estimated error range of $30.5 \pm 1.0\%$ of the instruments when determining the residual sample weight after TA, it can be stated that at least 88% Li_2O_2 purity (compared to 95% initial purity) is preserved during electrode preparation. It has to be mentioned that this method does not allow us to rule out LiOH contamination of the electrodes. However, the comparison of the X-ray diffraction patterns of electrodes prefilled with Li_2O_2 or LiOH (Fig. 1) allows us to exclude this.

In summary, the PEO binder acts as a scavenger for "nascent" oxygen released by Li_2O_2 decomposition, and therefore prevents the rapid and highly exothermic reaction of Li_2O_2 with carbon at moderate heating rates. At ≈ 300 °C, PEO is thereby decomposed to yield water, CO_2 and organic fragments. However, water and CO_2 are instantly taken up by the Li_2O that has been formed during the thermal decomposition of Li_2O_2. While PEO in the above described thermogravimetric experiments is a good model compound to mimic the reaction of glyme-based electrolytes (*e.g.*, DEGDME) during charging in lithium–air batteries, there are, however, two fundamental differences between the thermal and the electrochemical decomposition of Li_2O_2 which must be considered: (i) as the electrochemical charging of Li_2O_2 does not produce Li_2O, any H_2O or CO_2 formed during the oxidative decomposition of the electrolyte would indeed be evolved; and (ii) the fact that H_2O and CO_2 are not detected by OEMS during electrochemical charging points out that the reaction of "nascent" oxygen with the electrolyte at room temperature (*i.e.*, in a battery cell) leads to non-volatile partial oxidation products rather than the total oxidation of the electrolyte.

4. Conclusions

We have reported a novel preparation procedure for Li_2O_2-prefilled electrodes, using ink-processing solvents and binders which are stable in the presence of Li_2O_2.

It has been demonstrated that in-depth analysis of the composition and reactivity of Li_2O_2-prefilled carbon cathodes for lithium/air batteries by TGA-MS is feasible. The thermal decomposition of Li_2O_2 to Li_2O is suggested to produce highly reactive "nascent" oxygen. In Li_2O_2–C mixtures, this "nascent" oxygen reacts in a very rapid and highly exothermic reaction with carbon at already ≈ 300 °C, whereas gas-phase oxygen does not react with carbon until ≈ 500 °C. In Li_2O_2–PEO–C electrodes, this reaction does not occur at low heating rates, because the PEO binder acts as a scavenger for "nascent" oxygen. Thereby, PEO is decomposed to H_2O, CO_2, and organic oxidation products. H_2O and CO_2 are not released, but instantly react with Li_2O, yielding LiOH and Li_2CO_3. The thermal decomposition of these lithium salts at higher temperatures involves an oxidative degradation of the carbon support.

During the electrochemical charging procedure of Li–O_2 batteries containing Li_2O_2-prefilled carbon cathodes, oxygen is released at a lower rate than expected for a quantitative $2e^-$ process. As our TA results suggest, part of the formed "nascent" oxygen reacts with the DEGDME electrolyte which is chemically very closely related to PEO, the PEO binder, and/or the Vulcan carbon support. The extent of these degradation reactions depends on the specific area of the Li_2O_2–electrolyte interface. During the charging of electrodes prefilled with ≈ 1 μm-sized Li_2O_2 particles, this process consumes $\approx 5\%$ of the formed oxygen, whereas the charging of a previously discharged carbon cathode covered with a nanometer-sized Li_2O_2 film leads to a significantly larger amount of "missing" oxygen.

Clearly, this limited stability of the electrolyte, binder, and carbon support towards "nascent" oxygen produced by the electrochemical Li_2O_2 decomposition has to be overcome to successfully produce Li–air batteries with long cycle-life. Furthermore, the vigorous reaction of Li_2O_2-prefilled electrodes under thermal stress at high heating rates points out potential safety issues of carbon based Li–air cathodes, so that carbon is most likely not a feasible cathode material for Li–air batteries as it compromises both their long-term stability and thermal stability.

Acknowledgements

We would like to thank Arnd Garsuch from BASF SE for stimulating and fruitful discussions. Support of BASF SE in the framework of its scientific network on electrochemistry and batteries is acknowledged by TUM. N. Tsiouvaras acknowledges the Alexander von Humboldt Foundation for his postdoctoral researcher fellowship.

Notes and references

1 F. T. Wagner, B. Lakshmanan and M. F. Mathias, *J. Phys. Chem. Lett.*, 2010, **1**, 2204–2219.
2 Y.-C. Lu, H. A. Gasteiger, M. C. Parent, V. Chiloyan and Y. Shao-Horn, *Electrochem. Solid-State Lett.*, 2010, **13**, A69–A72.
3 Y.-C. Lu, D. G. Kwabi, K. P. C. Yao, J. R. Harding, J. Zhou, L. Zuin and Y. Shao-Horn, *Energy Environ. Sci.*, 2011, **4**, 2999–3007.
4 P. G. Bruce, S. A. Freunberger, L. J. Hardwick and J. M. Tarascon, *Nat. Mater.*, 2012, **11**, 19–29.
5 B. D. McCloskey, R. Scheffler, A. Speidel, D. S. Bethune, R. M. Shelby and A. C. Luntz, *J. Am. Chem. Soc.*, 2011, **133**, 18038–18041.
6 F. Mizuno, S. Nakanishi, Y. Lotani, S. Yokoishi and H. Iba, *Electrochemistry*, 2010, **78**, 403.
7 G. Girishkumar, B. McCloskey, A. C. Luntz, S. Swanson and W. Wilcke, *J. Phys. Chem. Lett.*, 2010, **1**, 2193–2203.
8 F. Li, T. Zhang and H. Zhou, *Energy Environ. Sci.*, 2013, **6**, 1125–1141.
9 Z. Peng, S. A. Freunberger, Y. Chen and P. G. Bruce, *Science*, 2012, **337**, 563–566.

10 S. A. Freunberger, Y. Chen, Z. Peng, J. M. Griffin, L. J. Hardwick, F. Bardé, P. Novak and P. G Bruce, *J. Am. Chem. Soc.*, 2011, **133**, 8040–8047.

11 B. D. McCloskey, D. S. Bethune, R. M. Shelby, G. Girishkumar and A. C. Luntz, *J. Phys. Chem. Lett.*, 2011, **2**, 1161–1166.

12 N. Tsiouvaras, S. Meini, I. Buchberger and H. A. Gasteiger, *J. Electrochem. Soc.*, 2013, **160**, A471–A477.

13 F. Mizuno, *Electrochemistry*, 2010, **78**, 403–405.

14 S. A. Freunberger, Y. Chen, N. E. Drewett, L. J. Hardwick, F. Bardé and P. G. Bruce, *Angew. Chem., Int. Ed.*, 2011, **50**, 8609–8613.

15 J. Herranz, A. Garsuch and H. A. Gasteiger, *J. Phys. Chem. C*, 2012, **116**, 19084–19094.

16 Y. C. Lu, H. A. Gasteiger and Y. Shao-Horn, *J. Am. Chem. Soc.*, 2011, **133**, 19048–19051.

17 D. Aurbach, M. L. Daroux, P. Faguy and E. B. Jeager, *J. Electroanal. Chem.*, 1991, **297**, 225–244.

18 V. S. Bryantsev, M. Blanco and F. Faglioni, *J. Phys. Chem. A*, 2011, **115**, 12399–12409.

19 R. Black, S. H. Oh, J. H. Lee, T. Yim, B. Adams and L. F. Nazar, *J. Am. Chem. Soc.*, 2012, **134**, 2902–2905.

20 K. U. Schwenke, S. Meini, X. Wu, H. A. Gasteiger and M. Piana, *Phys. Chem. Chem. Phys*, DOI: 10.1039/C3CP51531A.

21 H. Lim, E. Yilmaz and H. R. Byon, *J. Phys. Chem. Lett.*, 2012, **3**, 3210–3215.

22 S. Meini, M. Piana, H. Beyer, J. Schwämmlein and H. A. Gasteiger, *J. Electrochem. Soc.*, 2012, **159**, A2135–A2142.

23 B. D. McCloskey, D. S. Bethune, R. M. Shelby, T. Mori, R. Scheffler, A. Speidel, M. Sherwood and A. C. Luntz, *J. Phys. Chem. Lett.*, 2012, **3**, 3043–3047.

24 D. Chalasani and B. L. Lucht, *ECS Electrochem. Lett.*, 2012, **1**, A38–A42.

25 B. D. McCloskey, A. Speidel, R. Scheffler, D. C. Miller, V. Viswanathan, J. S. Hummelshoj, J. K. Norskov and A. C. Luntz, *J. Phys. Chem. Lett.*, 2012, **3**, 997–1001.

26 B. M. Gallant, R. R. Mitchell, D. G. Kwabi, J. Zhou, L. Zuin, C. V. Thompson and Y. Shao-Horn, *J. Phys. Chem. C*, 2012, **116**, 20800–20805.

27 R. Black, J. H. Lee, B. Adams, C. A. Mims and L. F. Nazar, *Angew. Chem., Int. Ed.*, 2013, **52**, 392–396.

28 M. M. OttakamThotiyl, S. A. Freunberger, Z. Peng and P. G. Bruce, *J. Am. Chem. Soc.*, 2013, **135**, 494–500.

29 V. Giordani, S. A. Freunberger, P. G. Bruce, J. M. Tarascon and D. Larcher, *Electrochem. Solid-State Lett.*, 2010, **13**, A180–A183.

30 W. Xu, K. Xu, V. V. Viswanathan, S. A. Towne, J. S. Hardy, J. Xiao, Z. Nie, D. Hu, D. Wang and J.-G. Zhang, *J. Power Sources*, 2011, **196**, 9631–9639.

31 W. Xu, V. V. Viswanathan, D. Wang, S. A. Towne, J. Xiao, Z. Nie, D. Hu and J.-G. Zhang, *J. Power Sources*, 2011, **196**, 3894–3899.

32 J. R. Harding, Y.-C. Lu, Y. Tsukada and Y. Shao-Horn, *Phys. Chem. Chem. Phys.*, 2012, **14**, 10540–10546.

33 G. V. Chase, S. Zecevic, T. Walker Wesley, J. Uddin, K. S. Sasaki, P. G. Vincent, V. Bryantsev, M. Blanco and D. D. Addison, *US Patent*, No. 2012/0028137 A1 2012.

34 O. A. Baturina, S. R. Aubuchon and K. J. Wynne, *Chem. Mater.*, 2006, **18**, 1498–1504.

35 A. B. Tsentsiper and Z. I. Kuznetsova, *Russ. Chem. Bull.*, 1965, **14**, 1873–1875.

36 Y. A. Ferapontov, N. V. Kokoreva, N. P. Kozlova and M. A. Ul'yanova, *Russ. J. Gen. Chem.*, 2009, **79**, 891–894.

37 G. K. Jones, A. R. McGhie and G. C. Farrington, *Macromolecules*, 1991, **24**, 3285–3290.

38 L. L. Zhang, T. Wei, W. Wang and X. S. Zhao, *Microporous Mesoporous Mater.*, 2009, **123**, 260–267.

39 S. Meini, N. Tsiouvaras, K. U. Schwenke, M. Piana, H. Beyer, L. Lange and H. A. Gasteiger, *Phys. Chem. Chem. Phys.*, DOI: 10.1039/C3CP51112J.

40 S. Meini, M. Piana, N. Tsiouvaras, A. Garsuch and H. A. Gasteiger, *Electrochem. Solid-State Lett.*, 2012, **15**, A45–A48.

41 S. E. Stein, in *Mass Spectra in NIST Chemistry WebBook, NIST Standard Reference Database Number 69*, ed. P. J. Linstromand and W. G. Mallard, National Institute of Standards and Technology, Gaithersburg, MD, 2013 20899, http://webbook.nist.gov, (retrieved February 12, 2013).

42 V. S. Bryantsev and F. Faglioni, *J. Phys. Chem. A*, 2012, **116**, 7128–7138.

43 R. C. Melucci and J. P. Wightman, *Carbon*, 1966, **4**, 467–472.

44 W. Walker, V. Giordani, V. S. Bryantsev, J. Uddin, S. Zecevic, D. Addison and G. V. Chase, *Abstract No. 1112*, Honolulu PRiME 2012.

45 V. Viswanathan, K. S. Thygesen, J. S. Hummelshøj, J. K. Nørskov, G. Girishkumar, B. D. McCloskey and A. C. Luntz, *J. Chem. Phys.*, 2011, **135**, 214704.

46 A. L. Dicks, *J. Power Sources*, 2006, **156**, 128–141.

47 K. Kinoshita, *Carbon*, John Wiley & Sons, New York, 1988.

48 S. r. R. J. Lewis, *Hawley's Condensed Chemical Dictionary*, John Wiley & Sons, New York, 14th edn, 2001, p. 677.

49 *CRC Handbook of Chemistry and Physics*, ed. D. R. Lide, CRC Press, Boca Raton, FL, 85th edn, 2004–2005, p. 60.

50 T. Tanifuji and S. Nasu, *J. Nucl. Mater.*, 1979, **87**, 189–195.

51 H. Y. Wu, H. Zhang, X. L. Cheng and L. C. Cai, *Phys. Lett. A*, 2006, **360**, 352–356.

52 in *CRC Handbook of Chemistry and Physics*, ed. D. R. Lide, CRC Press, Boca Raton, FL, 85th edn, 2004–2005, pp. 4–66.

53 H. A. Mosqueda, C. Vazquez, P. Bosch and H. Pfeiffer, *Chem. Mater.*, 2006, **18**, 2307–2310.

Supplementary Information
for

Thermal and Electrochemical Decomposition of Lithium Peroxide in Non-Catalyzed Carbon Cathodes for Li-Air Batteries

H. Beyer*[a], S. Meini[a], N. Tsiouvaras[a], M. Piana[a], and H. A. Gasteiger[a]

[a] *Institute of Technical Electrochemistry, Technische Universität München, Lichtenbergstr. 4, D-85748, Garching, Germany. Fax: +498928913674; Tel: +4 8928913658; E-mail: hans.beyer@tum.de*

Electrochemical oxidation of Li_2O_2 in prefilled electrodes using an LFP counterelectrode

To calculate the extent of oxygen consumption at the Li metal anode under the experimental conditions in Fig. 3 of the manuscript, a charging experiment of an identical Li_2O_2-prefilled cathode under the same conditions, but using a LFP anode and an additional solid electrolyte diffusion barrier (Ohara glass) is conducted (s. Fig. S1).

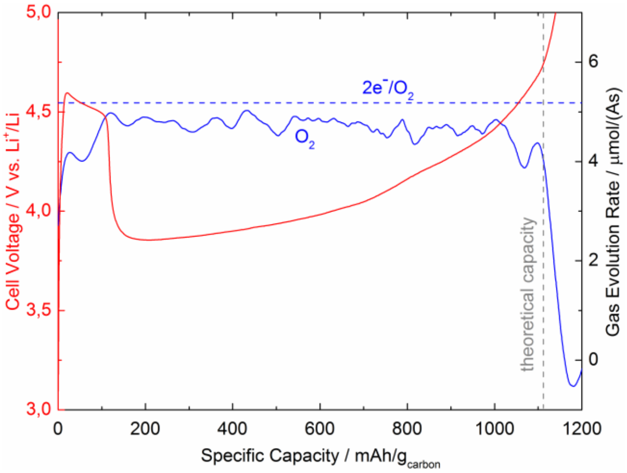

Fig. S1 Galvanostatic charging of a Li_2O_2-prefilled electrode (Li_2O_2/PEO/C) with 0.39 mg_{carbon}/cm^2) under argon at 120 mA/g_{carbon} (≡83 µA) in DEGDME with 0.2 M LiTFSI using an LFP counterelectrode and a solid electrolyte diffusion barrier (Ohara glass): *i)* red line: galvanostatic voltage profile; *ii)* blue line: current-normalized molar gas evolution rate of O_2. The dotted blue line shows the theoretical O_2 evolution rate corresponding to the desired oxygen evolution rate of $2e^-/O_2$ (according to Eq. 1 in the main manuscript); the vertical dashed gray line marks the theoretical charging capacity of 1110 mAh/g_{carbon} (based on a Li_2O_2/C weight ratio of 1/1 and 95% Li_2O_2 purity).

It is found that the average O_2 evolution rate in Fig. S1 corresponds to ≈4.70 µmol/(As). Comparing this rate to the average O_2 evolution rate of ≈4.45 µmol/(As) obtained in Fig. 3 of the manuscript, the oxygen consumption at the lithium anode in Fig. 3 equals ≈0.25 µmol/(As). This finding implies that the remaining discrepancy between the oxygen evolution in Fig. S1 and the theoretical oxygen evolution rate of 5.18 µmol/(As) has to be due to other side reactions, as further discussed in the manuscript.

TA of carbon (Vulcan XC72)

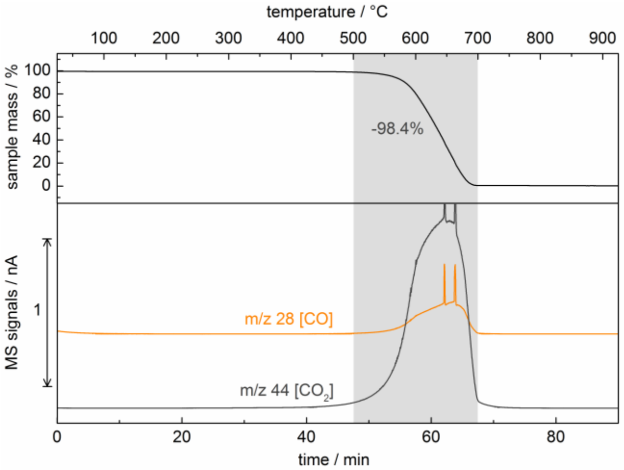

Fig. S2 TGA (sample mass vs. temperature) and on-line MS of evolved gases (mass traces with m/z of 28, and 44 attributed to CO, and CO_2, respectively) of carbon (Vulcan XC72). The percentage value given next to the TGA curve represents the measured mass loss, Δm meas, of the observed transition. The sample was ramped from 25 to 925°C in 67% O_2/Ar at a heating rate of 10 K/min.

The onset temperature of the thermal oxidation of carbon in 67%O_2/Ar is 500°C, as seen in Fig. S2. The oxidation product is CO_2 (as the intensities of the m/z 28 and 44 traces reflect the fingerprint ionization pattern of CO_2). The quantitative gasification of carbon is complete at 700°C.

TA of PEO/C

To better understand the TA of Li_2O_2/PEO/C electrodes, it is important to determine the reactions of a PEO/C mixture and the evolved gases during the same procedure that is used for the TA of electrodes. Thus, a PEO/C sample is first heated from 25 to 925°C in Ar, then held isothermal at 925°C while the atmosphere is switched from Ar to 67vol.% O_2 in Ar (s. Fig. S3).

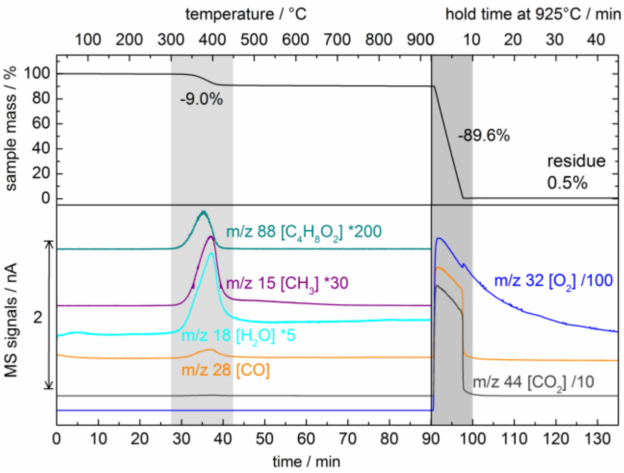

Fig. S3 TGA (sample mass vs. temperature) and on-line MS of evolved gases (mass traces with m/z of 32, 18, 28, 44, 15, and 88 attributed to O_2, H_2O, CO, CO_2, CH_3, and $C_4H_8O_2$, respectively) of C/PEO (mixing ratio 2/0.2). The percentage values given next to the TGA curve represent the measured mass losses, Δm meas, for each of the observed transitions. The multipliers/divisors in the mass trace labels represent the amplification factors used on the relative intensities of the respective signals. The sample was ramped at 10 K/min from 25 to 925°C in Ar and subsequently held isothermal at 925°C in 67vol.% O_2/Ar.

In the temperature range of roughly 300 to 450°C, PEO is decomposed quantitatively to volatile products (9.0% measured weight loss compared to 9.1% PEO content). Besides water and trace amounts of CO, also methyl- and/or dimethyl ether fragments (identified by the m/z 15 trace, which is also observed during the anodic oxidation of the chemically very similar DEGDME electrolyte shown in Fig. 2 of the manuscript) and 1,4-dioxane (generally accepted as the parent molecule of the m/z 88 trace)[1] are detected by the MS. The overall reaction is described in the manuscript, Tab. 3, reaction N°9. In Section 3.5 of the manuscript, the m/z 15 trace is chosen to monitor the decomposition of PEO to volatile organic fragments. Regarding the temperature range of PEO decomposition, it is expected to interfere with other processes in the thermal analysis of prefilled electrodes. The carbon fraction of the sample does not react up to 925°C under argon. When the atmosphere is switched to 67vol.% O_2 in Ar at 925°C, the total oxidation of carbon occurs, releasing CO_2 (the m/z 28 trace gives a signal ~1/9 of the intensity of the m/z 44 trace, which is consistent with the fingerprint of pure CO_2). Accordingly, no residue of the PEO/C sample is left at the end of the analysis.

TA of Li_2CO_3/C

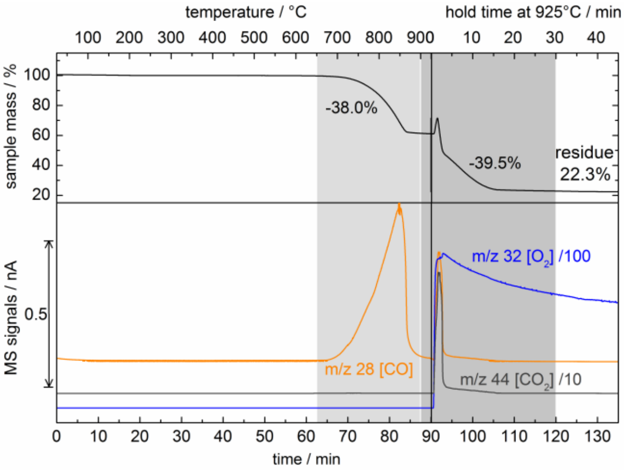

Fig. S4 TGA (sample mass vs. temperature) and on-line MS of evolved gases (mass traces with m/z of 32, 28, and 44 attributed to O_2, CO, and CO_2, respectively) of Li_2CO_3/C (mixing ratio 1/1). The percentage values given next to the TGA curve represent the measured mass losses, Δm meas, for each of the observed transitions. The multipliers/divisors in the mass trace labels represent the amplification factors used on the relative intensities of the respective signals. The sample was ramped from 25 to 925°C in Ar at a heating rate of 10 K/min and subsequently held isothermal at 925°C in 67vol.% O_2/Ar.

Fig. S4 shows that the presence of carbon changes both the temperature window and the reaction mechanism of Li_2CO_3 decomposition. Between 650 and 900°C, Li_2CO_3 reacts with carbon to form Li_2O and CO. The measured mass loss of 38.0% corresponds very well to the calculated loss of 37.9% for reaction N°14 (Tab. S1).

Table S1 Reactions of a Li_2CO_3/C mixture (mixing ratio 1/1) observed during thermal analysis.

N°	**T range [°C]**	**atmos-phere**	**reaction**	**Δm(total) theo./meas. [% sample]**	**Δm(LiX) theo./meas. [% sample]**	**Δm(C) theo./meas. [% sample]**	**evolved(↑) gases**	**ΔG_R at T_{onset}/T_{endset} [kJ/mol]**
(14)	650–900	Ar	$Li_2CO_3 + C \rightarrow Li_2O + 2\ CO$	-37.9 / -38.0	-29.8 / -29.9	-8.1 / -8.1	CO↑	+84/-2
(6)	925	O_2	$C + O_2 \rightarrow CO_2$	-41.9 / -39.5	0 / 0	-41.9 / -39.5	CO_2↑	-387

TA of LiOH/C

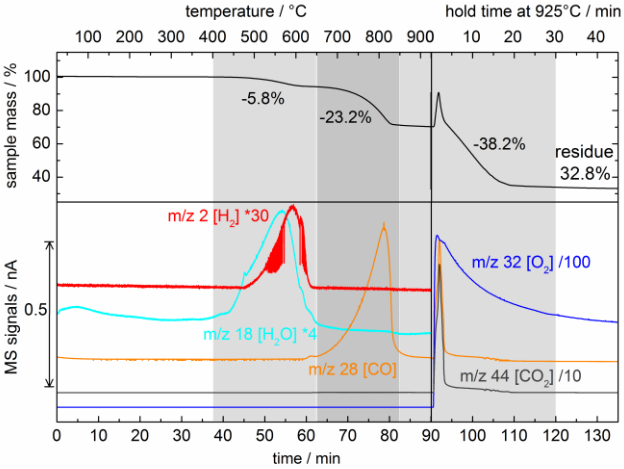

Fig. S5 TGA (sample mass vs. temperature) and on-line MS of evolved gases (mass traces with m/z of 32, 18, 28, 44, and 2 attributed to O_2, H_2O, CO, CO_2, and H_2, respectively) of LiOH/C (mixing ratio 1/1). The percentage values given next to the TGA curve represent the measured mass losses, Δm meas, for each of the observed transitions. The multipliers/divisors in the mass trace labels represent the amplification factors used on the relative intensities of the respective signals. The sample was ramped from 25 to 925°C in Ar at a heating rate of 10 K/min and subsequently held isothermal at 925°C in 67vol.% O_2/Ar.

The MS traces in Fig. S5 point out that the mass loss between 400 and 620°C arises from two distinct reactions: The decomposition of LiOH without the involvement of carbon (Tab. S2, N°3) produces H_2O, whereas the simultaneous reaction of LiOH with carbon (Tab. S2, N°13) releases H_2. Both reactions produce Li_2O, and reaction N°13 additionally yields Li_2CO_3, which subsequently decomposes between 650 and 900°C following the same mechanism as discussed for Li_2CO_3/C mixtures. The measured weight loss of 23.2 % during Li_2CO_3 decomposition indicates a transient Li_2CO_3 content of 29.7 wt.% in the sample. This number suggests that initially, 11.2 wt.% of the sample mass (=22.4 % of LiOH) react via N°3, whereas 38.8 wt.% (=77.6 % of LiOH) react via N°13. This ratio would theoretically arise from a weight loss of 5.8 % between 400 and 650°C (4.2 % from N°3 and 1.6 % from N°13), which exactly matches the actually measured value.

Table S2 Reactions of a LiOH/C mixture (mixing ratio 1/1) observed during thermal analysis.

N°	**T range [°C]**	**atmos-phere**	**reaction**	**Δm(total) theo./meas. [% sample]**	**Δm(LiX) theo./meas. [% sample]**	**Δm(C) theo./meas. [% sample]**	**evolved(↑) gases**	**ΔG_R at T_{onset}/T_{endset} [kJ/mol]**
(3)	400–650	Ar	$2\ LiOH \rightarrow Li_2O + H_2O$	-18.8 / -4.2	-18.8 / -4.2	0 / 0	H_2O↑	+42 / +10
(13)	400–650	Ar	$4\ LiOH + C \rightarrow Li_2CO_3 + Li_2O + 2\ H_2$	-2.1 / -1.6	+4.2 / +3.3	-6.3 / -4.9	H_2↑	-8 / -62
(14)	650–850	Ar	$Li_2CO_3 + C \rightarrow Li_2O + 2\ CO$	var. / -23.2	-17.7 / -18.2	-4.8 / -5.0	CO↑	+84 / ±15
(6)	925	O_2	$C + O_2 \rightarrow CO_2$	-38.9 / -38.2	0 / 0	-38.9 / -38.2	CO_2↑	-387

Thermodynamic data of lithium salts

Table S3 Data used for all thermodynamic calculations in this work. $G_{(T_0)}$, $S_{(T_0)}$ and $c_{p_{(T_0)}}$ values are generally taken from[2], except for $c_{p_{(T_0)}}$ of Li_2O_2, as discussed in Section 3.3.

compound	$\Delta H^f_{(T_0)}$ **[kJ/mol]**	$\Delta G^f_{(T_0)}$ **[kJ/mol]**	$S_{(T_0)}$ **[J/(molK)]**	$c_{p\,(T_0)}$ **[J/(molK)]**
Li (s)	0	0	29.1	24.8
C (s)	0	0	5.7	8.5
H_2 (g)	0	0	130.7	28.8
O_2 (g)	0	0	205.2	29.4
CO (g)	-110.5	-137.2	197.7	29.1
CO_2 (g)	-393.5	-394.4	213.8	37.1
H_2O (g)	-241.8	-228.6	188.8	33.6
Li_2O (s)	-597.9	-561.2	37.6	54.1
Li_2O_2 (s)	-634.3	-570.2	56.42	71.0
LiOH (s)	-487.5	-441.5	42.8	49.6
Li_2CO_3 (s)	-1215.9	-1132.1	90.4	99.1

Literature

1 G. K. Jones, A. R. McGhie, and G. C. Farrington, *Macromolecules*, 1991, **24**, 3285–3290.
2 D. R. Lide (Ed.), CRC Handbook of Chemistry and Physics, 85th ed., CRC Press, Boca Raton, FL, 2004–2005, pp. 5-4 – 5-60.

4.4 Conclusions

The results reported in this chapter provided further understand about the origins of the capacity fading observed for Li-O_2 cells based on carbon positive electrodes. The O_2 evolution determined by mass spectrometry from discharged electrodes in diglyme is always lower than the value expected for electrooxidation of the desired product Li_2O_2; similar results are obtained for Li_2O_2 model electrodes, suggesting that the lower current normalized evolution rate is not related to formation of minor Li_2O quantities, but rather to the reactivity of Li_2O_2 and the evolved oxygen with carbon and solvent at high voltages.

Fundamental studies performed by thermo gravimetric analysis revealed that Li_2O_2 is stable in presence of carbon at room temperature, however a violent thermal reaction occurs between 300-400 °C when a mixture of those two materials is heated at scan rates $\geq$10 K/min. The main gas evolved is CO, suggesting that the thermal decomposition of Li_2O_2 proceeds through an intermediate "nascent (or atomic) oxygen", capable of reacting with carbon at temperatures much lower than needed for combustion with dioxygen O_2 (>600 °C). On the other hand, the presence of polyethers (PEO, binder) or slower heating programs (<10 K/min) lead to the conversion of Li_2O_2 into Li_2CO_3.

The electrooxidation of Li_2O_2 using glyme electrolyte solvents resembles its thermal decomposition in presence of PEO binder (whose local chemical structure is identical to that of glymes), whereby Li_2CO_3 is the end product of the reaction of carbon with the "nascent oxygen" intermediate. Indeed, CO_2 evolved at the end of charge (detected by mass spectrometry) at high potentials suggests that Li_2CO_3 has been previously formed. The net O_2 consumed by processes that cannot be ascribed to measurement artifacts, the "nascent oxygen", accounts for only $\approx$5 % of the total oxygen evolved by Li_2O_2 electrooxidation.

As Li_2CO_3 and LiOH in non-catalyzed pre-filled electrodes can be electrooxidized only at voltages >4.8 V_{Li}, the conversion of a fraction of Li_2O_2 into non-Li_2O_2 products results in an irreversible deposition of those atop the electrode surface and thus to capacity fading due to electrode passivation upon cycling.

Chapter 5

Conclusions

Increasing environmental concerns related to the use of fossil fuels for powering private transportation translated into an increasing interest for electromobility. The total electrification of the consumer vehicular fleet would be a long-term solution to both environmental issues and to eventual shortages in the supply of liquid hydrocarbons. In order to power future electric vehicles, there is a need for advanced energy storage technologies characterized by long cycle life, high energy density, high specific energy and low cost. State of the art Li-ion batteries fulfill the first two needs; however their widespread implementation on full electric battery powered vehicles is prevented by their high weight and cost.

Non-aqueous rechargeable Li-air batteries can be a promising alternative to Li-ion technology for automotive applications. The projected practical specific energy of a fully packed Li-air battery is 3-fold higher than Li-ion batteries; moreover, the cathode material (O_2) is readily available from the atmosphere.

Unfortunately, despite some successful demonstrations in the early times of their development, where up to 100 cycles were obtained using a alkyl carbonate electrolyte solution, Li-air cells built with high surface carbon-based positive electrode suffer severe capacity fading and high overpotentials upon recharge. That combination leads to poor cycle life and low round-trip efficiency.

The development of rechargeable Li-air battery devices is projected to last until the 2050s; it is very important at this stage of development to get further basic knowledge of the electrochemical mechanisms involved in the discharge (oxygen reduction reaction and the role of intermediates) and the charge (oxygen evolution reaction, catalysis and parasitic reactions), in order to design solutions to the respective issues and make the technology viable. The fundamental research performed for this doctoral thesis provided essential understanding in both aspects.

In this thesis work, it was shown that oxygen electroreduction on non-catalyzed carbon surfaces at relatively high discharge rates leads to the precipitation of an electrically insulating film of discharge products, when electrolyte solutions that are stable to ORR intermediates are used. That kind of discharge mechanism denotes a very low rate capability of Li-air systems. The natural implication is that if the positive electrode porosity cannot be filled not even partially by discharge products, the discharge capacity will be limited to the surface area of the electrode material; as the theoretical improvement of Li-air batteries in terms of specific energy originate by the much higher specific capacity of the discharge products in comparison to Li-ion battery cathode materials, those limitations raise doubts on the effective advantage of Li-air technology.

Li-air discharge capacity is strongly influenced by substances that react with oxygen reduction reaction intermediates produced at the electrode surface; as a general rule, those substances tend to *increase* the discharge capacity by a factor of 3-15, depending on the nature of the reactant. The capacity enhancing activity of those substances seem to be related to the enhanced mobility/solubility of ORR intermediates/substance complexes, whose lifetime in solution is much longer than $LiO_2/O_2^{-\bullet}$; this results in a delayed passivation of the electrode surface. Several substances were demonstrated to have that ability; among the others, reactive alkyl carbonates like propylene carbonate, glyme degradation products and H_2O (the latter either added to the electrolyte solution or as vapor in the O_2 feed). The natural implication of those findings is that in order to avoid artifacts in capacity measurements, much effort must be invested in designing properly sealed cell hardware for testing, and that sporadic capacity enhancements should be critically evaluated. Less obvious observation, the capacity enhancing effect of some substances could be exploited to improve the rate capability of Li-air cells. A good "additive" in this respect should be first, stable in the conditions of a Li-air battery; second, have the ability to solvate ORR intermediates or enhance their mobility; third, promote the precipitation of Li_2O_2 as the only discharge product.

The search for stable electrolyte solvents was a common task in the most recent Li-air battery research. The definition of "stable" in Li-air batteries is pretty broad, and includes first, the stability at low potentials on (or the passivation of) the Li metal anode surface; second the stability in presence of O_2; third the stability towards ORR intermediates; fourth, the stability at high potentials during charge. In the most recent literature DMSO and some ionic liquids were revealed suitable candidates. In this thesis work, mostly glymes (i.e. ethers) were used as non-aqueous solvents for Li-O_2 cells electrolyte solutions. We demonstrated that glymes have high stability towards ORR intermediates, however they tend to decompose at potentials >4 V_{Li} in presence of O_2 leading to decomposition products which introduce artifacts in measuring discharge capacity. Glyme solvents are therefore *not ideal* solvents for Li-O_2 batteries, however they have several advantages over newly employed solvents (for instance, they are relatively stable on Li metal surfaces) that make their use still convenient.

The charge of Li-O_2 batteries with carbon-based positive electrodes is a major concern. Both on non-catalyzed and catalyzed carbon surfaces, the O_2 consumed during charge cannot be fully recovered on charge. The reaction of "nascent oxygen" partially formed during the electrooxidation of Li_2O_2 with carbon leads to Li_2CO_3, which cannot be fully electrooxidized within the voltage constraints applied in commonly used cycling procedures. The accumulation of non-Li_2O_2 products in the electrode matrix is responsible for the capacity fading that limits cycle life of Li-O_2 cells to less than 10 cycles. That intrinsic reactivity of Li_2O_2 (or nascent oxygen) with carbon puts severe limitations to the use of the latter inexpensive and well-characterized material, and triggered the development of carbon free positive electrodes. At the present stage, both the electrolyte solution and the carbon-based electrode of Li-O_2 cells seem to be unstable upon charge, introducing great confusion when studying parasitic reactions during charge. If reliable results on the stability of the electrolyte solution have to be obtained, efforts in the development of inert electrode materials (one example is the nanoporous gold electrode shown by Peter G. Bruce and coworkers) should be invested. Several projects for synthesizing and developing non-carbon materials have been recently started at TUM.

References

[1] Meadows, D.H.; Meadows, D.L.; Randers, J.; Behrens, W.W. III; *Limits to growth*, Universe Books, **1972**, New York (USA).

[2] Wagner, F.T.; Lakshmanan, B.; Mathias, M.F.; *J. Phys. Chem. Lett.* **2010**, 1, 2204-2219.

[3] Wipke, K.; Spirk, S.; Kurtz, J.; in *Handbook of Fuel Cells*, v. 6, Vielstich, W.; Yokokawa, H.; Gasteiger H.A. Eds.; John Wiley & Sons: Chichester, U.K., **2009**; pp 893-904, Chapter 60.

[4] Tarascon, J.-M.; *Phil. Trans. R. Soc. A* **2010**, 386, 3227-3241.

[5] Kraytsberg, A.; Enin-Eli, Y.; *Adv. Energy. Mater.* **2012**, 2, 922-939.

[6] Marom, R.; Amalraj, S.F.; Leifer, N.; Jacob, D.; Aurbach, D.; *J. Mater. Chem.* **2011**, 21, 9938-9954.

[7] Vesborg, P.C.K.; Jaramillo, T.F.; *RCS Advances* **2010**, 2, 7933-7947.

[8] Abraham, K.M.; Jiang, Z.; *J. Electrochem. Soc.* **1996**, 143, 1-5.

[9] Christensen, J.; Albertus, P.; Sanchez-Carrera, R.; Lohmann, T.; Kozinsky, B.; Liedtke, R.; Ahmed, J.; Koljc, A.; *J. Electrochem. Soc.* **2012**, 159, R1-R30.

[10] Girishkumar, G.; McCloskey, B.D.; Lunz, A.C.; Swanson, S.; Wilcke, W.; *J. Phys. Chem. Lett.* **2010**, 1, 2193-2203.

[11] Freunberger, S.A.; Chen, Y.; Drewett, N.E.; Hardwick, L.J.; Bardé, F.; Bruce, P.G.; *Angew. Chem. Int. Ed.* **2011**, 50, 8609-8613.

[12] Mitchell, R.R.; Gallant, B.M.; Thompson, C.V.; Shao-Horn, Y.; *Energy Environ. Sci.* **2011**, 4, 2952-2958.

[13] Gallant, B.M.; Mitchell, R.R.; Kwabi, D.G.; Zhou, J.; Zuin, L.; Thompson, C.V; Shao-Horn, Y.; *J. Phys. Chem. C* **2012**, 116, 20800-20805.

[14] Li, Y.; Wang, J.; Li, X.; Geng, D.; Li, R.; Sun, X.; *Chem. Commun.* **2011**, 47, 9438-9440.

[15] Yoo, E.; Zhou, H.; *ACS Nano* **2011**, 5, 3020-3026.

[16] Cao, Y.; Wei, Z.; He, J.; Zang, J.; Zhang, Q.; Zheng, M.; Dong, Q.; *Energy Environ. Sci.* **2012**, 5, 9765-9768.

[17] Lu, Y.-C.; Gasteiger, H.A.; Parent, M.C.; Chiloyan, V.; Shao-Horn, Y.; *Electrochem. Solid-State Lett.* **2010**, 13, A69-A72.

[18] Xiao, J.; Wang, D.; Xu, W.; Wang, D.; Williford, R.E.; Liu, J; Zhang, J.-G.; *J. Electrochem. Soc.* **2010**, 157, A487.

[19] Zhang, S.S.; Foster, D.; Read, J.; *J. Power Sources* **2010**, 195, 1235-1240.

[20] Zhang, G.Q.; Zheng, J.P.; Liang, R.; Zhang, C.; Wang, B.; Hendrickson, M.; Plichta, E.J.; *J. Electrochem. Soc.* **2010**, 157, A953-A956.

[21] Read, J.; *J. Electrochem. Soc.* **2002**, 149, A1190-A1195.

[22] Lu, Y.-C.; Kwabi, D.G.; Yao, K.P.C.; Harding, J.R.; Zhou, J.; Zuin, L.; Shao-Horn, Y.; *Energy Environ. Sci.* **2011**, 4, 2999-3007.

[23] Lu, Y.-C.; Xu, Z.; Gasteiger, H.A.; Chen, S.; Hamad-Schifferli, K.; Shao-Horn, Y.; *J. Am. Chem. Soc.* **2010**, 132, 12170-12171.

[24] Débart, A.; Paterson, A.J.; Bao, J.; Bruce, P.G.; *Angew. Chem.* **2008**, 47, 4521-4524.

[25] Read, J.; Mutolo, K.; Ervin, M.; Behl, W.; Wolfenstine, J.; Driedger A.; and Foster, D.; *J. Electrochem. Soc.* **2003**, 150, A1351-A1356.

[26] Lu, Y.-C.; Gasteiger, H.A.; Crumlin, E.; McGuire Jr. R.; Shao-Horn, Y.; *J. Electrochem. Soc.* **2010**, 157, A1016-A1025.

[27] Débart, A.; Bao, J.; Armstrong, G.; Bruce, P.G.; *J. Power Sources* **2007**, 174, 1177-1182.

[28] Oh, S.; Nazar, L.F.; *Adv. Energy Mater.* **2012**, 2, 903-910.

[29] Black, R.; Lee, J.-H.; Adams, B.; Mims, C.A.; Nazar, L.F.; *Angew. Chem. Int. Ed.* **2012**, 51, 392-396.

[30] Cheng, H.; Scott, K., *J. Power Sources* **2010**, 195, 1370-1374.

[31] Ogasawara, T.; Débart, A.; Holzapfel, M.; Novàk, P.; Bruce, P.G.; *J. Am. Chem. Soc.* **2006**, 128, 1390-1393.

[32] McCloskey, B.D.; Scheffler, R.; Speidel, A.; Bethune, D.S.; Shelby, R.M.; Luntz, A.C.; *J. Am. Chem. Soc.* **2011**, 133, 18038-18041.

[33] Harding, J.R.; Lu, Y.-C.; Tsukada, Y.; Shao-Horn, Y.; *Phys. Chem. Chem. Phys.* **2012**, 14, 10540-10546.

[34] Peled, E.; *J. Electrochem. Soc.* **1979**, 126, 2047-2051.

[35] Freunberger, S.A.; Chen, Y.; Peng, Z.; Griffin, J.M.; Hardwick, L.J.; Bardé, F.; Novàk, P.; Bruce, P.G.; *J. Am. Chem. Soc.* **2011**, 133, 8040-8047.

[36] Tsiouvaras, N.; Meini, S.; Buchberger, I.; Gasteiger, H.A.; *J. Electrochem. Soc.* **2013**, 160, A471-A477.

[37] McCloskey, B.D.; Bethune, D.S.; Shelby, R.M.; Girishkumar, G.; Luntz, A.C.; *J. Phys. Chem. Lett.* **2011**, 2, 1161-1166.

[38] Peng, Z.; Freunberger, S.A.; Hardwick, L.J.; Chen, Y.; Giordani, V.; Bardé, F.; Novàk, P.; Graham, D.; Tarascon, J.-M.; Bruce P.G.; *Angew. Chem. Int. Ed.* **2011**, 50, 6351-6355.

[39] O Laoire, C.; Mukerjee, S.; Plichta, E.J.; Hendrickson, M.A.; Abraham, K.M.; *J. Phys. Chem. C* **2010**, 114, 9178-9186.

[40] Bryantsev, V.S.; Blanco, M.; *J. Phys. Chem. Lett.* **2011**, 2, 379-383.

[41] Laino, T.; Curioni, A.; *Chem. Eur. J.* **2012**, 18, 3510-3520.

[42] Herranz, J.; Garsuch, A.; Gasteiger, H.A.; *J. Phys. Chem. C* **2012**, 116, 19084-19094.

[43] Bryantsev, V.S.; Giordani, V.; Walker, W.; Blanco, M.; Zecevic, S.; Sasaki, K.; Addison, D.; Chase, G.V.; *J. Phys. Chem. A* **2011**, 115, 12399-12409.

[44] Walker, W.; Giordani, V.; Uddin, J.; Bryantsev, S.; Chase, G.V.; Addison, D.; *J. Am. Chem. Soc.* **2013**, 135, 2076-2079.

[45] Schwenke, K.U.; Meini, S.; Piana, M.; Wu, X.; Gasteiger H.A.; *Phys. Chem. Chem. Phys.* **2013**, DOI: 10.1039/C3CP51531A.

[46] Gallant, B.M.; Kwabi, D.G.; Mitchell, R.R.; Zhou, J.; Thompson, C.V.; Shao-Horn, Y.; *Energy Envir. Sci.* **2013**, DOI: 10.1039/C3EE40998H.

[47] Albertus, P.; Girishkumar, G.; McCloskey, B.D.; Sànchez-Carrera, R.S.; Kozinsky, B.; Christensen, J.; Luntz, A.C.; *J. Electrochem. Soc.*, **2011**, 158, A343-A351.

[48] Hummelshøj, J.S.; Blomqvist, J.; Datta, S.; Vegge, T.; Rossmeisl, J.; Thygesen, K.S.; Luntz, A.C.; Jacobsen, K.W.; Nørskov, J.K.; *J. Chem. Phys.* **2010**, 132, 071101.

[49] Viswanathan, V.; Thygesen, K.S.; Hummelshøj, J.S.; Nørskov, J.K.; Girishkumar, G.; MCloskey, B.D.; Luntz, A.C.; *J.Chem. Phys.* **2011**, 135, 214704.

[50] Meini, S.; Piana, M.; Beyer, H.; Schwaemmlein, J.; Gasteiger, H.A.; *J. Electrochem. Soc.* **2012**, 159, A2135-A2142.

[51] Adams, B.D.; Radtke, C.; Black, R.; Trudeau, M.L.; Zaghib, K.; Nazar, L.F.; *Energy Environ. Sci.* **2013**, 6, 1772-1778.

[52] Mitchell, R.R.; Gallant, B.M.; Shao-Horn, Y.; Thompson, C.V.; *J. Phys. Chem. Lett.* **2013**, 4, 1060-1064.

[53] Gowda, S.R.; Brunet, A.; Wallraff, G.M.; McCloskey, B.D.; *J. Phys. Chem. Lett.* **2013**, 4, 276-279.

[54] Takechi, K.; Shiga, T.; Asaoka, T.; *Chem. Commun.* **2011**, 47, 3463-3465.

[55] Meini, S.; Piana, M.; Tsiouvaras, N.; Garsuch, A.; Gasteiger, H.A.; *Electrochem. Solid-State Lett.* **2012**, 15, A45-A48.

[56] Meini, S.; Tsiouvaras, N.; Schwenke, K.U.; Piana, M.; Beyer, H.; Lange, L.; Gasteiger, H.A.; *Phys. Chem. Chem. Phys.* **2013**, DOI: 10.1039/C3CP51112J.

[57] Beyer, H.; Meini, S.; Tsiouvaras N.; Piana M.; Gasteiger, H.A.; *Phys. Chem. Chem. Phys.* **2013**, DOI: 10.1039/C3CP51056E.

[58] McCloskey, B.S.; Speidel, A.; Scheffler, R.; Miller, D.C.; Viswanathan, V.; Hummelshoj, J.S.; Norskov, J.K.; Luntz, A.C.; *J. Phys. Chem. Lett.* **2012**, 3, 997-1001.

[59] Peng, Z.; Freunberger, S.A.; Chen, Y.; Bruce, P.G.; *Science* **2012**, 337, 563-566.

[60] Ottakam Thotiyl, M.M.; Freunberger S.A.; Peng, Z.; Bruce P.G.; *J. Am. Chem. Soc.* 2013, 135, 494-500.

[61] C.H. Hamann and W. Vielstich. Elektrochemie. Wiley/VCH, Weinheim, 2005. 4. Vollständig überarbeitete Auflage

[62] Huggins, R.; *Advanced Batteries: Materials Science Aspects*. Springer, **2009**.

[63] Bard, A.J.; Faulkner, L.R.; *Electrochemical Methods, Fundamentals and Applications*. John Wiley & Sons, New York, **2001**.

[64] Greef, R.; Peat, R.; Peter, L.M.; Pletcher, D.; Robinson, J.; *Instrumental Methods in Electrochemistry*. Ellis Horwood Ltd., Chircherster, **1985**.

[65] Marks, T.; Trussler, S.; Smith, A.J.; Xiong, D.; Dahn, J.R.; *J. Electrochem. Soc.* **2011**, 158, A51-A57.

[66] Aurbach, D.; *Nonaqueous Electrochemistry*. Marcel Dekker, New York, **1999**.

[67] Gampp, H.; Lippard, S.J.; *Inorg. Chem.* **1983**, 22, 357-358.

[68] Che, Y.; Tsushima, M.; Matsumoto, F.; Okajima, T.; Tokuda, K.; Ohsaka, T.; *J. Phys. Chem. A* **2009**, 113, 912-916.

[69] Lasia, A.; *Electrochemical Impedance Spectroscopy and its Applications. Modern Aspects of Electrochemistry*. Conway, B.E. and White, R.E. Edts., Kluwer Academic/Plenum Publishers, New York, **1999**, Vol. 32, p. 143-248.

[70] Barsoukov, E.; Macdonald, J.R.; *Impedance Spectroscopy, Theory, Experiment, and Applications*. John Wiley & Sons, New York, **2005**.

[71] Xu, W.; Viswanathan V.; Wang, D.; Towne, S.A.; Xiao, J.; Nie, Z.; Hu, D.; Zang, J.-G.; *J. Power Sources* **2011**, 196, 3894-3899.

[72] Tran, C.; Yang, X.-Q.; Qu, D.; *J. Power Sources* **2010**, 195, 2057-2063.

[73] McCloskey, B.D.; Bethune, D.S.; Shelby, R.M.; Mori, T.; Scheffler, R.; Speidel, A.; Sherwood, M.; Luntz, A.C.; *J. Phys Chem. Lett.* **2012**, 3, 3043-3047.

[74] Hayyan, M.; Mjalli, F.S.; Hashim, M.A.; AlNashef, I.M.; Al-Zahrani, A.M.; Chooi, K.L.; *J. Electroanal. Chem.* **2012**, 664, 25-32.

[75] Jung, H-.G.; Hassoun, J.; Park, J.-B.; Sun, Y.-K.; Scrosati, B.; *Nature Chemistry* **2012**, 4, 579-585.

[76] Zhang, T.; Zhou, H.; *Nature Communications* **2013**, DOI: 10.1038/ncomms2855.

[77] Giordani, V.; Freunberger, S.A.; Bruce, P.G.; Tarascon, J.-M.; Larcher, D.; *Electrochem. Solid-State Lett.* **2010**, 13, A180-A183.

[78] Melucci, R.C.; Wightman, J.P.; *Carbon* **1966**, 4, 467-472.

List of Figures

Figure 1.1. Schematic working principle of a Li-air battery 14
Figure 1.2. Typical voltage profile of a Li-air cell 15
Figure 1.3. Proposed mechanism for the degradation of alkyl-carbonate 17
Figure 2.1. Scheme of a typical battery cell configuration... 20
Figure 2.2. Comparison between two-electrode and three-electrode cell................... 22
Figure 2.3. Design differences between Li-ion and Li-air positive electrodes........... 23
Figure 2.4. Chemical structures of commonly used solvents and binders.................. 24
Figure 2.5. Electrode preparation 26
Figure 2.6. Airtight ZrO_2 ball mill jar... 27
Figure 2.7. Chemical structures of typical solvents and salts.................................... 28
Figure 2.8. Schematic illustration of the standard procedure for superoxide............. 28
Figure 2.9. Exploded view of the Li-air cell developed at TUM 31
Figure 2.10. Current profile of a rechargeable battery cell.. 32
Figure 2.11. Procedure for the determination of background currents....................... 34
Figure 2.12. Nyquist plot for presenting EIS data 35
Figure 2.13. Voltage and inner pressure profile 36
Figure 2.14. Scheme of the system used for O_2 consumption measurements 37
Figure 2.15. Technical scheme and real pictures of the OEMS 39
Figure 2.16. Schematic illustration of the data processing... 41
Figure 2.17. Regular sample holder for flat samples.. 43
Figure 2.18. Inner view of the TGA furnace 46

List of Tables

Table 1.1. Schematic working principle of a Li-air battery.. 45
Table 3.1. Typical voltage profile of a Li-air cell... 55

Acknowledgements

First, I would like to thank Dr. Michele Piana for his fundamental advice during the editing process of my doctoral thesis, and in general for his contribution to my doctoral education at TEC.

A warm acknowledgement is directed to Dr. Nikolaos Tsiouvaras, for the provided help during the preliminary writing period of my doctoral thesis and his great scientific support. Useless to say, for the great time in Munich as well.

Special thanks to Dr. Cuneyt Kavakli and Dr. Juan Herranz, for the scientific support and the great time spent at TEC during my doctoral period, improved by the convergent south European enthusiasm for garlic.

A warm acknowledgement to Dr. Hans Beyer, companion of "interesting" TGA experiments, and example of scientific rigor and experimental competence.

A big thank you to Uta Schwenke, for her provided help in the challenging characterization of my electrode samples.

Many thanks to Veronika Pichler, for making my stay at TUM technically possible, and for the great organization of the whole group.

An grateful acknowledgement is dedicated to Dr. Arnd Garsuch for the fruitful discussions and for organizing enjoyable project meetings at BASF.

A special greeting to Anna Eberle and Rebecca Zeh for the essential support in the laboratory and the great time in our office. A greeting to Dominik Haering and Thomas Mittermeier, the "male side of the office".

A passionate acknowledgement to Armin Siebel, the only hero I could talk pleasantly about informatics and electronics with.

Dulcis in fundo, I would like to thank Prof. Dr. Hubert A. Gasteiger for giving me the opportunity to join TEC and study energy storage and conversion. Under his supervision I learned the scientific rigor and depth of analysis which are basic skills of a successful researcher. A special thanks also for offering me opportunities to improve my knowledge and implement my newly developed skills.

To all of you, thank you!

Curriculum Vitae

Stefano Meini

Ständlerstr. 71
81549 Munich

Mobile: +49 (0) 176 36757039
e-mail: stefanomeini@gmail.com

Born: 26th of June 1985 in Florence, Italy
Nationality: Italian

Education

Doctoral Thesis *June 2010 – Present*

Chair of Technical Electrochemistry, Chemistry Department, Technische Universität München (TUM), Germany

Subject:	The Influence of Irreversible Electrochemical Reactions on the Fundamental Mechanisms Governing Capacity and Cycle-Life of Li-O_2 Batteries
Research Stay	Bar-Ilan University, Israel (January 2013 - March 2013)
Workshop	The 2nd International Fuel Cell Summer Seminar for Young Scientists University of Yamanashi, Japan (28 August 2011 - 02 September 2013)
Supervisor	Prof. Dr. Hubert A. Gasteiger

Master Studies Chemistry *October 2007 – December 2009*

Chemistry Department, University of Florence, Italy

Subject:	Tire Pyrolysis Using a Microwave Oven: Production of Hydrocarbons
Supervisor	Prof. Piero Frediani

B.Sc. in Chemistry *October 2004 – December 2007*

Chemistry Department, University of Florence, Italy

Subject:	A New Polyamonic Receptor as Fluorimetric Chemosensor for Nucleotide Anions
Supervisor	Prof. Dr. Andrea Bencini

School Education *September 1999 - July 2004*

Liceo Scientifico Ernesto Balducci, Pontassieve, Italy

Subjects:	Italian, Latin and English Literature, Mathematics, Physics, Chemistry
Degree	Diploma di Liceo Scientifico

Accomplishments

8 peer reviewed publications, 1 patent, 2 oral presentations in international conferences

Conference Oral Presentations

1. 2nd International Conference on Materials for Energy. Karlsruhe, Germany. May **2013**.

2. PRiME Pacific Rim Meeting on Electrochemical and Solid-State Science, Electrochemical Society. Honolulu, Hawaii. October **2012.**

Poster presentation

1. The 2nd International Fuel Cell Summer Seminar for Young Scientists. Nagano (Yamanashi) Japan. August **2012**.

2. 1st Colloquium of the Munich School of Engineering, Sustainable Energy Supply of the Future. Munich, Germany. July **2011**.

3. Joint Workshop Munich Catalysis Research Center with Northwestern University, Evanston IL, USA, Energy and Sustainability: Materials and Processes. Munich, Germany. May **2011**.

Munich, 14 of June 2013

Meini Stefano

List of Publications

1. **Meini S.**, Elazari R., Rosenman A., Salitra G., Garsuch A., and Aurbach D.; Enhancing Li_2S Utilization at Low Potential for Activating Electrodes for Li-S Battery Manufacturing, in preparation.
2. Kavakli C., **Meini S.**, Harzer G., Tsiouvaras N., Piana M., Siebel A., Garsuch A., Gasteiger H.A., and Herranz J.; Nano-Sized Carbon-Supported MnO_x-Phases as Li-O_2 Battery Cathode Catalysts. *ChemCatChem*, accepted.
3. **Meini S.**, Tsiouvaras N., Schwenke K.U., Piana M., Beyer H., Lange L., and Gasteiger H.A.; Rechargeability of Li-air Cathodes Filled with Discharge Products Using an Ether-Based Electrolyte: Implications for Rechargeability and Cycle-Life of Li-air Cells. *Phys. Chem. Chem. Phys.* **2013**, DOI:10.1039/C3CP51112J.
4. Beyer H., **Meini S.**, Tsiouvaras N., Piana M., and Gasteiger H.A.; Thermal and Electrochemical Decomposition of Lithium Peroxide in Non-Catalyzed Carbon Cathodes for Li-Air batteries. *Phys. Chem. Chem. Phys.* **2013**, DOI:10.1039/C3CP51056E.
5. Schwenke K.U., **Meini S.**, Piana M., Wu X., and Gasteiger H.A.; Stability of Superoxide Radical in Glyme Solvents for Non-Aqueous Li-O_2 Battery Electrolytes. *Phys. Chem. Chem. Phys.* **2013**, DOI:10.1039/C3CP51531A.
6. Tsiouvaras N., **Meini S.**, Buchberger I., and Gasteiger H.A.; A Novel On-Line Mass Spectrometer Design for the Study of Multiple Charging Cycles of a Li-O_2 Battery. *J. Electrochem. Soc.* **2013**, 160, A471-A477.
7. **Meini S.**, Piana M., Beyer H., Schwaemmlein J., and Gasteiger H.A.; Effect of Carbon Surface Area on First Discharge Capacity of Li-O_2 Cathodes and Cycle-Life Behavior in Ether-Based Electrolytes. *J. Electrochem. Soc.* **2012**, 159, A2135-A2142.
8. **Meini S.**, Piana M., Tsiouvaras N, Garsuch A., and Gasteiger, H.A.; The Effect of Water on the Discharge Capacity of a Non-Catalyzed Carbon Cathode for Li-O_2 Batteries. *Electrochem. Solid-State Lett.* **2012**, 15, A45-A48.
9. Undri A., **Meini S.**, Rosi L., Frediani M., and Frediani P.; Microwave Pyrolysis of Polymeric Materials: Waste Tires Treatment and Characterization of the Value-Added Products. *J. Anal. Appl. Pyrolysis*, DOI: 10.1016/j.jaap.2012.11.011.
10. Bazzicalupi C., Bencini A., Biagini S., Faggi E., **Meini S.**, Giorgi C., Spepi A., and Valtancoli B.; Exploring the Binding Ability of Phenanthroline-Based Polyammonium Receptors for Anions: Hints for Design of Selective Chemosensors for Nucleotides. *J.Org. Chem.* **2009**, 74, 7349-7363.

Patents

Frediani P., Rosi L., Frediani M., Undri A., Occhialini S., and **Meini S.**, “*Production of Hydrocarbons From Pyrolysis of Tires*”, WO/2012/110991A1.